CHALMERS
UNIVERSITY OF TECHNOLOGY

Performance optimization of CLT (NextGenCLT)

Master's thesis in Structural Engineering and Building Technology

Hanna Kurzawinska
Mohammad Tahmasebi

DEPARTMENT OF ARCHITECTURE AND CIVIL ENGINEERING
CHALMERS UNIVERSITY OF TECHNOLOGY

Gothenburg, Sweden 2023
www.chalmers.se

MASTER'S THESIS ACEX30

Performance optimization of CLT (NextGenCLT)

Master's thesis in Structural Engineering and Building Technology

Hanna Kurzawinska
Mohammad Tahmasebi

Department of Architecture and Civil Engineering
Division of Structural Engineering
Lightweight Structures
CHALMERS UNIVERSITY OF TECHNOLOGY
Göteborg, Sweden 2023

Performance optimization of CLT (NextGenCLT)

Master's Thesis in the Master's Programme Structural Engineering and Building Technology

HANNA KURZAWINSKA

MOHAMMAD TAHMASEBI

Examensarbete ACEX30
Institutionen för arkitektur och samhällsbyggnadsteknik
Chalmers tekniska högskola, 2023

Department of Architecture and Civil Engineering
Division of Structural Engineering
Lightweight Structures
Chalmers University of Technology
SE-412 96 Göteborg
Sweden
Telephone: + 46 (0)31-772 1000

Cover: Applying glue between lamellas when air gaps are introduced in a CLT panel.
Department of Architecture and Civil Engineering
Göteborg, Sweden, 2023

Performance Optimization of CLT panels (NextGenCLT)

Master's thesis in the Master's Programme Structural Engineering and Building Technology

HANNA KURZAWINSKA

MOHAMMAD TAHMASEBI

Department of Architecture and Civil Engineering
Division of Structural Engineering
Lightweight Structures
Chalmers University of Technology

ABSTRACT

Nowadays, the building and construction sector plays a significant role in energy consumption, leading to a growing demand for sustainable solutions and material optimization to reduce CO2 emissions. Cross-laminated timber (CLT) panels have gained attention due to their lightweight and renewable nature, ease of transportation and assembly, and excellent thermal and insulation properties. However, considering the environmental and economic aspects, minimizing the raw material usage in CLT panel production is crucial.

To investigate the effects of reducing material in the central part of a CLT panel through the introduction of air gaps in the cross-layers, shear and four-point bending tests were conducted on small and large samples produced in both a university workshop and a CLT factory. The experimental results were compared with FEM models created in MATLAB and ABAQUS.

The study focused on conducting shear tests on small specimens with five different configurations of air gaps, analysing their dimensions and arrangement. The deflection and bending capacity were compared with a solid CLT panel, with specific attention given to two configurations featuring central air gaps but differing in size.

The shear testing results of CLT panels with various air gap configurations revealed that configuration with overlapping between cross layers demonstrated the highest net rolling shear modulus and net shear strength. The amount of overlap impacted material saving and net shear strength and increasing the air gap size in centrally arranged configurations led to decreasing the net shear strength.

From the four-point bending test, the analysis of different configurations reveals that introducing air gaps with dimensions of 6 cm between cross layers leads to a 13% material reduction, which closely follows the bending stiffness of solid specimens. However, increasing the air gap dimension to 12 cm shows a 19% material reduction, but a significant decrease in bending stiffness is observed. The deflection increases with wider air gaps, leading to reduced bending stiffness in configuration with air gaps compared to solid panels. The results emphasize the importance of accurately defining factors such as κ_s in calculating deflection and bending stiffness, especially for panels with air gaps. Adjusting κ_s based on the panel's geometry and air gap arrangement is crucial for accurate predictions.

Keywords: Cross-laminated timber, CLT, material optimization, air gaps, shear strength, shear modulus, bending stiffness, strength test

Contents

List of figures

List of tables

Preface

We would like to express our deep gratitude to our considerate supervisor and examiner, Robert Jockwer, for imparting us with profound knowledge and for his invaluable guidance and unwavering support throughout the thesis. We would also like to extend our appreciation to our supervisor, Yutaka Goto, for his constant encouragement and expert guidance.

Additionally, we sincerely acknowledge the indispensable assistance, guidance, and patience provided by Tabita Nilsson, Peter Lindblom, and Per Lundström during the extensive hours spent in the workshop. We are also indebted to Sebastian Almfeldt and Anders Karlsson in the Structures Lab for their support and relentless optimism.

Hanna Kurzawinska, Gothenburg, June 2023

Mohammad Tahmasebi, Gothenburg, June 2023

Notations

Roman upper case letters

A	Area
D	Stiffness matrix
E	Young's modulus
EI	Stiffness
F	Point load
G	Shear modulus
G_v	Panel shear modulus of rigidity
I_{eff}	Effective moment of inertia
I_{net}	Net moment of inertia
$I_{x,net}$	Net moment of inertia along the x-axis
$I_{y,net}$	Net moment of inertia along the y-axis
L	Length
M	Moment
MOE	Modulus of elasticity
$M_{y,d}$	Moment design value about the y-axis
P_{max}	Maximum design force
S	Stress
$S_{x,net}$	Panel's net static moment
$S_{y,net}$	Panel's net static moment
V	Volume
V	Shear
$V_{xz,d}$	Design shear force
$V_{yz,d}$	Design shear force
$W_{x,net}$	Panel's net moment of resistance

Roman lower case letters

a	Distance
b	Width
f_d	Design strength value
f_k	Characteristic strength value
$f_{m,xlay,d}$	Bending strength design value,
f_r	Planer (rolling) shear strength
$f_{v,9090,xlay,d}$	Design value for the rolling shear strength of the boards
$f_{v,9090,xlay,k}$	Characteristic rolling shear strength of the boards
$f_{v,9090,ylay,d}$	Design value for the longitudinal shear strength of the boards
$f_{v,9090,ylay,k}$	Characteristic longitudinal shear strength of the boards
h	Height of the CLT panel
k_{mod}	Modification factor
k_{sys}	System strength factor
m	Weight
q	Uniformly distributed load
t	Thickness
w	Deflection

Greek letters

α	Angle
γ_i	Gamma-factor
γ_M	Partial factor for material properties
$\Delta_{bending}$	Bending deflection
Δ_{shear}	Shear deflection
η_A	Pressure area ratio
η_L	Length ratio
η_M	Material reduction factor
η_S	Shear ratio
η_v	Volume ratio
κ	Shear correction factor
λ	Void ratio
ν	Poisson's ratio
ρ	Density
$\sigma_{m,y,d}$	Bending stress in the CLT panel's plane
$\tau_{Rv,yz,d}$	Design value of rolling shear strength
$\tau_{Rv,xz,d}$	Design value of shear strength

1 Introduction

The buildings and construction sector were responsible for 37 percent of global energy consumption in 2021. It exceeded the level by 5 percent compared to the year 2020 and the peak in 2019 by 2 percent. Other data shows that the construction materials such as concrete, steel, or cement are the main contributors to the emission of greenhouse gasses and represent about 9 percent of CO2 global emissions. Based on the trends and predictions, it is not possible to reach decarbonization in the building sector by 2050, so significant changes should be made. Some recommendations on how to lower carbon dioxide have been presented in UN global report and include minimizing the CO2 emissions by value chain of the industries or zero-carbon strategy implementation for new and existing buildings [1]. This means that more sustainable solutions and materials should be widely introduced to decrease the CO2 emission produced by the building industry and stop the global warming process [1].

Some green materials or eco-friendly design concepts have already been used in the construction sector and are constantly being developed. They include green roofs, straw, bamboo, or different wood-based products. Cross-laminated timber panels are relatively new structural wood materials, and the first small-scale CLT buildings were constructed in Sweden in the 2000s [2]. They are more widely used nowadays because of many advantages, including very good load-bearing capacity and sustainable aspects, compared to traditional construction materials. However, besides many pros of using CLT as a construction material, the panels can be manufactured in a more efficient way [3]. It might be possible to use less raw material and achieve load-bearing capacity at the same level when the lamellas and the air gaps are arranged in a proper way.

The aim of the thesis is to develop new type of cross-laminated timber (CLT) panels by implementing air gaps between cross-layers and optimizing the composition and amount of timber. As a result, the amount of raw material used to produce CLT panels will reduce significantly, leading to more environmentally friendly and possibly used in a more efficient way in designing and building new structures.

1.1 Background

CLT is the abbreviation of cross-laminated timber. CLT is a well-known engineered product which used as structural components, primarily walls, and floors, in many buildings such as industrial, houses, hospitals, and so on. The structure of a CLT panel allows bearing loads in and out of the plane. CLT is an environmentally friendly material, and it can be recycled and used in new structures. There are many advantages to using CLT, such as being lightweight, which makes them easy to transport and assemble, and having good thermal insulation and fire safety protection. Flexible production, small tolerance in manufacturing, and easy to produce any shape and size [4].

The usage of CLT in Sweden comes back to the 1990s; the development of CLT in the 1990s was motivated to find a way to use lower-quality boards (lamellas) for a higher-value product [5]. The first residential building that used CLT reflecting

the current state of the art was in 1995 by Moser [6]. Gülzow [7]used a frequency measurement to determine elastic and shear modulus . The first European standard for CLT was published in 2015 and design of CLT elements will be included in the next generation of the European timber design code as EN 1995-1-1. An overview and development of CLT were published in 2016 by Brandner [8] that contains useful information about the historical development of cross-laminated timber.

Using Wood for CLT production is a sustainable solution and has some environmental advantages; for example, a hybrid CLT building can reduce 26.5% the global warming potential compared to a traditional reinforced concrete building [9], but it is an inefficient point of structural use of the material. The center and core part of the CLT panels does not contribute much to the structure behavior except for shear. Paul Mayencourt and his colleagues [10] showed that around 20 percent of the material could be saved without a significant effect on structural behavior when the optimized panel was analyzed and tested in bending. Research done by Ben Toosi [11] showed that around 70 percent of the production cost for a CLT panel is for raw materials; this Figure can go down to around 59 percent in other studies [12]. The load capacity of an optimized CLT panel in one configuration with equal air gap arrangements between cross layers was examined by Mayencourt. The results show that the new panels were 21.8 percent lighter than the standard ones and the stiffness was reduced between 8.1 to 14.2 percent, and the load capacity was reduced to about 31 percent due to the low bond and poor glue between the layers, and the main failure mode was delamination of cross-layer [10].

George Silly and his colleagues showed the possible options for the optimization of the CLT panels. They explained that there are some advantages of using air gaps between cross layers, such as a significant reduction of material and the possibility of using these spaces to improve insulation and acoustic properties. On the other hand, it leads to raising new questions regarding the design process and significant reduction of shear and transverse bending stiffness [13]. Lorenzo Franzoni and his colleagues studied the bending behavior of regularly spaced CLT panels experimentally and theoretically. They concluded that the bending stiffness would be reduced as the space between lamellas increases and follows the wood volume fraction within the panel, and the number of layers has a small influence on the bending stiffness reduction. The transversal shear stiffness results show that the reduction of stiffness does not follow the volume fraction, and it is also affected by the aspect ratio of lamellas [14].

Moberg and Xiao did their master's thesis regarding the optimization of the CLT panels with different configurations. They found that a symmetric air gap layout configuration with a width of air gap equal to 120 mm has the highest material saving, equal to 20 percent, but the failure load was about 50 percent compared to the solid CLT panels. For the air gap width equal to 60 mm 14 percent of material reduction was obtained and the failure load was reduced to 57 to 67 percent compared to the solid configuration In general, they realized that optimized CLT panels with a symmetric airgap layout are more effective compared to the shifted airgap configuration. Moreover, by increasing the air gap width, the shear strength of the panels decreases significantly [15]. Therefore, it is evident

that CLT panels can be optimized by introducing air gaps between cross layers to improve the sustainability aspect as a construction material and reduce the production cost and making it even more attractive for clients and the building industry, but there is also a lot of uncertainties about the structural performance of these types of CLT panels.

1.2 Aim

The project aims to develop an innovative cross-laminated timber panel for load-bearing structures in buildings. The research focuses on the optimization of CLT panels, using experimental and numerical analysis methods for small and large-scale CLT panels.

The main objective of this thesis is to perform shear tests of small-scale specimens in six different configurations of cross-layers and air gaps. Three arrangements are studied for centered air gaps CLT panels, while the others are for shifted air gaps, and all results are compared with an ordinary solid CLT panel and finite element modeling in ABAQUS software. Furthermore, the strength tests are conducted to analyze the large-scale panel behavior that will be produced by Stora Enso company, and the results are compared with a numerical model.

1.3 Methodology

The work was carried out by doing experimental tests on the small and large-scale CLT panels; in addition, the Finite Element Method was used to compare and validate the results. The project was performed in four phases, as explained below.

1. Literature study

As a first step, the literature study was conducted in order to get enough background knowledge regarding the CLT panels, including grading, design, and test methods.

2. Preparation and manufacturing

The small specimens based on the six different sizes and arrangements of the cross layers were produced in the Architecture wood workshop at the Chalmers University of Technology. An adhesive was applied between the wood lamellas, and they were pressed together by using the hand-screw steel clamp. In addition, the large-scale panels were produced by the Stora Enso company in Austria.

3. Testing and evaluation of results

In this phase, the rolling shear and stiffness of the small and large-scale specimens were tested in the Structural Lab at the Chalmers University of Technology. For the full-scale panels, the bending test with loads perpendicular to the plane and the small CLT panels shear test was carried out according to the SS-EN 16351:2015 (E).

4. Numerical Analysis

A numerical model for all samples was created and analyzed in the ABAQUS software, and the strength properties were compared with the physical strength properties that come from experimental data and test results.

1.4 Limitations

The master thesis was carried out as a part of a research project funded by FORMAS called "Novel wood panel for the efficient and healthy built environment" (registration number: 2020-01784.) Furthermore, StoraEnso is an external advisor and industrial partner of the project.

The main goal is to analyze the structural performance of the optimized CLT panels so the other properties, such as hygrothermal performance, are not included in the project.

The small-scale specimens are subjected to shear tests in order to derive the rolling shear strength and stiffness of the elements. On the other hand, the stiffness of the large-scale specimens are obtained from the bending test. The small-scale specimens are built from five layers, and each layer has a thickness of 20 mm and a width of 100 mm, and the lengths depend on the panel's configuration. The layers are glued together using PVAC-based adhesive for creating the specimens; only one wood species is used, which is Scandinavian Spruce.

The analyses and evaluations are performed based on the climatic and load conditions that occur in Sweden. Moreover, the results are assessed according to Swedish standards.

2 Theory

This chapter explores the theory and properties of Cross-Laminated Timber (CLT) panels, focusing on important aspects such as strength grading, density, and modulus of elasticity (MOE). Additionally, it examines Euler-Bernoulli and Timoshenko's design theories, which help analyze CLT panel behavior under different loads. Moreover, the crucial role of the CLT Handbook in guiding design practices is discussed. The chapter covers the shear strength test method and the four-point bending test method, both used to assess the structural performance of CLT panels. Furthermore, it is touched upon the use of FEM modeling in ABAQUS software for simulating and analyzing CLT panel behavior. Finally, prospective failure modes, including shear failure, bending failure, and delamination, are examined.

2.1 CLT properties

Wood is an anisotropic material, and its properties vary in three main directions. However, they are not random, so wood is considered a cylindrical orthotropic material. The main three directions are illustrated in Figure 2-1.

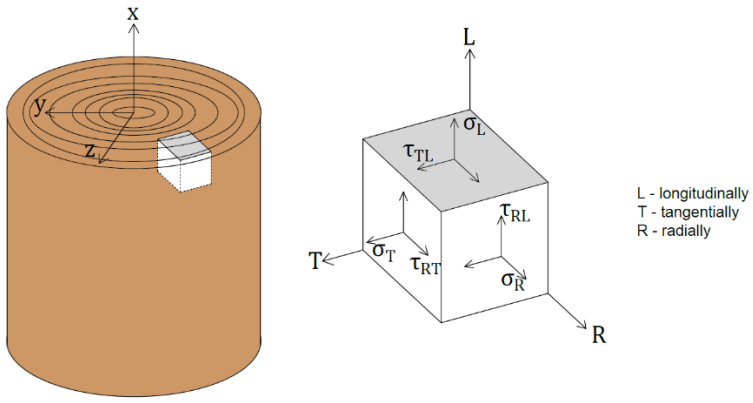

Figure 2-1 Three main directions in the wood.

One of the main properties is stiffness (modulus of elasticity), and the relation between three different directions in the longitudinal, radial, and tangential directions followed the ratio of 20:1.6:1, respectively [16]. Due to this significant difference between the longitudinal and two other directions, the modulus of elasticity is considered as zero for the direction perpendicular to the grains [2].

There are many applications for CLT panels, for example, floors, walls, and beam elements. There are two ways of loading such elements. A load can be applied perpendicular to the plane or out of the plane, named plate action, and it can be loaded parallel to the plane as wall elements, named panel action, see Figure 2-2.

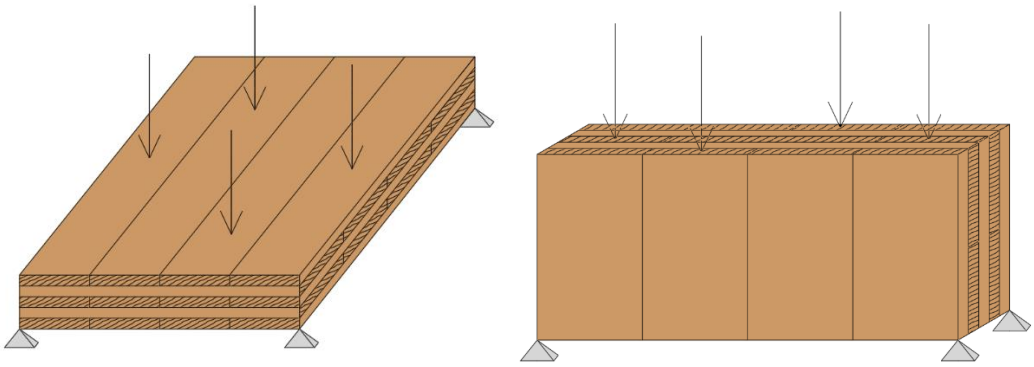

Figure 2-2 Two ways of loading CLT panels: plane and panel actions.

The final properties of CLT panels depend on many parameters, as listed below:

- Strength and stiffness of each layer
- Thickness of layers
- Arrangement of layers
- Number of layers

In addition, moisture and loading time will affect the strength of a CLT panel. With the increasing moisture and loading time, the strength will decrease.

2.1.1 Strength grading of timber

In order to estimate the material properties of wood, it is necessary to grade the material. The strength classes are determined by a combination of visual grading and machine strength grading. Visual grading involves assessing the surface appearance of the timber to determine the presence and severity of defects such as knots, shakes, and splits. Higher-grade woods have fewer defects and are therefore stronger and more suitable for load-bearing applications. Machine strength grading involves testing the timber's mechanical properties using non-destructive or destructive methods, such as ultrasound, bending tests, dynamic vibration test or X-Ray measurement.
EN 14081 and EN 338 are European standards that include grading and strength classification of sawn timber. Numerous strength classes for softwood lumber are defined based on their mechanical properties, for example:

C14 - This is the weakest strength class and includes lumber with a modulus of elasticity (MOE) of less than or equal to 8000 MPa and a modulus of rupture (MOR) of less than or equal to 14 MPa. It is suitable for non-structural uses such as packing cases and crates.

C16 - This strength class includes lumber with MOE greater than 8000 MPa and MOR greater than 16 MPa. It is suitable for use in non-load-bearing applications such as cladding, decking, and fencing.

C18 - This strength class includes lumber with MOE greater than 10,000 MPa and MOR greater than 18 MPa. It is suitable for use in load-bearing applications such as beams, joists, and studs.

C24 - This defines wood with MOE greater than 11,500 MPa and MOR greater than 24 MPa. It is suitable for use in high-load applications such as heavy construction, bridges, and laminated beams.

2.1.2 Density

Wood density refers to the mass or weight of wood per unit volume. It is commonly expressed in terms of kilograms per cubic meter (kg/m^3). Wood density is influenced by various factors, including the species of wood, growth conditions, age of the tree, and wood moisture content.

Density can affect the physical and mechanical properties of wood, including its strength, hardness, and durability. Dense woods tend to be stronger and more resistant to wear, while lighter woods may have better insulation properties. The density can be calculated by the below equation.

$$\rho = \frac{m}{V} \tag{2-1}$$

Where m is the weight, and V is the specimens' volume that can be calculated as below:

$$V = L \times b \times t \ [m^3] \tag{2-2}$$

Where L is the length, b is the width, and t is the thickness of the boards.

2.1.3 Modulus of elasticity

The modulus of elasticity (MOE) is a measure of the stiffness of wood, and it can be determined using several different testing methods. Some common methods for determining MOE of wood are:

- Static bending test: In this method, a sample of wood is supported at its ends and subjected to a load at its midpoint. The resulting deflection of the sample is measured, and the MOE is calculated using the sample dimensions and the load and deflection measurements.
- Eigenfrequency: In this method, a small piece of wood is subjected to a vibrational load, and the resulting resonant frequency is measured. The MOE can then be calculated using the density of the wood and the resonant frequency.
- Ultrasonic method: In this method, high-frequency sound waves are transmitted through a sample of wood, and the resulting velocity of the waves is measured. The MOE can then be calculated using the density of the wood and the velocity of the waves.

The eigenfrequency method was used for the determination of the MOE of the board used in the production of small specimens in this master thesis, was done by Anna Moberg and Linda Xiao [15].
Based on this method, the MOE can be calculated by the below equation:

$$MOE_{dyn,long} = \rho v^2 \ [Pa] \tag{2-3}$$

Where the ρ is the density and ν is the velocity of the sound in m/s.

Regardless of the method used, it is important to prepare the wood sample properly to ensure accurate results. The sample should be conditioned to a specific moisture content before testing to ensure that the results are consistent. It is worth noting that the MOE of wood can vary depending on several factors, including species, grain orientation, and moisture content. Therefore, it is important to standardize the testing conditions and sample preparation procedures to ensure consistent results.
All of the boards that are used to produce samples in this master thesis are categorized as C24 by the material supplier.

2.1.4 Coordinate system

As it is mentioned, wood is an orthotropic material, therefore, the orthotropic coordinate (L,T,R) should be used when the material parameters are defined. However, in the wood, these directions are different for each lamella due to the annual ring pattern. Thus the coordinate system (L,N,Z) is used instead of the orthotropic coordinates (L, T, R), see Figure below.

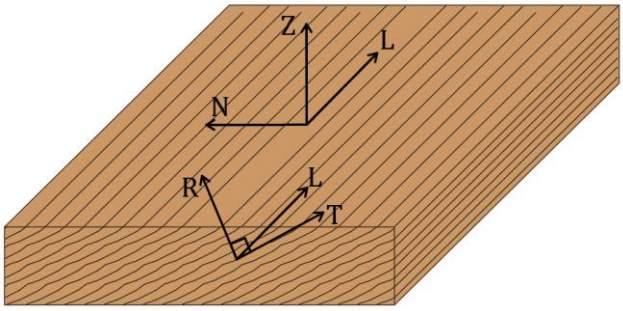

Figure 2-3 Lamella's coordinate system instead of the wood's orthotropic.

Therefore, the local coordinate system for lamellas is defined as shown in the figure below.

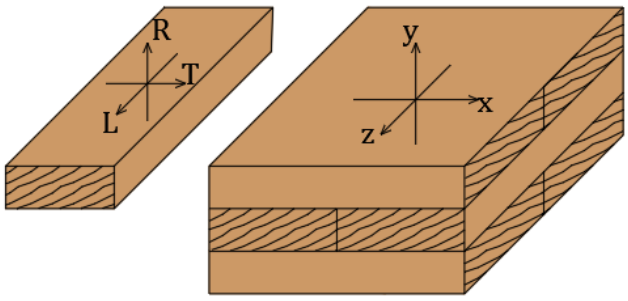

Figure 2-4 Local coordinate system for longitudinal and cross-layers.

Based on the CLT handbook [4] and [17], materials parameters are defined below; see Table 2-1. It is necessary to mention that the shear modulus is corrected based on the experimental results, and it is considered as 780 MPa instead of 690 MPa, which is mentioned in the CLT handbook, and the relation between rolling shear

modulus and shear modulus is assumed to be one-tenth. The value for density is the average of the density of lamellas that are used for production.

Table 2-1 Parameters of the CLT lamellas.

	E_L [MPa]	E_N [MPa]	E_Z [MPa]	G_{ZN} [MPa]	G_{LZ} [MPa]	u_{ZN} [-]	u_{LZ} [-]	u_{LN} [-]	r_{mean} [kg/m^3]
Longitudinal lamellas properties	11000	400	400	78	780	0.51	0.4	0.5	490

2.2 CLT design theories

In CLT panels, loads can be applied or distributed in three main directions. These directions based on SS-EN 16351 are defined below:

- X-axis is parallel to the grain of the outermost layer, and 0 represents the local axis parallel to the grain.
- Y-axis is perpendicular to the grain of the outermost layer, and 90 represents the local axis perpendicular to the grain both in a tangential and radial direction.
- Z-axis is perpendicular to the x-y plane, 090 is for a local plane spanned by local axis 0 and local axis 90, and 9090 is for a local plane spanned by local axis 90 and local axis 90.

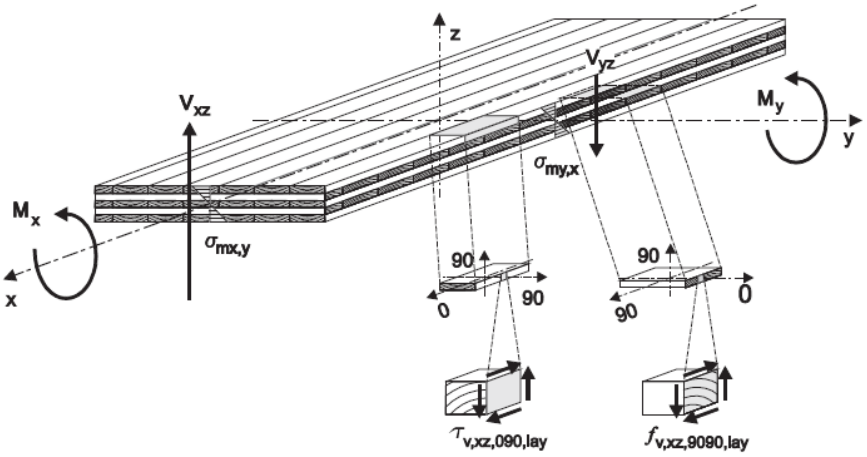

Figure 2-5 The definition of the axes and indices for forces, moments, stresses, and strengths in a CLT panel loaded out of a plane,figure from SS-EN 16351.

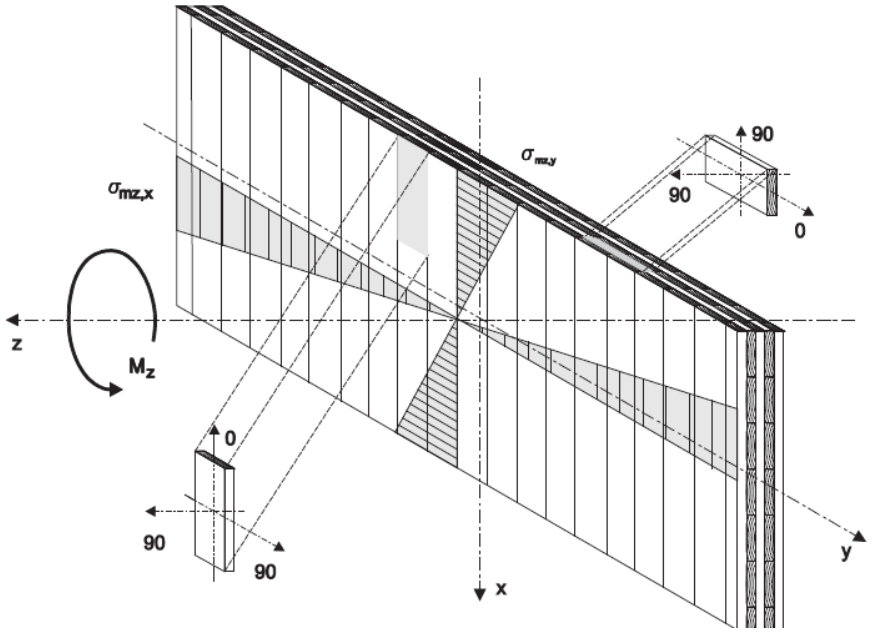

Figure 2-6 The definition of the axes and indices for forces, moments, stresses, and strengths in a CLT panel loaded in a plane, figure from SS-EN 16351.

CLT panels are sensitive to rolling shear when subjected to out-of-plane loading because they consist of relatively thick layers (compared to plywood). As mentioned above, wood as a material is the weakest in the tangential direction and is sensitive to split in that direction as well. When CLT is subjected to out-of-plane loading, rolling shear stresses occur in the panel. Rolling shear is observed due to the low resistance of the wood lamination in two of the weakest directions: radial and tangential.
Some research showed that CLT layup design and mechanical properties connected to thinner layers or smaller gaps between laminations are even more beneficial than sensitivity to rolling shear [16]. This means that for the CLT panels with the gaps that are the main object of the thesis, planar shear might govern the panel design. Since CLT panels have lightweight compared to other construction materials such as concrete slabs and composite floors, design is governed by the serviceability criteria such as deflection and vibration, and their strength, like shear and bending, has less effect.

2.2.1 Euler-Bernoulli theory

A beam behavior can be described by the Euler-Bernoulli beam theory of bending. The relation between the load, shear, moment, deflection, and slope can be described by the differential equation below.

$$\frac{d^2w}{dx^2} = \frac{M}{EI} \tag{2-4}$$

$$\frac{d^3w}{dx^3} = \frac{1}{EI}\frac{dM}{dx} = \frac{V}{EI} \tag{2-5}$$

$$\frac{d^4w}{dx^4} = \frac{1}{EI}\frac{dV}{dx} = \frac{q(x)}{EI} \tag{2-6}$$

Where M,V,q,w, and EI are moment, shear, uniformly distributed load, deflection, and stiffness, respectively. The nodal force and displacement can be expressed as a vector form, and by applying the force and moment equilibrium equations for a differential element of a beam substituting them in the bending energy expression, the preceding result can be summarized in a matrix form as below [18]. The effect of the cross layers in the stiffness can be considered by using the Gamma method and using the effective stiffness in the formulation.

$$\begin{bmatrix} F_{y1} \\ M_1 \\ F_{y2} \\ M_2 \end{bmatrix} = \begin{bmatrix} 12EI_{eff}/L^3 & 6EI_{eff}/L^2 & -12EI_{eff}/L^3 & -6EI_{eff}/L^2 \\ 6EI_{eff}/L^2 & 4EI_{eff}/L & -6EI_{eff}/L^2 & 2EI_{eff}/L \\ -12EI_{eff}/L^3 & -6EI_{eff}/L^2 & 12EI_{eff}/L^3 & -6EI_{eff}/L^2 \\ 6EI_{eff}/L^2 & 2EI_{eff}/L & -6EI_{eff}/L^2 & 4EI_{eff}/L \end{bmatrix} \begin{bmatrix} w_1 \\ \theta_1 \\ w_2 \\ \theta_2 \end{bmatrix} \quad (2\text{-}7)$$

For a four-point bending test, the maximum deflection of a beam can be calculated by the analytical formula below:

$$w_{global} = \frac{Fl_2(3l^2 - 4l_2^2)}{24E_L I_{eff}} \quad (2\text{-}8)$$

2.2.1.1 Gamma method

Due to rolling shear in cross layers, shear beside bending plays an important role in deflection. As an approximation, the share of shear in deformation is about 30 percent of bending [19]; see the figure below.

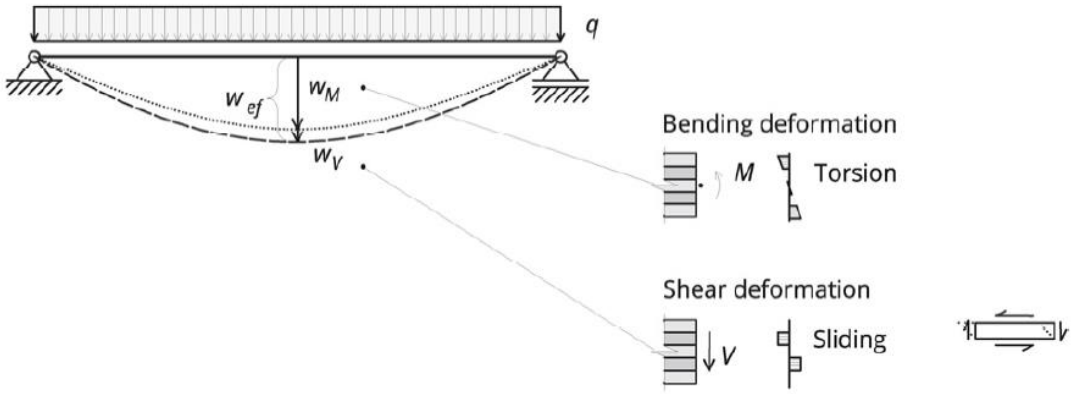

Figure 2-7 Contribution of shear in total deformation of a cross-laminated timber beam, figure from [19].

To address deformation from shear forces, a simplified method, named the gamma method, which is based on the beam theory, is used in Eurocode 5 by introducing an effective moment of inertia. This method can be applied to CLT panels with 3 and 5 layers. Based on this method, the moment of inertia of the longitudinal layers is reduced by the gamma factor to consider the effect of the shear flexibility of the cross layers. The main advantage of this method is that the deformation can be calculated by using the pure bending formulation, and there will be no separate

term for the contribution of shear in deformation. On the other hand, the main cons are that the effective moment of inertia will be dependent on the span length, which is a system-dependent value.

The reference length for different support systems with a length of a span equal to L, is defined below:

- For a single span simply supported beam, l_{ref} = L.
- For continuous simply supported beam l_{ref} = 0.8 . L.
- For a cantilevered beam l_{ref} = 2L.
- For buckling member $l_{ref} = l_{ki}$. where l_{ki} is the buckling length

For a symmetrical cross-section of 5-layer CLT with the same grade and thickness (t_1=t_3=t_5) of lamellas in layers, the effective moment of inertia can be calculated by the below equation [2].

$$I_{x,ef} = \frac{b_x t_1^3}{12} + \gamma_1 b_x t_1 a_1^2 + \frac{b_x t_3^3}{12} + \frac{b_x t_5^3}{12} + \gamma_5 b_x t_5 a_5^2 = b_x \left(3\frac{t_1^3}{12} + 2\gamma_1 t_1 a_1^2 \right) \quad (2\text{-}9)$$

$$\gamma_1 = \frac{1}{1 + \frac{\pi^2 E_{x,1} t_1}{l_{ref}^2} \frac{t_2}{G_{9090,2}}} \left[\frac{1}{m}\right] \quad (2\text{-}10)$$

$$a_1 = \frac{t_1}{2} + t_2 + \frac{t_3}{2} - a_3 \quad (2\text{-}11)$$

$$a_3 = \frac{\gamma_1 \frac{E_{x,1}}{E_{ref}} b t_1 \left(\frac{t_1}{2} + t_2 + \frac{t_3}{2}\right) - \gamma_5 \frac{E_{x,5}}{E_{ref}} b t_5 \left(\frac{t_3}{2} + t_4 + \frac{t_5}{2}\right)}{\gamma_1 \frac{E_{x,1}}{E_{ref}} b t_1 + \gamma_3 \frac{E_{x,3}}{E_{ref}} b t_3 + \gamma_3 \frac{E_{x,5}}{E_{ref}} b t_5} \quad (2\text{-}12)$$

And for a symmetrical cross-section with the same strength, γ_1=γ_5.

The Gamma method is based on four main assumptions [20]:

- There is little shear deformation of the individual components (large spans).
- Beams with simply supported and loaded uniformly distributed, the gamma coefficient is only constant if a sinusoidal distributed load is applied over the beam length.
- Continuous fasteners with constant stiffness over the member.
- Maximum of three individual components non-abutted over the member length.

2.2.2 Timoshenko beam theory

In the Timoshenko theory model, the bending effects are taken into account together with shear strains in order to describe the behavior of the beam. It means that the final deformation depends on shear and bending. The testing method, which is described in EN 16351, Annex C, is based on the Timoshenko method.

In Timoshenko beam theory, the moment of inertia depends only on longitudinal layers, and it is assumed that the transverse layers do not provide any stiffness. The net moment of inertia is calculated based on the formula below.

$$I_{net} = \frac{bt_1^3}{12} + bt_1a_1^2 + \frac{bt_3^3}{12} + bt_3a_3^2 + \frac{bt_5^3}{12} + bt_5a_5^2 \qquad (2\text{-}13)$$

Where: t_x is the thickness of each layer, a_x is the distance between the center of gravity and the center of each longitudinal layer, and b is the width of the cross-section.
The stiffness matrix can be described as:

$$\begin{bmatrix} F_{y1} \\ M_1 \\ F_{y2} \\ M_2 \end{bmatrix} = \frac{E}{1+m} \begin{bmatrix} 12I_{net}/L^3 & 6I_{net}/L^2 & -12I_{net}/L^3 & -6I_{net}/L^2 \\ 6I_{net}/L^2 & 4I_{net}(1+m/4)/L & -6I_{net}/L^2 & 2(1-m/2)I_{net}/L \\ -12I_{net}/L^3 & -6I_{net}/L^2 & 12I_{net}/L^3 & -6I_{net}/L^2 \\ 6I_{net}/L^2 & 2(1-m/2)I_{net}/L & -6I_{net}/L^2 & 4(1+m/4)I_{net}/L \end{bmatrix} \begin{bmatrix} w_1 \\ \theta_1 \\ w_2 \\ \theta_2 \end{bmatrix} \qquad (2\text{-}14)$$

Where: $\mathrm{m} = \frac{12}{\mathrm{L}^2} * \frac{\mathrm{E*I}}{\mathrm{G*A}_{net}*\kappa_s}$, E is Young's modulus, G is a shear modulus, A is a cross-section area, I is a moment of inertia, κ_s is a shear correction factor, and can be calculated by the below equation [4]:

$$\kappa = \frac{(\sum(EI + EAa^2))^2}{\sum G_i b t_i \int \frac{S^2(z)E^2(z)}{G(z)b(z)} dz} \qquad (2\text{-}15)$$

Where E is the modulus of elasticity, S is the static moment, I is the moment of inertia, G_i is the shear modulus of each layer, b is the width of the layers, t_i is the thickness of each layer, a is the distance between the center of gravity and the center of each longitudinal layer, and A is the cross-section area.

There are different suggestion numbers for a shear correction factor; for five layers of cross-laminated timber with different thicknesses of 20, 30, and 40 mm the below range is suggested, and for the rectangular and homogeneous, it can be considered as 0.83 [19].

$$0.18 \leq \kappa_s \leq 0.20$$

This value for symmetrical build-up CLT with equal laminate thickness and with the assumption of $\frac{G_{90}}{G_0} = \frac{1}{10}$, Jöbstl[19] recommends a value of 0.24.
The total deformation of the beam can be calculated by using the principal of virtual work by equations:

$$w_{total} = \Delta_{bending} + \Delta_{shear} \tag{2-16}$$

$$w_{total} = \int \frac{M.\bar{M}}{E.I_{net}} dx + \int \frac{V.\bar{V}}{G.A_s} dx \tag{2-17}$$

Then, the total deflection of the beam in a four-point bending test at the mid-span can be derived by the equation below:

$$w = w_{global} = \frac{F l_2 (3l^2 - 4l_2^2)}{24 E_L I_{net}} + \frac{F}{D_{GA}} l_2 \tag{2-18}$$

Where: $D_{GA} = \kappa_s \sum_{i=1}^{n} A_i G_i$

2.3 Design of CLT

For designing CLT structures, the partial factor method is used, according to EC5. Based on that approach, the design value for the load effect should be less than the design value for the resistance. The CLT structural elements are usually checked in two limit states: ultimate limit state (ULS) and serviceability limit state (SLS).

2.3.1 Limit states

In the ultimate limit state, the design resistance (or strength) is calculated by dividing the characteristic value by the partial factor for material properties and multiplying the value by the modification factor. An example can be shown below:

$$f_d = \frac{k_{mod} * f_k}{\gamma_M} \tag{2-19}$$

Where:
f_d is the design strength value, k_{mod} is a modification factor, f_k is the characteristic strength value, γ_M is a partial factor for material properties.

On the other hand, in designing in the serviceability limit state the stiffness of the element should prevent vibrations and deformation of the structure. The stiffness of the CLT panel depends on many factors like load duration, moisture content of the element or temperature.

2.3.2 Partial factors and modification factors

The value of the partial factor varies between the countries, and there is no required one for Sweden, however γ_M as 1.25 is recommended. The partial factor depends on the quality of control during the design and manufacturing process and the level of the material's homogeneity.

The next factor that is used in design calculations of wood and CLT panels is the modification factor k_{mod}. The factor considers the effect of the duration of load and the moisture content. The values of k_{mod} can be found in Table 3.1 in EC5.
The tensile and bending strength of the CLT panels can be increased by k_{sys} factor. The factor can be included in the calculation due to the interaction of parallel boards that can increase the characteristic strength of the panel. The system effect factor can be determined based on the formula:

$$k_{sys} = min\begin{cases} 1.15 \\ 1 + 0.1b \end{cases} \tag{2-20}$$

where b is the effective width of the cross-section in m.

2.3.3 Analytical verification of rolling shear strength and bending stiffness of the panels

The main part of the experiment is to subject the small-scale panels to a shear test and large-scale panels to a bending test. In this subchapter, the analytical verifications of shear strength and bending strength of the panels designed in the ultimate limit state are presented. The formulas are valid for solid CLT panels without any air gaps.

2.3.3.1 Verification of the shear parallel to the grain

In a CLT panel subjected to the shear forces perpendicular to the panel, shear stresses occur. The panel should be verified in both directions. The shear parallel to the grain in layer 3 and layer 2 or 4 can be checked by the formula:

$$\tau_{Rv,xz,d} = \frac{S_{x,net} * V_{xz,d}}{I_{x,net} * b_x} \leq f_{v,090,ylay,d} = k_{mod} * \frac{f_{v,090,ylay,k}}{\gamma_M} \tag{2-21}$$

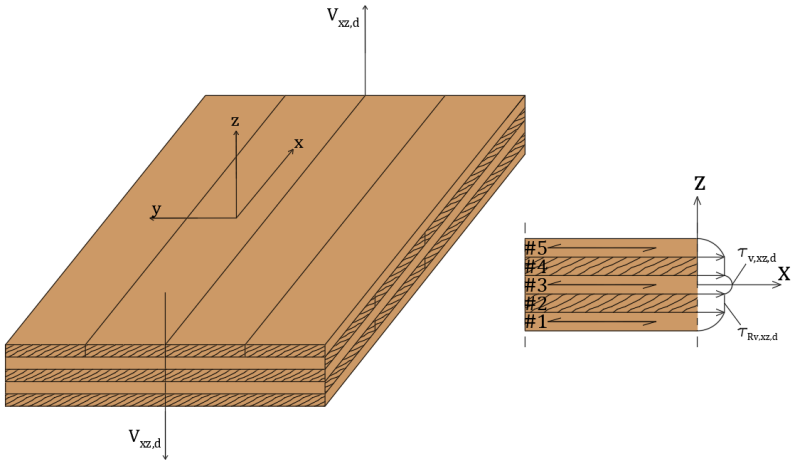

Figure 2-8 Shear stress from shear force $V_{xz,d}$ in CLT panel.

where: $\tau_{Rv,xz,d}$ is the design value of shear strength, $V_{xz,d}$ is the design shear force, $S_{x,net}$ is the panel's net static moment, $I_{x,net}$ is the net moment of inertia along the x-axis, b_x is the width of the layer, k_{mod} is the modification factor, $f_{v,9090,ylay,d}$ is the design value for the longitudinal shear strength of the boards, $f_{v,9090,ylay,k}$ is the characteristic longitudinal shear strength of the boards, γ_M is the partial factor of the material.

2.3.3.2 Verification of rolling shear strength

The transversal rolling shear strength to the grain is much lower than along the grain so layers 2, and 4 should be checked together with layer 3 which is placed in between:

$$\tau_{Rv,yz,d} = \frac{S_{y,net} * V_{yz,d}}{I_{y,net} * b_y} \leq f_{v,9090,xlay,d} = k_{mod} * \frac{f_{v,9090,xlay,k}}{\gamma_M} \qquad (2\text{-}22)$$

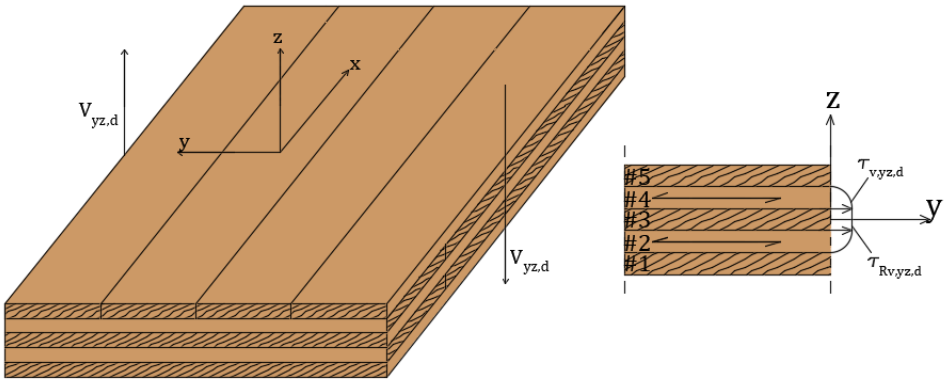

Figure 2-9 Shear stresses from shear force $V_{yz,d}$ in CLT panel.

where: $\tau_{Rv,yz,d}$ is the design value of rolling shear strength, $V_{yz,d}$ is the design shear force, $S_{y,net}$ is the panel's net static moment, $I_{y,net}$ is the net moment of inertia along the y-axis, b_y is the width of the layer, k_{mod} is the modification factor, $f_{v,9090,xlay,d}$ is the design value for the rolling shear strength of the boards, $f_{v,9090,xlay,k}$ is the characteristic rolling shear strength of the boards, γ_M is the partial factor of the material.

The panel's net static moment can be calculated based on the formula below.

$$S_{y,net} = bt_5(\frac{t_3}{2} + t_4 + \frac{t_5}{2}) \qquad (2\text{-}23)$$

2.3.3.3 Verification of bending stress in the CLT panel's plane

For a CLT panel subjected to bending moment about its y-axis, the checking should follow the formula:

$$\sigma_{m,y,d} = \frac{M_{y,d}}{W_{x,net}} \leq f_{m,xlay,d} = k_{sys} * k_{mod} * \frac{f_{m,xlay,k}}{\gamma_M} \qquad (2\text{-}24)$$

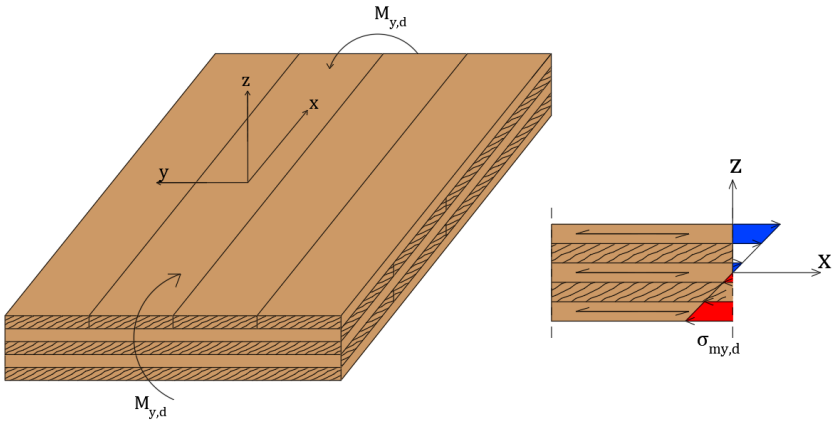

Figure 2-10 Bending stresses in CLT panel with moment about the y-axis.

where: $M_{y,d}$ is the moment design value about the y-axis, $W_{x,net}$ is the panel's net moment of resistance, $f_{m,xlay,d}$ is the bending strength design value, k_{sys} is a system factor, k_{mod} is a modification factor, $f_{m,xlay,k}$ is the characteristic bending strength, $\gamma_M$is the partial factor for the material.

Additionally, the panel's net moment of resistance is calculated by the formula (2-25).

$$W_{x,net} = \frac{2I_{x,net}}{h} \tag{2-25}$$

2.4 Strength testing of CLT

2.4.1 Shear strength test

EN 16352:2015 (E) is provided a test method for measuring the rolling shear strength and stiffness of a cross-laminated timber panel. The test configuration is shown in the figure below.

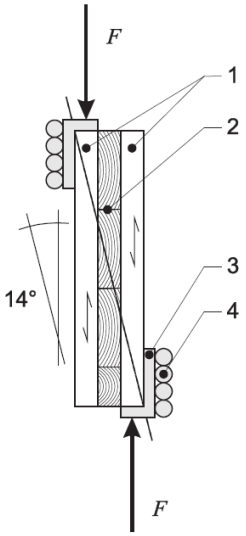

1 Longitudinal layer of specimens
2 Cross-layer of the specimen
3 Steel angles for load transmission
4 Friction-free support

Figure 2-11 Shear test configuration with cross-laminated timber, figure from EN 16352.

Shear stiffness and strength can be calculated based on EN789. The corresponding formula is presented below.
Planer (rolling) shear modulus of rigidity:

$$G_r = \frac{(F_2 - F_1) * cos(\beta) * t}{(u_2 - u_1) * l * b} \quad [Pa] \qquad (2\text{-}26)$$

Where:
F_2-F_1 is load increments between $0.1F_{max}$ and $0.4F_{max}$ [N], see Figure 2-12.
u_2-u_1 is the deflection increment according to F_2-F_1 by using a linear regression line [N], see Figure 2-12 .
b is the width of the test specimen [m].
l is the length of test specimens [m].
t is the thickness of the test specimen [m].

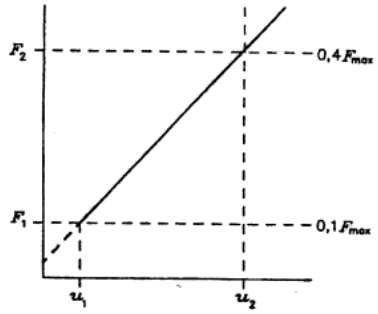

Figure 2-12 Load-deflection graph within the range of elastic deformation.

Planer (rolling) shear strength:

$$f_r = \frac{F_{max} * cos(\beta)}{l * b} \quad [Pa] \qquad (2\text{-}27)$$

F_{max} is the maximum load obtained during testing [N].
b is the width of the test specimen [m].
l is the length of test specimens [m].
β angle between the load direction and the longitudinal axis.

Panel shear modulus of rigidity can be calculated as below:

$$G_v = \frac{0.5 * (F_2 - F_1) * l_1}{(u_2 - u_1) * l * t} \quad [Pa] \qquad (2\text{-}28)$$

F_2-F_1 is load increments between $0.1F_{max}$ and $0.4F_{max}$ [N].
u_2-u_1 is the deflection increment according to F_2-F_1 by using a linear regression line [m].
b is the width of test specimen [m].
l is the length of test specimen along the center line of the shear area [m]
t is the thickness of the test specimen [m].
l_1 is the gauge length [m].

2.4.2 Four-point bending test

Shear strength and stiffness of a CLT panel are evaluated by a four-point bending test based on EN-16351. The test configuration is shown in Figure 2-13,

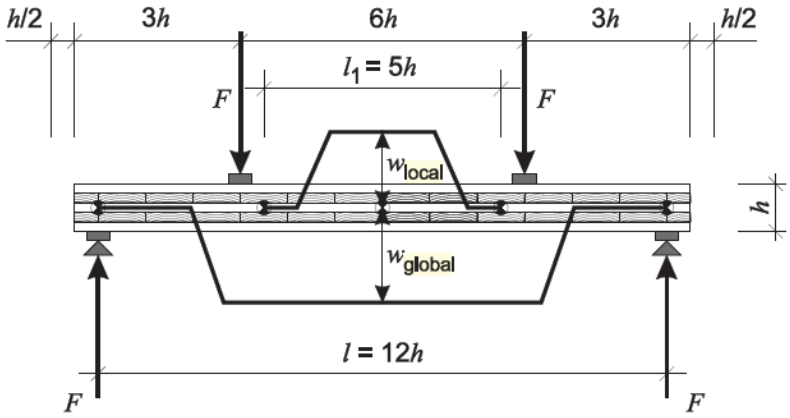

Figure 2-13 Set up of the four-point bending test, Figure from EN-16351.

w_{local}= deflection measured over the length of the shear stress-free area
w_{global}= deflection measured over the entire span

Three possible failure modes are bending failure, longitudinal shear, and rolling shear failure. As the shear strength in the longitudinal direction is significantly larger than the rolling shear strength, thus the most likely shear failure mode is rolling shear failure.

The maximum loading failure force in bending and shear can be calculated by the equations (2-29) and (2-30).

$$F_{max,m} = \frac{f_{m,xlay,d} * W_{x,net}}{l_2} \tag{2-29}$$

Where l_2 is the distance between the support and the point load position in the four-point bending test.

$$F_{max,Rv} = \frac{f_{v,9090,xlay,d} * I_{y,net} * b_y}{S_{R,y,net}} \tag{2-30}$$

As the shear force between the applied loads in the four-point bending test is zero, the local deflection represents the bending deflection and can be calculated below.

$$w_{local} = \frac{F * l_2 * l_1^2}{8 * (EI)_{local,net}} \tag{2-31}$$

In EN-16351:2015 it is referred to EN-789:2004 for the formula for calculating the rolling shear and stiffness values. In this standard, the relation between load and deflection is considered linear, and data corresponding to the 0.1Fmax and

0.4Fmax are used to calculate the stiffness and rolling shear strength. Thus, the bending stiffness can be calculated based on the formula below.

$$(EI)_{local,net,EN\ 789} = \frac{l_2 * l_1^2 * (F_2 - F_1)}{8 * (w_{l,2} - w_{l,1})} \quad (2\text{-}32)$$

Where F_2-F_1 is the increment of load between $0.1F_{max}$ and $0.4F_{max}$.
And $w_{l,2}$-$w_{l,1}$ is the increment of deflection to F_2-F_1.

In addition, the global bending stiffness can be calculated by using the equation (2-33) and Figure 2-12, based on the Euler-Bernoulli beam theory as below:

$$(EI)_{global,net} = \frac{l_2 * (3l^2 - 4l_2^2)}{24} * \frac{(F_2 - F_1)}{(w_{g,2} - w_{g,1})} \quad (2\text{-}33)$$

In the local stiffness, the deflection is only dependent on the bending; however, in global stiffness calculation also, the effect of shear is included. Also, based on the Timoshenko method, the global stiffness can be calculated as below:

$$(EI)_{global,Timoshenko} = \frac{l_2 * (3l^2 - 4l_2^2)}{24 * \left(\frac{(w_{g,2} - w_{g,1})}{(F_2 - F_1)} - \frac{l_2}{\kappa_s * G * A_{net}}\right)} \quad (2\text{-}34)$$

This equation is simplified in SS-EN 408:2010 by considering the $\kappa_s = \frac{5}{6}$ and $I = \frac{bh^3}{12}$ as below:

$$E_{m,global,EN\ 408} = \frac{l_2 * (3l^2 - 4l_2^2)}{2 * b * h^3 \left(\frac{(w_{g,2} - w_{g,1})}{(F_2 - F_1)} - \frac{6 * l_2}{5 * G * b * h}\right)} \quad (2\text{-}35)$$

Based on SS-EN 408:2010, the G value can be considered as 650 N/mm^2 or infinitive to consider the share of the shear on a deflection.

2.5 FEM Modelling

An orthotropic material model can be used to model a wood material. The three principal axes can be named L for longitudinal direction and R and T for radial and tangential direction, respectively. For an orthotropic material, a linear elastic relation between stress and strain can be defined by using the equation below.

$$\sigma = \mathbf{D}\varepsilon \quad (2\text{-}36)$$

The stiffness matrix **D** can be defined by using the nine independent elastic stiffness parameters as below [21].

$$\begin{Bmatrix}\sigma_{11}\\ \sigma_{22}\\ \sigma_{33}\\ \sigma_{12}\\ \sigma_{13}\\ \sigma_{23}\end{Bmatrix} = \begin{bmatrix} D_{1111} & D_{1122} & D_{1111} & 0 & 0 & 0 \\ & D_{2222} & D_{2233} & 0 & 0 & 0 \\ & & D_{3333} & 0 & 0 & 0 \\ & sym & & D_{1212} & 0 & 0 \\ & & & & D_{1313} & 0 \\ & & & & & D_{2323} \end{bmatrix} \begin{Bmatrix}\varepsilon_{11}\\ \varepsilon_{22}\\ \varepsilon_{33}\\ \gamma_{12}\\ \gamma_{13}\\ \gamma_{23}\end{Bmatrix} \quad (2\text{-}37)$$

Where the D matrix can be defined as equations below:

$D_{1111} = E_1(1 - \nu_{23}\nu_{32})\Upsilon$
$D_{2222} = E_2(1 - \nu_{13}\nu_{31})\Upsilon$
$D_{3333} = E_3(1 - \nu_{12}\nu_{21})\Upsilon$
$D_{1122} = E_1(\nu_{21} + \nu_{31}\nu_{23})\Upsilon = E_2(\nu_{12} + \nu_{32}\nu_{13})\Upsilon$
$D_{1133} = E_1(\nu_{31} + \nu_{21}\nu_{32})\Upsilon = E_3(\nu_{13} + \nu_{12}\nu_{23})\Upsilon$
$D_{2233} = E_2(\nu_{32} + \nu_{12}\nu_{31})\Upsilon = E_3(\nu_{23} + \nu_{21}\nu_{13})\Upsilon$
$D_{1212} = G_{12}$
$D_{1313} = G_{13}$
$D_{2323} = G_{23}$

$$\Upsilon = \frac{1}{1 - \nu_{12}\nu_{21} - \nu_{23}\nu_{32} - \nu_{31}\nu_{13} - 2\nu_{21}\nu_{32}\nu_{13}}$$

For wood, three main directions can be described below:
Direction 1 is equal to longitudinal L, which is an axis parallel to the grain.
Direction 2 is equal to tangential T, which is an axis tangential to the annual ring.
Direction 3 is equal to radial R, which is an axis radial to the annual ring.

In Abaqus/ACE usage: Property module: material editor: Mechanical → Elasticity → Elastic: Type: Orthotropic
Also, orthotropic elasticity can be defined by engineering constant. Twelve orthotropic material constants are needed to define the stiffness matrix: Three modulus of elasticity in three main directions, E_L, E_R, E_T, three shear modulus of elasticity G_{LR}, G_{LT}, G_{RT}, and six Poisson's ratio υ_{LT}, υ_{LR}, υ_{RT}, υ_{RL}, υ_{TL}, and υ_{TR}.
In general, υ_{ij} is not equal to υ_{ji} and they are related by the below relation [21]:

$$\frac{\upsilon_{ij}}{E_i} = \frac{\upsilon_{ji}}{E_j} \quad (2\text{-}38)$$

In Abaqus/ACE usage: Property module: material editor: Mechanical → Elasticity → Elastic: Type: Engineering Constants
Based on the material properties mentioned in Table 2-1, the stiffness matrix can be calculated based on formulas that are shown in this section; the summarized result is presented in the table below:

Table 2-2 Stiffness matrix elements.

D_{1111}	D_{2222}	D_{3333}	D_{1122}	D_{1133}	D_{2233}	D_{1212}	D_{1313}	D_{2323}
11342	552	554	365	392	288	780	780	78

2.6 Failure modes

The failure modes observed in CLT panels can be classified into the following categories:

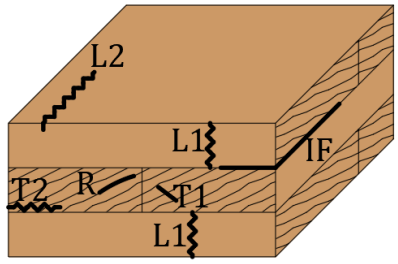

Figure 2-14 Classification of crack modes in a CLT panel.

L1: Tension failure in the longitudinal direction and a crack propagate perpendicular to the grain. The main reason for such cracks is irregularities such as knots in the wood lamellas.
L2: Compression failure in the longitudinal direction.
R: Tension failure in the radial direction. That happens because of either rolling shear stress or shear stress parallel to the grain.
T1: Tension failure in the transverse direction as a result of rolling shear stress.
T2: Tension failure in the tangential direction that can happen as a result of the superposition of global rolling shear stress by bending stress perpendicular to the grain or stress perpendicular to the single layer.
IF: Interface failure between single layers.

3 Shear test

The chapter includes a description of the methodology used for performing rolling shear tests for small-scale specimens.

3.1 Methodology

The specimens for the rolling shear test were fully manufactured in the Architecture workshop at the Chalmers University of Technology. This subchapter describes the preparation of the boards and configurations, the manufacturing process, and the testing method of the rolling shear experiment.

3.1.1 Designing of configurations

Six different configurations of CLT panels were produced at the workshop, one solid panel without any airgaps between cross-layers and five CLT samples with different cross-layer configurations with airgaps between them, see section 3.4.3

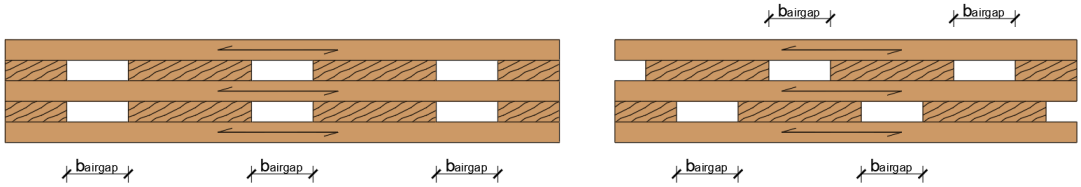

Figure 3-1 The examples of the specimens with varying locations of the air gaps: aligned (left picture) or shifted (right picture).

The width of the air gaps that were introduced in the cross-layers might vary depending on the type of configuration as well as their position of them. The air gaps can be located centrally or the cross-layers can be shifted in relation to other ones, as shown in Figure 3-1.

3.1.1.1 Void, volume, and shear ratio and material reduction factor

A sketch of a cross-section of a spaced CLT panel is shown in the figure below.

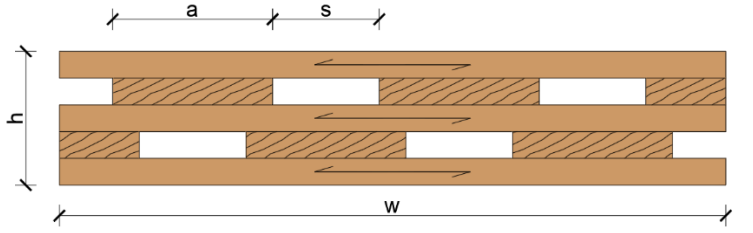

Figure 3-2 Cross-section of a spaced CLT panel.

The void ratio for CLT specimens is defined based on equation (3-1).

$$\lambda = \frac{a}{a+s} \tag{3-1}$$

As an air gap is introduced between the cross layers, it will reduce the overall volume of the panel. The volume ratio can be calculated by equation (3-2):

$$\eta_v = \frac{V_{spaced}}{V_{solid}} \quad (3\text{-}2)$$

Where the V_{spaced} is the actual volume of wood that is used in a CLT panel with an air gap, and V_{solid} is the volume of a solid CLT panel. Based on the volume ratio, the material reduction factor can be calculated according to equation (3-3).

$$\eta_M = (1 - \eta_v) * 100 \ [\%] \quad (3\text{-}3)$$

The shear ratio also can be calculated based on the comparison of the shear strength of the other configuration with airgaps with the solid one, see equation (3-4).

$$\eta_S = \frac{Shear\ strength_{Spaced}}{Shear\ strength_{Solid}} \quad (3\text{-}4)$$

3.1.1.2 Moisture content

The moisture content of cross-laminated timber (CLT) panels for shear and bending tests will depend on the specific testing standard being followed. However, in general, the moisture content of the CLT panels should be within a certain range to ensure accurate and consistent test results. It is important to note that the moisture content of CLT panels can affect their mechanical properties, and therefore it is critical to control and monitor the moisture content during manufacturing and testing.

For example, according to ASTM D1037/D1037M-12a (Standard Test Methods for Evaluating Properties of Wood-Base Fiber and Particle Panel Materials), the moisture content of the test specimens should be between 6% and 14% at the time of testing. This standard covers the testing of various types of wood-based panel materials, including CLT, for a range of mechanical properties, including shear and bending strength.

Similarly, EN 16351 (Timber structures - Cross laminated timber - Requirements) states that the moisture content of CLT panels for testing should be between 8% and 12%. And it is mentioned that "if the specimens are not conditioned according to EN 408, they shall have a moisture content of u=(12±3)%."

3.1.2 Preparation and assigning of boards to configurations

For each CLT configuration, three different specimens were produced. The longitudinal layers were always assigned from high-MOE boards, but the cross-layers were constructed from low, average, or high- MOE. Consequently, for a particular configuration, one specimen was produced using low-MOE boards for cross-layers and high MOE for longitudinal layers (Sample 1), the second specimen with an average MOE of cross-layers and high MOE of longitudinal layers (Sample 2), and the third specimen with both high MOE of cross-layers and longitudinal layers (Sample 3). The boards with MOE in a range between 12000 and 17000 were considered for production. The specimens are categorized based on different MOE values to make a difference between them and also because of the lack of boards with the same MOE for the production of all specimens. In this master thesis the effect of MOE was not studied. Low-MOE boards were

determined as 10 – 20 % below the average MOE of the relevant boards. The low-MOE elements have the value of modulus of elasticity in a range between 11609 and 13060. Furthermore, the average value of MOE of all relevant boards is equal to 14511. The range of MOE that boards were considered as an average was between 13060 and 15962. Boards with high MOE were used for longitudinal layers and some of cross-layers. High modulus of elasticity was determined as 10 – 20 % above the average value of MOE. The high-MOE boards have MOE in a range between 15962 and 17413.

3.1.3 Manufacturing

The small-scale specimens were manufactured in an Architecture wood workshop at Chalmers University of Technology. The process was divided into smaller steps that are described further in this chapter. At the beginning of production, the boards were cut by circular saw to obtain smaller lengths and simplify the next stages. Furthermore, the boards were planed by using a planing machine to get smooth surfaces for each element. When the boards were cut and planed to the correct dimensions, the layers of specimens could be glued to get each type of configuration. The small-scale specimens were clamped for the time when the adhesive was hardening, and at the end, each block was cut to obtain the final dimensions.

3.1.3.1 Sawing and planing

In the beginning, all the boards were cut to decrease the lengths and prepare them for the next steps. Initially, the length of raw material elements was around 2 meters, so it was cut into smaller pieces to be able to plan the dimensions of longitudinal layers and cross-layers. The dimension of the raw material cross-section was 127 mm x 25 mm. The first cut was done by the circular saw, see Figure 3-3, and the boards were cut to around half-meter-long elements.

Figure 3-3 Circular saw used for cutting the boards.

Furthermore, the wooden elements were planed using planing machine to make the material smoother, remove irregularities and obtain the right angles. The planing process removed a few millimeters of thickness and width of the board. The planing machine can be shown in Figure 3-4.

Figure 3-4 The planing machine and the planing process along the width of the board.

The final planing of the boards could be done using another planing machine see Figure 3-5. The desired thickness of the boards can be adjusted manually so the machine planes the boards based on the user's needs. The final thickness was set to 20 mm.

Figure 3-5 Planing machines used for obtaining desired thickness.

In the end, the half-meter boards were cut using a circular saw to get the elements with the correct dimensions and to be able to build different configurations. The example of the boards used for the production of one configuration is presented in Figure 3-6.

Figure 3-6 Longitudinal layers and cross-layers ready for production of a specimen.

3.1.3.2 Applying the adhesive and clamping

To connect the longitudinal layers with cross-layers Cascol Indoor glue was used, see Figure 3-7. An adhesive that is based on polyvinyl acetate (PVAC) is used, with a 5 minutes opening time and a 10 minute pressing time, letting specimens be made quickly.. PVAC glue is water soluble, non-toxic and dries quickly giving relatively high bond strength. PUR adhesives, which are more typical for commercial CLT production, were not used because it is not allowed to be used by students at ACE lab and has a longer curing time. Each time the glue was applied at the top of the previous layer at the correct places depending on the configuration of the specimen. The glue was spread using a brush to provide an even distribution, see Figure 3-7.

Figure 3-7 Application of the glue on the longitudinal layers at the places where cross-layers will be attached.

Figure 3-8 The spread of the glue at the longitudinal layer where the cross-layers will be placed.

When the adhesive was applied and spread at the correct areas, the next layers could be added, see Figure 3-8. The cross-layers were placed at the glue zones with transversal direction and the elements were clamped to provide enough pressure to glue the layers together.

Figure 3-9 Gluing of the cross-layers.

Two types of clamps were used for that process, the small ones and the big ones. The small ones were used to prevent the horizontal movement of the layers before the glue is dry enough, see Figure 3-10. Both types of clamps were used for merging the layers together and keeping them in the vertical direction. The remaining layers were glued together following the same process, so the longitudinal layer was glued on the cross-layers, the cross-layers were glued to the longitudinal layer, and the specimen was clamped. The waiting time for clamping before removing and adding new layers was 10-15 minutes. When the last layers were added, six big clamps were assembled for the final time of drying the glue, see Figure 3-11. The specimen was left for around one hour, and the clamps were removed after that time.

Figure 3-10 Clamping the first and second layers to prevent sliding of the cross-layers.

Figure 3-11 The final clamping and drying of the specimen.

The specimen of Configuration IV after the removal of the clamps can be seen in Figure 3-12.

Figure 3-12 The specimen after removing the clamps.

3.1.3.3 Obtaining final dimensions and cutting the edges

After the gluing process, the specimens were left for ten days for conditioning in a climate room. After that period of time, the four sides of each element were cut using the circular saw to get the final dimensions of the samples. The width is constant for all of the specimens and is equal to 110 mm and the length varies based on the layer-configuration. The picture below presents three CLT blocks in Configuration IV after cutting to the final dimensions.

Figure 3-13 Configuration IV with the appropriate dimensions.

When the samples were cut to desired dimensions, the two opposite diagonal edges had to be sawn in order to place the specimen in a hydraulic press, see Figure 3-14.

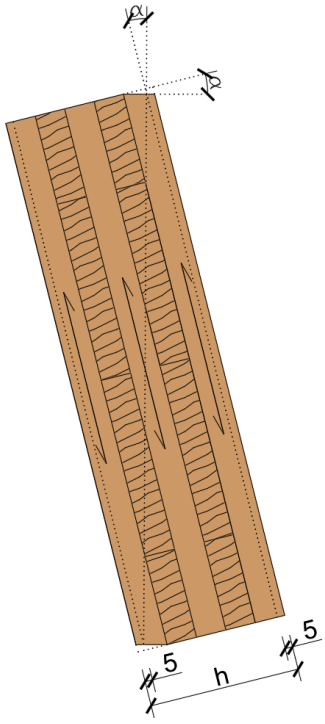

Figure 3-14 The illustration of the specimen with sawn edges.

The α angle that should be cut in order to attach the CLT block to the machine can be calculated based on the equation:

$$\alpha = \arctan\left(\frac{h - 2 * 5\ mm}{L}\right) \quad (3\text{-}5)$$

Where h is the total thickness of the specimen, and L is the length in mm. The thickness was reduced by 5 mm from both sides to approximate the vertical axis closer to the center of the support area rather than the corners of the sample.

3.1.4 Preparation of the specimens for DIC analysis

In order to use the ARAMIS measuring system, one side of each specimen has to be covered with a contrast pattern. The pattern allows using the Digital Image Correlation method to be able to obtain the results of the study in the form of a graphical representation of displacements or surface strains.

Figure 3-15 The process of covering the specimens with white paint.

The specimens were painted using white paint and the roller that is presented in the picture above, Figure 3-15. When all of the blocks were dried and finished, the pattern could be applied on the surface. The pattern was done using black paint and small pieces of a doormat, see Figure 3-16. The material was dipped in the paint and dabbed on the white side of the CLT specimens creating black dots. The goal was to have 50% of the side covered with the white paint, 50% covered with the black paint and the size of the black dots should be around 1 mm.

Figure 3-16 Covering the specimens with the pattern.

3.2 Testing of small-scale specimens

The testing of small-scale specimens took place in the Structural Lab at Chalmers University of Technology. A hydraulic press was used to conduct the experiment, and the ARAMIS optical system was followed and monitored throughout the process. Before the session where the main specimens were tested, it was decided to perform the trial test with one additional CLT block and check if the equipment worked correctly. Additionally, every time when the specimens were not tested, they were kept in the climate chamber to provide an accurate moisture content.

3.2.1 Test equipment

The specimens were tested using a hydraulic press and the procedure was monitored by ARAMIS optical system based on the Digital Image Correlation method. Moreover, to be able to attach the specimen to the equipment one set of fixtures was used for carrying out the experiment.

3.2.1.1 Hydraulic press

The shear strength test was conducted using the hydraulic press with a maximum force of 250 kN, see Figure 3-17.


Figure 3-17 Hydraulic press.

3.2.1.2 Fixtures

Fixtures were used to be able to attach the specimens to the hydraulic press. They consisted of one part that was fastened into the hydraulic press and one replaceable plate that works as a support for the specimens. Additionally, the thickness of lamella for each specimen is constant, so it was enough to use one pressure plate for all specimens. The length of the plates is slightly larger than the dimension of the attached specimen in order to ensure that the load is distributed along the whole pressure area. Moreover, the specimen should be placed between the pressure plates in a way that it aligns with the outer edges of the plates. The fixtures and the pressure plates are shown in Figure 3-18.


Figure 3-18 Fixtures and the steel plates.

3.2.1.3 ARAMIS system

. A pattern was applied to the specimens to provide contrast so that the ARAMIS optical system could be used to monitor changes in strain at the surfaces of the

blocks. When the loading process started, the system was adjusted to take one picture per second (1Hz). The ARAMIS optical system is shown in the picture below.

Figure 3-19 ARAMIS optical system.

When the loading procedure began, two software started to work at the same time. GOM Correlate Pro software was used for establishing an image of the specimens and monitoring the specimens under deformation. Moreover, MTS FlexTest software allowed to save the load and deformation data at each step so that it was able to analyze the results and create the graphs afterward.

3.2.1.4 The loading rate of the hydraulic press

Based on the SS-EN-789:2004, the loading rate must be selected in a way that the maximum load is reached within the time in the range of 300±120 seconds. In this master thesis, the loading rate is selected at 0.5 mm/min for all of the configurations.

3.3 FEM modelling in ABAQUS

The FEM models were created using ABAQUS software in order to complete experimental results and explain them by numerical analysis. Each configuration was modeled under shear loading, assuming high MOE for both longitudinal and layers and cross-layers.

3.3.1 Modeling of the elements

All the layers were constructed as 3D deformable elements with a solid shape and extrusion type. The bottom and top longitudinal layers were created with an inclined edge that represents the loading area, see Figure 3-20. Furthermore, for the cross-layers, two elements were created; one having a width of 120 mm and

the second one with a width of 60 mm. There was used in different arrangements depending on the configuration's type.

Figure 3-20 Front views of the longitudinal layer with an inclined edge on the right-hand side.

3.3.2 Material properties

The CLT panels were constructed from C24 strength class. The average density of high MOE boards was calculated as 490 kg/m^3,and the elastic model behavior was set as orthotropic type. The input data for the orthotropic elastic stiffness matrix were calculated based on the equations presented in section 2.5 and the values are presented in the Table 3-1 below:

Table 3-1 Stiffness matrix elements.

D_{1111}	D_{2222}	D_{3333}	D_{1122}	D_{1133}	D_{2233}	D_{1212}	D_{1313}	D_{2323}
11342	552	554	365	392	288	780	780	78

Additionally, all parts were assigned as solid and homogeneous sections. The material orientation of the cross-layers had to be changed because the cross-layers are located perpendicular to the longitudinal layers. In order to do that, the material orientation was assigned to the longitudinal layers so that it follows the global coordinate system. On the other hand, the material orientation of the cross-layers was changed so that they are placed in a transverse direction to the main one, see Figure 3-21.

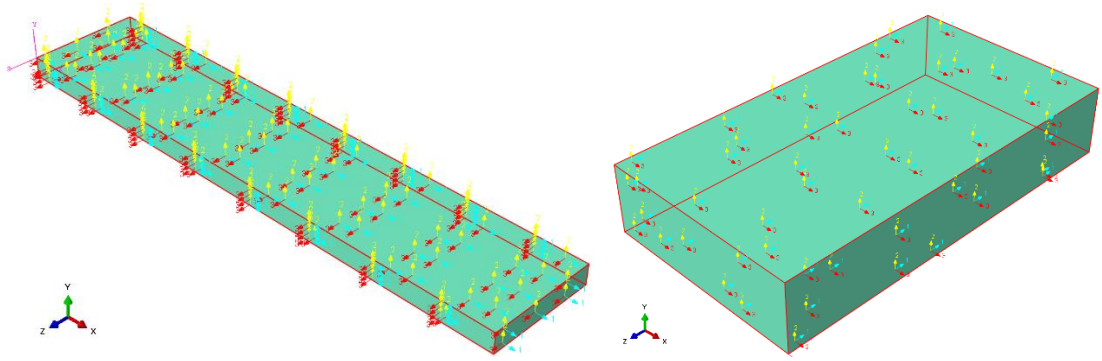

Figure 3-21 Material orientation of the longitudinal layer (left picture) and cross-layer (right picture).

3.3.3 Interaction

The interactions between neighboring layers were modeled as tie constraints. The constraints were set between the surface of the longitudinal layer with the surface of the cross-layer that attached to each other. Moreover, no interaction was modeled between cross-layers as no edge-bonding was assumed.

3.3.4 Boundary conditions

In order to represent the shear test in numerical analysis, the boundary conditions were applied at two inclined surfaces. The displacement/rotation type of boundary condition was chosen, and one surface was fixed in all three directions

while the second surface was fixed in the y- and z-direction. Furthermore, the boundaries were free to rotate around all of the axes, and the same conditions were applied to the rest of the configurations.

3.3.5 Load application

The load was also applied at two inclined surfaces belonging to the upper and bottom longitudinal layers. The load was distributed uniformly at the surfaces, so the pressure type of load was chosen. Furthermore, the same magnitude of the load was applied at both sides, and each load was directed toward the specimen. LSF represents the magnitude of the load, and it is different for different configurations depending on the length of the specimen and the pressure area.

3.3.6 Load Scale Factor

In order to compare the results of different configurations, a LSF was introduced. Since the pressure area differs depending on the type of configuration, the area ratio was calculated, and it includes the inclined area where the load is applied and the reference pressure area. The equation of the pressure area ratio is presented below.

$$\eta_A = \frac{A_p}{A_{p,ref}} \; [-] \tag{3-6}$$

where A_p is the pressure area of the particular configuration and $A_{p,ref}$ is the reference area pressure.

LSF also depends on the length of the configuration. To be able to calculate a length ratio, the length of the particular configuration should be divided by the reference length according to the equation:

$$\eta_L = \frac{L}{L_{ref}} \; [-] \tag{3-7}$$

Where L is the length of the configuration and L_{ref} is the reference length of the specimen.

The load Scale Factor can be calculated by multiplying the pressure area ratio by the length ratio, as presented below.

$$LSF = \eta_A * \eta_L \; [-] \tag{3-8}$$

where η_A is the pressure area ratio and η_L is the length ratio.

3.3.7 Mesh and convergence study

In order to find the most appropriate mesh size so that the results are accurate and the computation time is not too long, the mesh convergence study was performed. Two different configurations of CLT panels were analyzed using C3D8R hex shape mesh and structured technique of meshing. For the convergence study, four different mesh sizes were checked: 10, 6, 4, and 3, the mesh sizes are

in millimetres. For each configuration, the vertical path was created between the air gaps, see Figure 3-22 and Figure 3-23.

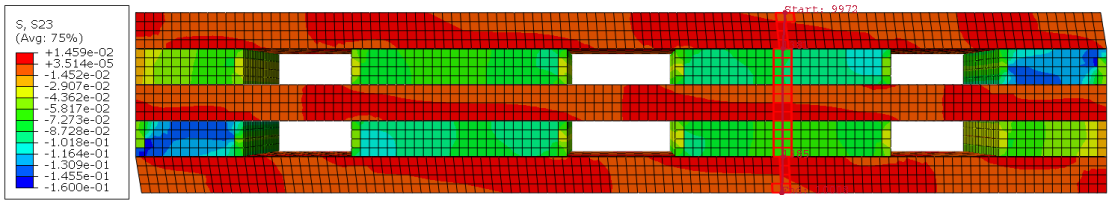

Figure 3-22 Location of the path of Configuration II.

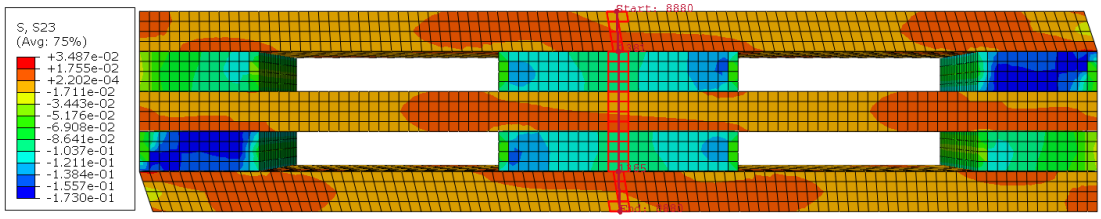

Figure 3-23 Location of the path for Configuration IV.

For each mesh size and configuration, the graphs that present the shear stresses in RT-direction vs the height distance generated by the path were plotted. The graphs are presented in Figure 3-24 and Figure 3-25.

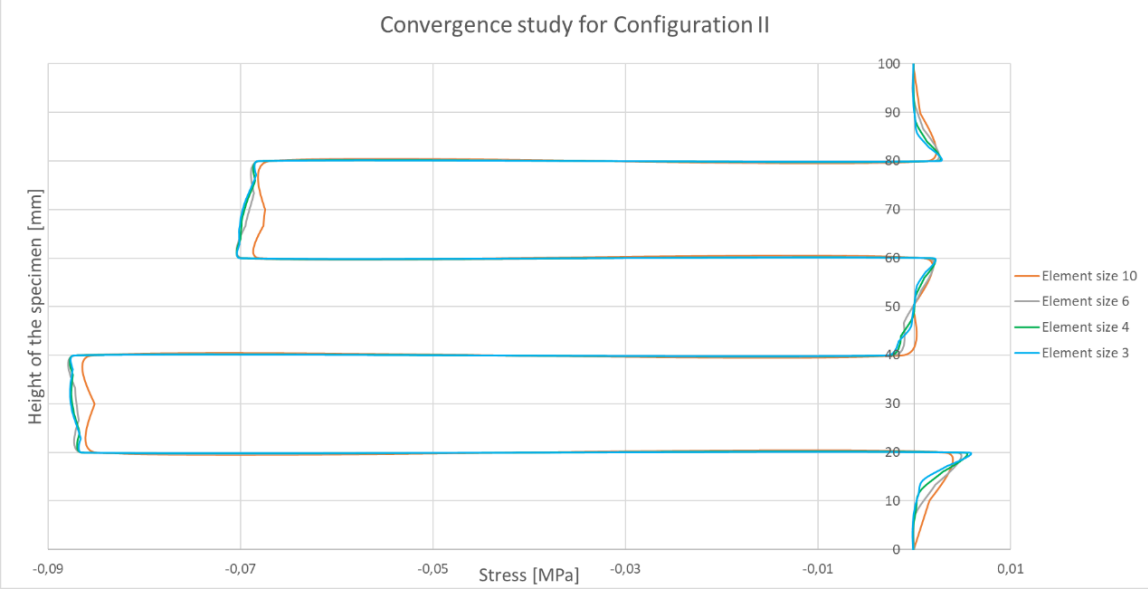

Figure 3-24 Mesh convergence study for Configuration II. Shear stress in RT-direction vs. distance within the path for different mesh sizes.

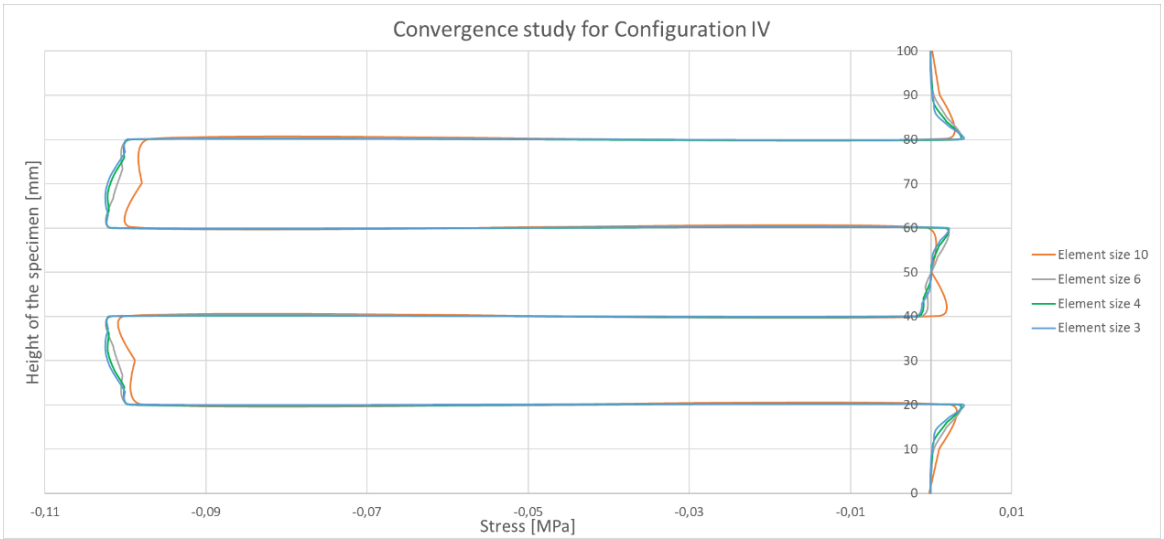

Figure 3-25 Mesh convergence study for Configuration IV. Shear stress in RT-direction vs. distance within the path for different mesh sizes.

The minimum value of stress was found for each configuration, and the results were plotted regarding the number of elements included in different mesh sizes, see Figure 3-26, and Figure 3-27. It can be concluded that between element size 10 and 4, the difference in the stress value is relatively significant, whereas between element size 4 and 3, the graph becomes almost constant, so the values converge.

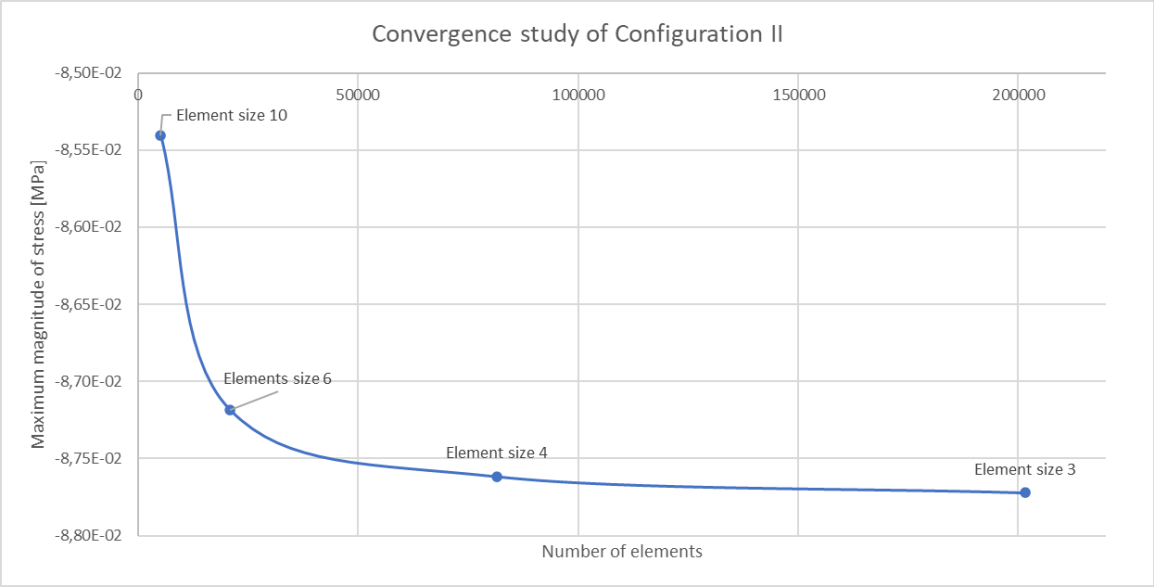

Figure 3-26 Convergence study for Configuration II. The number of elements vs. the minimum value of stress for each mesh size.

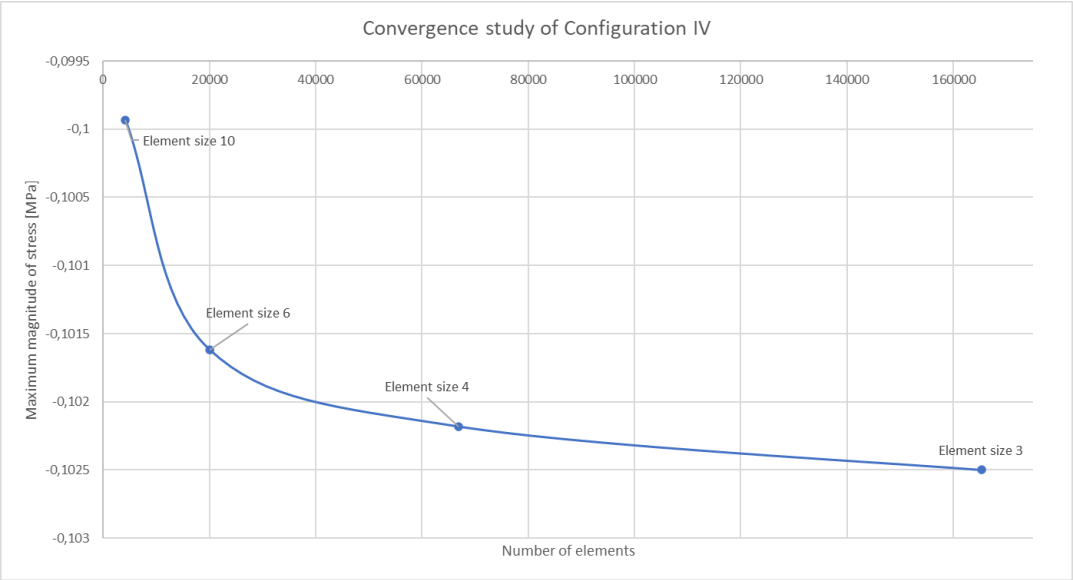

Figure 3-27 Convergence study for Configuration IV. The number of elements vs. the minimum value of stress for each mesh size.

To sum it up, the mesh with element size 4 was chosen for further analyses of all configurations so that the results should be accurate enough and the computation time is not exceeded, Figure 3-28.

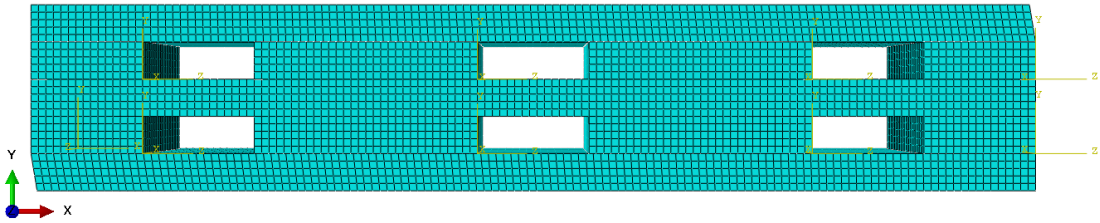

Figure 3-28 Mesh with element size 4 for Configuration II.

3.4 Modification and configurations summary

The shear strength of a solid specimen without any air gaps can be calculated based on equation (2-27) explained in section 2.4.1. As air gaps are introduced between the cross-layer of a CLT panel in this thesis, the equation for calculating the shear strength and rolling shear modulus must be modified with regards to the effective length of a CLT panel, in addition to comparing the results between different configurations that have different length the failure loads also need to be adjusted based on the pressure area and specimen length.

3.4.1 Modified shear strength formula

The rolling shear failure of the specimens with air gaps can be calculated based on the below equation, and it is named as effective rolling shear strength:

$$f_{r,eff} = \frac{F_{max} * cos(\beta)}{l_c * b} \quad [Pa] \qquad (3\text{-}9)$$

F_{max} is the maximum load obtained during testing [N].
b is the width of the test specimen [m].

l_c is the effective length of test specimens (length of the cross-layer bond lines) [m].
β is the angle between the load direction and the longitudinal axis.

The rolling shear modulus of rigidity can be calculated based on equation (2-26), but for the specimens that are tested in this master thesis, when the load is applied, the surface is not perfectly parallel to the clamp, see Figure 3-29.

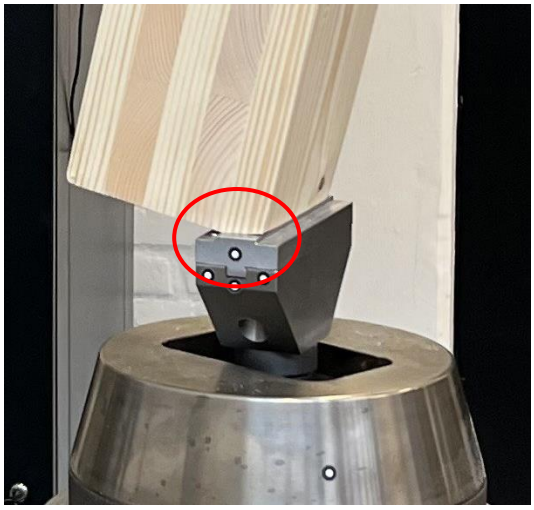

Figure 3-29 The connection between a specimen and the hydraulic press clamp.

Thus, there is some nonlinearity at the beginning of the applying load, and therefore the relation between the load and displacement is not linear at the beginning. But after a while, as the load is applied smoothly over the pressure area, the load-displacement relation becomes linear. For this reason, equation (2-26) is modified in this way so that the range between 30 and 60 percent of the maximum load is considered a linear part. Based on the test result, the length is also modified as the effective length of a cross-layers bond line. Therefore, the panel shear modulus of the rigidity equation is revised as below:

$$G_{r,eff} = \frac{(F_2 - F_1) * cos(\beta) * t}{(u_2 - u_1) * l_c * b} \quad [Pa] \qquad (3\text{-}10)$$

Where:
F_2-F_1 is load increments between $0.3F_{max}$ and $0.6F_{max}$ [N].
u_2-u_1 is the deflection increment according to F_2-F_1 by using a linear regression line [N].
b is the width of the test specimen [m].
l_c is the effective length of test specimens (length of the cross-layer bond lines) [m].
t is the thickness of the test specimen [m].
β is the angle between the load direction and the longitudinal axis.

3.4.2 Failure load ratio

Since the length of the different configurations are different, the failure load is adjusted based with regard to the length of the specimens, the length of the

specimen in Configuration I (solid CLT panel) is considered as a reference length; see equation (3-11), and then the failure loads of the other configuration are adjusted based on this, see equation (3-12),

$$\eta_L = \frac{L}{L_{ref}} \quad [-] \tag{3-11}$$

$$F_{adjusted} = \frac{F_{max}}{\eta_L}[N] \tag{3-12}$$

By adjusting the failure load based on the length of the specimens then, the failure load ratio can be calculated. The failure load of Configuration I (solid CLT panel) is considered as a reference load; see equation (3-13).

$$\eta_F = \frac{F_{adjusted}}{F_{ref}}[-] \tag{3-13}$$

3.4.3 Configurations

This subchapter provides a summary of information about the density and MOE of lamellas used in the production of small specimens. Besides that, the geometrical information is presented in summary tables for each configuration.

3.4.3.1 Density and MOE

As mentioned in section 3.1.2, all of the longitudinal layers were assigned from the boards with high MOE, and each specimen in a particular configuration is produced from cross-layers with low, average, or high MOE. Sample 2 was taken as the reference sample with average MOE of the cross-layers. The table includes the values of MOE and density of each sample and presents how MOE and density of the Sample 1 and 3 decreases or increases with regard to Sample 2, respectively, see Table 3-2.

Table 3-2 Average values for density and MOE for longitudinal layers and cross-layers.

		Sample 2 [MPa]	Sample 1 [MPa]	Decrease/ Increase [%]	Sample 3 [MPa]	Decrease/ Increase [%]
Specimen I-IV		**MOE [MPa]**				
	Cross-layers	14550.6	12479.2	-14.2	16480.4	13.3
	Longitudinal layers	16978.7				
		Density [kg/m³]				
	Cross-layers	460.2	485.5	5.5	486.5	5.7
	Longitudinal layers	501.8				
Specimen V		**MOE [MPa]**				
	Cross-layers	14550.6	12479.2	-14.2	16480.4	13.3
	Longitudinal layers	17911.9				
		Density [kg/m³]				
	Cross-layers	460.2	485.5	5.5	486.5	5.7
	Longitudinal layers	537.9				
Specimen VI		**MOE [MPa]**				
	Cross-layers	14550.6	12479.2	-14.2	16480.4	13.3
	Longitudinal layers	16174.2				
		Density [kg/m³]				
	Cross-layers	460,2	495,8	7,7	495,8	7,7
	Longitudinal layers	495,8				

3.4.3.2 Configuration I

Configuration I depicts a solid five-layer specimen with no air gaps in cross-layers.

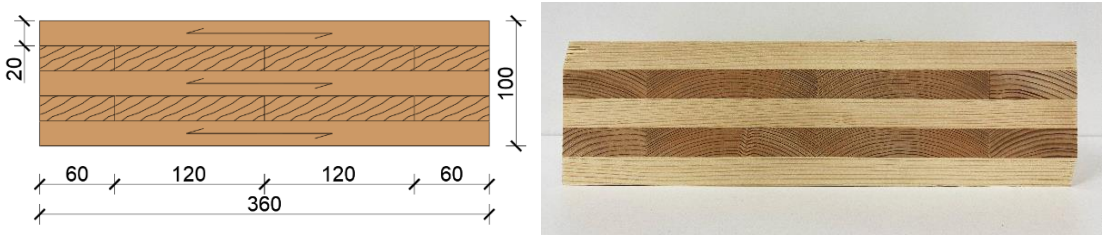

Figure 3-30 Geometry of Configuration I.

Table 3-3 Geometrical properties of Configuration I.

Air gap width b_{airgap} [mm]	0
Wood volume V_{wood} [mm³]	3 960 000
Maximum possible volume [mm³]	3 960 000
Relative volume η_V [-]	1.00
Material reduction η_M [%]	0.00

3.4.3.3 Configuration II

Configuration II is a five-layer configuration with air gaps located in cross-layers. The air gaps are 60 mm wide and are aligned symmetrically in the layers, see Figure 3-31.

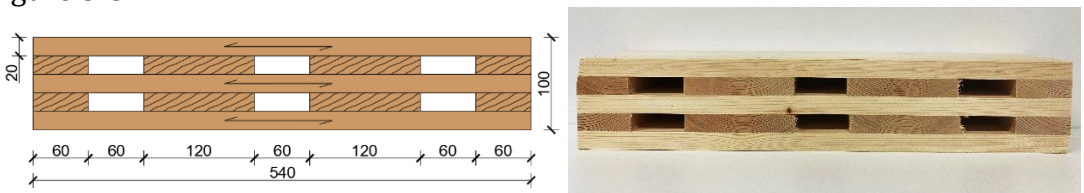

Figure 3-31 Geometry of Configuration II.

Table 3-4 Geometrical properties of Configuration II.

Air gap width b_{airgap} [mm]	60
Wood volume V_{wood} [mm³]	5 148 000
Maximum possible volume [mm³]	5 940 000
Relative volume η_V [-]	0.87
Material reduction η_M [%]	13.33

3.4.3.4 Configuration III

Configuration III is also a five-layer configuration with air gaps in cross-layers. The airgaps are shifted horizontally 90 mm in relation to other cross-layer and they are 60 mm wide, which results in 30 mm of overlapping between lamellas, see Figure 3-32.

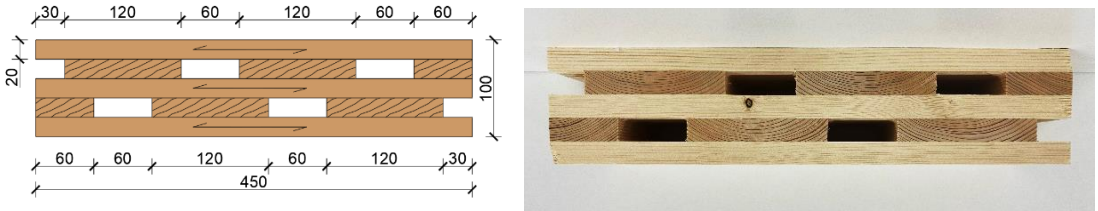

Figure 3-32 Geometry of Configuration III.

Table 3-5 Geometrical properties of Configuration III.

Air gap width b_{airgap} [mm]	60
Wood volume V_{wood} [mm³]	4 290 000
Maximum possible volume [mm³]	4 950 000
Relative volume η_V [-]	0.87
Material reduction η_M [%]	13.33

3.4.3.5 Configuration IV

Configuration IV represents a configuration with centrally aligned air gaps. The air gaps are 120 mm wide and have the same dimension as the cross-layer lamellas, see Figure 3-33.

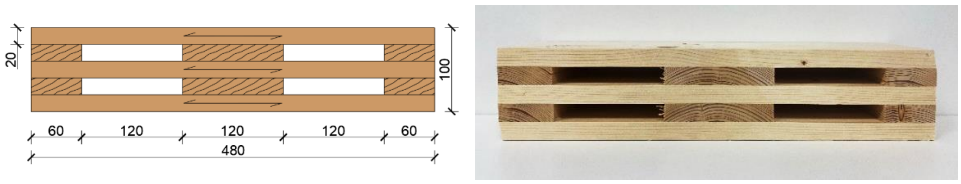

Figure 3-33 Geometry of Configuration IV.

Table 3-6 Geometrical properties of Configuration IV.

Air gap width b_{airgap} [mm]	120
Wood volume V_{wood} [mm³]	4 224 000
Maximum possible volume [mm³]	5 280 000
Relative volume η_V [-]	0.80
Material reduction η_M [%]	20.00

3.4.3.6 Configuration V

Configuration V is a five-layer configuration with air gaps that have the same dimensions as the timber lamellas in cross-layers. The air gaps are 120 mm wide and are shifted also 120 mm horizontally versus other cross-layer, see Figure 3-34.

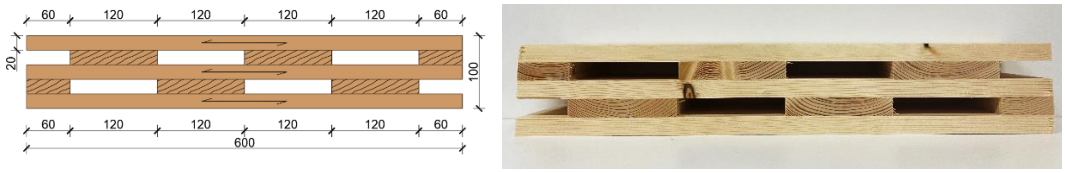

Figure 3-34 Geometry of Configuration V.

Table 3-7 Geometrical properties of Configuration V.

Air gap width b_{airgap} [mm]	120
Wood volume V_{wood} [mm³]	5 280 000
Maximum possible volume [mm³]	6 600 000
Relative volume η_V [-]	0.80
Material reduction η_M [%]	20.00

3.4.3.7 Configuration VI

Configuration VI depicts a five-layer configuration with air gaps in the cross-layers. The air gaps are 80 mm wide and are shifted 100 mm horizontally in relation to another cross-layer.

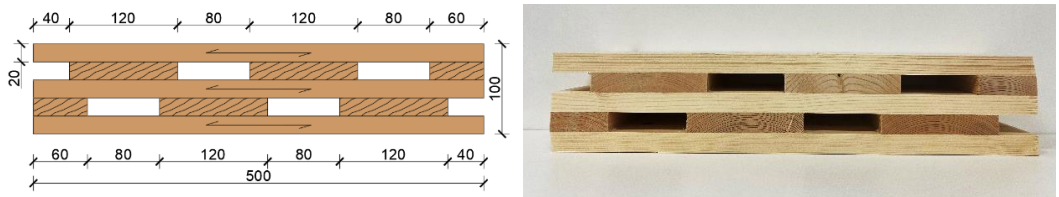

Figure 3-35 Geometry of Configuration VI.

Table 3-8 Geometrical properties of Configuration VI.

Air gap width b_{airgap} [mm]	80
Wood volume V_{wood} [mm³]	4 620 000
Maximum possible volume [mm³]	5 500 000
Relative volume η_V [-]	0.84
Material reduction η_M [%]	16.00

3.5 Shear tests results

All of the different CLT panel configurations are tested in shear according to the explanation in section 2.4.1. The results for each configuration are presented in this section.

3.5.1 Testing results from the rolling shear experiment for each configuration

3.5.1.1 Configuration I

3.5.1.1.1 Failure modes

The test results and parameters, including the maximum load and displacement, time of the failure, and loading rate are presented in Table 3-9. In addition, the failure mode is indicated for each specimen.

Table 3-9 The shear test results data and failure mode of Configuration I.

Specimen's name	Failure load [kN]	Maximum displacement [mm]	Time [s]	Loading rate [mm/min]	Failure mode
Sample 1	52.6	3.4	305.6	0.5	R, T2
Sample 2	51.9	4.1	275.5	0.5	R, T2
Sample 3	45.8	2.2	251.6	0.5	R, T2

Figure 3-36 presents results from the shear test of Configuration I. As can be seen, the main failure mode for the three samples is rolling shear failure.

Figure 3-36 Shear test results of Configuration I, with the order from top to bottom, Sample 1, Sample 2, and Sample 3, respectively.

Figure 3-37 Detailed results from the shear test of Configuration I, with the order from top to bottom, Sample 1, Sample 2, and Sample 3, respectively.

More details for the failure path of each sample are presented in Figure 3-37; for Sample 1, failure of the top cross layer led to the failure of the specimen. The crack path and directions are presented in Figure 3-38. The first cracks happened in the cross layers, and then one crack propagated significantly, leading to cracks in the transition zones at the neighbouring boards. As a result, rolling shear failure occurred.

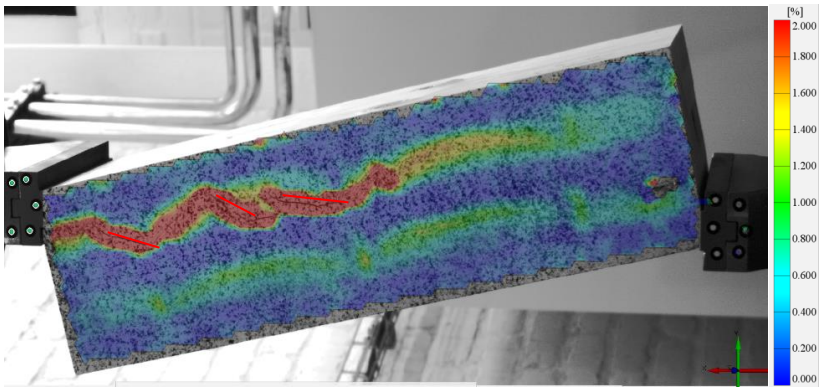

Figure 3-38 The strain distribution of Sample 1 at time 309 s and the load 41 kN [ARAMIS data, Configuration I].

For Sample 2, the first crack also happened at the cross-layer, and then it propagated in the interface zones, finally leading to the failure of the specimen (see Figure 3-39). For Sample 3, the cracks at the interfaces occurred first, and the rolling shear failure happened in the cross-layer. As a result, the specimen failed (brittle failure).

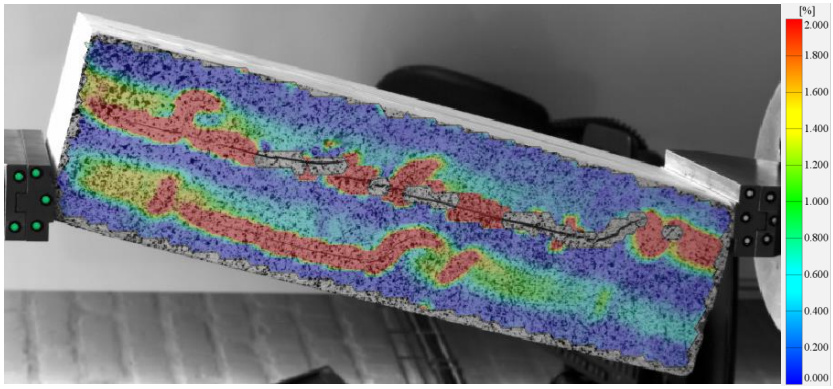

Figure 3-39 The strain distribution of Sample 2 at time 339 s and the load 25 kN [ARAMIS data, Configuration I].

3.5.1.1.2 Load deformation graphs

The load-deformation graph for Configuration I is presented in Figure 3-40. It can be seen that the failure load of Sample 1 and Sample 2 is almost the same and reaches 52.6 kN and 51.9 kN, respectively. The failure load is the lowest for Sample 3 and is equal to 45.8 kN. The maximum displacements were obtained by Sample 2, and the value is equal to 4.1 mm. The maximum deformations of Sample 1 reach 3.4 mm and of Sample 3 – 2.2 mm.

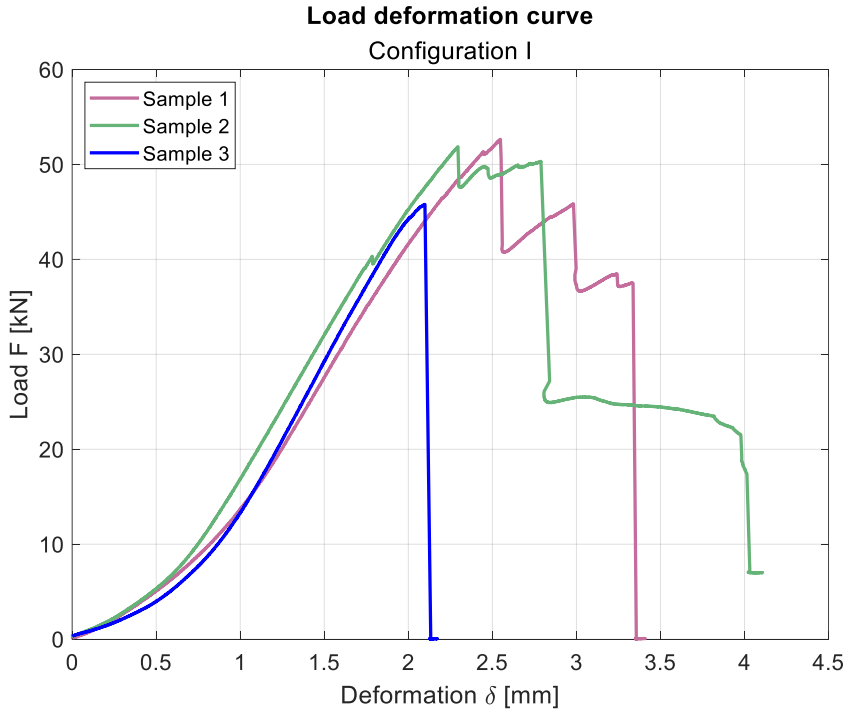

Figure 3-40 Load-deformation graph for Configuration I.

3.5.1.1.3 Shear strain from ARAMIS Software at failure load

The shear strain contour from ARAMIS software is presented in the pictures below. As can be seen, the maximum strain occurs in the cross-layers, which have a lower shear strength compared to the longitudinal ones. The same pattern can be observed for Samples 2 and 3, but the magnitude of the deformations in critical regions is higher, see Figure 3-41.

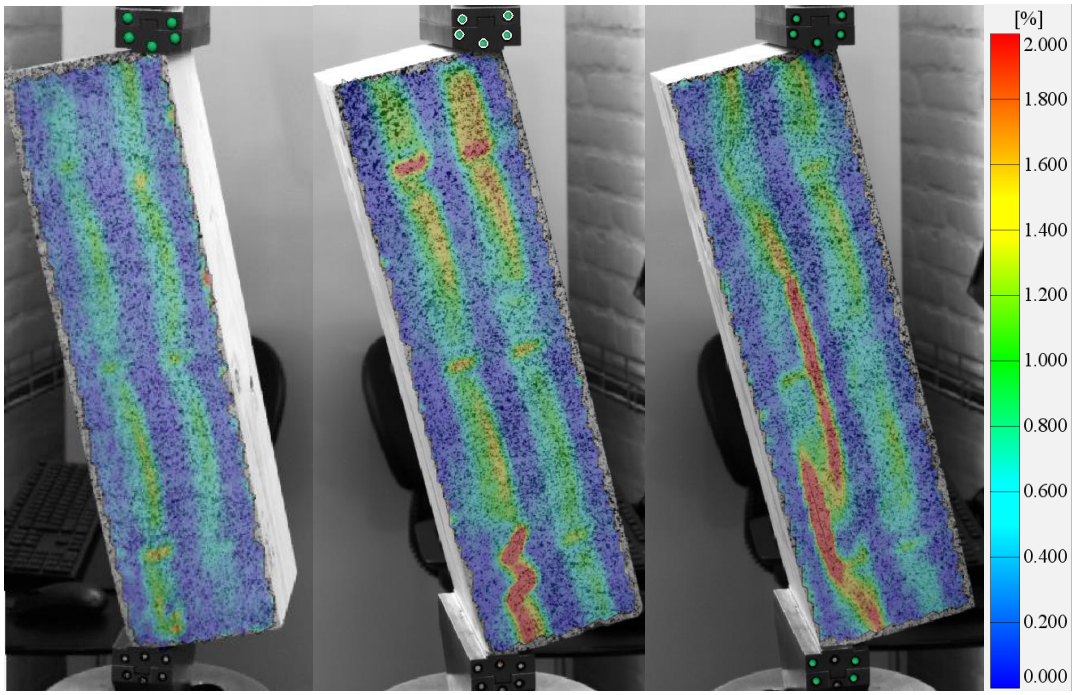

Figure 3-41 Strain distribution using ARAMIS at the failure load for Samples 1, 2, and 3 and Configuration I from left to right, respectively.

3.5.1.1.4 Rolling shear modulus and shear strength

The rolling shear modulus is calculated based on equation (2-26), and the shear strength is calculated based on equation (2-27). The results are presented in the table below; see Table 3-10. In addition, the rolling shear modulus equation is revised, and the range of the forces in equation (2-26) is changed to 0.3 and 0.6 of the maximum load to represent the linear part of the load-deformation curve, as can be seen in the load-deformation curve, see Figure 3-40. The new values of the rolling shear modulus are then calculated and shown in the table below.

Table 3-10 The values of effective shear strength, net shear strength, net shear strength ratio, and rolling shear modulus extracted based on the experimental data of Configuration I.

Specimen's name	Effective shear strength [MPa]	Net shear strength [MPa]	Normalized net shear ratio [-]	Net rolling shear modulus [MPa]
Sample 1	1.29	1.29	0.91	70.97
Sample 2	1.27	1.27	0.90	73.39
Sample 3	1.12	1.12	0.79	78.15

The highest shear strength is reached by Sample one, and the value is equal to 1.29 MPa; the shear strength of Sample 2 is 1.27 MPa, and for Sample 3, it is 1.12 MPa. Based on the revised equation, the highest rolling shear modulus reaches 78.15 MPa for Sample 3, and the value is the lowest for Sample 1 – 70.97 MPa.

3.5.1.2 Configuration II

3.5.1.2.1 Failure modes

The test results and parameters, including the maximum load and displacement, time of the failure, and loading rate, are presented in Table 3-11. In addition, the failure mode is indicated for each specimen.

Table 3-11 The shear test results data and failure mode of Configuration II.

Specimen's name	Failure load [kN]	Maximum displacement [mm]	Time [s]	Loading rate [mm/min]	Failure mode
Sample 1	43.3	2.3	258.7	0.5	R, T2
Sample 2	42.0	2.9	330.0	0.5	R, T2
Sample 3	40.5	2.8	299.1	0.5	R, T2

Figure 3-42 presents results from the shear test of Configuration II. As can be seen, the main failure mode for the three samples is rolling shear failure.

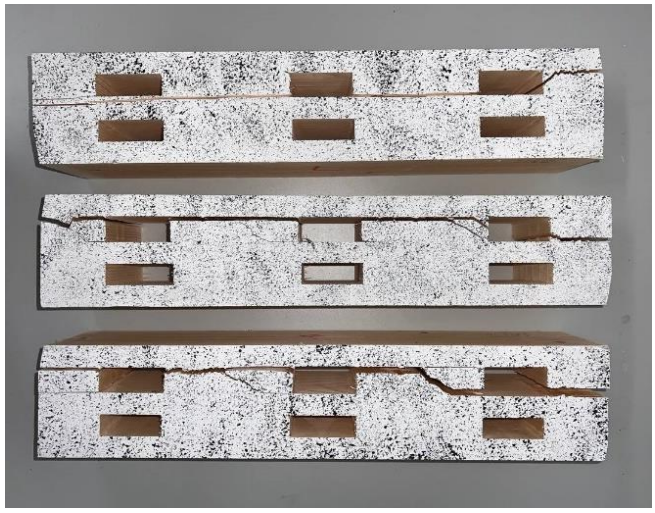

Figure 3-42 Shear test results of Configuration II, with the order from top to bottom, Sample 1, Sample 2, and Sample 3, respectively.

Figure 3-43 Detailed results from the shear test of Configuration II, with the order from top to bottom, Sample 1, Sample 2, and Sample 3, respectively.

For Sample 1, the crack occurred first at the corner of the air gaps between cross-layers due to stress concentrations in these parts; see Figure 3-44. However, the higher strain happened in the tangential direction of the cross-layer on the right side, see Figure 3-44, which led to the failure of the specimens.

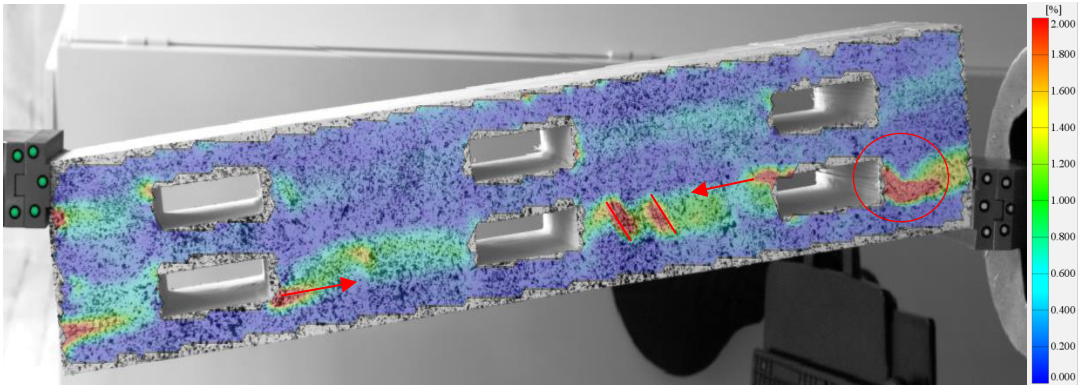

Figure 3-44 The strain distribution of Sample 1 at time 269 s and the load 39 kN (ARAMIS data, Configuration II).

The same failure and crack modes happened for Sample 2. As it is shown in Figure 3-45, the crack occurred in the interface zones, and the cross-layer failed in the region near the air gap between the cross-layers.

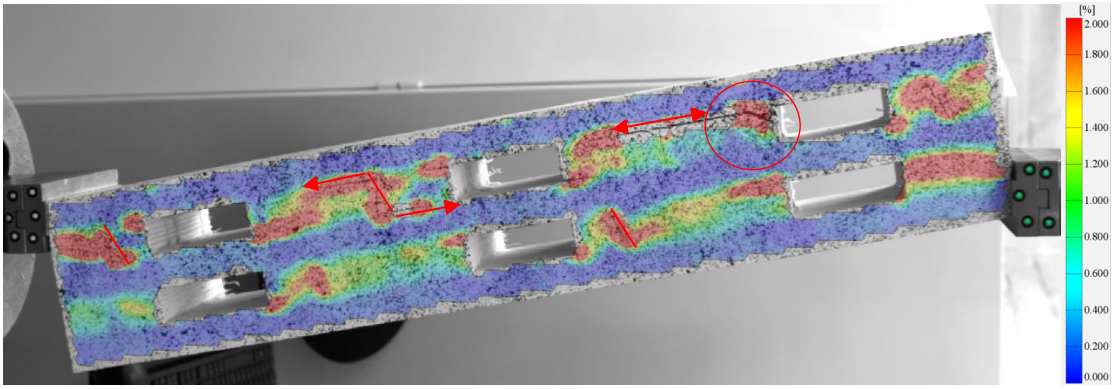

Figure 3-45 The strain distribution of Sample 2 at time 340 s and the load 40.7 kN (ARAMIS data, Configuration II).

Also, for Sample 3, the primary failure mode is rolling shear failure due to creating cracks and propagation in the cross-layers. The main cracks are indicated in Figure 3-46.

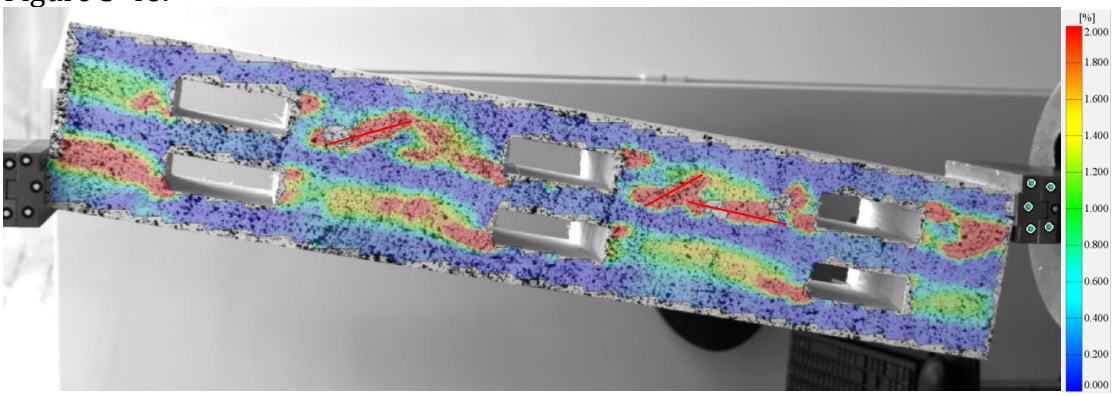

Figure 3-46 The strain distribution of Sample 3 at time 301 s and the load 40 kN (ARAMIS data, Configuration II).

3.5.1.2.2 Load deformation graphs

The load-deformation graph for Configuration II is presented in Figure 3-47. It can be seen that the failure load of all three samples is almost the same and reaches 43.3 kN, 42.0 kN, and 40.5 kN, respectively. The maximum deformations are the highest for Sample 2 and are equal to 2.9 mm; for Sample 3, the value reaches 2.8 mm, and for Sample 1 - 2.3 mm.

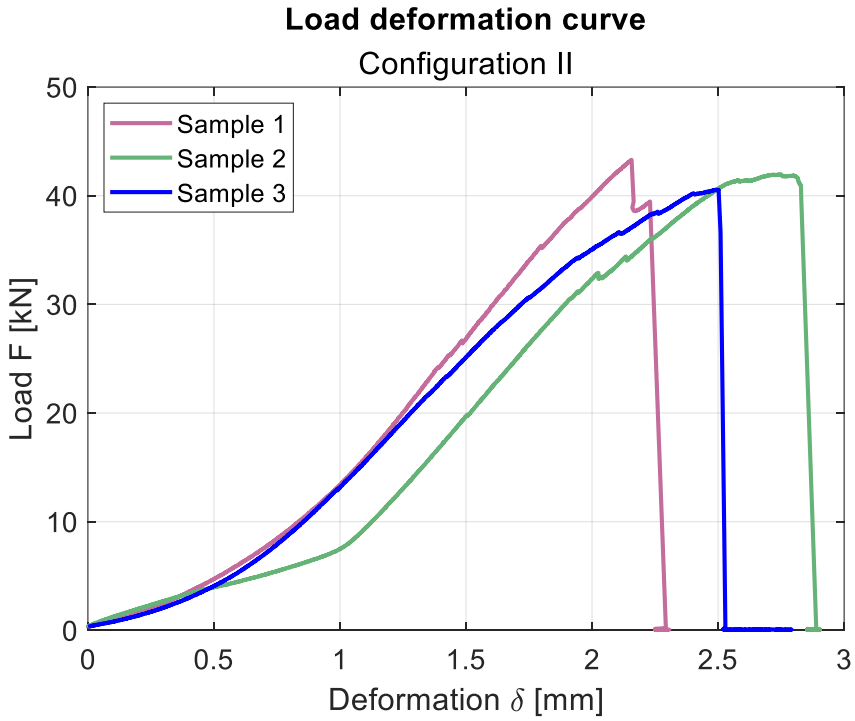

Figure 3-47 Load-deformation graph for Configuration II.

3.5.1.2.3 Shear strain from ARAMIS Software before failure

The shear strain contour from ARAMIS software is presented in the pictures below. The maximum strain can be found in the cross-layers with a lower shear strength than the longitudinal ones. The same pattern can be observed for samples 2 and 3, as shown in Figure 3-48. The magnitude of the strain reaches 2% for Samples 2 and 3, and it is higher for Sample 1. The reason could be that the failure of Samples 2 and 3 has a brittle character, so the specimens broke when the failure load was applied. On the other hand, Sample 1 broke after the time when the maximum load was applied, so the maximum deformations did not occur at the moment of failure load.

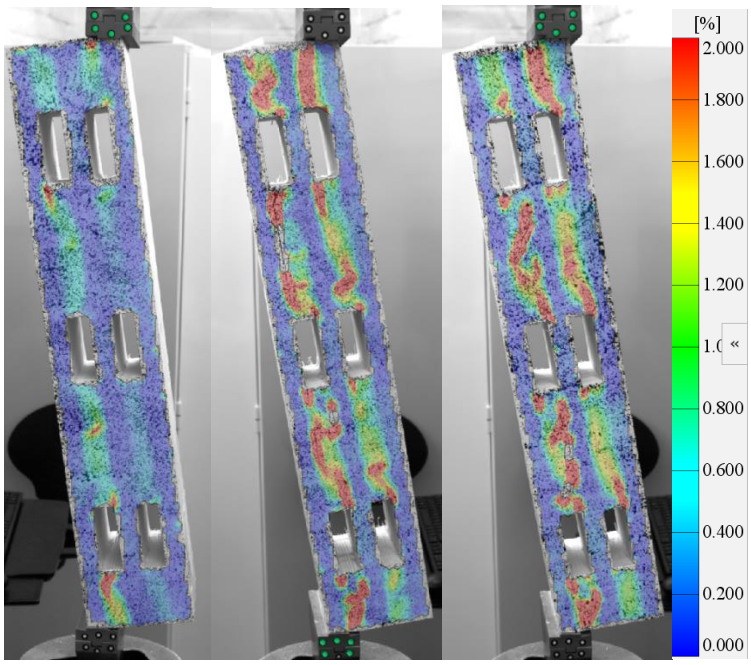

Figure 3-48 Strain distribution using ARAMIS at the failure load for samples 1, 2, and 3 and Configuration II from left to right, respectively.

3.5.1.2.4 Rolling shear modulus and shear strength

The rolling shear modulus is calculated based on equation (2-26), and the shear strength is calculated based on equation (2-27). The results are presented in the table below; see Table 3-12. In addition, the rolling shear modulus equation is revised, and the range of the forces in equation (2-26) is changed to 0.3 and 0.6 of the maximum load to represent the linear part of the load-deformation curve, as can be seen in the load-deformation curve, see Figure 3-47. The new values of the rolling shear modulus are then calculated and shown in the table below.

Table 3-12 The values of effective shear strength, net shear strength, net shear strength ratio, and rolling shear modulus extracted based on the experimental data of Configuration II.

Specimen's name	Effective shear strength [MPa]	Net shear strength [MPa]	Normalized net shear ratio [-]	Net rolling shear modulus [MPa]
Sample 1	1.08	0.72	0.51	45.23
Sample 2	1.05	0.70	0.49	43.99
Sample 3	1.01	0.67	0.48	39.32

The highest shear strength is reached by Sample 1, and the value is equal to 1.08 MPa; the shear strength of Sample 2 is 1.0.5 MPa, and for Sample 3, it is 1.01 MPa. Based on the revised equation, the highest net rolling shear modulus reaches 45.23 MPa for Sample 1, and the value is the lowest for Sample 3 – 39.32 MPa.

3.5.1.3 Configuration III

3.5.1.3.1 Failure modes

The shear test result and parameters for Configuration III are provided in Table 3-13. In addition, the failure mode is indicated for each specimen.

Table 3-13 The shear test results data and failure mode of Configuration III.

Specimen's name	Failure load [kN]	Maximum displacement [mm]	Time [s]	Loading rate [mm/min]	Failure mode
Sample 1	48.0	2.5	294.7	0.5	R, T2
Sample 2	47.6	3.3	390.5	0.5	R, T2
Sample 3	44.0	2.7	271.1	0.5	R, T2

The shape of each sample of Configuration III after failure is presented in Figure 3-49; as it can be seen, the collapse happened when a cross-layer failed.

Figure 3-49 Shear test results of Configuration III, with the order from top to bottom, Sample 1, Sample 2, and Sample 3, respectively

More details about failure modes are presented in Figure 3-50. It is evident that the cross-layers failed in rolling.

Figure 3-50 Detailed results from the test of Configuration III, from the top: Sample 1, Sample 2, Sample 3.

An example of the moment of failure is presented in Figure 3-51 for Sample 2. The rolling shear failure of cross-layers can be indicated in this picture.

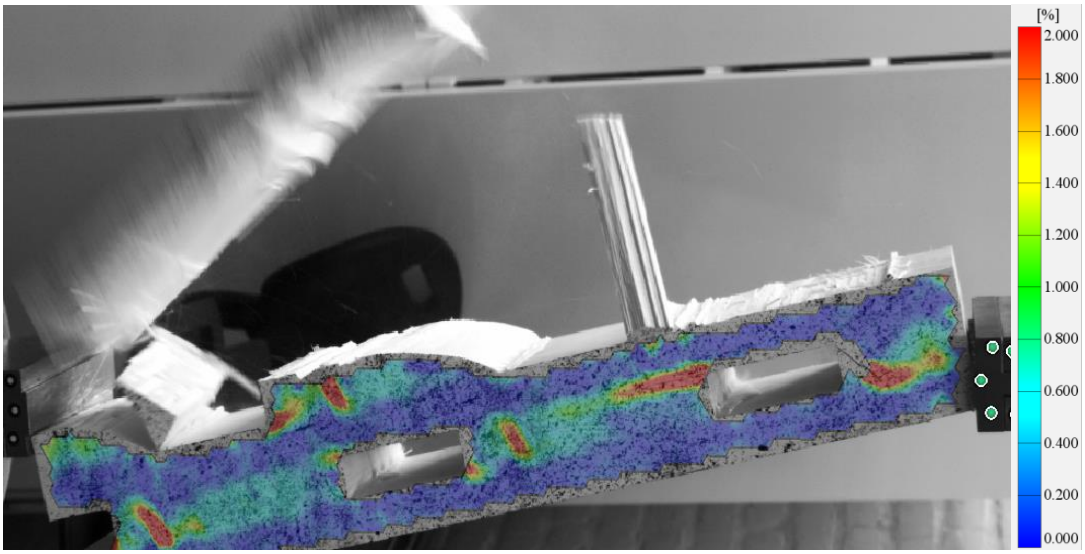

Figure 3-51 The failure moment of Sample 2 of Configuration III at time 403 s.

3.5.1.3.2 Load deformation graphs

The load-deformation graph for Configuration III can be found in Figure 3-52. The failure load of Sample 1 and Sample 2 reaches the highest values of 48 kN and 47.8 kN. The failure load of Sample 3 is equal to 44 kN. The maximum deformations are the highest for Sample 2 and are equal to 3.3 mm; for Sample 3, the value reaches 2.7 mm, and for Sample 1 - 2.5 mm. Additionally, it can be observed that the failure of Specimen 1 and 2 was brittle, while the failure of Specimen 3 was more ductile.

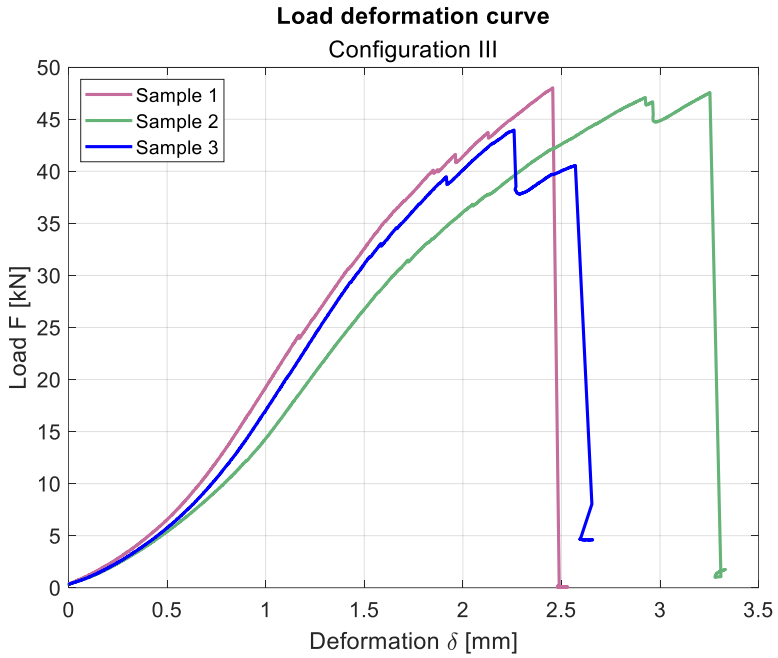

Figure 3-52 Load-deformation graph for Configuration III.

3.5.1.3.3 Shear strain from ARAMIS software before failure

The strain distribution of each three samples at failure load is shown in Figure below. It can be seen that higher strain happened in the cross-layers. Moreover, the highest values could usually be found near the corners of air gaps.

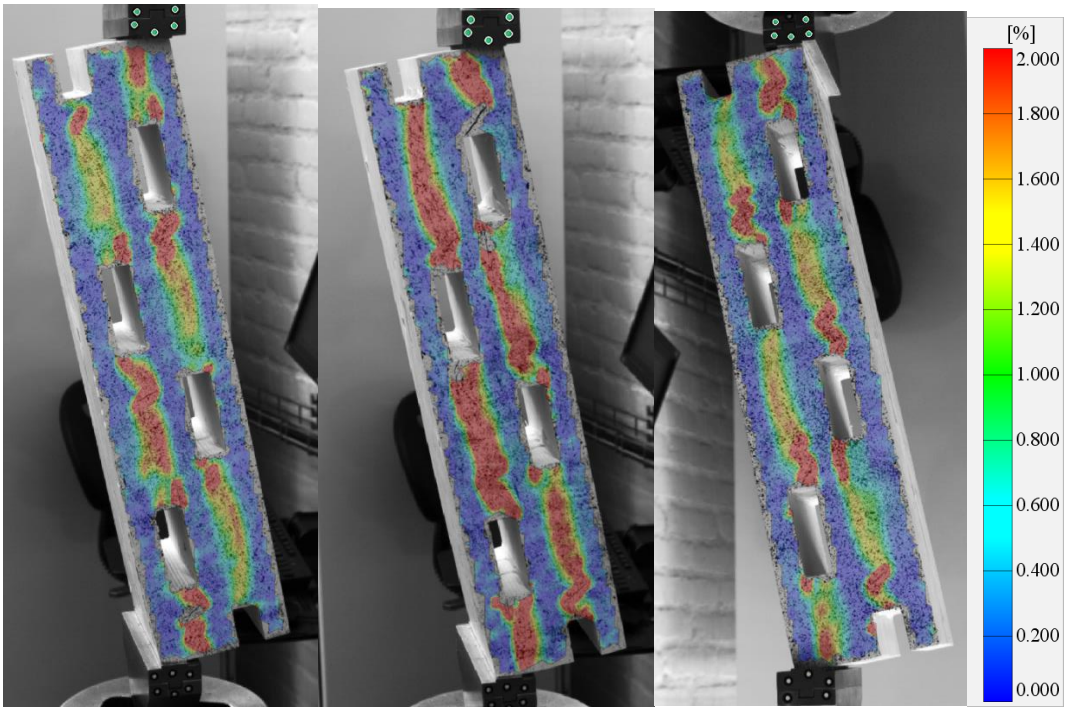

Figure 3-53 Strain distribution using ARAMIS at the failure load for Samples 1, 2, and 3 and Configuration III from left to right, respectively.

3.5.1.3.4 Rolling shear modulus and shear strength

The rolling shear modulus is calculated based on equation (2-26), and the shear strength is calculated based on equation (2-27). The results are presented in the table below. In addition, the rolling shear modulus equation is revised, and the range of the forces in equation (2-26) is changed to 0.3 and 0.6 of the maximum load to represent the linear part of the load-deformation curve, as can be seen in the load-deformation curve, see Figure 3-52. The modified values of the rolling shear modulus are calculated then and shown in the table below.

Table 3-14 The values of effective shear strength, net shear strength, net shear strength ratio and rolling shear modulus extracted based on the experimental data of Configuration III.

Specimen's name	Effective shear strength [MPa]	Net shear strength [MPa]	Normalized net shear ratio [-]	Net rolling shear modulus [MPa]
Sample 1	1.43	0.95	0.67	55.51
Sample 2	1.41	0.94	0.67	48.46
Sample 3	1.31	0.87	0.62	56.69

The highest shear strength was obtained by Sample 1, and the value is equal to 1.43 MPa. The shear strength of Sample 2 is 1.41 MPa, and Sample 3 has a strength

of 1.31 MPa. The net rolling shear modulus calculated based on the revised equation is the highest for Sample 3 – 56.69MPa. The net rolling shear modulus for Sample 1 is equal to 55.51 MPa, and for Sample 2 is 48.46 MPa.

3.5.1.4 Configuration IV

3.5.1.4.1 Failure modes

The test results and parameters, including the maximum load and displacement, time of failure, and loading rate, are presented in Table 3-15. In addition, the failure mode is indicated for each specimen.

Table 3-15 The shear test results data and failure mode of Configuration IV.

Specimen's name	Failure load [kN]	Maximum displacement [mm]	Time [s]	Loading rate [mm/min]	Failure mode
Sample 1	38.9	3.1	364.8	0.5	R, T2
Sample 2	35.6	2.7	310.2	0.5	R, T2
Sample 3	32.7	2.6	303.1	0.5	R, T2

Figure 3-54 presents results from the shear test of Configuration IV.

Figure 3-54 Shear test results of Configuration IV, with the order from top to bottom, Sample 1, Sample 2, and Sample 3, respectively.

Figure 3-55 Detailed results from the shear test of Configuration IV, with the order from top to bottom, Sample 1, Sample 2, and Sample 3, respectively.

Sample 1 failed in brittle character. The figure below shows the crack pattern before cracking. It can be seen that the higher strain happened in cross-layers, and the crack started in the middle of the cross-layer center and the edge near the air gaps at the stress concentration points.

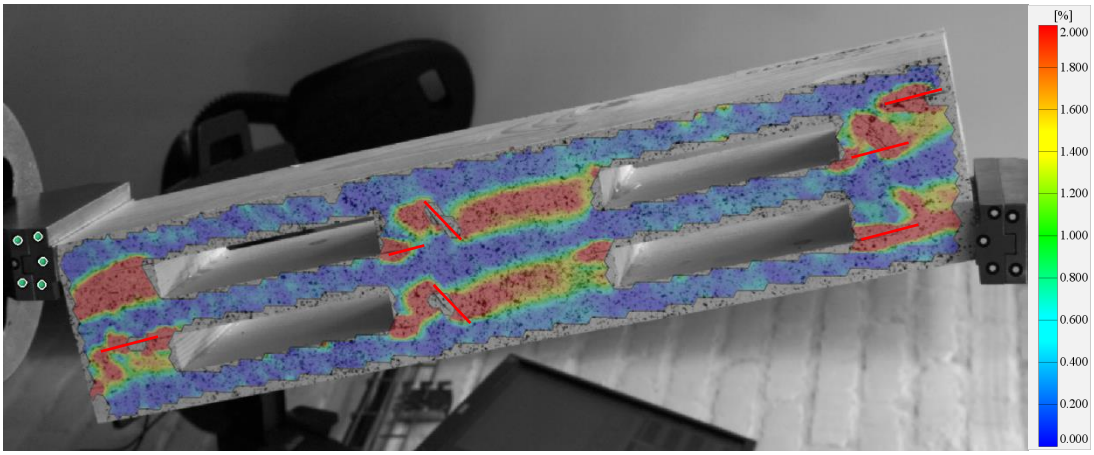

Figure 3-56 The strain distribution of Sample 1 at 366 s and the load 38.5 kN (ARAMIS data, Configuration IV).

For Sample 2, the broken specimen shows better crack patterns than the Aramis picture (see Figure 3-60). The crack's paths are indicated in Figure 3-57. It is evident that the rolling shear with the combination of interface failure between layers is the failing governing mode.

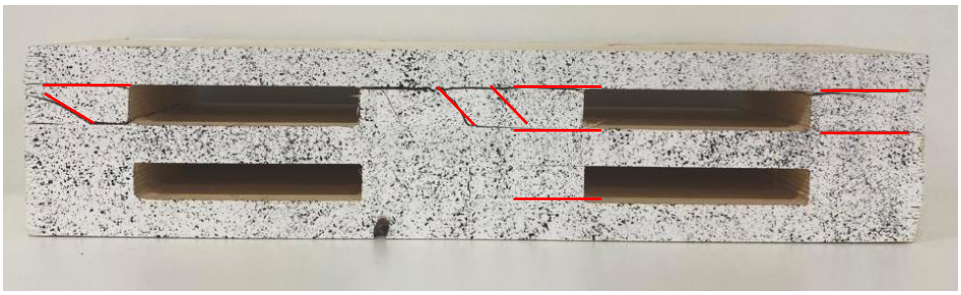

Figure 3-57 The crack's pattern of Sample 2 of Configuration IV.

Sample 3, similar to the previous ones, failed in the rolling shear failure of cross-layer and interface loss of layers, that marked in the Figure below.

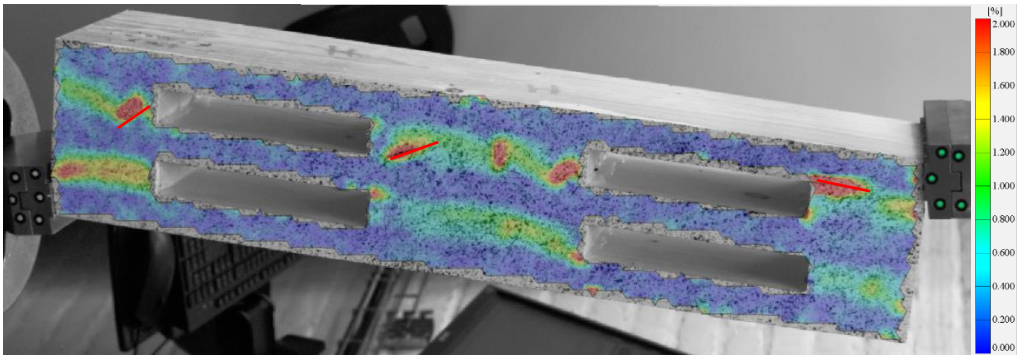

Figure 3-58 Crack patterns of Sample 3 of configuration IV for at 304 s and the load 32.3 kN (Aramis data).

3.5.1.4.2 Load deformation graphs

The load-deformation graph for Configuration IV is presented in Figure 3-59. The failure load for Sample 1 reaches the highest value of 38.9 kN. The failure load of Samples 2 and 3 is lower and is equal to 35.6 kN and 32.7 kN, respectively. Additionally, the highest deformations can also be observed at Sample 1, and they reach 3.1 mm, and the maximum displacements for Sample 2 and Sample 3 are equal to 2.7 mm and 2.6 mm. The failure of all three samples is brittle.

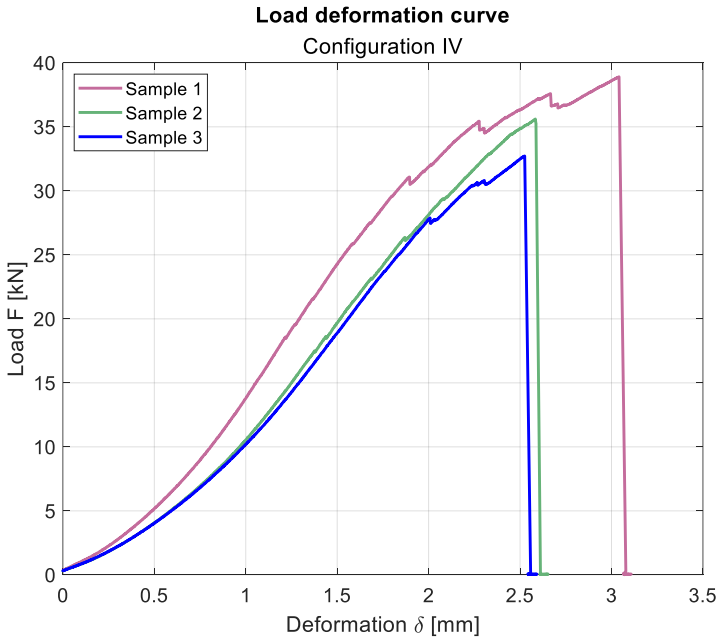

Figure 3-59 Load-deformation graph for Configuration IV.

3.5.1.4.3 Shear strain from ARAMIS Software before failure

The shear strain contour from ARAMIS software is presented in the pictures below. The maximum deformations occur in the cross-layers with a lower shear strength than in longitudinal layers. The peak values of strain at the failure load can be found close to the corners of air airgaps. The cracks are created at that points and lead to the failure of the specimen.

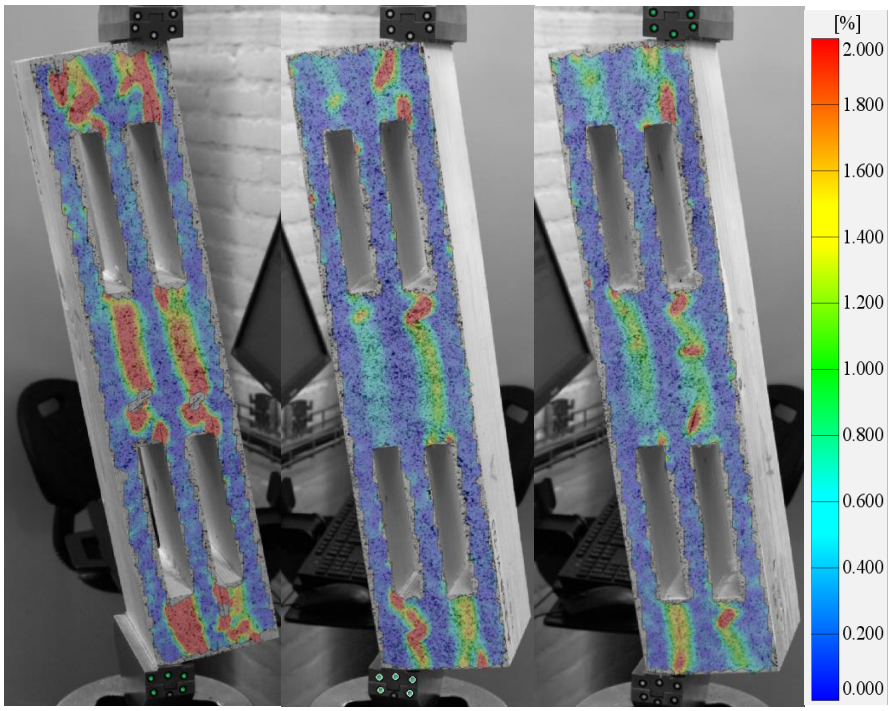

Figure 3-60 Strain distribution using ARAMIS at the failure load for Samples 1, 2, and 3 and Configuration IV from left to right, respectively.

3.5.1.4.4 Rolling shear modulus and shear strength

The rolling shear modulus is calculated based on equation (2-26), and the shear strength is calculated based on equation (2-27). The results are presented in the table below. In addition, the rolling shear modulus equation is revised, and the range of the forces in equation (2-26) is changed to 0.3 and 0.6 of the maximum load to represent the linear part of the load-deformation curve, as can be seen in the load-deformation curve, see Figure 3-59. The modified values of the rolling shear modulus are calculated then and shown in the table below.

Table 3-16 The values of effective shear strength, net shear strength, net shear strength ratio, and rolling shear modulus were extracted based on the experimental data of Configuration IV.

Specimen's name	Effective shear strength [MPa]	Net shear strength [MPa]	Normalized net shear ratio [-]	Net rolling shear modulus [MPa]
Sample 1	1.45	0.72	0.51	39.12
Sample 2	1.33	0.66	0.47	34.49
Sample 3	1.22	0.61	0.43	32.47

As for the previous configurations, the highest shear strength has Sample 1, and the value is equal to 1.45 MPa. The shear strength of Sample 2 is 1.33 MPa, and Sample 3 reaches the value of 1.22 MPa. The highest value of net rolling shear modulus that is calculated based on the revised equation is equal to 39.12 MPa for Sample 1, the modulus for Sample 2 has a value of 34.49 MPa, and Sample 3 is 32.47 MPa.

3.5.1.5 Configuration V

3.5.1.5.1 Failure modes

The test results and parameters, including the maximum load and displacement, time of failure, and loading rate, are presented in Table 3-17 The shear test results data and failure mode of Configuration V. In addition, the failure mode is indicated for each specimen.

Table 3-17 The shear test results data and failure mode of Configuration V.

Specimen's name	Failure load [kN]	Maximum displacement [mm]	Time [s]	Loading rate [mm/min]	Failure mode
Sample 1	45.1	2.8	330.3	0.5	R, T2
Sample 2	28.9	2.3	244.5	0.5	T2
Sample 3	32.4	2.4	256.5	0.5	R, T2

Figure 3-61 presents results from the shear test of Configuration V.

Figure 3-61 Shear test results of Configuration V, with the order from top to bottom, Sample 1, Sample 2, and Sample 3, respectively.

Figure 3-62 Detailed results from the test of Configuration V, from the top: Sample 1, Sample 2, Sample 3.

Sample 1 has a brittle character failure. As can be seen in Figure 3-63, the first cracks happened in the cross-layers at 142 sec and for a force equal to about 19 kN. After that, the cracks start growing in the position beside the air gaps and propagate between the interface layers. At the same time, more cracks appear in cross-layers, as shown in Figure 3-68, at the failure load.

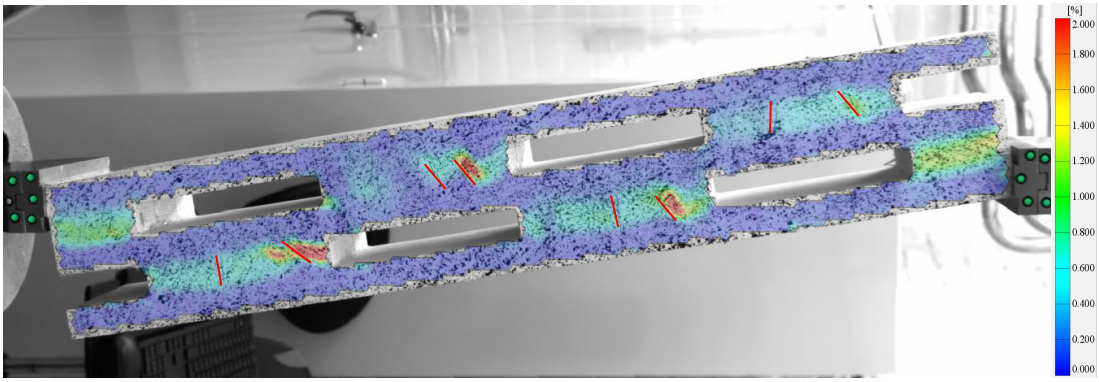

Figure 3-63 The strain distribution of Sample 1 at time 142 s and the load 19 kN (ARAMIS data, Configuration V).

For Sample 2, there was a crack already between the middle longitudinal layer and the bottom cross layer at the beginning. It led to stress concentration and higher strain in that area. The crack propagated, and finally, failure of the specimen occurred. It can also be seen in Figure 3-65 that the failure happened by the delamination of the cross-layer near the glue bond.

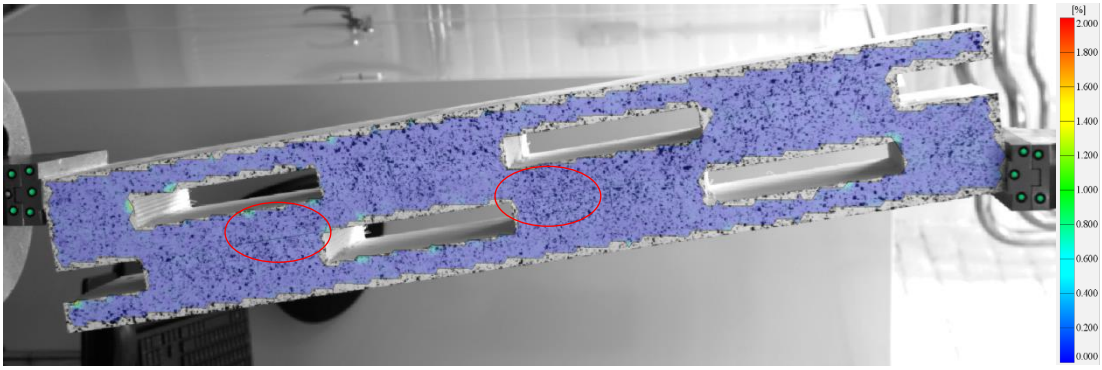

Figure 3-64 Initial crack observed before loading Sample 2 of Configuration V (ARAMIS data).

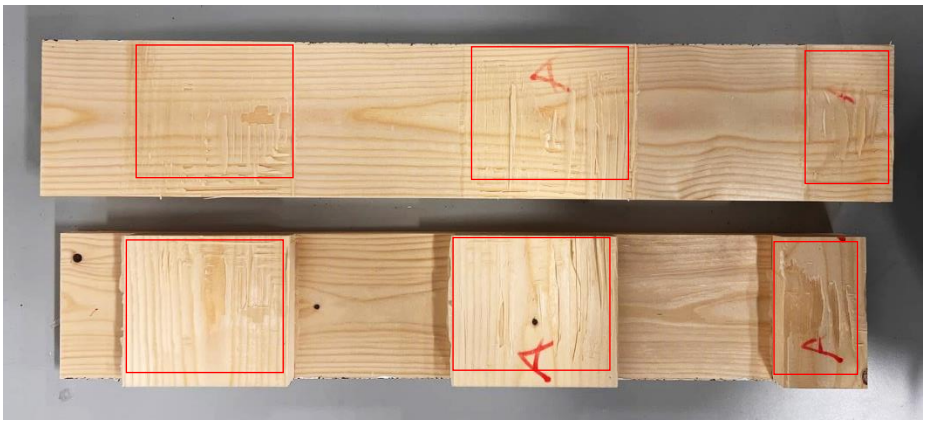
Figure 3-65 Delamination of cross-layers of Sample 2 from Configuration V.

Sample 3 failed in ductile character. Figure 3-66 shows the primary failure mode, which is rolling shear at the top cross-layer. The cracks started in the cross-layers at the corner of the air gaps and finally propagated, leading to the specimen's failure.

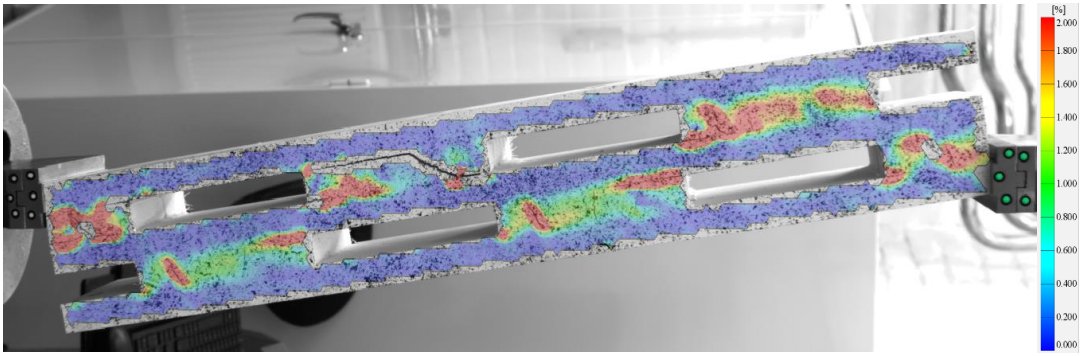

Figure 3-66 The strain distribution of Sample 3 at time 275 s and the load 21.5 kN (ARAMIS data, Configuration V).

3.5.1.5.2 Load deformation graphs

The load-deformation graph for Configuration V is presented in Figure 3-67. The highest failure load is reached by Sample 1 and is equal to 45.1 kN. The inclination of the elastic part of the Figure of Sample 1 is the highest, so this sample has the highest stiffness compared to Sample 2 and Sample 3. The failure load of Sample 2 and Sample 3 is 28.9 kN and 32.4 kN, respectively. Additionally, it can be observed that the failure of Sample 1 is brittle, while the failure of Sample 2 and Sample 3 is more ductile. The maximum deformations can be observed in Sample 1, and they are equal to 2.8 mm. The maximum strain for Sample 2 is 2.3 mm, and

the maximum deformations of Sample 3 that were computed by the system reached the value of 2.4 mm.

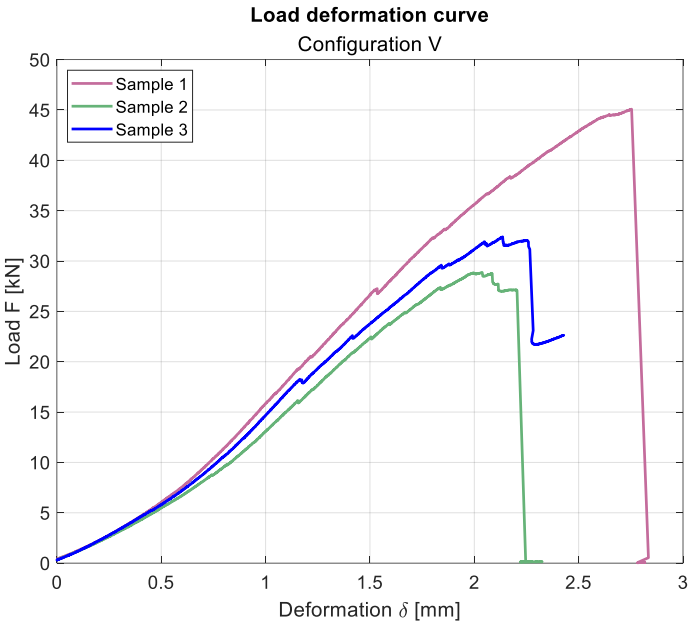

Figure 3-67 Load-deformation graph for Configuration V.

3.5.1.5.3 Shear strain from ARAMIS Software before failure

The strain distribution contour from ARAMIS software is presented in the pictures below. As can be seen, the maximum strain occurs in the cross-layers, which have a lower shear strength compared to the longitudinal ones. The pictures show that the highest strain concentration can be mainly found at the corners of the air gaps. Additionally, many areas with a high magnitude of deformations have a shape that might represent the rolling shear mode of failure.

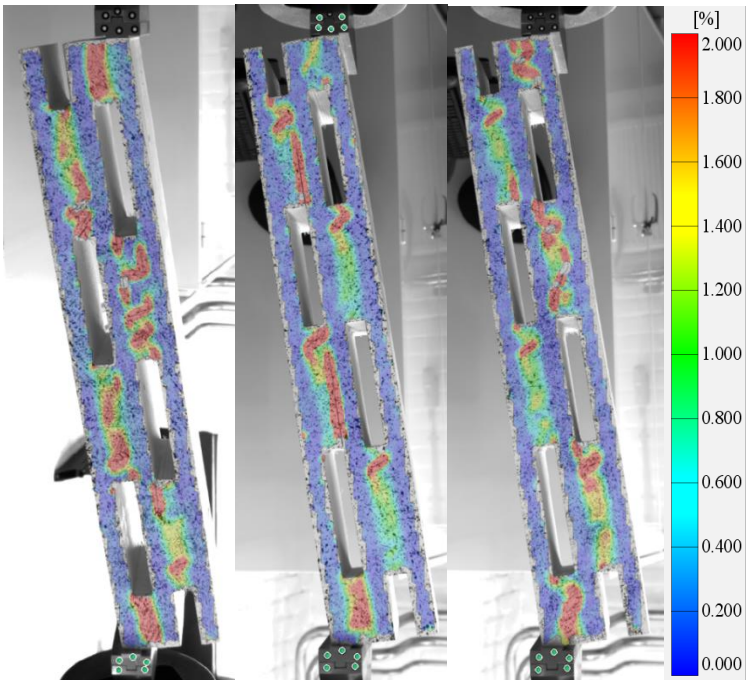

Figure 3-68 Strain distribution using ARAMIS at the failure load for Samples 1, 2, and 3 and Configuration V from left to right, respectively.

3.5.1.5.4 Rolling shear modulus and shear strength

The rolling shear modulus is calculated based on equation (2-26), and the shear strength is calculated based on equation (2-27). The results are presented in the table below. In addition, the rolling shear modulus equation is revised, and the range of the forces in equation (2-26) is changed to 0.3 and 0.6 of the maximum load to represent the linear part of the load-deformation curve, as can be seen in the load-deformation curve, see Figure 3-67. The modified values of the rolling shear modulus are calculated then and shown in the table below.

Table 3-18 The values of effective shear strength, net shear strength, net shear strength ratio, and rolling shear modulus were extracted based on the experimental data of Configuration V.

Specimen's name	Effective shear strength [MPa]	Net shear strength [MPa]	Normalized net shear ratio [-]	Net rolling shear modulus [MPa]
Sample 1	1.35	0.68	0.48	32.42
Sample 2	0.86	0.43	0.31	26.19
Sample 3	0.97	0.49	0.34	28.92

The highest shear strength has Sample 1, and the value is equal to 1.35 MPa. The shear strength of Sample 2 is 0.86 MPa, and Sample 3 reaches the value of 0.97 MPa. The highest value of net rolling shear modulus that is calculated based on the revised equation is equal to 32.42 MPa for Sample 1, the modulus for Sample 2 has a value of 26.19 MPa, and Sample 3 is 28.92 MPa.

3.5.1.6 Configuration VI

3.5.1.6.1 Failure modes

The test results and parameters, including the maximum load and displacement, time of the failure, and loading rate, are presented in Table 3-19. In addition, the failure mode is indicated for each specimen.

Table 3-19 The shear test results data and failure mode of Configuration VI.

Specimen's name	Failure load [kN]	Maximum displacement [mm]	Time [s]	Loading rate [mm/min]	Failure mode
Sample 1	45.3	2.5	272.9	0.5	R, T2
Sample 2	39.3	2.5	247.0	0.5	R, T2
Sample 3	42.9	2.7	316.6	0.5	R, L1

Figure 3-69 shows the specimens after the shear test.

Figure 3-69 Shear test results of Configuration VI, with the order from top to bottom, Sample 1, Sample 2, and Sample 3, respectively.

Figure 3-70 Detailed results from the shear test of Configuration VI, with the order from top to bottom, Sample 1, Sample 2, and Sample 3, respectively.

In Sample 1, the first cracks occurred in the cross layers; see Figure 3-71. After that, some cracks started in the edge corner of air gaps, and more cracks appeared in the cross layers. Finally, the specimen broke with a brittle character.

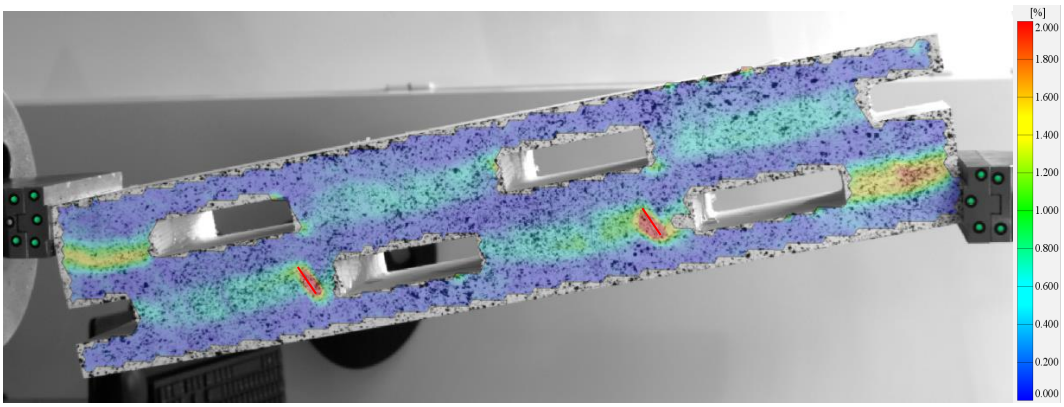

Figure 3-71 The strain distribution of Sample 1 at time 154 s and the load 25.2 kN (ARAMIS data, Configuration VI).

However, in Sample 2, the first cracks appeared in the corner of the air gaps, see Figure 3-72. But finally, the interface and rolling shear failure happened in the cross-layer, leading to the specimen's failure in brittle character.

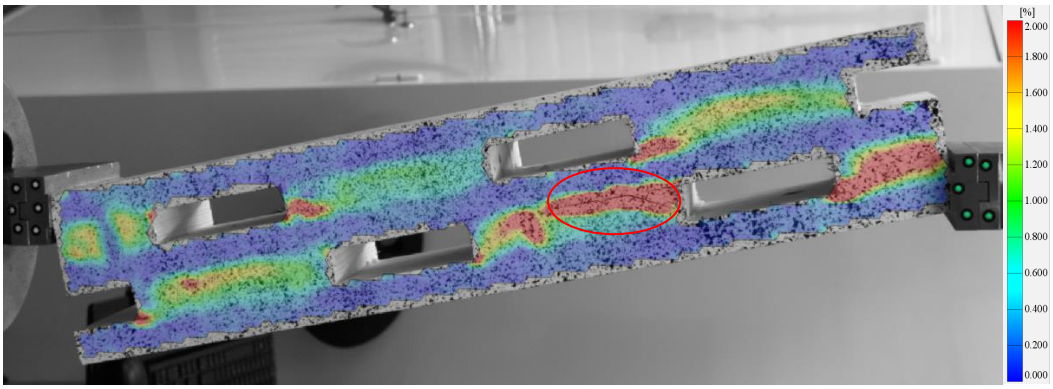

Figure 3-72 The strain distribution of Sample 2 at time 248 s and the load 36.5 kN (ARAMIS data, Configuration VI).

Cracks in Sample 3 started in the cross-layer in the radial direction and also in the longitudinal layer in the L-direction. The failure had a brittle character, and the ARAMIS picture does not show what the failure mode is, but by looking at the specimen after failure, see Figure 3-73, it can be seen the rolling shear happened.

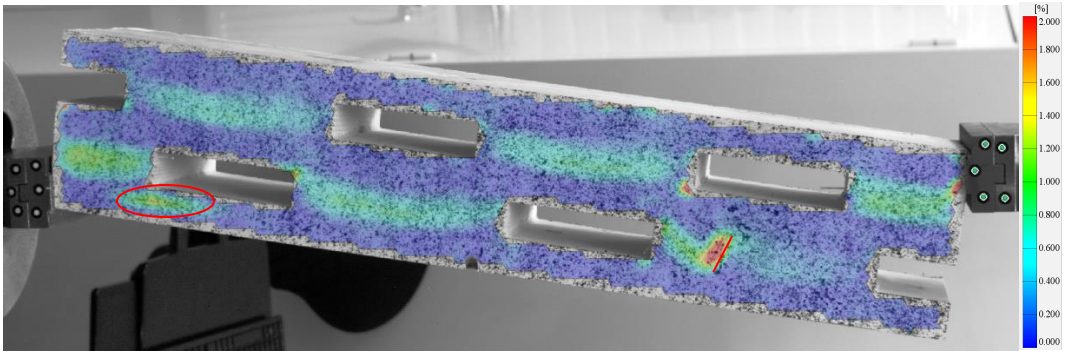

Figure 3-73 The strain distribution of Sample 3 at time 258 s and the load 36.6 kN (ARAMIS data, Configuration VI).

3.5.1.6.2 Load deformation graphs

The load-deformation graph for Configuration VI is presented in Figure 3-74. Sample 1 reaches the highest failure load and it is equal to 45.4 kN; the failure load for Sample 2 is 39.3 kN, and for Sample 3, it is 42.9 kN. Maximum displacements for Sample 1 and Sample 2 are equal to 2.5 mm, and for Sample 3, they are equal to 2.7 mm. The failure of Samples 1 and 3 is brittle, while the failure of Sample 2 is more ductile.

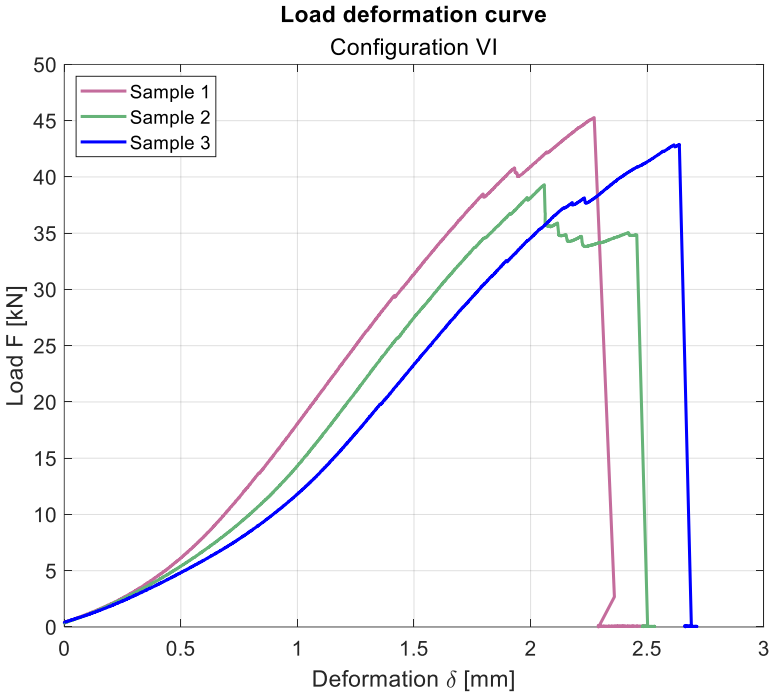

Figure 3-74 Load-deformation graph for Configuration VI.

3.5.1.6.3 Shear strain from ARAMIS Software before failure

The shear strain contour from ARAMIS software is presented in the pictures below. The maximum strain occurs in the cross-layers, which have a lower shear strength compared to the longitudinal ones. Moreover, the highest magnitude of the deformation can be observed near the corners of the air gaps, see Figure 3-75.

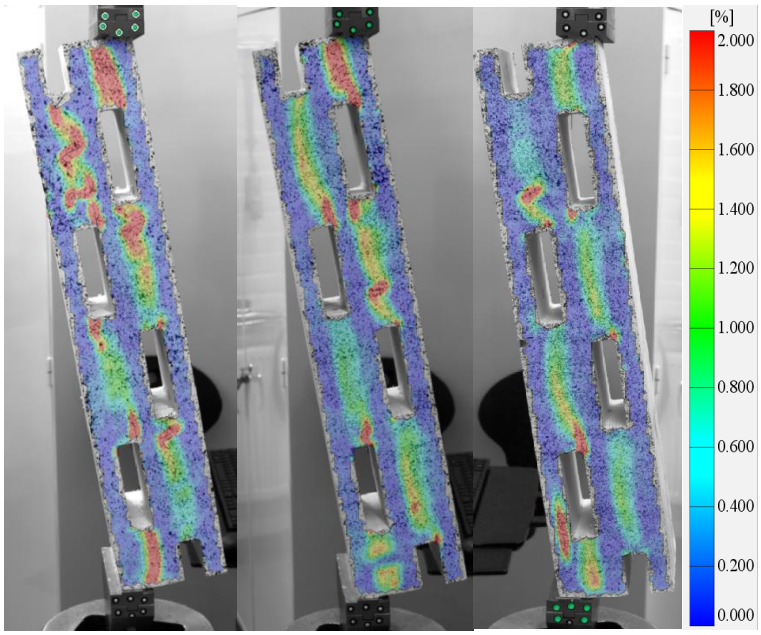

Figure 3-75 Strain distribution using ARAMIS at the failure load for Samples 1, 2, and 3 and Configuration VI from left to right, respectively.

3.5.1.6.4 Rolling shear modulus and shear strength

The rolling shear modulus is calculated based on equation (2-26), and the shear strength is calculated based on equation (2-27). The results are presented in the table below. In addition, the rolling shear modulus equation is revised, and the

range of the forces in equation (2-26) is changed to 0.3 and 0.6 of the maximum load to represent the linear part of the load-deformation curve, as can be seen in the load-deformation curve, see Table 3-20. The new values of the rolling shear modulus are then calculated and shown in the table below.

Table 3-20 The values of effective shear strength, net shear strength, net shear strength ratio and rolling shear modulus extracted based on the experimental data of Configuration VI.

Specimen's name	Effective shear strength [MPa]	Net shear strength [MPa]	Normalized net shear ratio [-]	Net rolling shear modulus [MPa]
Sample 1	1.35	0.81	0.63	48.87
Sample 2	1.17	0.70	0.55	45.81
Sample 3	1.28	0.77	0.60	42.33

The highest shear strength in Configuration VI was reached by Sample 1, which is 1.35 MPa. The shear strength of Sample 2 is 1.17 MPa, and Sample 3's shear strength is 1.28 MPa. The net rolling shear modulus calculated based on the revised equation is 48.87 MPa for Sample 1, which was the highest value. The modulus for Sample 2 was equal to 45.81 MPa, and for Sample 3, it was 42.33 MPa.

3.5.2 Primary results summary of shear test of the small specimens

In this summary, the results of shear tests conducted on CLT panels will be presented. The tests were performed in accordance with standard procedures and evaluated key parameters such as shear strength, and stiffness. The results provide valuable insights into the structural behavior of CLT panels and can inform design and construction decisions for buildings that utilize this innovative material. In Table 3-21 the summary information about the specimens of each configuration are presented.

Table 3-21 Summary of the specimens including length of the specimen, volume ratio, material reduction, and void ratio.

Specimen name	Figure	Length of the specimen [mm]	Volume ratio [-]	Material reduction [%]	Void ratio [-]
I	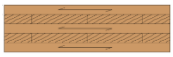	360	1	0	1
II		540	0.87	13	0.67
III	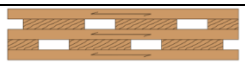	450	0.87	13	0.67
IV	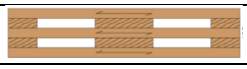	480	0.80	20	0.5
V	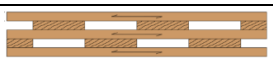	600	0.80	20	0.5
VI	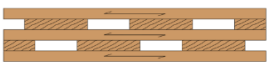	500	0.84	16	0.6

In addition, the summary results of the test result including shear strength and shear modulus of elasticity and failure modes are shown in Table 3-22. From this

table it can be seen that the dominate failure mode is as a result of rolling shear failure of the cross-layers.

Table 3-22 Summary results of the shear strength, rolling shear modulus and failure mode.

	Specimen name	Effective shear strength [MPa]	Effective rolling shear modulus [MPa]	Net rolling shear modulus [MPa]	Failure modes
Configuration I	Sample 1	1.29	70.97	70.97	R, T2
	Sample 2	1.27	73.39	73.39	R, T2
	Sample 3	1.12	78.15	78.15	R, T2
	Average	**1.23**	**74.17**	**74.17**	
Configuration II	Sample 1	1.08	67.85	45.23	R, T2
	Sample 2	1.05	65.98	43.99	R, T2
	Sample 3	1.01	58.98	39.32	R, T2
	Average	**1.04**	**64.27**	**42.84**	
Configuration III	Sample 1	1.43	83.29	55.51	R, T2
	Sample 2	1.41	72.70	48.46	R, T2
	Sample 3	1.31	85.04	56.69	R, T2
	Average	**1.38**	**80.34**	**53.55**	
Configuration IV	Sample 1	1.45	78.25	39.12	R, T2
	Sample 2	1.33	68.98	34.49	R, T2
	Sample 3	1.22	64.94	32.47	R, T2
	Average	**1.33**	**70.72**	**35.36**	
Configuration V	Sample 1	1.35	64.85	32.42	R, T2
	Sample 2	0.86	52.38	26.19	T2
	Sample 3	0.97	57.84	28.92	R, T2
	Average	**1.06**	**58.35**	**29.17**	
Configuration VI	Sample 1	1.35	81.45	48.87	R, T2
	Sample 2	1.17	76.36	45.81	R, T2
	Sample 3	1.28	70.55	42.33	R, L1
	Average	**1.27**	**76.12**	**45.67**	

The average values of the shear strength and rolling shear modulus for each configuration were calculated and the results are presented in Figure 4-77 and Figure 3-77. The range of the shear strength fluctuates between 1.04 MPa for Configuration II and 1.38 for Configuration III. On the other hand, the lowest average value for rolling shear modulus was calculated for Configuration V and it is equal to 58,36 MPa. The highest value is found for Configuration III and it is 80.34 MPa.

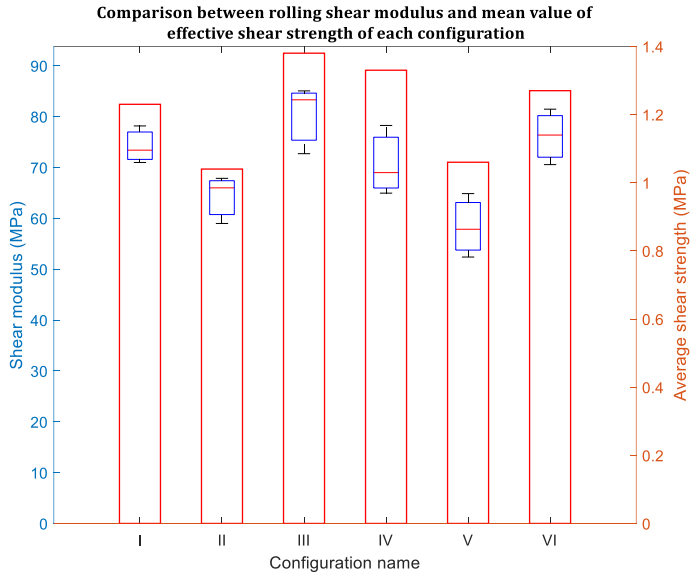

Figure 3-76 Graphical representation of rolling shear modulus (boxplot) and average effective shear strength (bar chart).

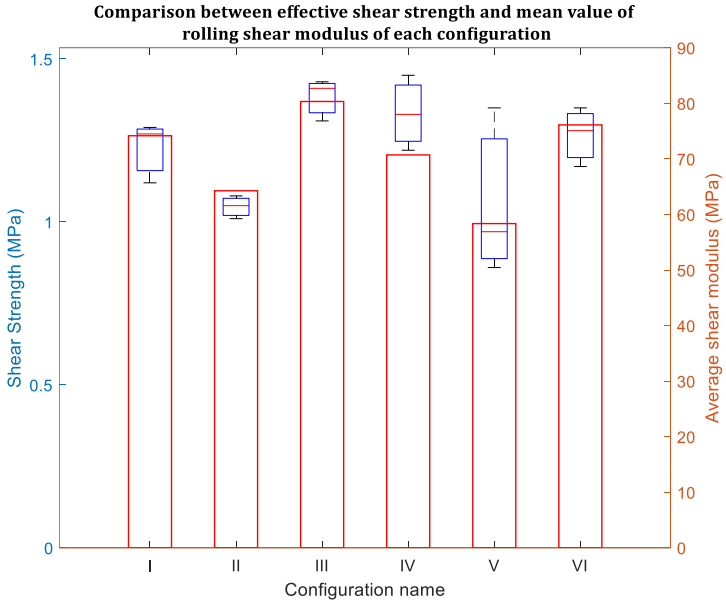

Figure 3-77 Graphical representation of effective shear strength (boxplot) and average shear modulus (bar chart).

It can be observed that the shear strength and the rolling shear modulus change proportionally: when the value of shear strength in one configuration is lower than the one in the other configuration the rolling shear modulus is also lower. Additionally, the experiment shows that the specimens from Configurations III, IV, and VI are marked by better effective shear strength than solid specimens from Configuration I. The rolling shear modulus is lower for Configuration II and V than for Configuration I which represents a solid specimen.

In Configuration II and IV the cross-layers are arranged centrally in relation to each other and from these two configurations, the better effective shear strength was found for Configuration IV with larger width of the air gaps. When it comes to the shifted arrangement of the cross-layers, the highest values for both rolling shear modulus and shear strength were calculated for Configuration III, with 60

mm wide and overlapping air gaps. The parameters were slightly lower for Configuration VI with the width of the air gaps of 80 mm. The lowest shear strength and rolling shear modulus are found for Configuration V with the width of the air gaps of 120 mm that are not overlapping.

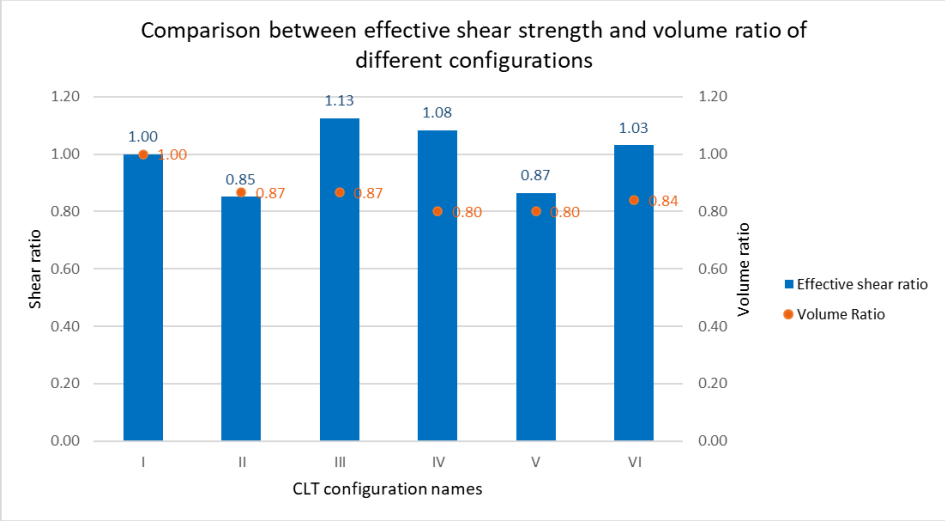

Figure 3-78 Comparison between effective shear strength (bar chart) and volume ratio for each configuration.

Figure 3-79 depicts a comparison between the effective shear strength ratio and volume ratio of each configuration. It can be seen that the highest shear ratio is for Configuration III, while the lowest one is for Configuration II. The main observation that can be seen in this graph is that Configurations III and IV have better structural behavior when it comes to the comparison between effective shear strength, at the same time the material that is used for the production of a CLT panel can be saved with about 13 and 20 percent, respectively for these configurations.

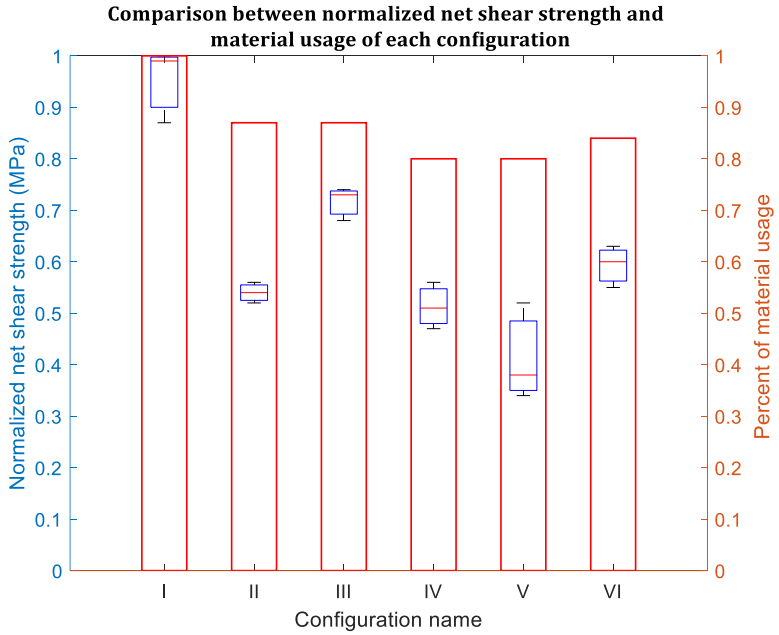

Figure 3-79 Comparison between normalized net shear strength (boxplot) and percentage of material usage (bar chart) for each configuration.

For the calculation of normalized net shear strength, each net shear strength was compared with the highest one from Configuration I, and the ratio of two values was obtained. The figure of comparison of normalized net shear strength and material usage is shown above. It can be concluded that the highest net shear strength has solid Configuration I however material used for panel production is not saved at all. The highest normalized net shear strength ratio from specimens with airgaps can be found for Configuration III, where 13 % of the material can be saved. In Configuration IV and V 20 % of timber might be spared but these two configurations have the lowest normalized net shear strength ratio from all types of specimens at the same time.

3.6 FEM modeling results

3.6.1 Effect of the size of the airgaps for the centered arrangement of the cross-layers (Configuration II and IV)

3.6.1.1 Normal stress S11

The distribution of normal stresses of the CLT panels with centered air gaps for configurations II and IV are compared for a path at the bottom line of the upper cross-layers edges upper part of the middle longitudinal layer, as it is shown in Figure 3-80.

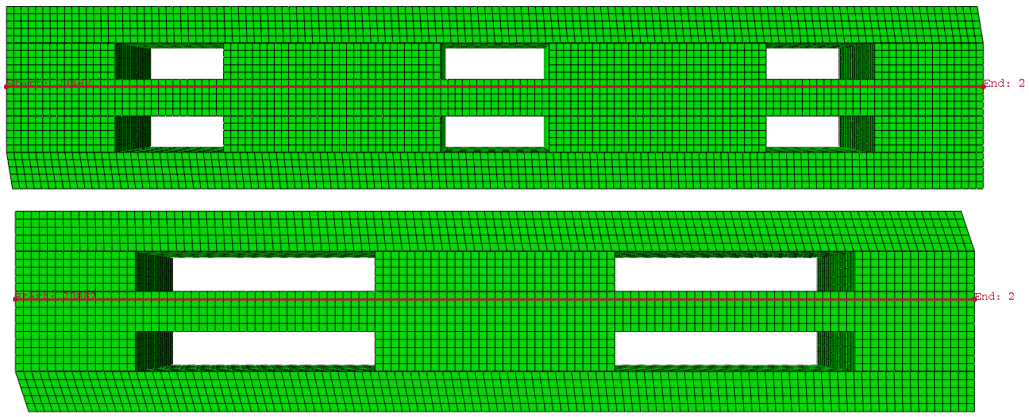

Figure 3-80 The location of the path for plotting normal stresses S11.

The normal stresses are plotted for normalized distance because of the different lengths of the specimens. As can be seen, the higher positive and negative stresses occurred near the air gaps due to stress concentrations in these areas. The magnitude of the stress in these locations is almost double for Configuration IV compared to Configuration II, due to the larger air gap space between the cross layers, see Figure 3-81.

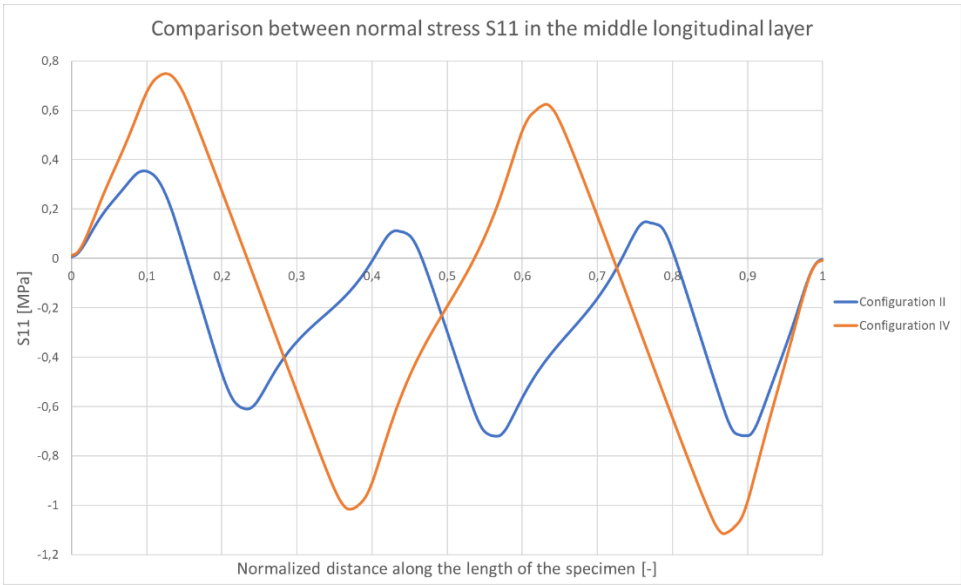

Figure 3-81 Comparison between normal stress S11 plotted along the path at the middle longitudinal layer for Configuration II and IV.

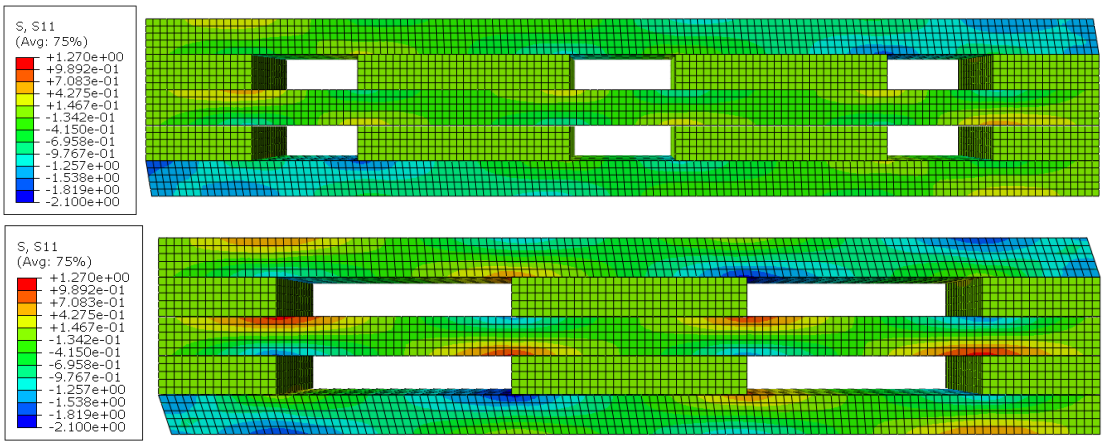

Figure 3-82 Distribution of normal stress S11 of Configuration II and IV in, shown respectively.

Figure 3-82 shows the normal stress in both Configuration II and IV, the high-stress concentration can be seen near the air gaps in both configurations however the magnitude in Configuration IV is much higher compared to Configuration II.

3.6.1.2 Normal stress S22

The principal stress S22 of these two configurations is also compared for a path in the cross-layer below the top longitudinal layer as shown in the figure below.

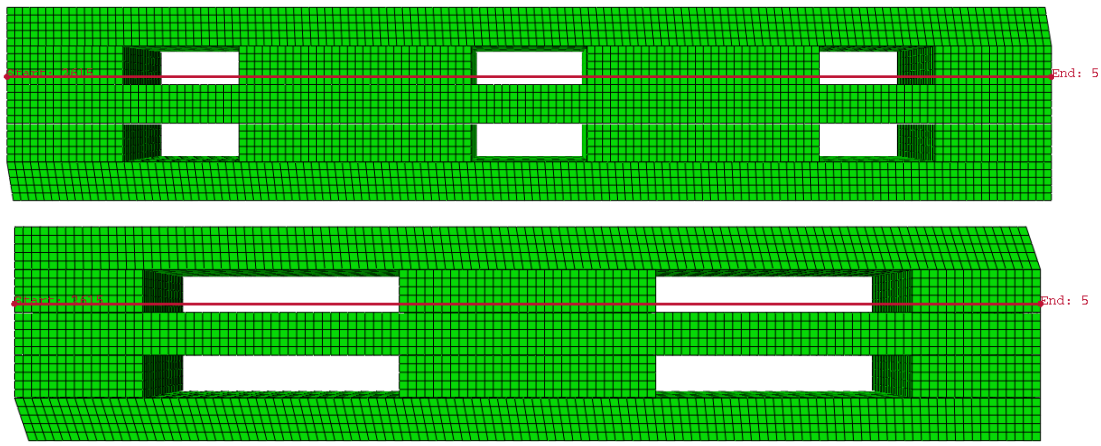

Figure 3-83 The location of the path for plotting normal stresses S22 and shear stresses S23.

The contour of normal stress S22 is plotted for both configurations as presented in Figure 3-84.

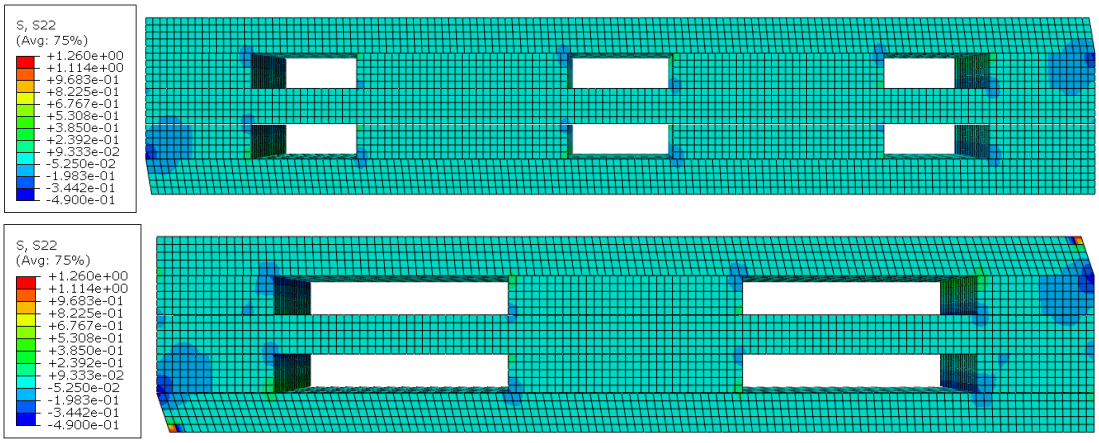

Figure 3-84 Distribution of normal stress S22 of Configuration II and IV, shown respectively.

The results are plotted in Figure 3-85. The same pattern for S22 can be seen, and there is stress concentration at the corner of the air gaps in the cross layers, however, the magnitude in these cases is much closer to each other, although it is still higher in the cross-layer of Configuration IV.

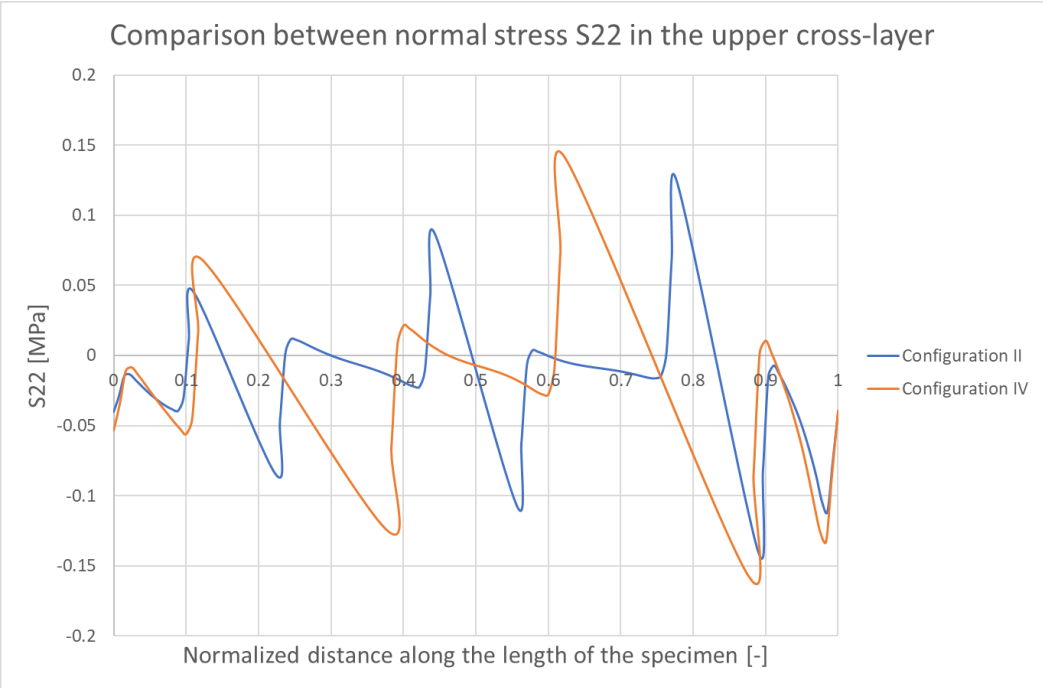

Figure 3-85 Comparison between normal stress S22 plotted along the path at the middle longitudinal layer for Configuration II and IV.

3.6.1.3 Shear stress S23

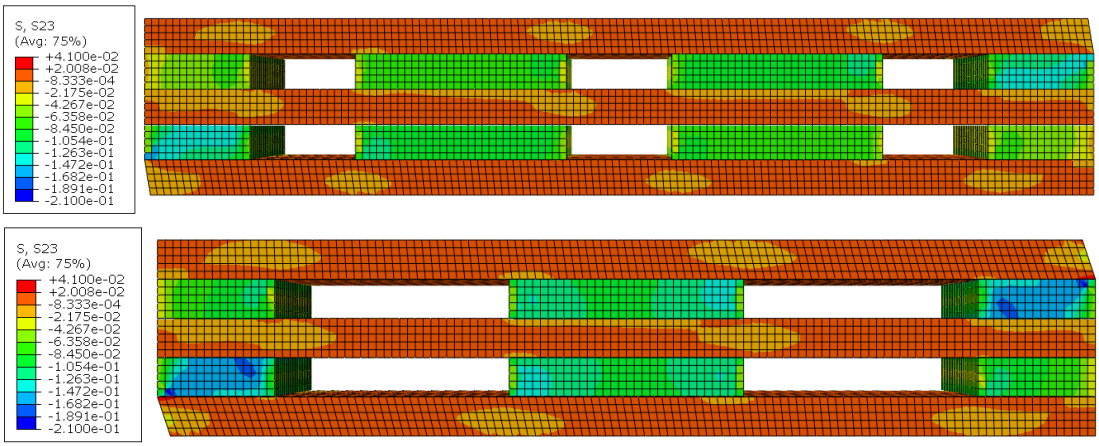

Figure 3-86 Distribution of shear stress S23 of Configuration II and IV, shown respectively.

Figure 3-86 shows the shear stress distribution in RT-plane. It can be seen that the cross-layers are subjected to compression stresses with the highest values close to the load application surfaces. On the other hand, the longitudinal lamellas are subjected to tensile stresses with higher magnitude in Configuration IV.

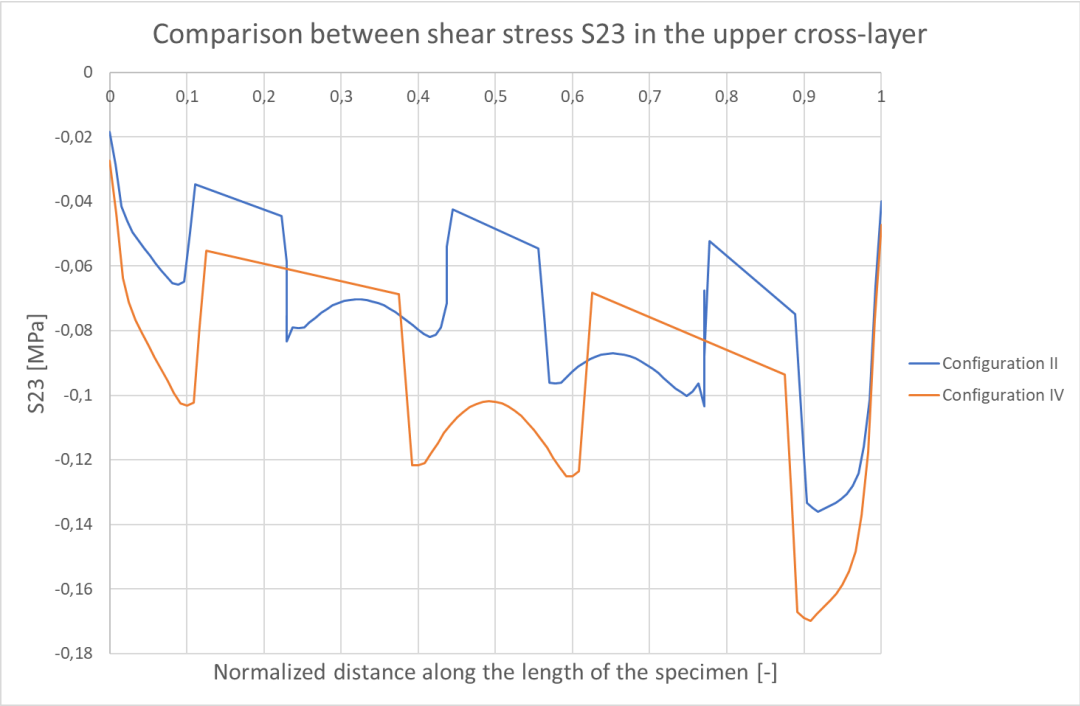

Figure 3-87 Comparison between shear stress S23 in the upper cross-layer.

Figure 3-87 shows the comparison of the shear stress in the path as indicated in Figure 3-82. It can be seen that the upper cross-layer is subjected only to compression stress. The peak of the value can be found closer to the right side due to the load application in the right upper surface. It is clear that there is higher compression stress in the cross-layer of Configuration IV. Moreover, the highest differences in the stress magnitude are observed close to the boundaries of the air gaps.

3.6.2 Effect of shifting of cross-layer with the same size of the air gap, Configuration II and III

The normal stress for both Configurations II and III is compared for a path shown in the figure below.

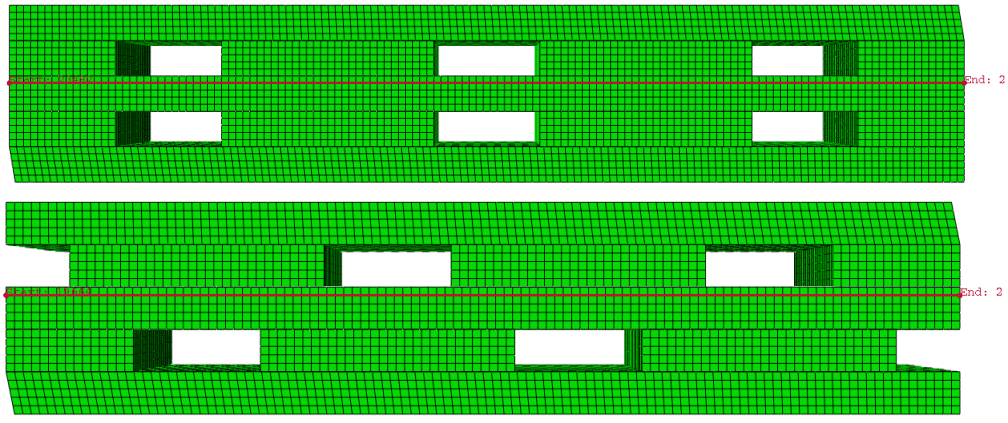

Figure 3-88 The path for S11 comparison of Configuration II and III, respectively.

The stress contour of S11 for Configurations II and III is shown in Figure 3-89. As can be seen, the magnitude of the normal stress in Configuration II with a centered air gap is much larger than in Configuration III with shifted air gap due to the stress concentration in the corner of the air gaps in Configuration II, while in

Configuration III the stress has a smoother path over because of the overlap of the cross-layer with a longitudinal layer in a larger area.

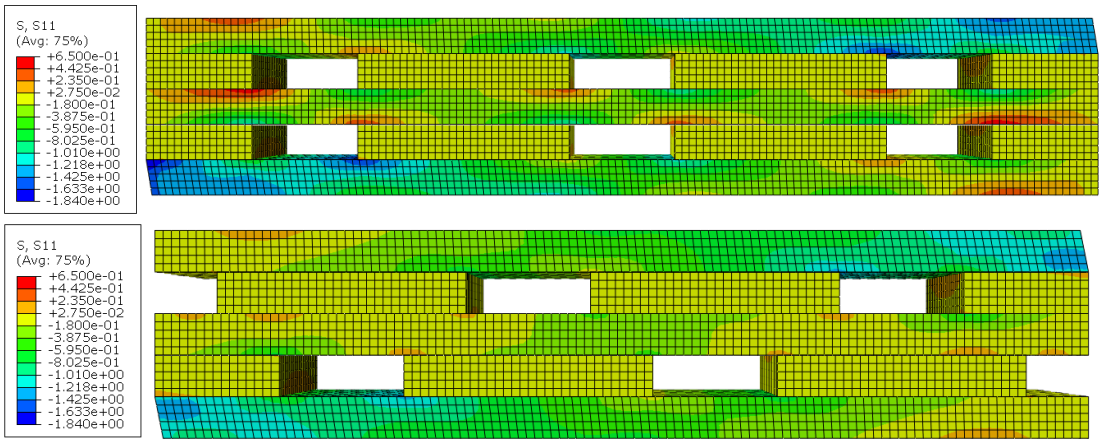

Figure 3-89 Distribution of normal stress S11 of Configuration II and III, shown respectively.

The normal stress, S11, for Configurations II and III are plotted in a normalized axis, see Figure 3-90. As it is clear in this graph, the stress fluctuated less in Configuration III compared to Configuration II. In Configuration III, on the right side, near the corner where the load is applied, there is significant compression stress. Still, by increasing the distance from the applying load, the stress decreases until it reaches almost zero on the other side. In contrast, in Configuration II, the stress fluctuated between tension and compression, and the tensile stress increased significantly on the other side. Another interesting point is in Configuration III, there is almost no area with tension stress, while in Configuration II, the stress sign changed in the front edge of an air gap.

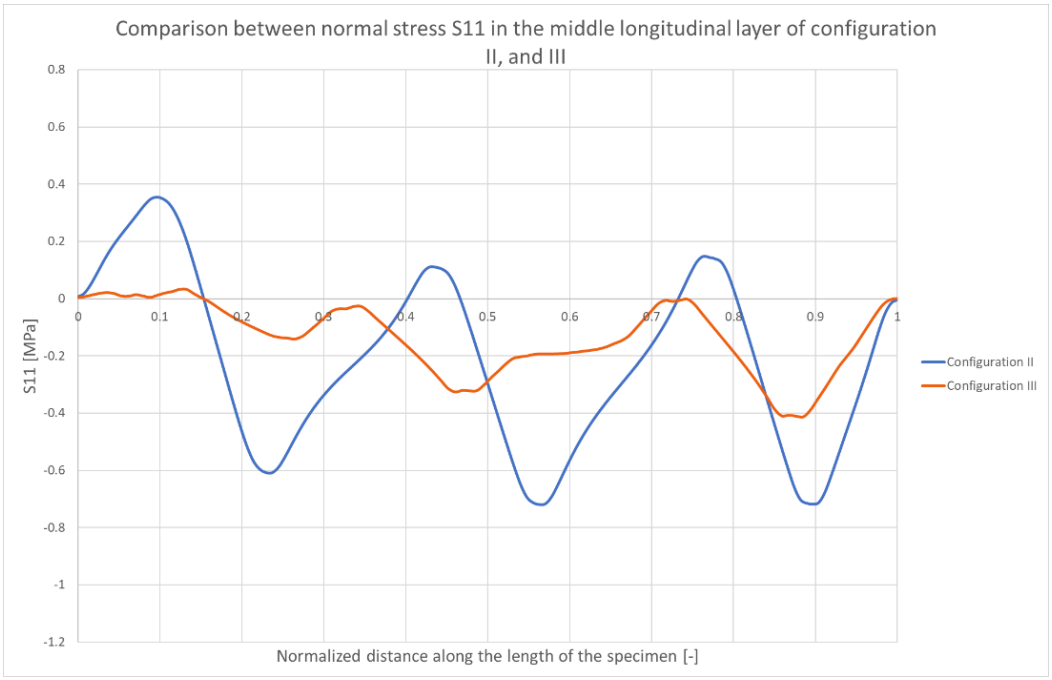

Figure 3-90 Comparison between S11 stress in the middle longitudinal layer of Configuration II and III.

3.6.2.1 Normal stress S22

The distribution of normal stresses S22 of Configuration II and III are presented below. It can be observed that only some parts of the edges and corners of the air gaps are in tension while the major parts of the specimens are in compression. The highest values of compression are found close to the loading application surfaces. The range of the values of stress is comparable.

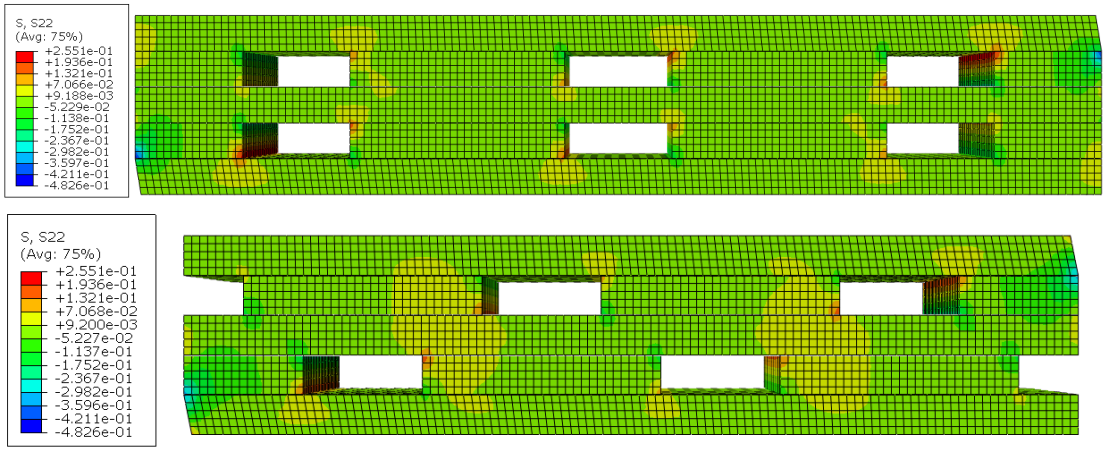

Figure 3-91 Distribution of normal stress S22 of Configuration II and III, shown respectively.

The graph below shows the comparison of the normal stresses S22 plotted along the path in the upper cross-layer of Configuration II and III. It can be seen that the range of the stresses is very similar for both configurations. However, the graph is shifted due to the location of the air gaps.

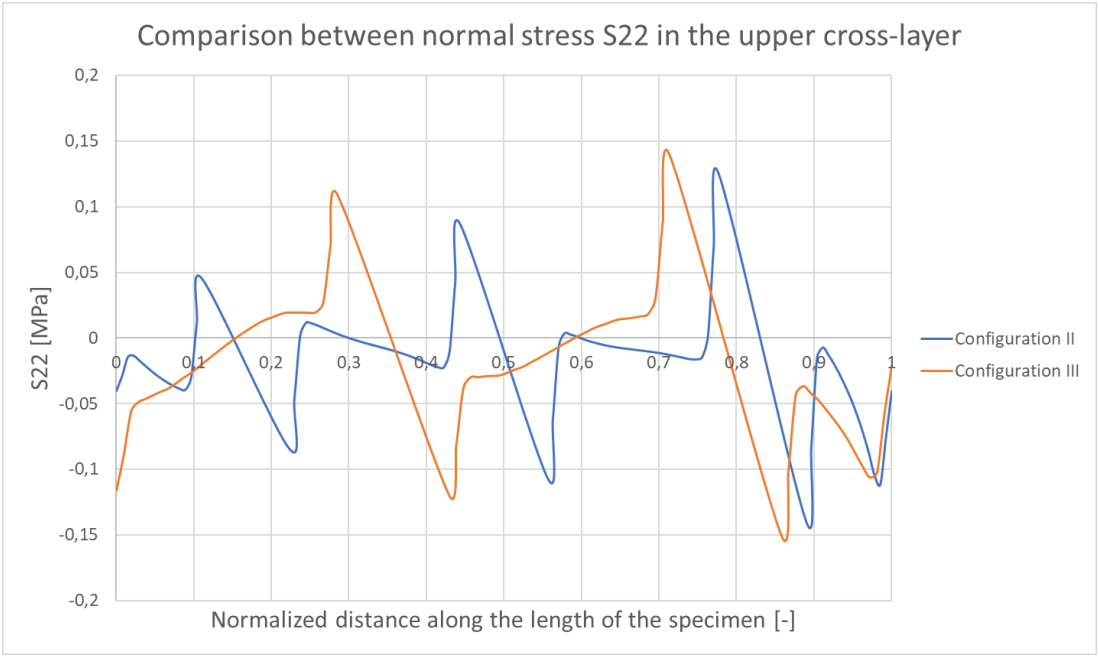

Figure 3-92 Comparison between normal stress S22 plotted along the path at the middle longitudinal layer for Configuration II and III.

3.6.2.2 Shear stress S23

The contours below show the distribution of the shear stress S23 of Configuration II and III. Cross-layers of two specimens are subjected to compressive stress while the longitudinal lamellas are in tension. The highest values of compression are

found in the areas close to the load application. At the same time, the highest values of the tensile stresses are located at the longitudinal layers, where they intersect the cross-layers close to the supports and load surfaces.

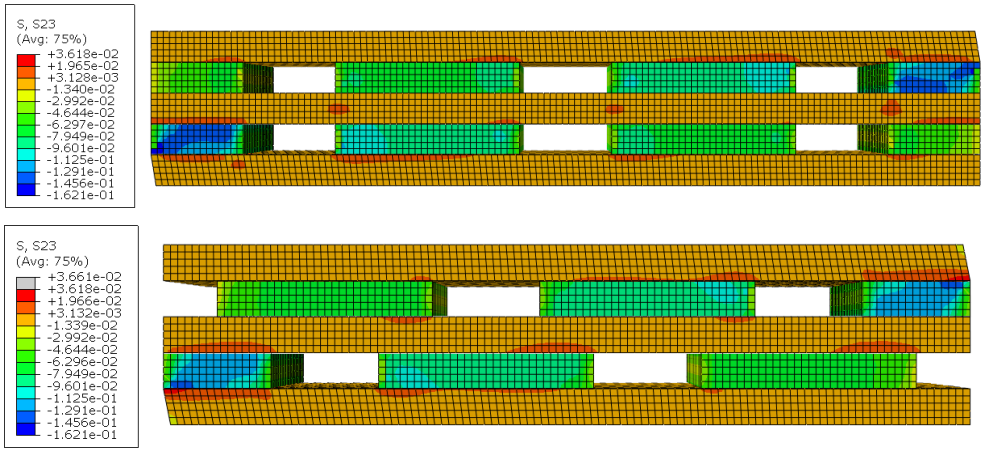

Figure 3-93 Distribution of shear stress S23 of Configuration II and III, shown respectively.

The comparison between shear stress S23 in the upper cross-layer (the same path as the previous comparison) for Configuration II and III is shown in Figure 3-94. As it can be seen from the comparison of S22 stresses, the range of S23 stresses as well as their shapes of them are the same but the graph of Configuration II is shifted in relation to Configuration II due to the location of the air gaps. The highest compression stresses along the path are found on the right part close to the location of the loading.

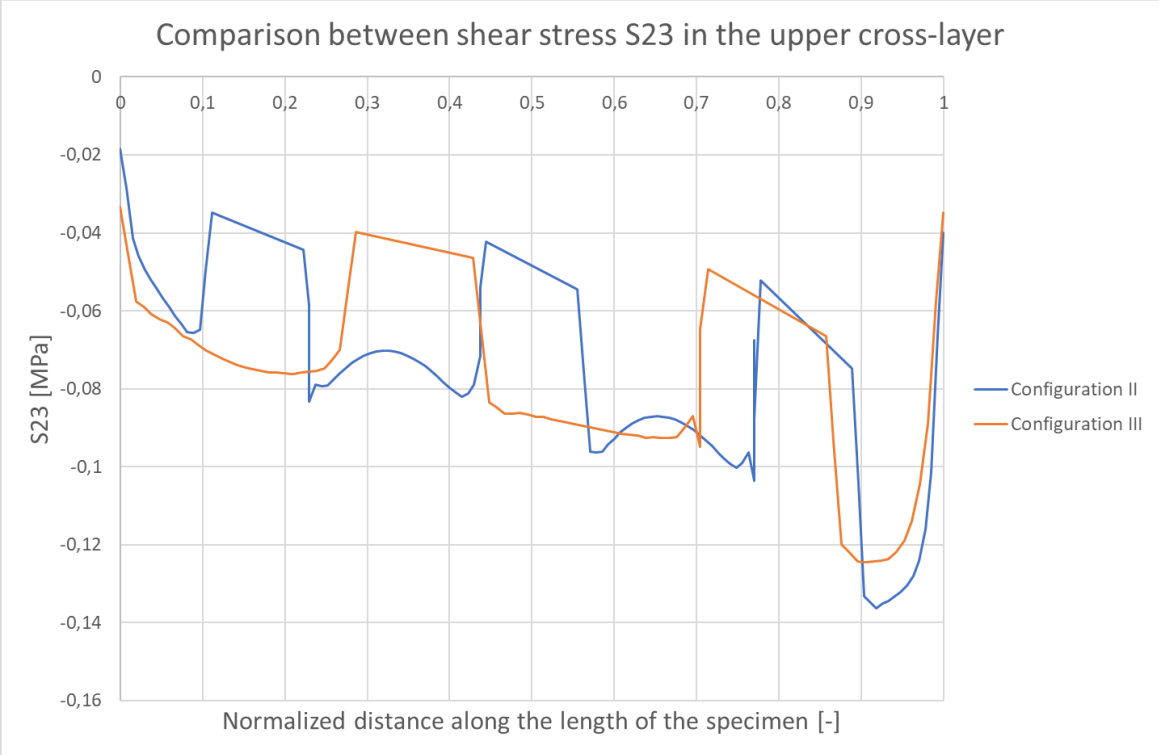

Figure 3-94 Comparison between shear stress S23 plotted along the path at the middle of the top cross-layer for Configuration II and III.

3.6.3 Effect of the size of the air gap in configuration with shifted cross-layers, comparison between Configurations III, V, and VI

The normal stress, S11, is plotted for Configuration III, V, and VI for a path which is shown in Figure 3-95 below.

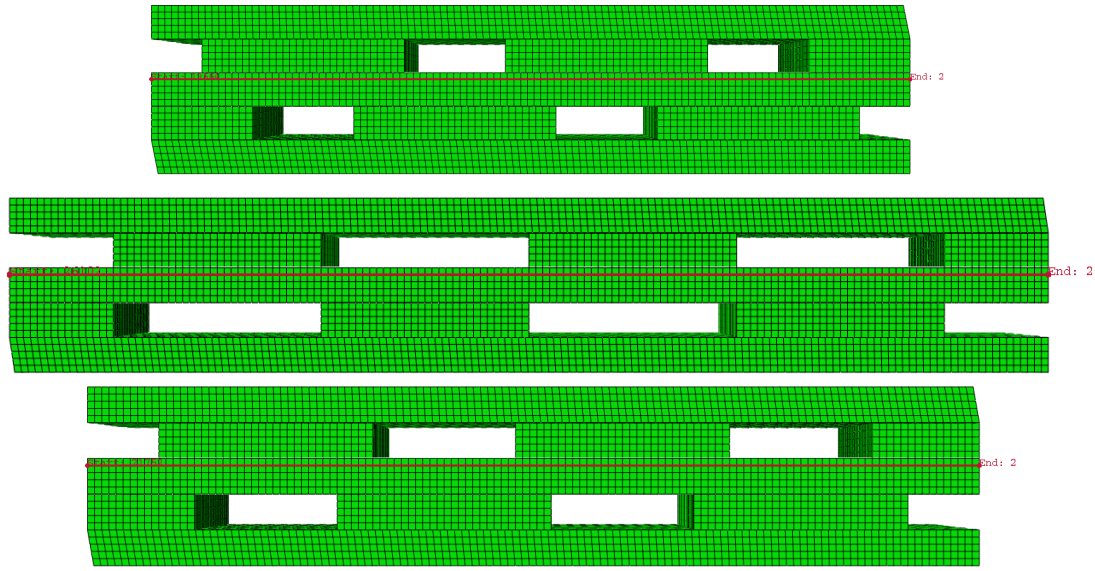

Figure 3-95 Location of the path for studying the S11 for Configuration III, V, and VI, respectively.

The S11 stress contour is plotted for these three configurations and shown in Figure 3-96. By comparison of these three configurations, it can be seen that in Configuration V, where there is no overlapping between the cross-layer and middle longitudinal layer, there is a higher stress concentration, and it is almost double the lower one, which is for Configuration III with a lager overlapping between cross-layer and the middle longitudinal layer.

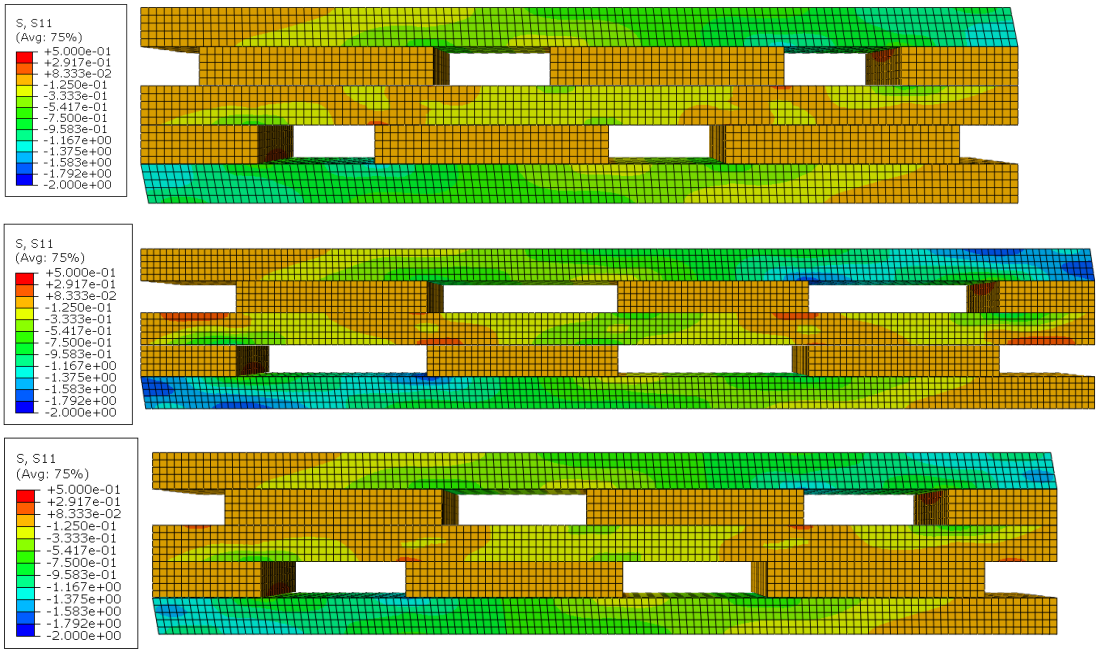

Figure 3-96 Distribution of normal stress S11 of Configuration III, V, and VI, shown respectively.

The stress over the path that is shown in Figure 3-95 is plotted with respect to the normalized x-axis. The overlapping space between the cross-layer and middle longitudinal layer is equal to 30, 0, and 20 mm for Configurations III, V, and VI, respectively. It can be seen that by increasing the distance, the stress concentration will reduce. The summary of the comparison between the maximum tensile and compressive stress is presented in Table 3-23.

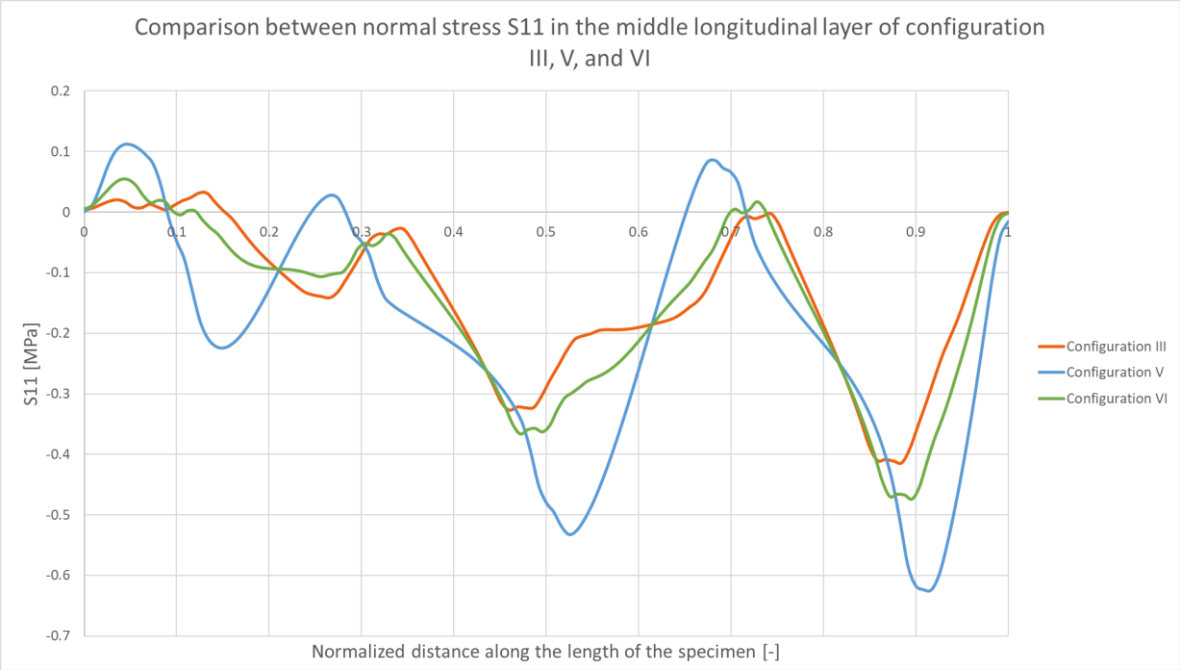

Figure 3-97 Comparison between normal stress S11 plotted along the path at the middle longitudinal layer for Configuration III, V and VI.

Table 3-23 Comparison between maximum tensile and compressive stress between Configurations III, V and VI.

	III	VI	V	Percentage of increase/decrease between V and III [%]	Percentage of increase/decrease between VI and V [%]	Percentage of increase/decrease between VI and III [%]
Overlap distance[1] [mm]	30	20	0	-100	-100	-33.3
Maximum tensile stress [MPa]	0.0318	0.054	0.1118	251	107	70
Maximum compressive stress [MPa]	-0.414	-0.473	-0.624	51	32	15

[1] Overlap distance is equal to distance between cross-layers and middle longitudinal lamella in the CLT panel.

3.6.3.1 Normal stress S22

Normal stresses S22 and shear stresses S23 for comparison of Configuration III, V, and VI were plotted along the paths located along the cross-layer, Figure 3-98.

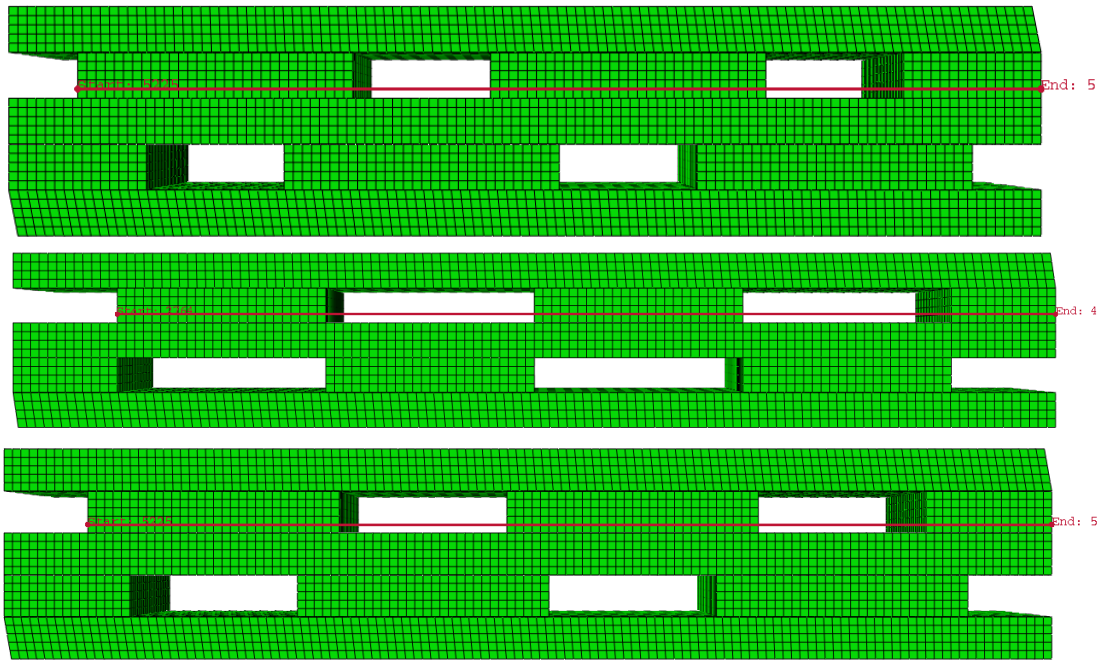

Figure 3-98 Locations of the paths for studying the normal stresses S22 and shear stresses S23 of Configurations III, V and VI.

The distribution of normal stresses S22 of Configuration III, V and VI is presented below, see Figure 3-99. It can be seen that only some parts of the edges and corners of the air gaps are in tension while the major parts of the specimens are in compression. The highest values of compression are found close to the loading application surfaces. The range of the values of stress is comparable however, the highest compressive stresses and tensile tresses are found in Configuration V.

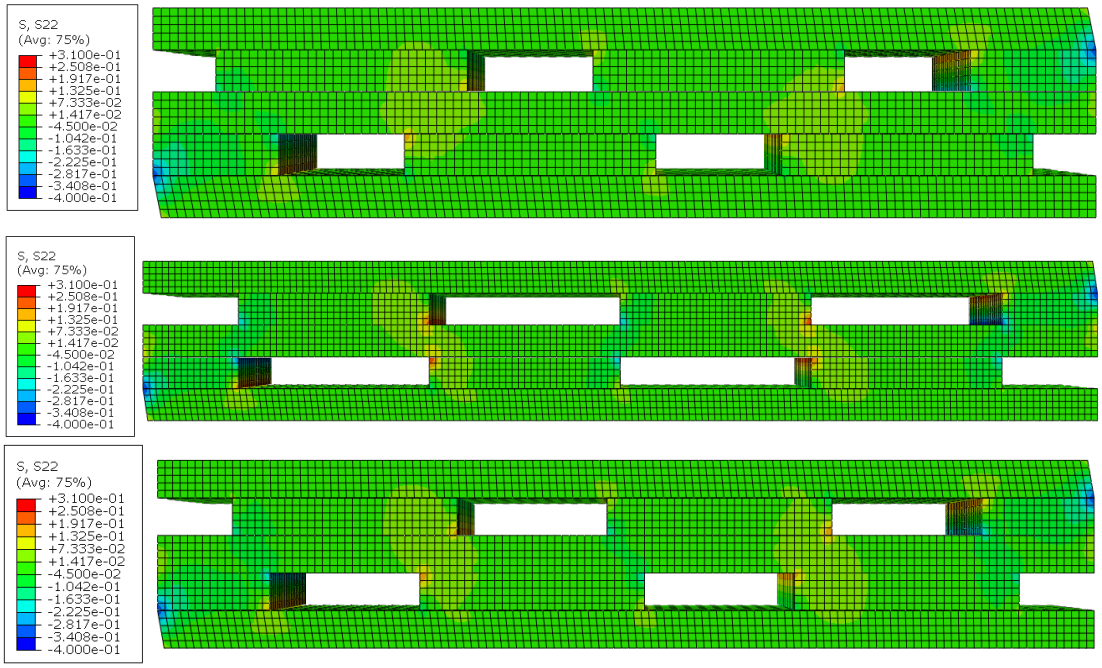

Figure 3-99 Distribution of normal stress S22 of Configuration III, V and VI, shown respectively.

The comparison between normal stress S22 plotted for the path in the upper cross-layer of Configuration III, IV and VI can be found in Figure 3-100. It can be seen that the highest values are located around the air gaps and the pattern on the plots is very similar for each configuration. The highest magnitude of the stress

can be observed for Configuration V and the lowest one for Configuration III which has the smallest length of the air gaps.

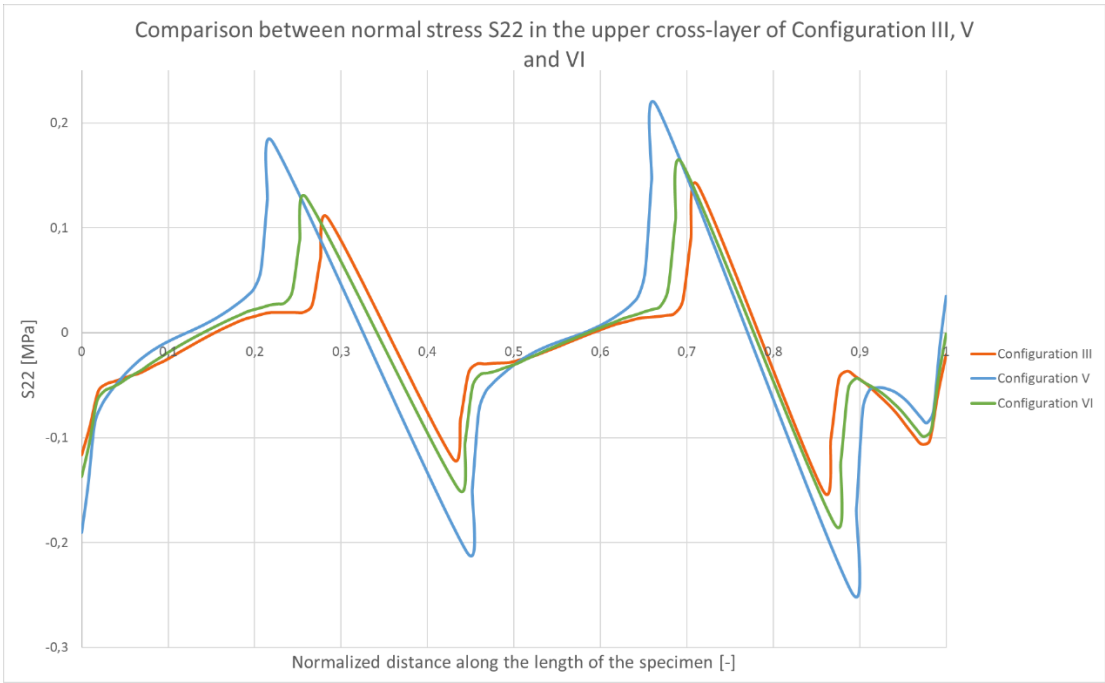

Figure 3-100 Comparison between normal stress S22 plotted along the path at the cross-layer layer for Configuration III, V, and VI.

3.6.3.2 Shear stress S23

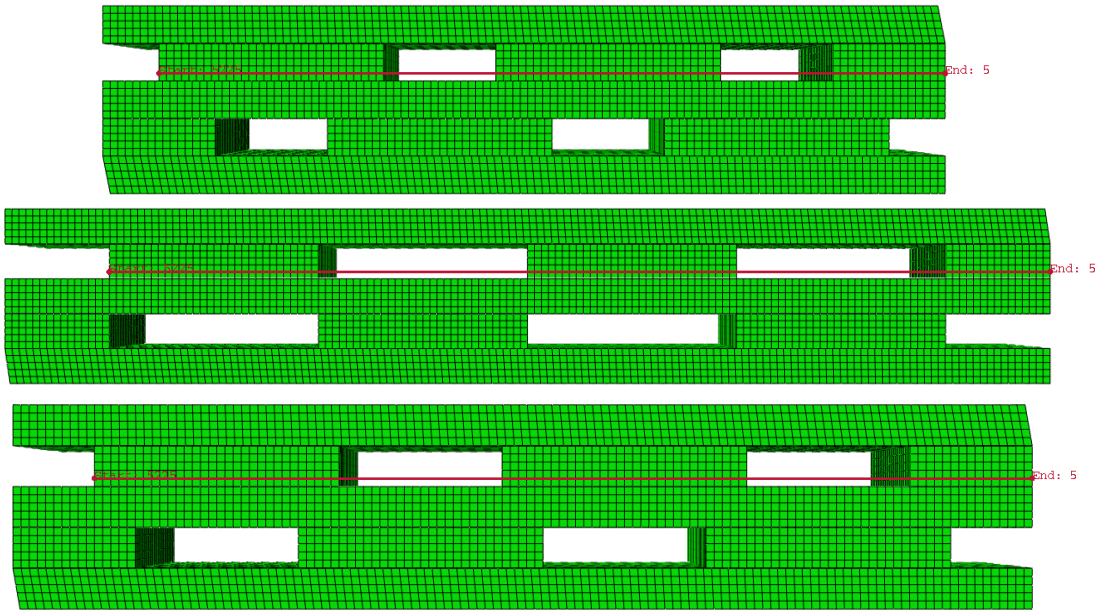

Figure 3-101 Locations of the paths for studying the normal stresses S23 and shear stresses S23 of Configurations III, V, and VI.

The shear stress contour is plotted below for the path indicated in Figure 3-101. As can be seen, the highest compressive stress occurred in Configuration V, which has no overlap distance between the cross-layer and middle longitudinal lamella. Although the maximum tensile stress is highest in Configuration VI, the area of the maximum tensile stress in Configuration VI is limited to a small region near the

applied load. In Configuration V, the significantly more extensive area in the longitudinal lamellas experienced sizeable tensile stress.

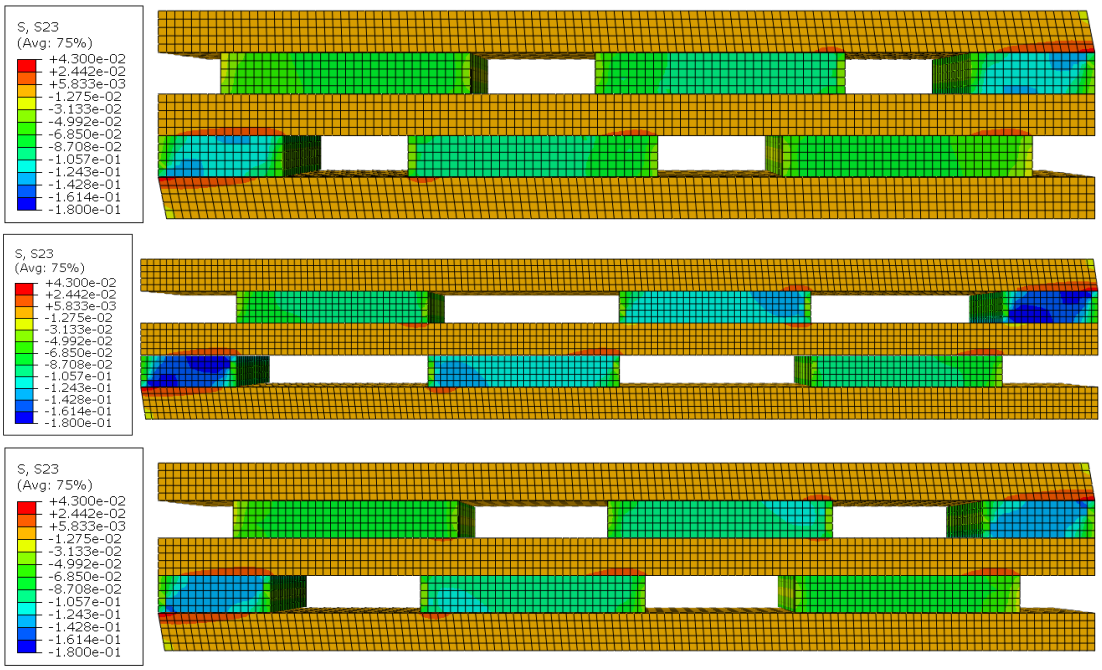

Figure 3-102 Distribution of shear stress S23 of Configuration III, V, and VI, respectively.

The shear stress over the normalized axis is plotted for Configurations III, V, and VI, as shown in Figure 3-103. It can be seen that the maximum compressive stress happened in the area in the corner of the air gaps due to stress concentration. Also, the maximum stress in the corners of the air gaps increases by decreasing the overlap distance.

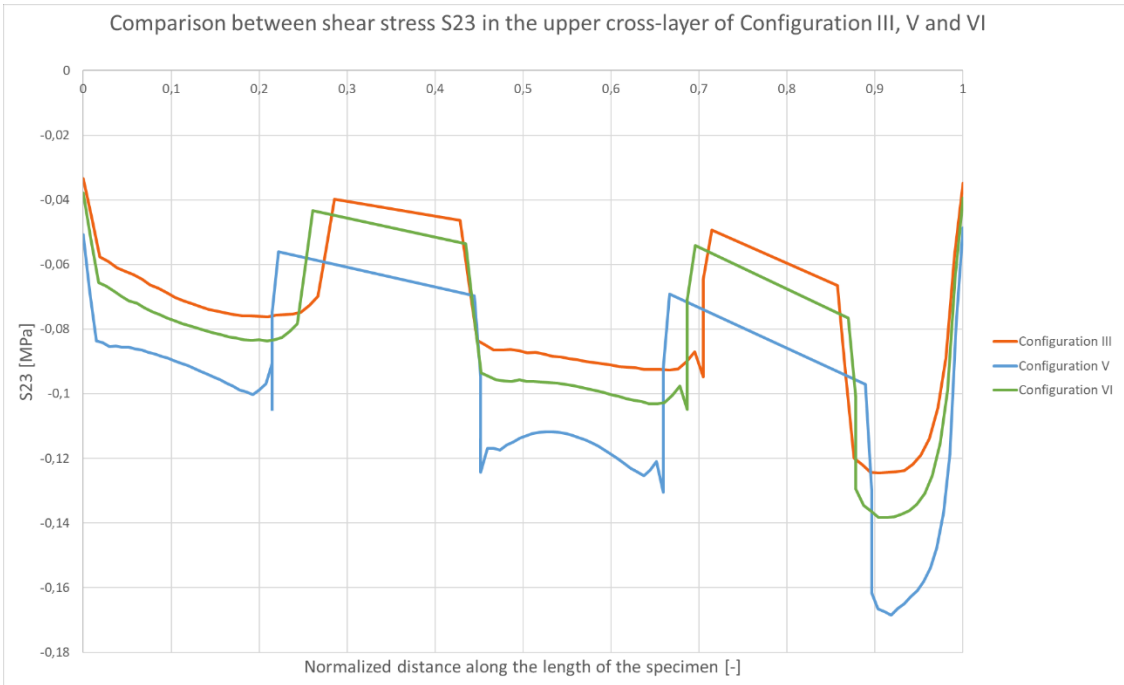

Figure 3-103 Comparison between shear stress S23 plotted along the path at the middle of the top cross-layer for Configuration III, V, and VI.

3.6.4 Results summary of FE analysis in Abaqus

3.6.4.1 Effect of the size of the airgaps for the centered arrangement of the cross-layers

The ABAQUS models show that the highest normal stresses are found close to the edges of the air gaps. The normal stress S11 is two times higher for Configuration IV with 12 cm wide air gaps compared to Configuration II when the width of the air gap is 6 cm. The magnitude of normal stresses S22 is similar for both configurations, but the maximum value is slightly higher for Configuration IV. Additionally, shear stresses S23 are 1/3 higher for Configuration IV than for Configuration II. To conclude, the values of the normal and shear stresses are higher for configurations with the wider air gaps.

3.6.4.2 Effect of shifting of cross-layer with the same size of the air gap

For the comparison of the configurations with centered and shifted air gaps, the numerical modelling shows that the normal stresses S11 reach higher values for Configuration II, the one with centered air gaps. On the other hand, normal stresses S22 and shear stresses S23 obtain similar values for both configurations.

3.6.4.3 Effect of the size of the air gap in configuration with shifted cross-layers

The results from ABAQUS of comparison of configurations with shifted airgaps show that the values of the normal stresses S11 are the highest when there is no overlapping between the airgaps in neighboring cross-layers. The magnitude decreases when the distance of overlapping increases. Similarly, the normal stress S22 and shear stresses reach the highest value for Configuration V, the one without overlapping and the widest air gaps.

3.7 Comparison between experimental data and FEM modeling for small specimens' shear tests

In general, the experimental data follows the results expected from FEM modeling when it comes to comparing the highest stress generation in the models and the final net shear capacity of the specimens in different configurations. Configurations that show the highest stress concentrations also showed lower average net shear strength in the experiment. In Configuration IV, there is less material usage than in Configuration II, but the values of net shear strength for both configurations are very similar, see Figure 3-79, only about 4 percent higher for Configuration II. Comparing these two configurations in the FEM modeling shows that the stress concentration in Configuration IV is much higher than in Configuration II; therefore, the lower net shear strength in the experiments should be expected for that configuration.

The average of the results which comes from experiments is used for comparison between different configurations. Additionally, as it was explained, Configurations II and IV do not follow the expected results from FEM modeling that show the maximum shear stress in Configuration IV is about 27 percent higher than Configuration II, see Figure 3-77. One reason for this could be due to having only three samples in the experiments. Therefore, to increase the scatter in the data and have more reliable results, it was decided to produce three more samples for these two configurations and one more for others.

3.8 Testing results of extra samples

3.8.1 Configuration I

3.8.1.1 Failure modes

The test results and parameters, including the maximum load and displacement, time of the failure, and loading rate, are presented in Table 3-24. In addition, the failure mode is indicated for the specimen.

Table 3-24 The shear test results data and failure mode of an extra sample of Configuration I.

Specimen's name	Failure load [kN]	Maximum displacement [mm]	Time [s]	Loading rate [mm/min]	Failure mode
Sample 4	63.5	3.9	462.0	0.5	R, T2

Figure 3-104, and Figure 3-105 present the results from the shear test of Configuration I. As can be seen, the main failure mode for the three samples is rolling shear failure.

Figure 3-104 Shear test results of an extra sample of Configuration I.

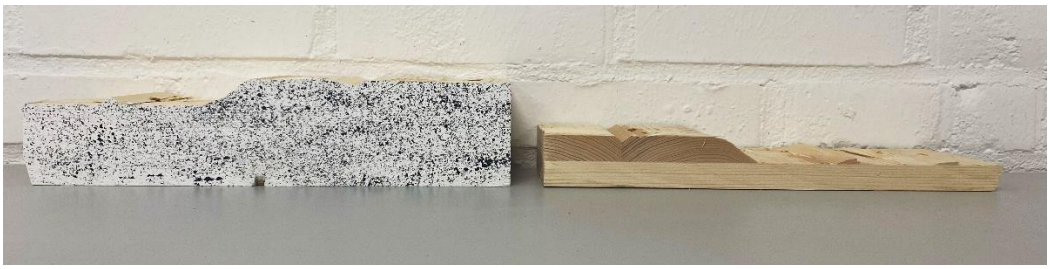

Figure 3-105 Detailed results from the shear test of an extra sample of Configuration I.

3.8.1.2 Load deformation graphs

Figure 3-106 below presents the load-deformation curves for Configuration I with an extra sample shown by a black line. The failure load of Sample 4 is higher than for previous samples and reaches 63.5 kN. For that load, the maximum deformation is equal to 3.9 mm. The maximum time that the failure occurred is 462 s with a loading rate of 0.5 mm/min and it slightly exceeds the time that is recommended by the standard.

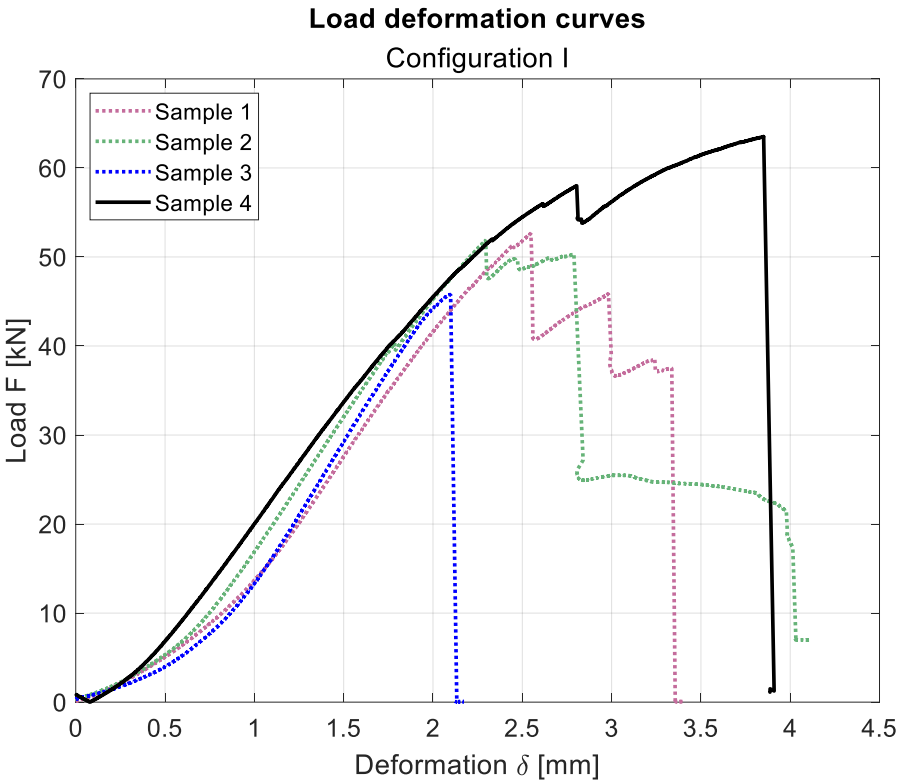

Figure 3-106 Load-deformation graph for Configuration I with an extra sample.

3.8.1.3 Shear strain from ARAMIS software

Figure 3-107 shows the strain distribution over Sample 4 at load 57.9 kN, when the first crack initiation can be observed in the top cross-layer.

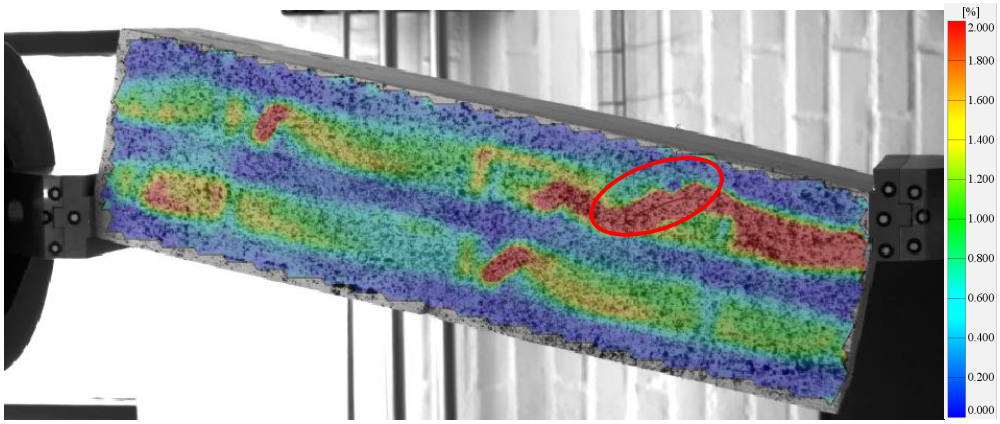

Figure 3-107 The strain distribution of Sample 4 at time 369 s and the load 57.9 kN [ARAMIS data, Configuration I].

By increasing the load, the strain in the cross-layers became larger and larger, and it also can be seen in different locations in the top and bottom cross-layers. The strain increased until the CLT panel failed in a brittle mode at the load of 63.5 kN, see Figure 3-108 and Figure 3-109.

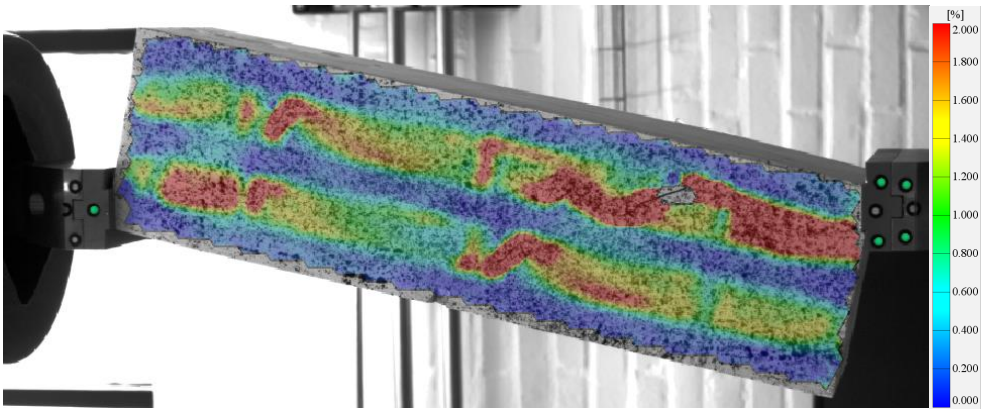

Figure 3-108 The strain distribution of Sample 4 at time 462 s and the load 63.5 kN [ARAMIS data, Configuration I].

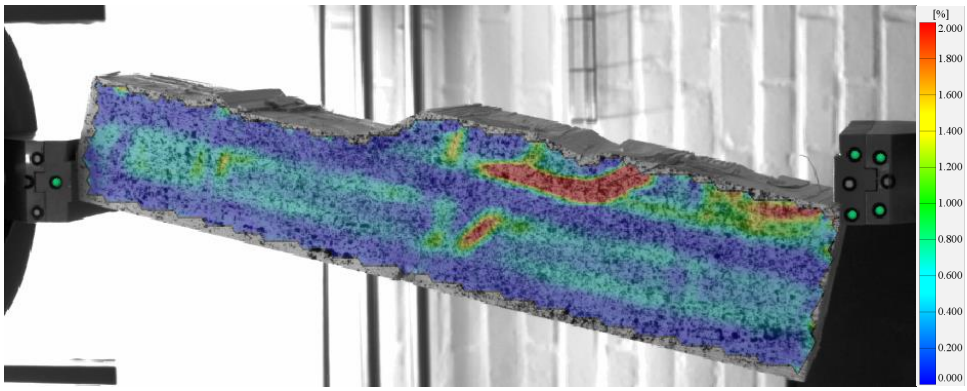

Figure 3-109 The brittle failure mode of Sample 4 in Configuration I.

3.8.1.4 Rolling shear modulus and shear strength

The effective shear strength was calculated based on formula (2-27), and for net shear strength calculation, formula (3-9) was used. For configuration without any air gaps, the effective length is the same as the length of the specimen, so both values are the same. Sample 4 of Configuration IV reached the highest value of net shear strength, so all normalized net shear strength ratios of other specimens are calculated regarding that value. On the other hand, Sample 4 has the lowest stiffness from specimens of Configuration I, and the rolling shear modulus is 65.83 MPa.

Table 3-25 The values of effective shear strength, net shear strength, net shear strength ratio and rolling shear modulus were extracted based on the experimental data of an extra sample of Configuration I.

Specimen's name	Effective shear strength [MPa]	Net shear strength [MPa]	Normalized net shear ratio [-]	Net rolling shear modulus [MPa]
Sample 4	1.56	1.56	1.00	65.83

3.8.2 Configuration II

3.8.2.1 Failure modes

The test results and parameters, including the maximum load and displacement, time of the failure, and loading rate, are presented in Table 3-26. In addition, the failure mode is indicated for each specimen.

Table 3-26 The shear test results data and failure mode of extra samples of Configuration II.

Specimen's name	Failure load [kN]	Maximum displacement [mm]	Time [s]	Loading rate [mm/min]	Failure mode
Sample 4	55.1	3.52	413.5	0.5	R,T2
Sample 5	45.9	2.52	278.5	0.5	R,T2
Sample 6	72.1	3.01	337.0	0.5	L2

Figure 3-110 presents results from the shear test of extra samples of Configuration II. As can be seen, the main failure mode for the three samples is rolling shear failure.

Figure 3-110 Shear test results of extra samples of Configuration II, with the order from top to bottom, Sample 4, Sample 5, and Sample 6, respectively.

Figure 3-111 Detailed results from the shear test of extra samples of Configuration II, with the order from top to bottom, Sample 4, Sample 5, and Sample 6, respectively.

3.8.2.2 Load deformation graphs

Figure 3-112 below shows the load-deformation curves for Configuration II with extra samples presented as solid lines. The failure load of Sample 6 is the highest and reaches 72.1 kN after 337 s. The highest deformation can be found for Sample 4 – 3.52 mm at the failure load of 55.1 kN. From three extra samples, the lowest load can be handled by Sample 5, and the value is 45.9 kN with deformation of 2.52 mm. The failure of each sample is rapid, so it can be characterized as brittle.

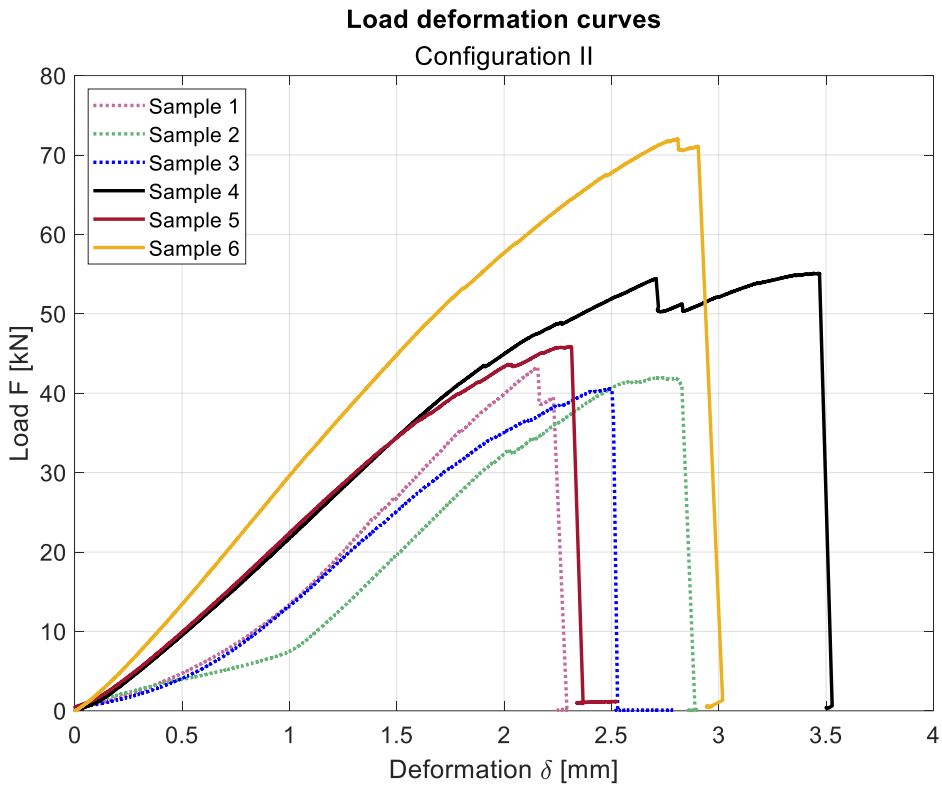

Figure 3-112 Load-deformation graph for Configuration II with extra samples.

3.8.2.3 Shear strain from ARAMIS software

The distribution of the strains at the failure load of each sample is presented in Figure 3-113 below. The highest magnitude of the deformation can be observed at the cross-layer lamellas.

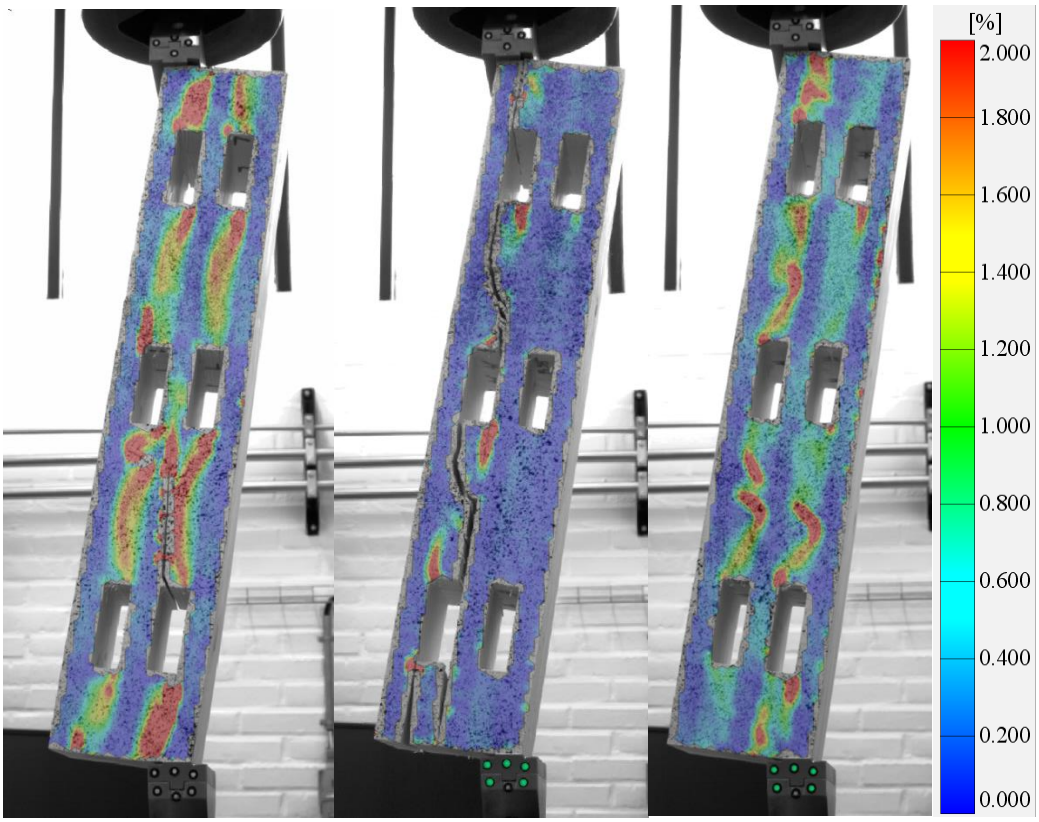

Figure 3-113 Strain distribution using ARAMIS at the failure load for Samples 4, 5, and 6 and Configuration II from left to right, respectively.

As it is shown in Figure 3-113, for Sample 4, the crack started at the edge near the airgap, and it grew over the cross-layer at the load of 55.1 kN. The sample broke in a brittle mode. By looking at the pictures of the failed CLT panel in Figure 3-111, it can be observed that the CLT panel did not fail as a result of the first cracking, and it failed as a result of rolling shear failure in other cross-layers. For Sample 5, from the figure above, the specimen failed due to rolling shear failure at the cross-layer. For Sample 6, although the strain is larger in the cross-layers compared to the longitudinal ones, specimens failed not because of rolling failure in the cross-layers. This can be observed by looking at the failed picture of the sample shown in Figure 3-110 and Figure 3-111. The failure mode is considered L2. The main reason for this difference is that the lamellas used in the cross-layers to produce this sample were from a different batch of wood and had different densities and MOE. This happened due to the lack of the 2 cm thickness board with a high MOE, the one with 3 cm thickness was taken from a different batch of lamellas, and it was planned until 2 cm thickness; therefore, the boards were crated from various locations of the cross-section of the log, see Figure 3-114.

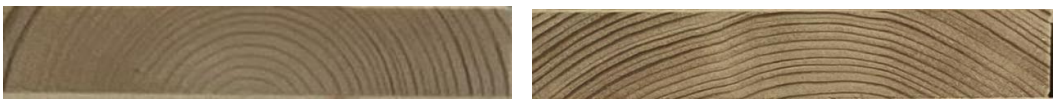
Figure 3-114 Different cross-sections cut from various locations in a log.

3.8.2.4 Rolling shear modulus and shear strength

The effective shear strength was calculated based on formula (3-9), and for net shear strength calculation, formula (2-27) was used. The rolling shear modulus for Sample 4 and Sample 5 is very similar as the angle of the graph above in an elastic part is almost the same. For Sample 6, the shear strength and rolling shear

modulus are not calculated for this specimen as the failure mode was not the rolling shear failure.

Table 3-27 The values of effective shear strength, net shear strength, net shear strength ratio, and rolling shear modulus were extracted based on the experimental data of the extra sample of Configuration II.

Specimen's name	Effective shear strength [MPa]	Net shear strength [MPa]	Normalized net shear ratio [-]	Net rolling shear modulus [MPa]
Sample 4	1.37	0.91	0.59	42.14
Sample 5	1.14	0.76	0.49	41.83
Sample 6	-	-	-	-

3.8.3 Configuration III

3.8.3.1 Failure modes

The test results and parameters, including the maximum load and displacement, time of the failure, and loading rate, are presented in Table 3-28. In addition, the failure mode is indicated for the specimen.

Table 3-28 The shear test results data and failure mode of an extra sample of Configuration III.

Specimen's name	Failure load [kN]	Maximum displacement [mm]	Time [s]	Loading rate [mm/min]	Failure mode
Sample 4	47.5	5.02	435.8	0.5	T2

Figure 3-115 Shear test results of an extra sample of Configuration III. presents results from the shear test of an extra sample of Configuration III. As can be seen, the main failure mode for the sample is rolling shear failure.

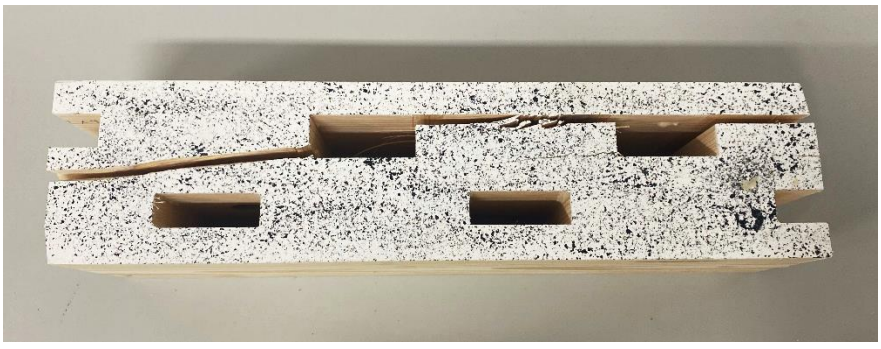

Figure 3-115 Shear test results of an extra sample of Configuration III.

Figure 3-116 Detailed results from the shear test of an extra sample of Configuration III.

3.8.3.2 Load deformation graphs

The graph below presents the load-deformation curves for Configuration III with an extra sample. The failure load of Sample 4 is equal to 47.5 kN, and it was reached after 435.8 s with a loading rate of 0.5 mm/min. Additionally, it can be seen that the failure mode of the Sample 4 was ductile.

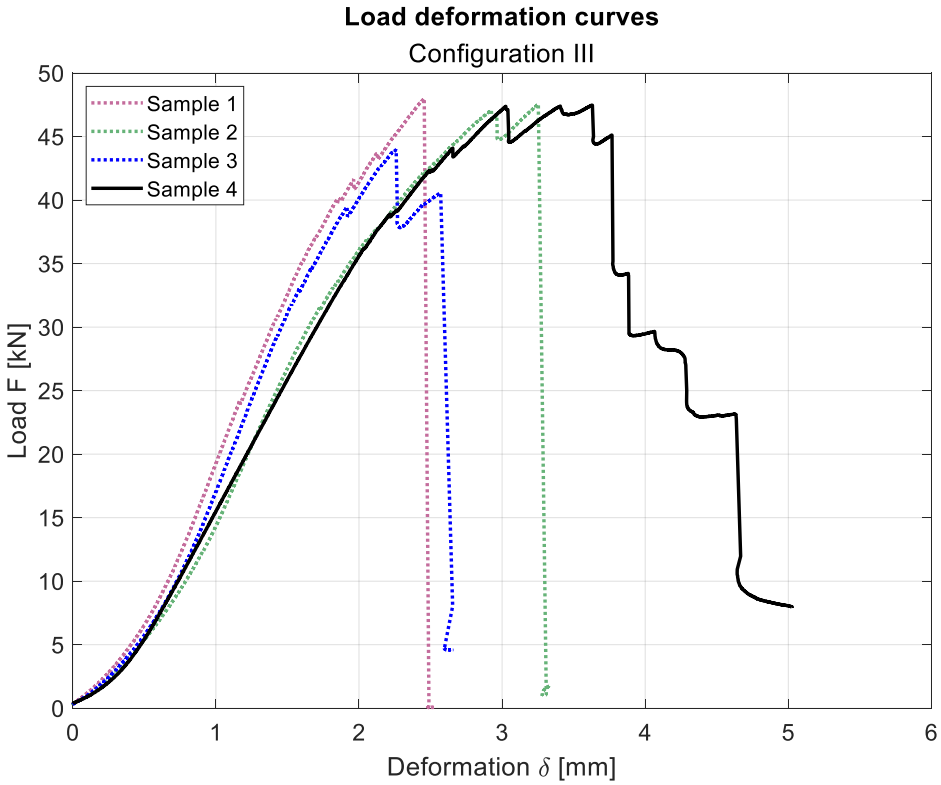

Figure 3-117 Load-deformation graph for Configuration II with an extra sample.

3.8.3.3 Shear strain from ARAMIS software at failure load

The strain distribution over Sample 4 at the moment of the first crack initiation shows that the first crack happened in the position at the corner of the airgap, which is supposed to have a high-stress concentration in this position, see Figure 3-118.

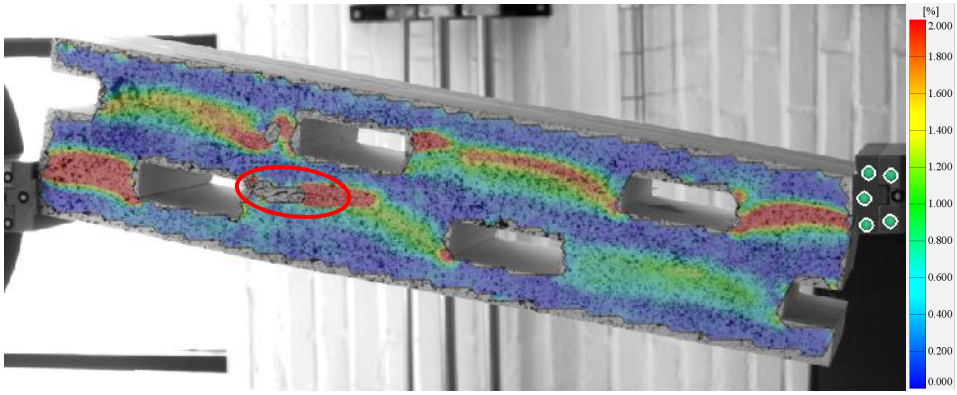

Figure 3-118 The strain distribution of Sample 4 at time 369 s and the load 43.8 kN [ARAMIS data, Configuration III].

By increasing the load, the crack propagates over the cross-layer, and finally, the specimen failed at load 47.5 kN.

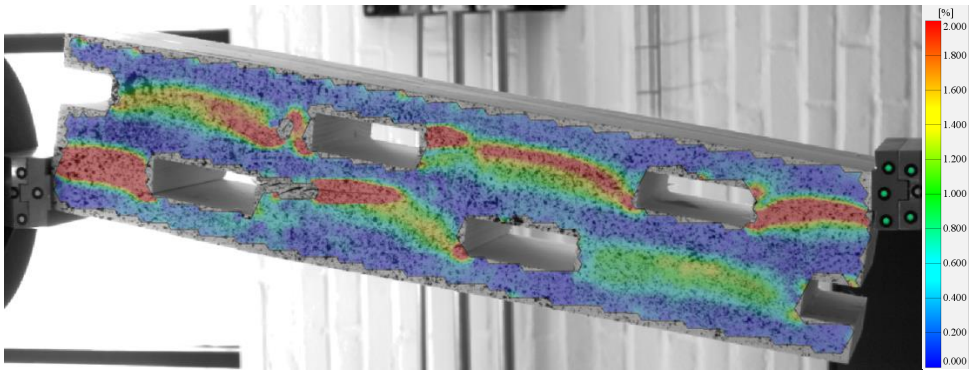

Figure 3-119 The strain distribution of Sample 4 at time 411 s and the load 47.3 kN [ARAMIS data, Configuration III].

And finally, the test was stopped at time 599 sec, see Figure 3-120.

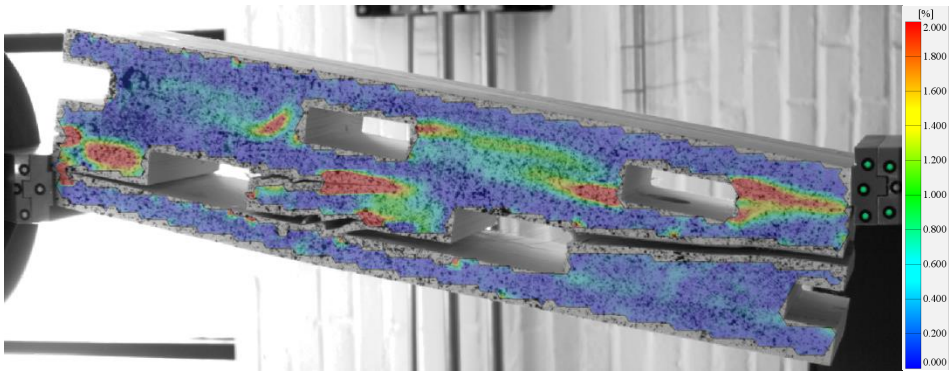

Figure 3-120 The strain distribution of Sample 4 at time 599 s and the load 7.3 kN [ARAMIS data, Configuration III].

3.8.3.4 Rolling shear modulus and shear strength

For Sample 4, the effective shear strength was calculated as 1.41 MPa, and the net shear strength is equal to 0.94 MPa. The normalized shear strength ratio in relation to the specimen from Configuration I is equal to 0.60, and the rolling shear modulus was calculated and equal to 61.46 MPa, see Table 3-29.

Table 3-29 The values of effective shear strength, net shear strength, net shear strength ratio, and rolling shear modulus were extracted based on the experimental data of an extra sample of Configuration III.

Specimen's name	Effective shear strength [MPa]	Net shear strength [MPa]	Normalized net shear ratio [-]	Net rolling shear modulus [MPa]
Sample 4	1.41	0.94	0.60	40.97

3.8.4 Configuration IV

3.8.4.1 Failure modes

The test results and parameters, including the maximum load and displacement, time of the failure, and loading rate, are presented in Table 3-30. In addition, the failure mode is indicated for the specimen.

Table 3-30 The shear test results data and failure mode of extra samples of Configuration IV.

Specimen's name	Failure load [kN]	Maximum displacement [mm]	Time [s]	Loading rate [mm/min]	Failure mode
Sample 4	38.0	3.16	374.5	0.5	R, T2
Sample 5	31.9	2.98	345.0	0.5	R, T2
Sample 6	41.3	3.29	381.8	0.5	R, T2

Figure 3-121 presents results from the shear test of extra samples of Configuration IV. As can be seen, the main failure mode for the three samples is rolling shear failure.

Figure 3-121 Shear test results of extra samples of Configuration IV, with the order from top to bottom, Sample 1, Sample 2, and Sample 3, respectively.

Figure 3-122 Detailed results from the shear test of extra samples of Configuration IV, with the order from top to bottom, Sample 1, Sample 2, and Sample 3, respectively.

3.8.4.2 Load deformation graphs

The graph below presents the load-deformation curves for specimens of Configuration IV. The failure load for sample 6 is the highest of all samples from Configuration IV, and it is equal to 43.1 kN with a maximum deformation of 3.29 mm. The failure load of Sample 4 is slightly lower, and it is equal to 38 kN, and the maximum deformations are 3.16 mm. Sample 5 is marked by the lowest value of failure load from extra samples, and it is 31.9 kN with maximum displacement of 2.98 mm.

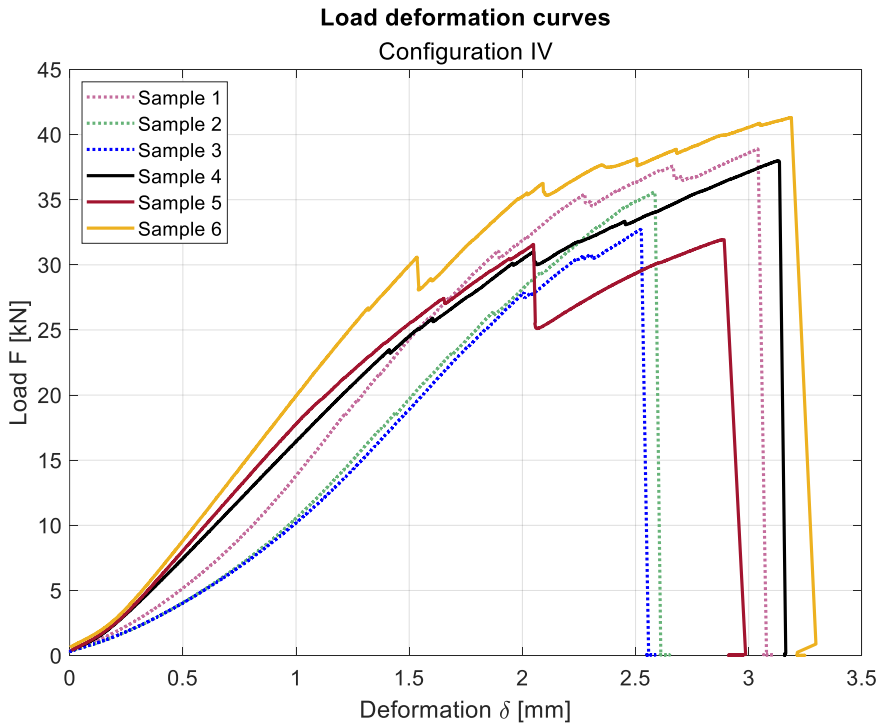

Figure 3-123 Load-deformation graph for Configuration IV with extra samples.

3.8.4.3 Shear strain from ARAMIS software at failure load

The shear strain contour from ARAMIS software is presented in the pictures below. The maximum deformations occur in the cross-layers with a lower shear strength than in longitudinal layers. The peak values of strain at the failure load can be found close to the corners of air airgaps. The cracks are created at that points and lead to the failure of the specimen. Because of the same reason that was explained for Sample 6 of Configuration II, a lamella from a different batch of wood was used for the production of the cross-layers for Sample 6. Thus, this sample test's results are not used for the conclusion. The failure mode for these three samples was brittle.

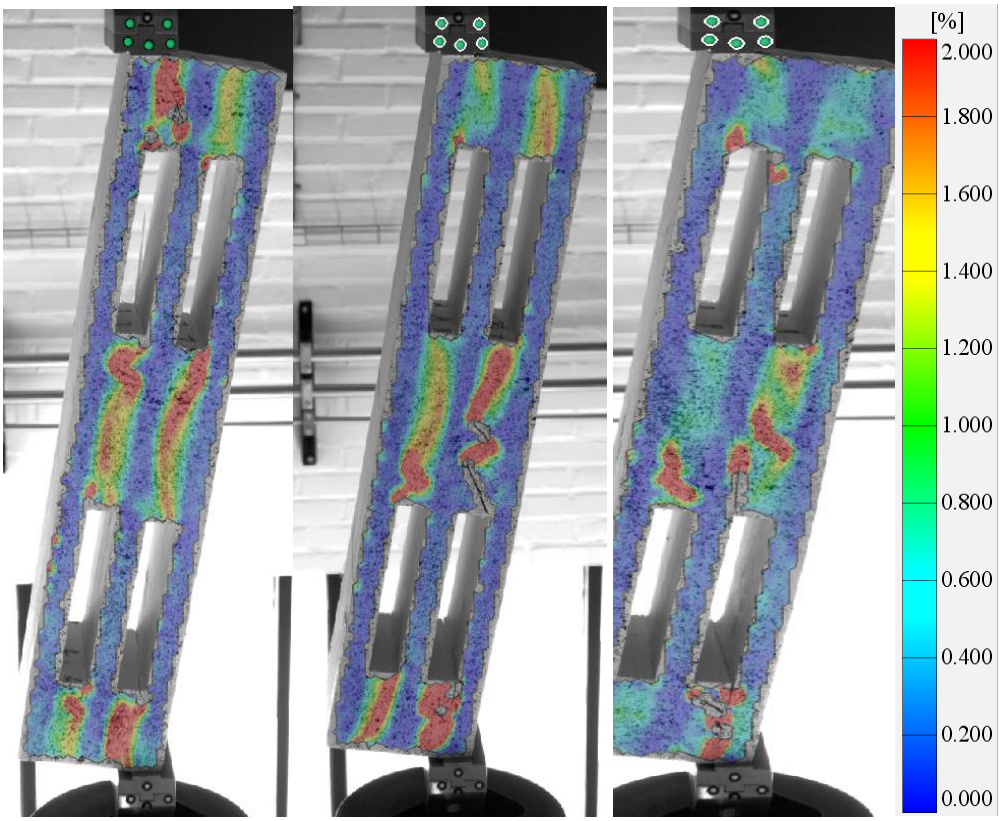

Figure 3-124 Strain distribution using ARAMIS at the failure load for Samples 4, 5, and 6 and Configuration IV from left to right, respectively.

3.8.4.4 Rolling shear modulus and shear strength

The Table 3-31 presents the strength parameters calculated for extra specimens of Configuration IV. Due to the fact that cross-layers of Sample 6 were created from 3 cm thick board, the lamellas have different properties, and the results of Sample 6 cannot be compared to the results of other samples. The effective shear strength and the net shear strength of Sample 4 are higher than those of Sample 5, and they are equal to 1.41 MPa and 0.71 MPa, respectively. The normalized net shear strength ratio is 0.34 for Sample 4, and the rolling shear modulus is 64.64 MPa. The effective shear strength of Sample 5 is 1.19 MPa, and the net shear strength is 0.59 MPa. Additionally, the normalized net shear strength ratio is 0.38 for Sample 5, and the rolling shear modulus is 65.70 MPa.

Table 3-31 The values of effective shear strength, net shear strength, net shear strength ratio, and rolling shear modulus were extracted based on the experimental data of the extra sample of Configuration IV.

Specimen's name	Effective shear strength [MPa]	Net shear strength [MPa]	Normalized net shear ratio [-]	Net rolling shear modulus [MPa]
Sample 4	1.41	0.71	0.45	32.85
Sample 5	1.19	0.59	0.38	35.84
Sample 6	-	-	-	-

3.8.5 Configuration V

3.8.5.1 Failure modes

The test results and parameters, including the maximum load and displacement, time of the failure, and loading rate, are presented in Table 3-32. In addition, the failure mode is indicated for the specimen.

Table 3-32 The shear test results data and failure mode of an extra sample of Configuration V.

Specimen's name	Failure load [kN]	Maximum displacement [mm]	Time [s]	Loading rate [mm/min]	Failure mode
Sample 4	45.39	2.82	274.38	0.5	R, T2

Figure 3-125 presents results from the shear test of an extra sample of Configuration III. As can be seen, the main failure mode for the sample is rolling shear failure.

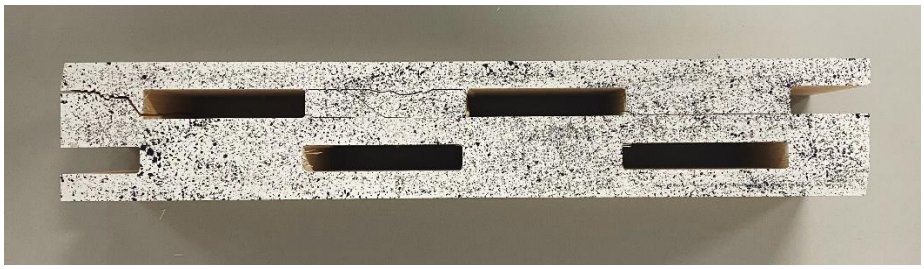

Figure 3-125 Shear test results of an extra sample of Configuration V.

Figure 3-126 Detailed results from the shear test of an extra sample of Configuration V.

3.8.5.2 Load deformation graphs

The graph below shows the load-deformation curves for Configuration V with an extra sample. The failure load of Sample 4 is equal to 45.39 kN, and it was reached after 274.38 s with a loading rate of 0.5 mm/min. The maximum displacement is equal to 2.82 mm. Additionally, the failure mode of Sample 4 was ductile.

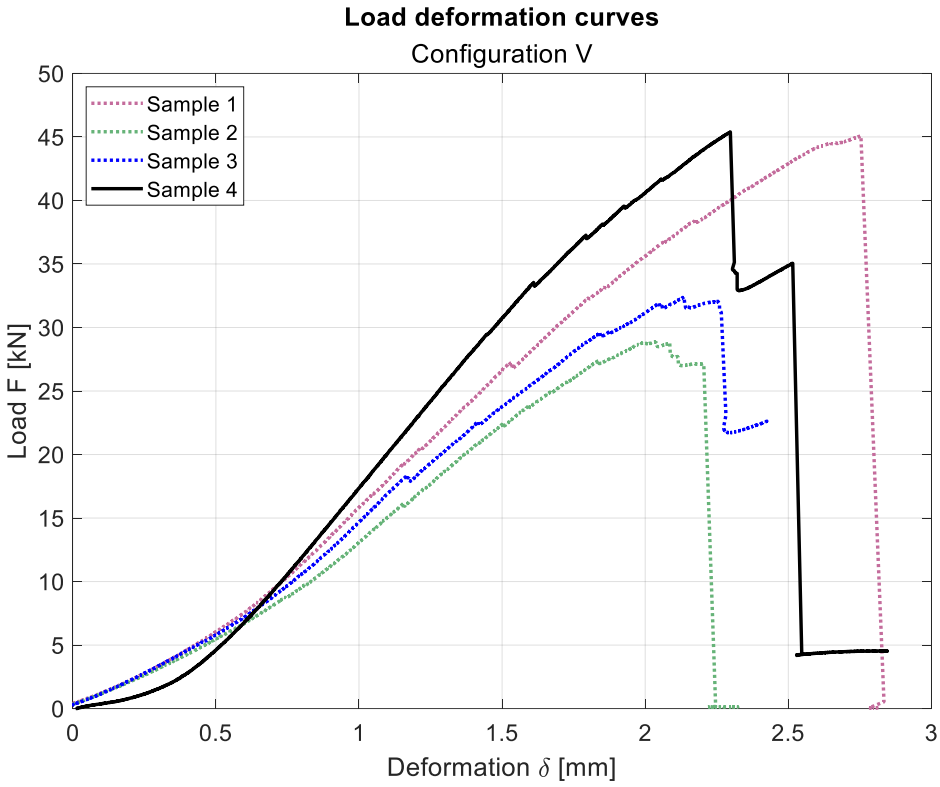

Figure 3-127 Load-deformation graph for Configuration IV with an extra sample.

3.8.5.3 Shear strain from ARAMIS software at failure load

The strain distribution contour from ARAMIS software before and after the failure load is presented in the pictures below. The pictures show that the highest strain concentration can be mainly found at the corners of the air gaps. Leading to the crack initiation and propagation over the cross-layers. The failure mode was ductile for this sample.

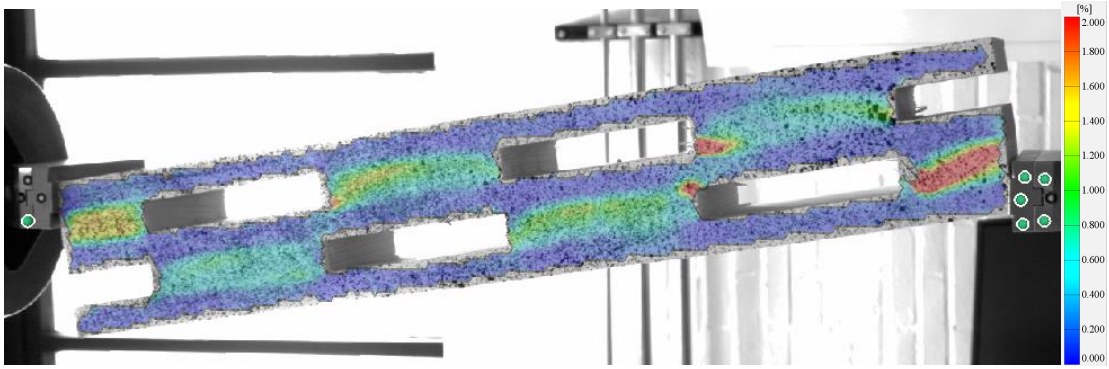

Figure 3-128 The strain distribution of Sample 4 at time 276 s and the load 45.2 kN [ARAMIS data, Configuration V].

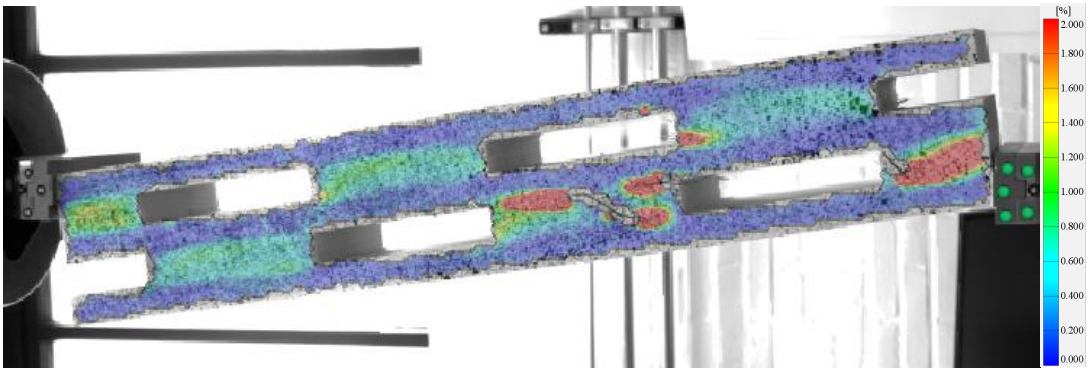

Figure 3-129 The strain distribution of Sample 4 at time 277 s and the load 34.8 kN [ARAMIS data, Configuration V].

3.8.5.4 Rolling shear modulus and shear strength

The parameters calculated for an extra sample of Configuration V are presented in Table 3-33 below. The effective shear strength is 1.36 MPa, and the value of net shear strength is 0.68 MPa. The normalized net shear ratio in relation to Sample 4 from Configuration I is equal to 0.44. The rolling shear modulus is relatively high, and it is equal to 81.97 MPa due to the high slope of the elastic part of Figure 3-127.

Table 3-33 The values of effective shear strength, net shear strength, net shear strength ratio, and rolling shear modulus were extracted based on the experimental data of an extra sample of Configuration V.

Specimen's name	Effective shear strength [MPa]	Net shear strength [MPa]	Normalized net shear ratio [-]	Net rolling shear modulus [MPa]
Sample 4	1.36	0.68	0.44	40.98

3.8.6 Configuration VI

3.8.6.1.1 Failure modes

The test results and parameters, including the maximum load and displacement, time of the failure, and loading rate, are presented in Table 3-34. In addition, the failure mode is indicated for the specimen.

Table 3-34 The shear test results data and failure mode of an extra sample of Configuration VI.

Specimen's name	Failure load [kN]	Maximum displacement [mm]	Time [s]	Loading rate [mm/min]	Failure mode
Sample 4	51.41	3.48	403.7	0.5	R

Figure 3-130 presents results from the shear test of an extra sample of Configuration VI. As can be seen, the main failure mode for the sample is rolling shear failure.

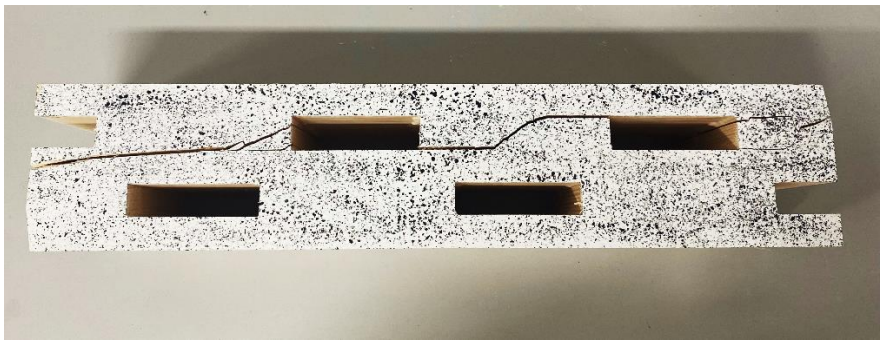

Figure 3-130 Shear test results of an extra sample of Configuration VI.

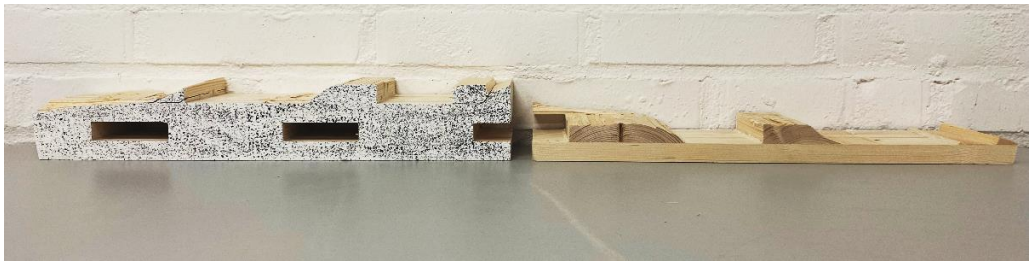

Figure 3-131 Detailed results from the shear test of an extra sample of Configuration VI.

3.8.6.1.2 Load deformation graphs

The graph below presents the load-deformation curves for Configuration VI with an extra sample. The failure load of Sample 4 is equal to 54.41 kN, and the load reached after 403.7 s with a loading rate of 0.5 mm/min. The maximum displacement is equal to 3.48 mm. Additionally, the failure mode of Sample 4 was brittle.

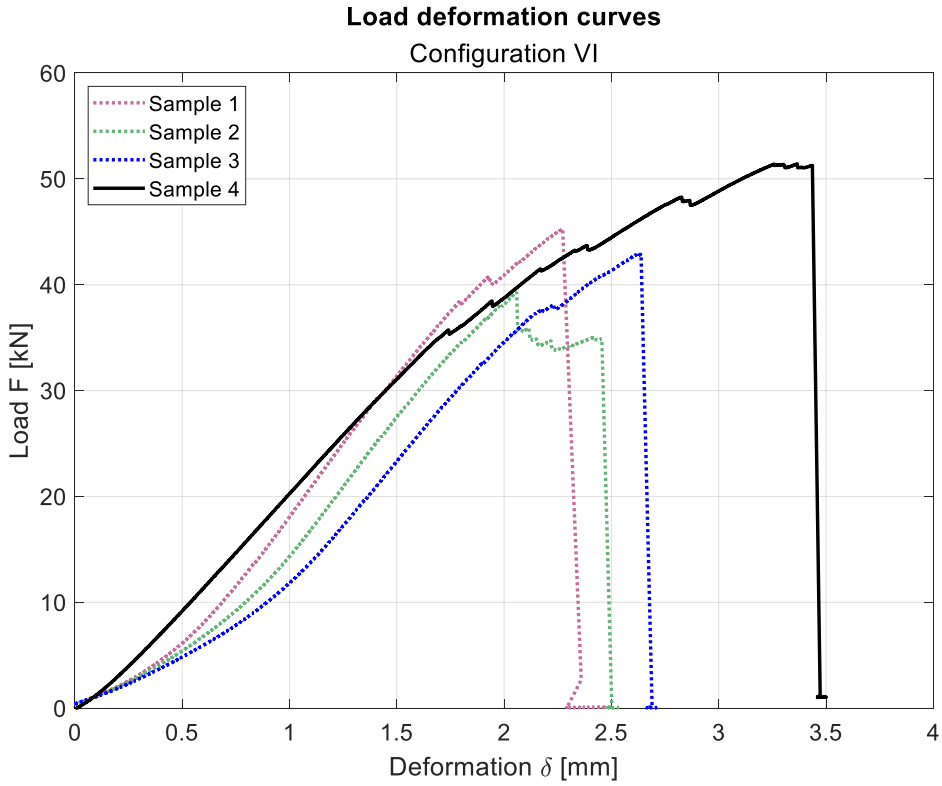

3.8.6.1.3 Shear strain from ARAMIS software at failure load

The shear strain contour from ARAMIS software is presented in the pictures below. As can be seen, the first cracks happened in the cross-layers and near the edge corner due to stress concentration in these points. The specimens failed in the brittle mode.

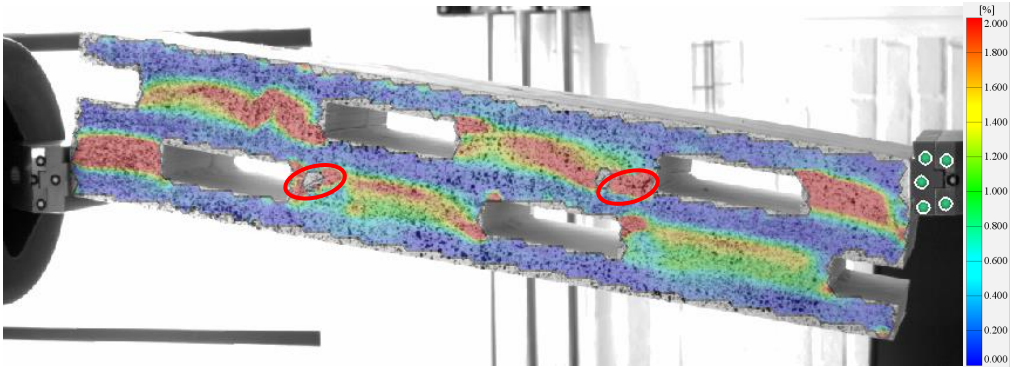

Figure 3-132 The strain distribution of Sample 4 at time 412 s and the load 51.2 kN [ARAMIS data, Configuration V].

3.8.6.1.4 Rolling shear modulus and shear strength

The parameters calculated for Sample 4 Configuration VI are presented in Table 3-35 below. The effective shear strength is 1.53 MPa, and the value of net shear strength is 0.92 MPa. The normalized net shear ratio in relation to Sample 4 from Configuration I is equal to 0.59. The rolling shear modulus is equal to 65.34 MPa.

Table 3-35 The values of effective shear strength, net shear strength, net shear strength ratio, and rolling shear modulus were extracted based on the experimental data of an extra sample of Configuration VI.

Specimen's name	Effective shear strength [MPa]	Net shear strength [MPa]	Normalized net shear ratio [-]	Net rolling shear modulus [MPa]
Sample 4	1.53	0.92	0.59	39.2

3.9 Final results of primary and extra samples

The following table summarizes the results of the shear tests on the small specimens. As can be seen that by increasing scatter in the data, the results fit much better with the FEM model in ABAQUS. Configuration II has a 16 % higher average net shear strength than Configuration IV, which is more discernible than the previous results, which were only 4% higher for Configuration II.

Table 3-36 Summary results of the effective shear strength, net shear strength, and rolling shear modulus.

	Specimen name	Effective shear strength [MPa]	Net shear strength [MPa]	Effective rolling shear modulus [MPa]	Net rolling shear modulus [MPa]
Configuration I	Sample 1	1.29	1.29	70.97	70.97
	Sample 2	1.27	1.27	73.39	73.39
	Sample 3	1.12	1.12	78.15	78.15
	Sample 4	1.56	1.56	65.83	65.83
	Average	**1.31**	**1.31**	**72.08**	**72.08**
Configuration II	Sample 1	1.08	0.72	67.85	45.23
	Sample 2	1.05	0.70	65.98	43.99
	Sample 3	1.01	0.67	58.98	39.32
	Sample 4	1.37	0.91	63.22	42.14
	Sample 5	1.14	0.76	62.74	41.83
	Average	**1.13**	**0.79**	**63.75**	**42.50**
Configuration III	Sample 1	1.43	0.95	83.29	55.51
	Sample 2	1.41	0.94	72.7	48.46
	Sample 3	1.31	0.87	85.04	56.69
	Sample 4	1.41	0.94	61.46	40.97
	Average	**1.39**	**0.93**	**75.62**	**50.40**
Configuration IV	Sample 1	1.45	0.72	78.25	39.12
	Sample 2	1.33	0.66	68.98	34.49
	Sample 3	1.22	0.61	64.94	32.47
	Sample 4	1.41	0.71	65.7	32.85
	Sample 5	1.19	0.59	71.69	35.84
	Average	**1.32**	**0.66**	**69.91**	**34.95**
Configuration V	Sample 1	1.35	0.68	64.85	32.42
	Sample 2	0.86	0.43	52.38	26.19
	Sample 3	0.97	0.49	57.84	28.92
	Sample 4	1.36	0.68	81,97	40.98
	Average	**1.14**	**0.57**	**64.26**	**32.12**
Configuration VI	Sample 1	1.35	0.81	81.45	48.87
	Sample 2	1.17	0.70	76.36	45.81
	Sample 3	1.28	0.77	70.55	42.33
	Sample 4	1.53	0.92	65.34	39.2
	Average	**1.33**	**0.80**	**73.43**	**44.05**

According to these results, the highest average rolling shear modulus is for Configuration III, which is for a CLT panel with 6 cm shifted air gaps and a 2 cm overlap between the cross layers. In terms of net shear strength after a solid CLT panel, Configuration III has the highest average net shear strength, which is 29% lower than solid. Furthermore, 13% less material can be saved in this

configuration compared to solid. In addition, configurations with overlapped cross layers showed higher rolling shear modulus and net and effective shear strength than configurations without overlapped cross layers. The ABAQUS FEM model explains it as overlapping airgap positions leading to a reduction in stress concentrations. Figure 3-133 and Figure 3-134 show the effective shear strength and shear modulus results using bar and boxplots. Clearly, configurations with higher shear modulus also have higher effective shear strengths and vice versa.

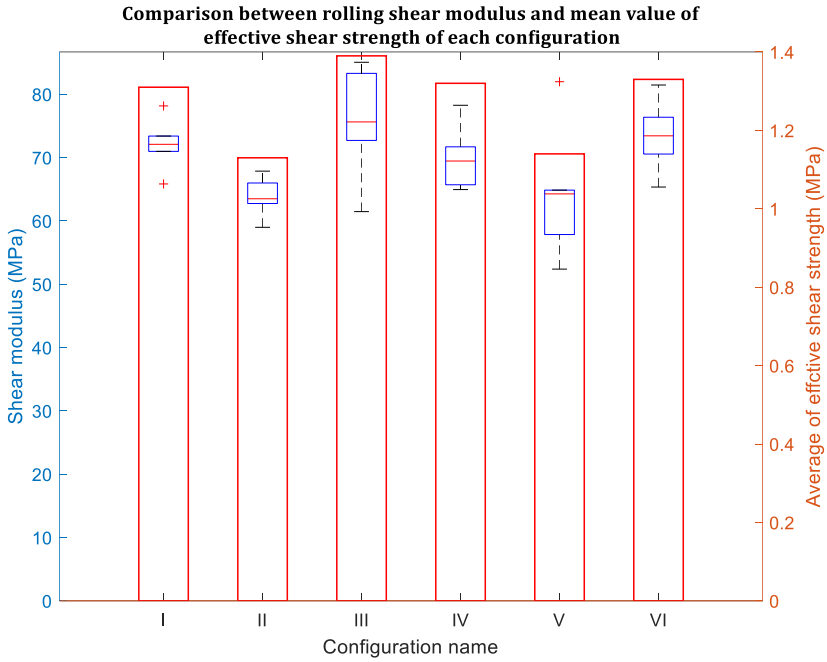

Figure 3-133 Rolling shear modulus and the average value of the effective shear strength for different CLT configurations, shear test results.

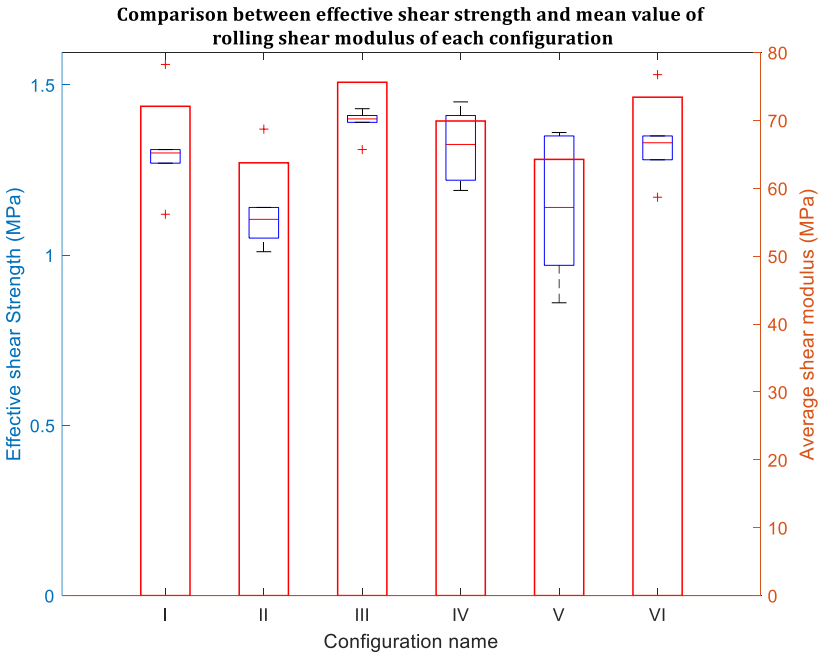

Figure 3-134 Effective shear strength (boxplot) and average shear modulus (bar chart) for each configuration.

Based on a comparison of net shear strength and percentage of the material used in the production of CLT panels, configurations with higher reductions in the material have lower net shear strengths. At the same time, Configurations II and III have the same material reduction (13%). In this case, Configuration III has overlaps between the arrangement of cross layers and has a higher net shear strength (13% higher). For Configuration of IV and V, both of them have the same percent of material reduction (20%); however, Configuration V has shifted cross layers without any overlap, while Configuration IV has centered cross layers with air gaps. In this case, it can be seen that Configuration IV has a higher net and effective shear strength, as well as shear modulus.

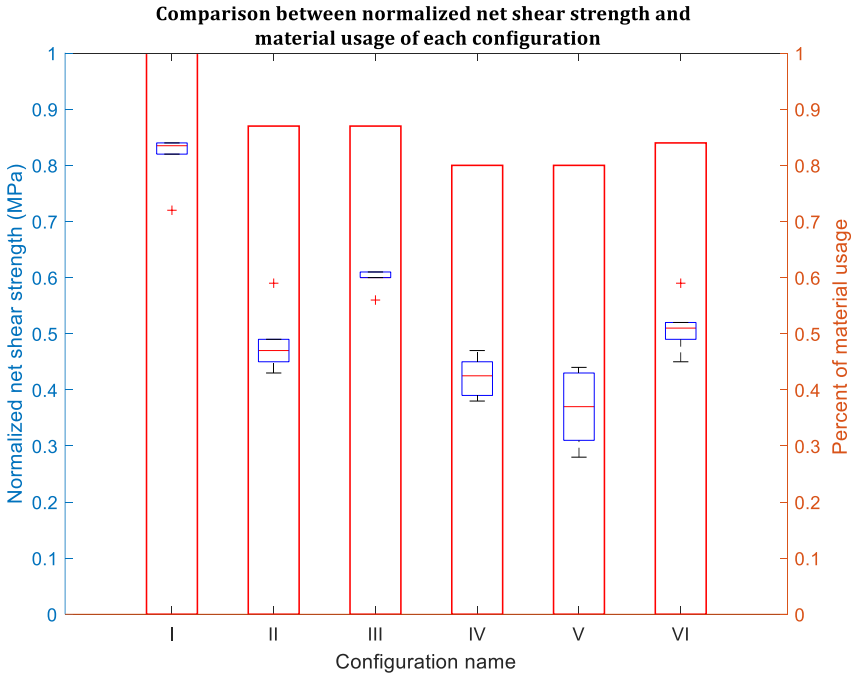

Figure 3-135 Normalized net shear strength (boxplot) and percentage of material usage (bar chart) for each configuration.

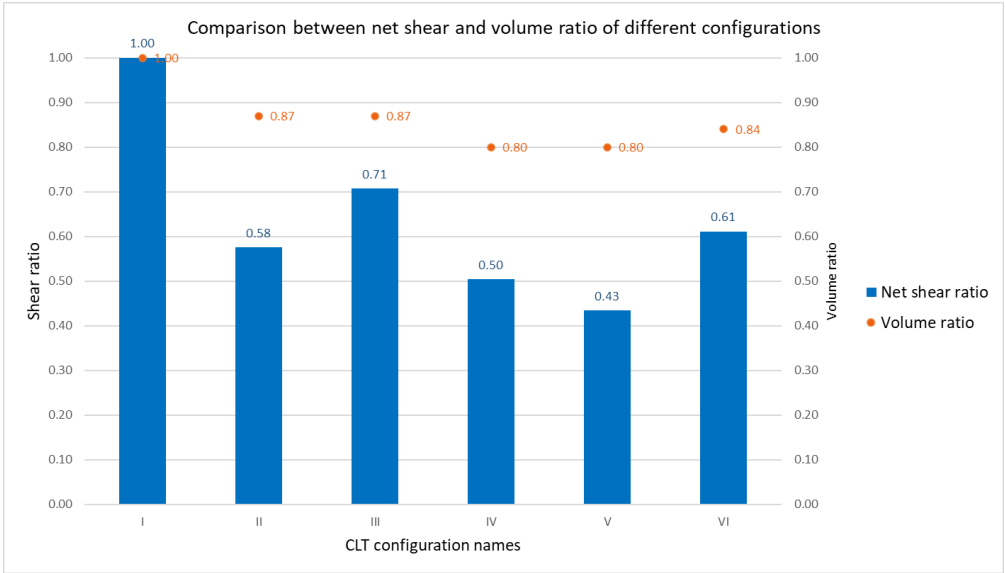

Figure 3-136 Comparison between normalized net shear strength ratio (bar chart) and volume ratio for each configuration.

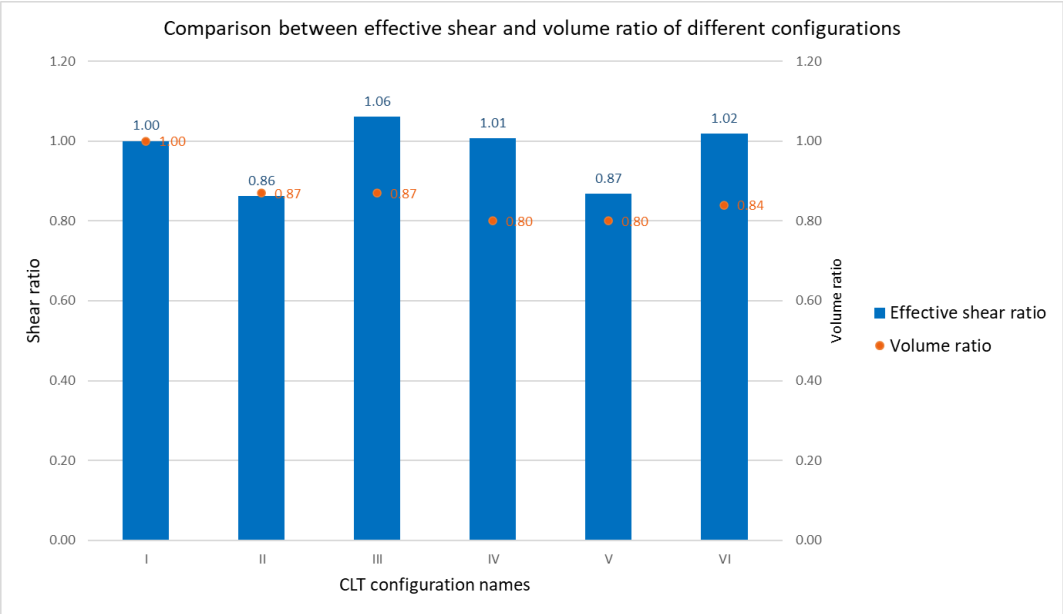

Figure 3-137 Comparison between effective shear strength ratio (bar chart) and volume ratio for each configuration.

The two graphs above present a comparison between normalized nest shear strength ratio and volume ratio, see Figure 3-136 and a comparison between effective shear strength ratio and volume ratio for each configuration, see Figure 3-137. It can be observed that Configuration III, which has 6 cm wide air gaps, reached the highest value of normalized shear strength ratio as 0.71 and effective shear ratio that is equal to 1.06 from all configurations with air gaps. At the same time, material usage is the highest for Configuration III and II. The graphs also show that from Configurations II and III that have the same width of air gaps, Configuration II, with centered air gaps, has a lower both effective shear ratio and normalized net shear strength ratio. For Configuration IV and V that have 12 cm air gaps and the same material reduction, Configuration IV has higher shear ratios, so it can be concluded that cantered airgaps factor into better shear properties than the airgaps in the panel without overlapping.

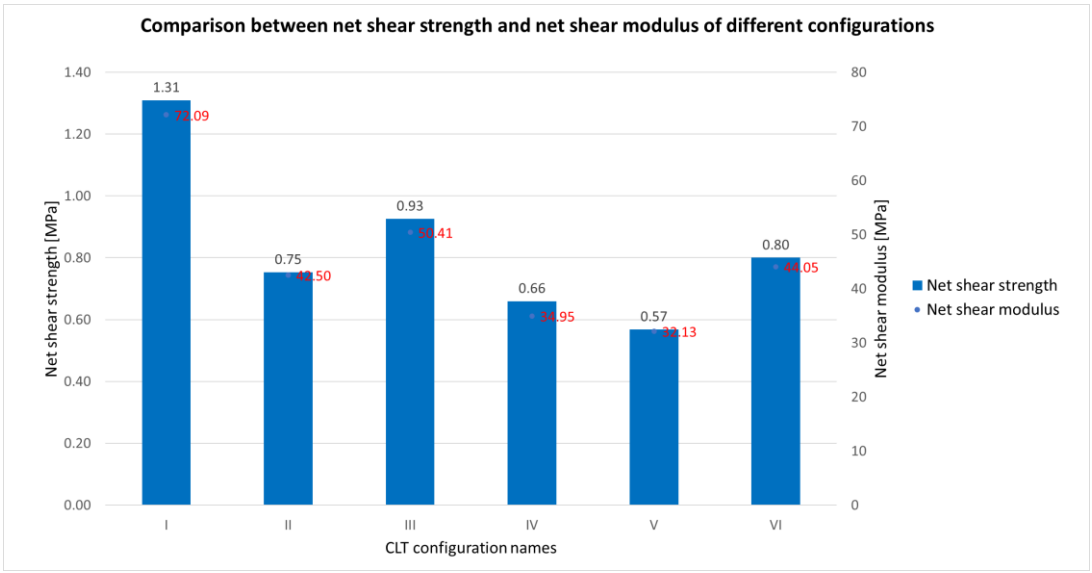

Figure 3-138 Comparison between net shear strength ratio (bar chart) and net shear modulus of each configuration.

Figure 3-138 shows the average of net shear modulus and net shear strength calculated for all configurations. In comparison to the other configurations with air gaps between the cross layers, configuration III has a higher net shear modulus and net shear strength. Compared to the solid configuration, configuration III saves 13% more material. In addition, Configuration VI, with its 16% material reduction, has the highest net shear strength and net shear modulus after Configuration III.

3.10 A. Moberg and L. Xiao master thesis's results

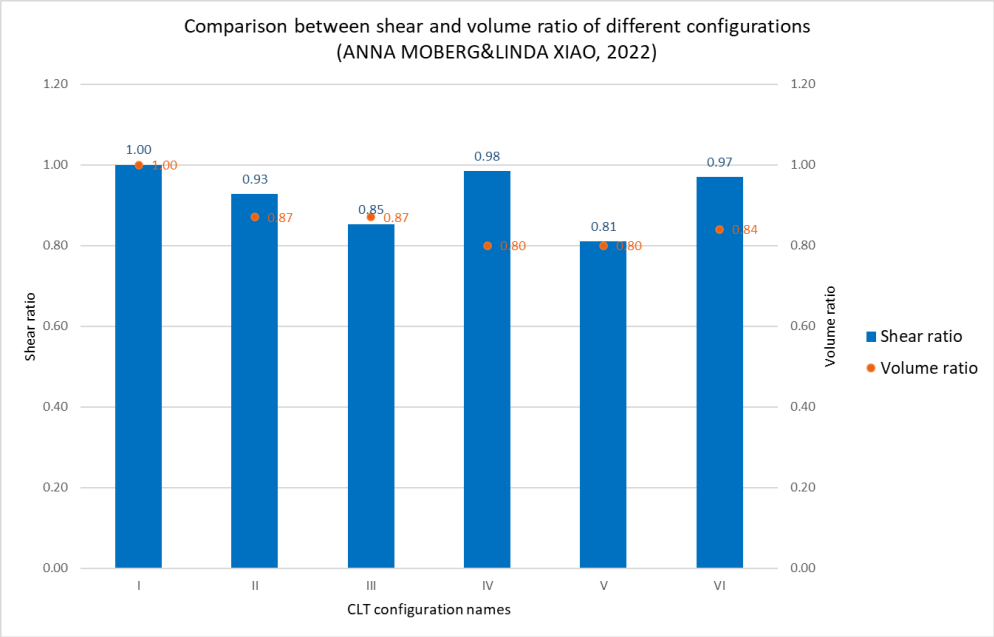

Figure 3-139 Comparison between effective shear ratio and volume ratio of the specimens from last year's test.

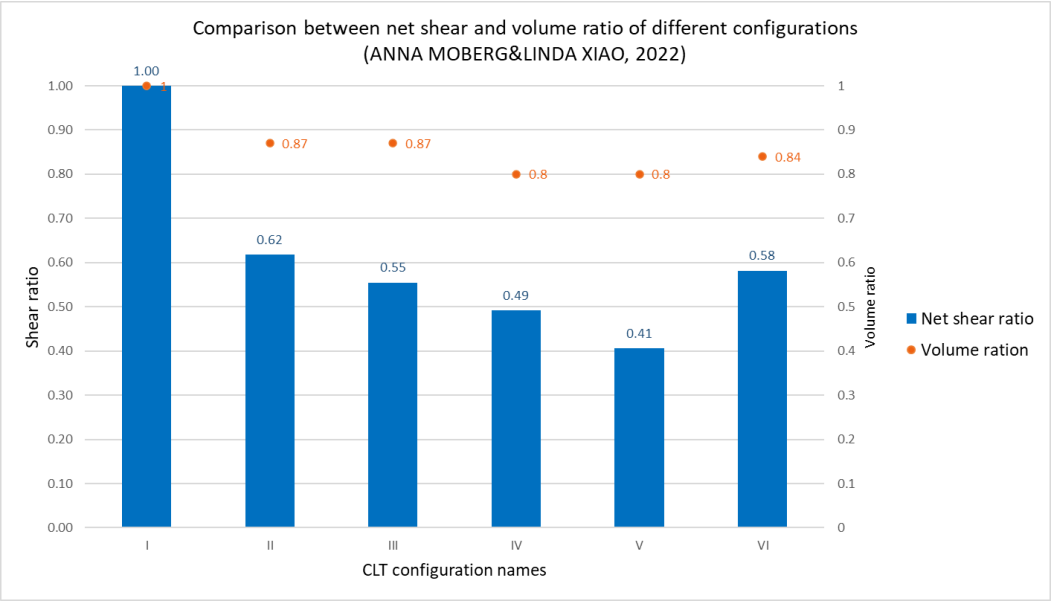

Figure 3-140 Comparison between net shear strength ratio and volume ratio of the specimens from last year's test.

Figure 3-139 and Figure 3-140 show the comparison between net shear and volume ratio, Figure 3-139, and the comparison between effective shear ratio and volume ratio, Figure 3-140 created based on data from A. Moberg and L. Xiao's master thesis [13]. It can be seen that the plots generally follow the same trend as it is observed in Figure 3-136 and Figure 3-137. The major difference can be found for Configuration III that the net shear ratio and effective shear ratio were quite low and equal to 0.55 and 0.85, respectively. The net shear ratio was higher than Configuration IV and V and the effective shear ratio was only higher than Configuration V. The results from the last year might be different than the ones from this Master's thesis because of a couple of reasons. First of all, the production methods were different, and the vacuum press was used last year instead of clamps in the manufacturing process. Additionally, the failure mode of the specimen was different which factors into the final strength properties.

4 Four-point bending test

4.1 Methodology

The chapter includes a description of the methodology used for performing a rolling shear test for a four-point bending test for big-scale beams that were produced in the factory.

4.1.1 Manufacturing

The StoraEnso factory in Austria manufactured the large-scale specimens used for the four-point bending test. At the beginning of the production process, the dimensions of the boards used for cross-layers were checked to see if they were correct and fit the longitudinal lamellas, see Figure 4-1.

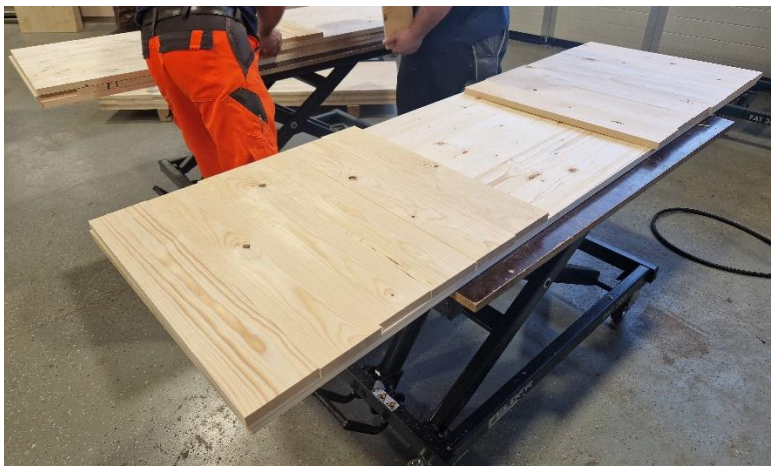

Figure 4-1 Preliminary assembling of the boards.

In the next step, the adhesive was applied on the longitudinal layer by gluing machine in order to be able to tack the cross-layers on the board, see Figure 4-2.

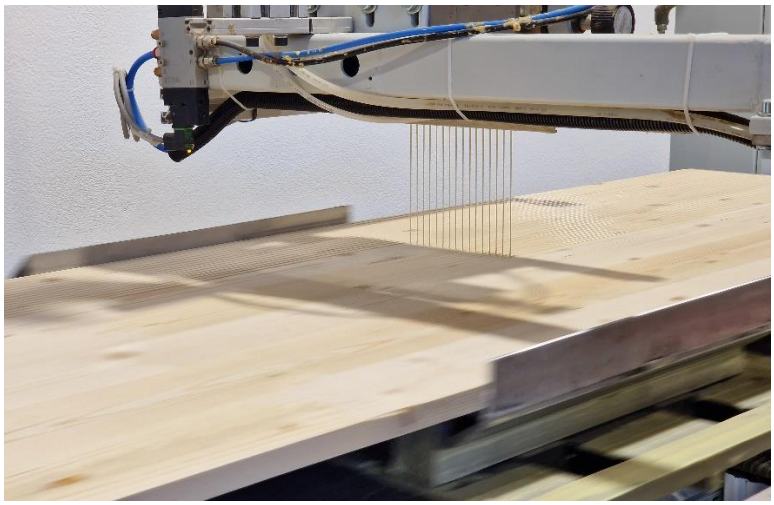

Figure 4-2 Glue application on a longitudinal board of a CLT panel.

When the glue was put on the longitudinal lamella, the cross-layer boards were manually placed on it, see Figure 4-3 and the adhesive was added on the next longitudinal board.

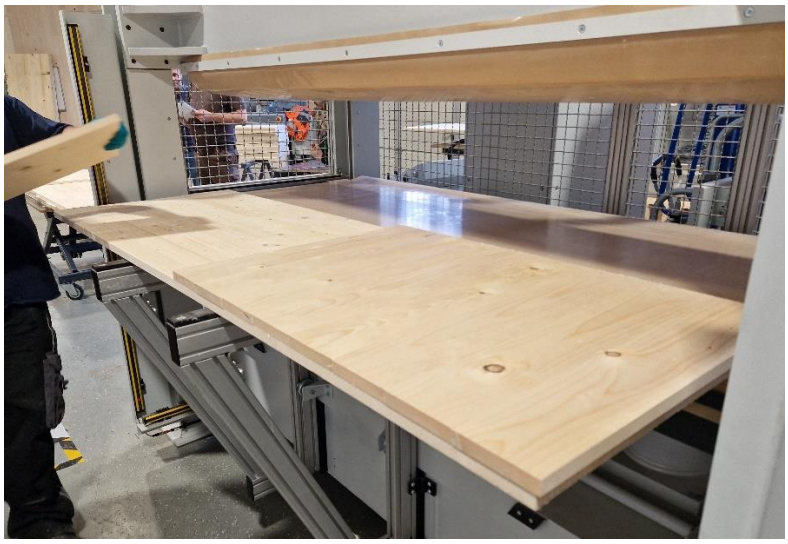

Figure 4-3 Manual assembling of the cross-layer boards.

For the middle longitudinal layer, the glue was applied on both surfaces in order to be able to join the first and the second cross-layer at both sides. The picture below shows all five layers after the gluing process.

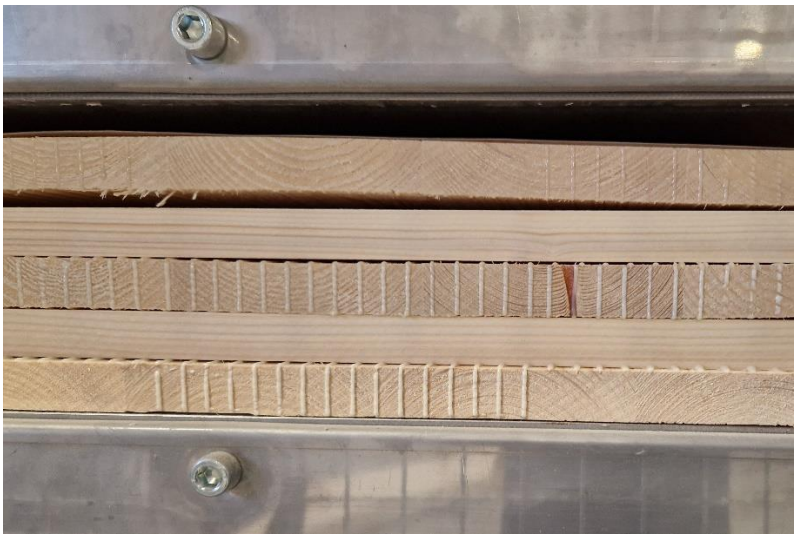

Figure 4-4 The boards after gluing process.

When the glue was applied, the panel was ready for pressing by the hydraulic press, see Figure 4-4.

Figure 4-5 Hydraulic press and the pressing process.

The panels with air gaps introduced in the cross-layers were produced in a similar way. However, in order to keep the boards in the cross-layers in the correct places, the timber elements were screwed at the edges of the panels. Furthermore, when the panels were pressed, they were disassembled, see Figure 4-6.


Figure 4-6 Timber elements at the edges of the cross-layers (left) and the CLT panel after disassembly (right).

4.1.2 Configurations

All three configurations of the beam are made of lamellas with a thickness of 20 mm and a strength class of C24. The global dimensions of each configuration are the same, so the beam is 2000 mm long, 200 mm wide, and the height is 100 mm.

4.1.3 Configuration A

Configuration A depicts the solid CLT beam without any air gaps. The longitudinal layers are formed from three pieces of boards having different widths and lengths, but the cross-layers are produced from 120 mm lamellas in the middle of the layer and 100 mm boards at the edges. The geometry and geometrical properties of Configuration A are shown below; see Figure 4-7, and Table 4-1.

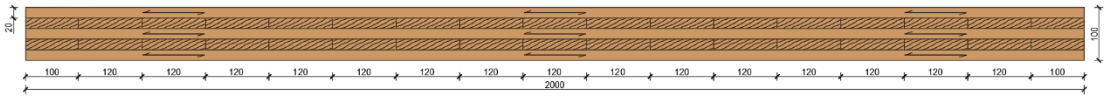

Figure 4-7 Geometry of the Configuration A used for the four-point bending test.

Table 4-1 Geometrical properties of Configuration A used for the four-point bending test.

Air gap width b_{airgap} [mm]	0
Wood volume V_{wood} [mm³]	40 000 000
Maximum possible volume [mm³]	40 000 000
Relative volume η_V [-]	1.00
Material reduction η_M [%]	0

4.1.4 Configuration B

The second configuration includes air gaps in the cross-layers. The air gaps are not shifted; they are 60 mm wide and located every 120 mm. The lamellas at the boundaries of the cross-layers are 70 mm wide. The figure and table below present the geometry, dimensions, and geometrical properties; see Figure 4-8 and Table 4-2 Geometrical properties of Configuration B used for the four-point bending test.

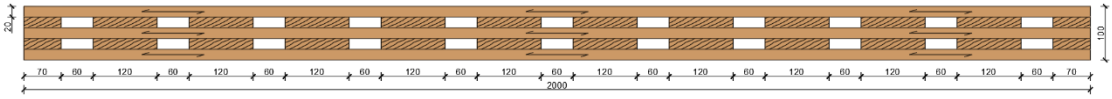

Figure 4-8 Geometry of Configuration B used for the four-point bending test.

Table 4-2 Geometrical properties of Configuration B used for the four-point bending test.

Air gap width b_{airgap} [mm]	60
Wood volume V_{wood} [mm³]	34 720 000
Maximum possible volume [mm³]	40 000 000
Relative volume η_V [-]	0.87
Material reduction η_M [%]	13.20

4.1.5 Configuration C

In Configuration C, centrally aligned air gaps are also introduced, but the width of them is 120 mm. The timber lamellas in the middle of the cross-layers are 120 mm wide, and at the edge, they are 20 mm shorter. Configuration C´s geometry and geometrical properties are shown in a figure and table below; see Figure 4-9 and Table 4-3.

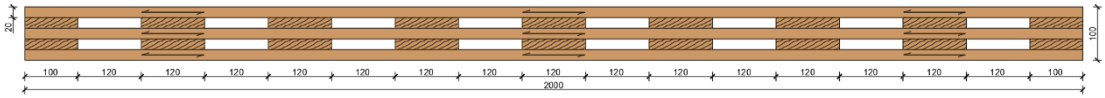

Figure 4-9 Geometry of Configuration C used for the four-point bending test.

Table 4-3 Geometrical properties of Configuration C used for the four-point bending test.

Air gap width b_{airgap} [mm]	120
Wood volume V_{wood} [mm³]	32 320 000
Maximum possible volume [mm³]	40 000 000
Relative volume η_V [-]	0.81
Material reduction η_M [%]	19.20

4.1.6 Preparation of the specimens for DIC analysis

The CLT beams were covered in the pattern of black dots on white paint in order to be able to perform Digital Image Correlation. The procedure was the same as it was presented in section 3.1.431. Figure 4-10 presents the big-scale samples that are prepared for the four-point bending test.

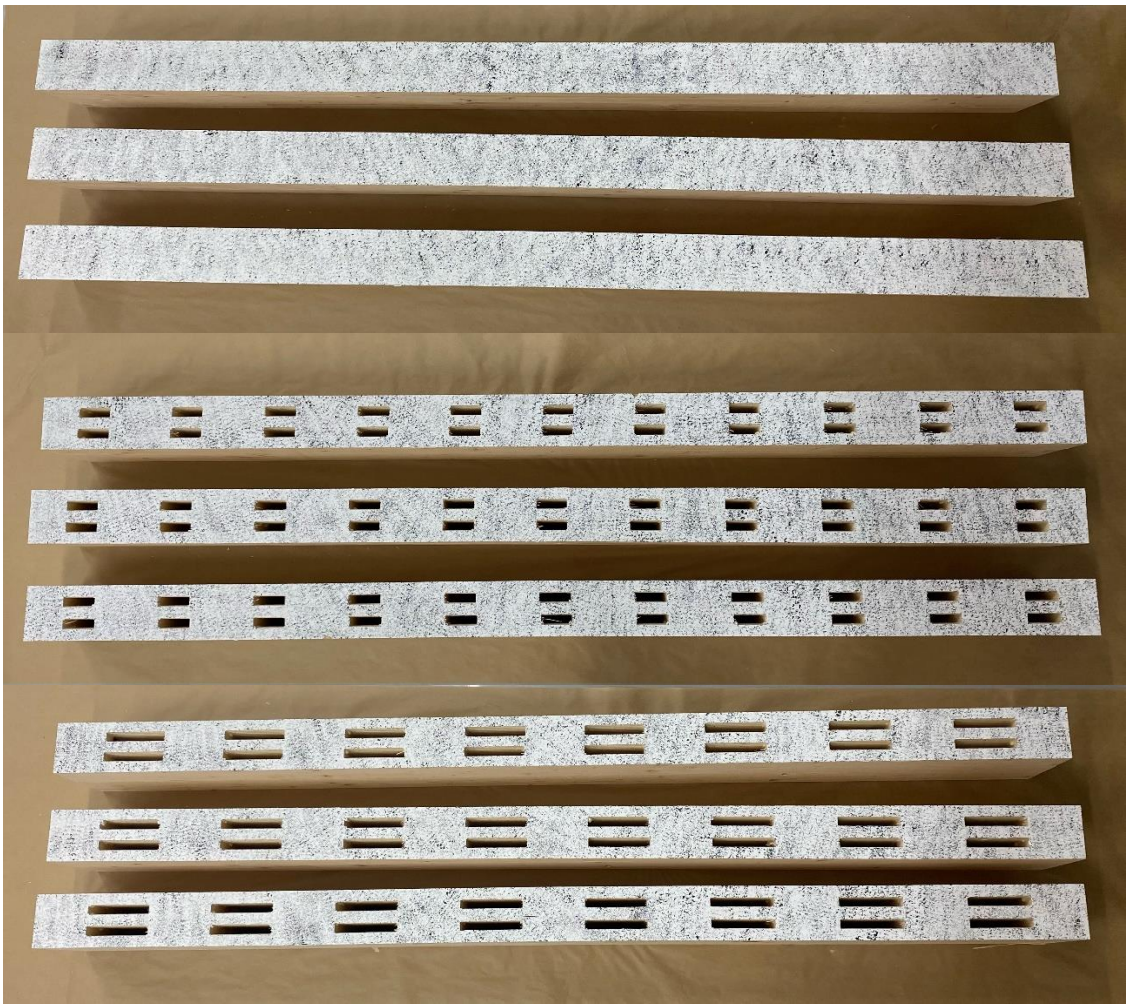

Figure 4-10 Configuration A, B, and C covered by the pattern.

4.1.7 Testing of big-scale specimens

The four-point bending test took place in the Structural Lab at Chalmers University of Technology. There were used three different configurations of CLT panels, and there were three samples tested for each of the configurations. The detailed geometry is shown in sections 4.1.3, 4.1.4, and 4.1.5. This subchapter presents the equipment that was used for conducting the test, the measurement set, and the method of applying the load.

4.1.7.1 Test equipment

The setup of the equipment and the beam of each configuration is presented below, see Figure 4-11.

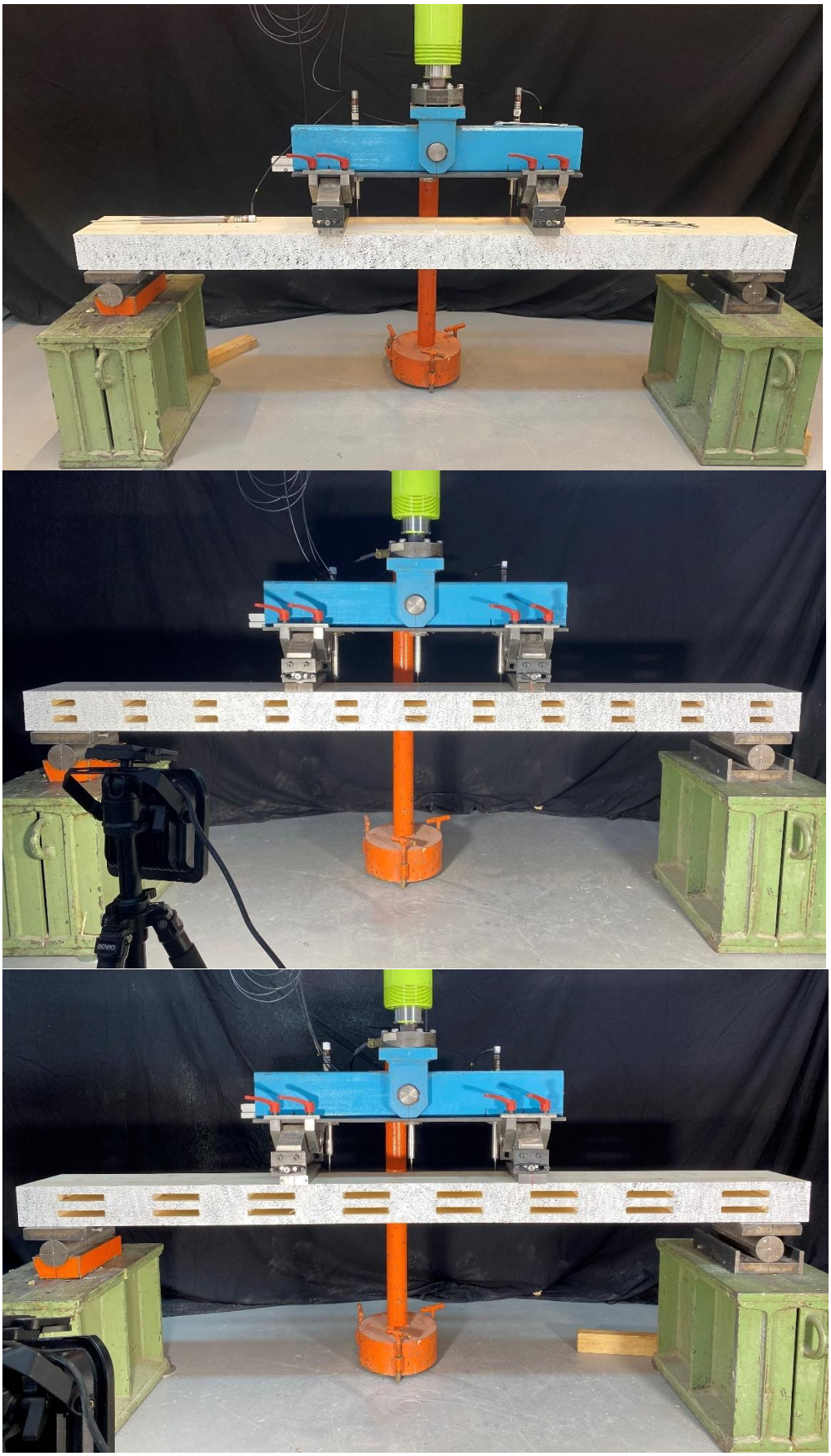

Figure 4-11 The setup of the equipment of the beam and location of the load with regard to the arrangement of airgaps.

The experiments were performed in a hydraulic test machine that was connected to the beam element that distributed the load to two points. The load was applied to the beam through two rollers that were placed on the steel plates so, the load was distributed along the surface of the element. The steel plates were placed on the position of 0.7l and 1.3l so 700 mm and 1300 mm from the edge of the beam. The dimensions of the steel plates used in the load application were 250×70 mm. The image of the roller and the plate is present in Figure 4-12.

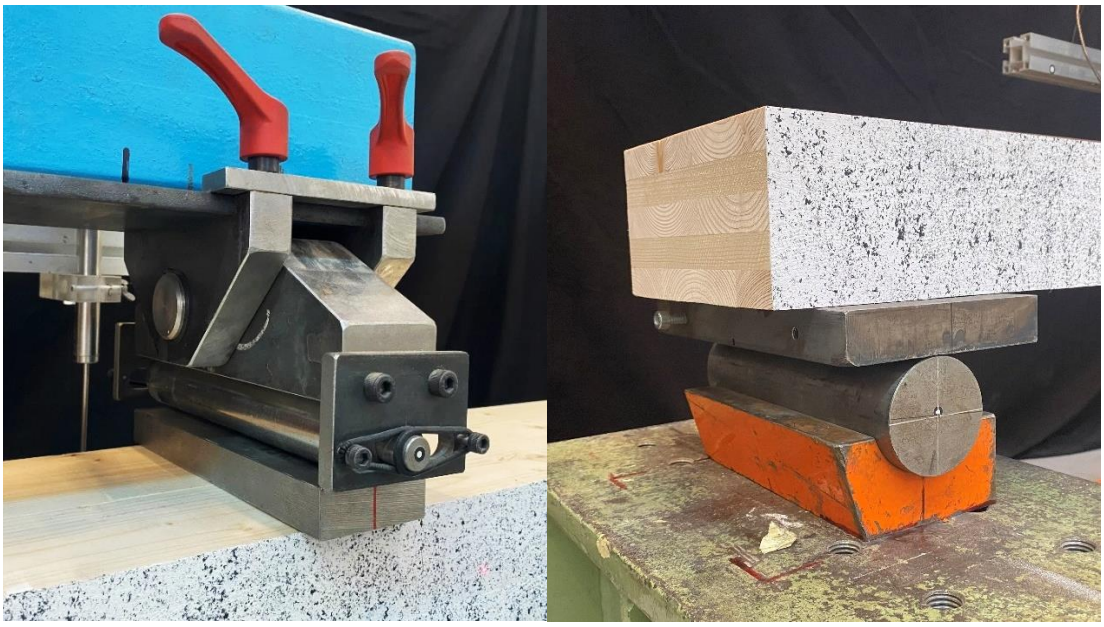

Figure 4-12 The roller with the plate that distributes the load (left picture) and the left support (right picture).

The beams were simply supported during the test, and they were placed on the steel plates to avoid the local cracks; the picture of the left support can be seen in Figure 4-12. The supports were placed 100 mm from the beam edge, and the dimensions of the steel plates were 250×150 mm.

The displacements were measured by linear variable differential transformers (LVDTs), and they were placed on the brackets that were temporarily screwed behind the beam for the time of the experiment. The one in the center of the beam measured the global deflection, and two other measured local displacements. The sensors were arranged at the points of 0.75l, 1.0l, and 1.25l, so 750 mm, 1000 mm, and 1250 mm from the edge of the beam, see Figure 4-13.

Figure 4-13 The location of sensors behind the beam.

4.1.7.2 ARAMIS system

The specimens were covered by the pattern that provided the contrast that the ARAMIS optical system can monitor and provide a graphical representation of changes in deformation at the surface of the beam. When the loading process started, the system was adjusted to take one picture per second (1Hz). The range of the camera was allowed to include only about 80 cm of the beam length, so it was decided to analyze the part from the right support to the left point load of the panel. The ARAMIS optical system is shown in the picture below.

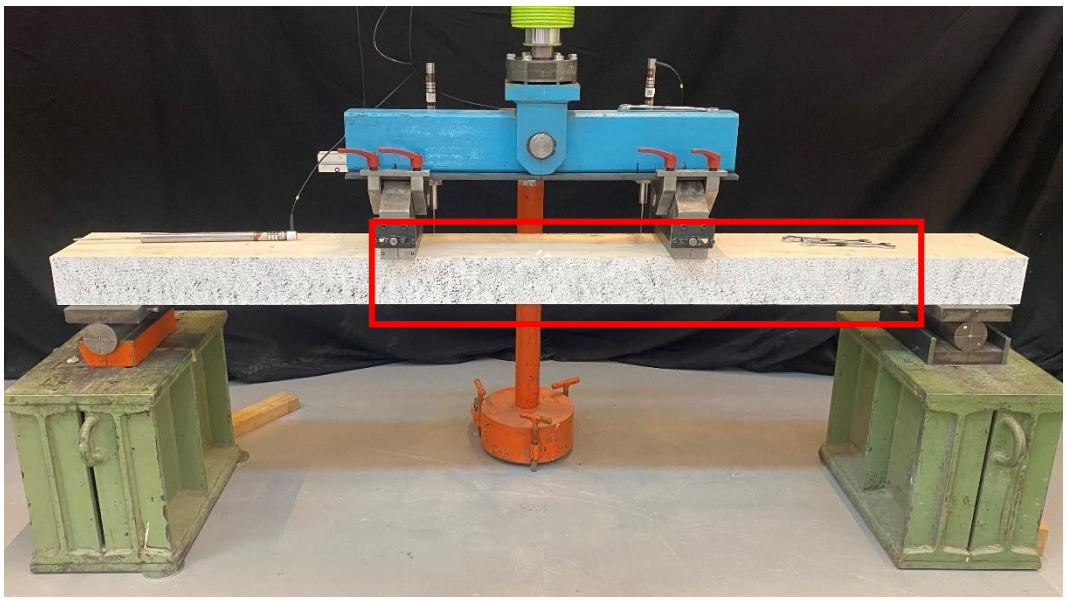

Figure 4-14 The range of the beam that is captured by ARAMIS.

4.1.7.3 Loading sequence

The test was carried out in three steps. For the first sample, a pre-load of 11 kN was applied to eliminate the influence of the air gaps between connections or steel plates in the loading device. Then the beam was unloaded to 2 kN and loaded again until the failure happened. For other samples in Configuration A, the boundary loads were equal to 10 kN and 2.5 kN, respectively; for Configuration B it was reduced to 8 kN and 2 kN. For the final configuration, it was decided to pre-load the beam until 7 kN and unload to 1 kN before the beginning of the loading and the final failure. The loading rate for the first specimen was set to 10 mm/min, and it was decreased to 5 mm/min for other configurations due to an early failure of the first sample.

4.1.8 Hand calculations

By rewriting the equation (2-21), (2-22), and (2-24), the expected force can be derived:

$$P_{mean.m} = \frac{f_{m.xlay.mean} W_{x.net}}{c_1} \tag{4-1}$$

$$P_{mean.v} = \frac{f_{v.9090.xlay.mean} I_{y.net} b_x}{S_{y.net}} \tag{4-2}$$

$$P_{mean.r} = \frac{f_{v.9090.ylay.mean} I_{x.net} b_y}{S_{x.net}} \tag{4-3}$$

where, $f_{m,xlay,mean}$ is the mean value of bending strength, $W_{x,net}$ is the panel's net moment of resistance, c_1 is the distance from applying load to the support $f_{v,9090,xlay,mean}$ is the mean value for the rolling shear strength of the boards, $I_{y,net}$ is the net moment of inertia along the y-axis, b_x is the width of the layer, $S_{y,net}$ is the panel's net static moment, $f_{v,9090,ylay,mean}$ is the mean value for the longitudinal shear strength of the boards, $I_{x,net}$ is the net moment of inertia along the x-axis, b_y is the width of the layer, $S_{x,net}$ is the panel's net static moment. The results are presented below; detailed calculations, are provided in the appendix.

Table 4-4 Maximum mean values of loads that can be applied to the model based on bending and shear verifications.

$P_{mean,m}$ (Bending stress verification)	$P_{mean,v}$ (Shear verification)	$P_{mean,r}$ (Rolling shear verification)
73.9 kN	242.6 kN	25.41 kN

Therefore, the maximum applied force is the minimum value of the load presented in the table above, which is equal to 25.4 kN.

4.1.9 MATLAB analysis

Based on the Euler-Bernoulli and Timoshenko theory, the deflection of a beam under four-point testing can be calculated. The calculation is done by the use of MATLAB and using the MATLAB Calfem toolbox [22]. For the Timoshenko method to consider the effect of the different shear modulus of the longitudinal and transverse layers, a mean value of the cross-section can be calculated by the equation below.

$$G_{mean} = \frac{G_{LT}(t_1 + t_2 + t_3) + G_{RT}(t_2 + t_4)}{h} \quad (4\text{-}4)$$

Where t is for the thickness of the different layers of lamellas and h is the total thickness of the CLT panel.
The boundary condition is applied to the model by considering the no deflection in the y-direction at supports. The shear correction factor for five-layer CLT panels with equal thickness and the ration of the shear modulus of $\frac{G_{90}}{G_0} = \frac{1}{10}$ is considered 0.24 [19]. The convergence study was done for different numbers of elements, and the element size equal to 10 with 200 elements is chosen, see Figure 4-15.

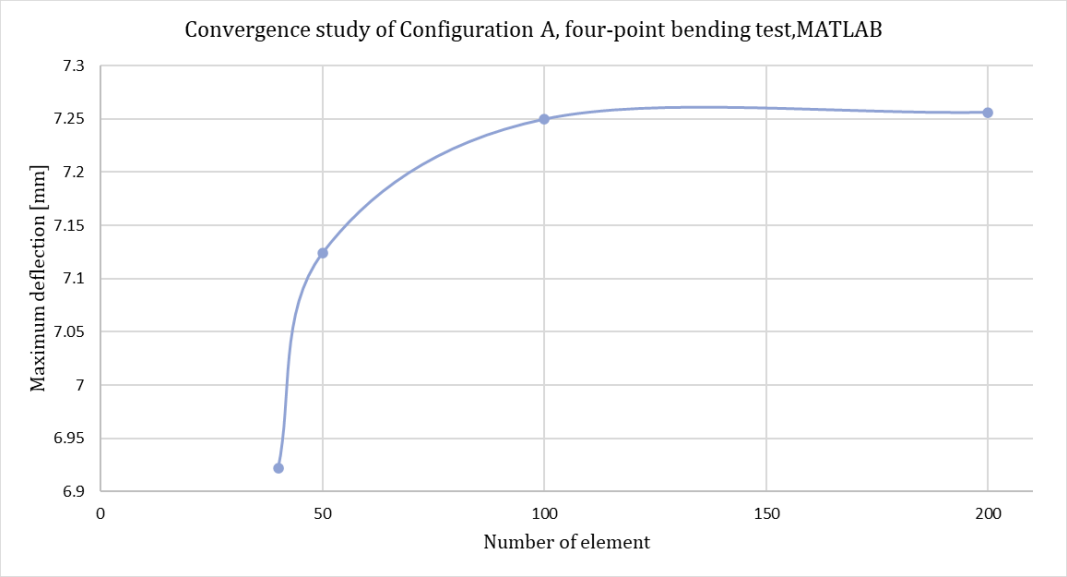

Figure 4-15 Convergence study for MATLAB (Deflections are related to the Bernoulli beam theory).

For a solid CLT panel, the deflection of the beam at a load equal to 5 kN is calculated; see Figure 4-16. As it can be seen, the Timoshenko method for a beam with a width equal to 20 cm predicted higher deflection compared to the Bernoulli theory.

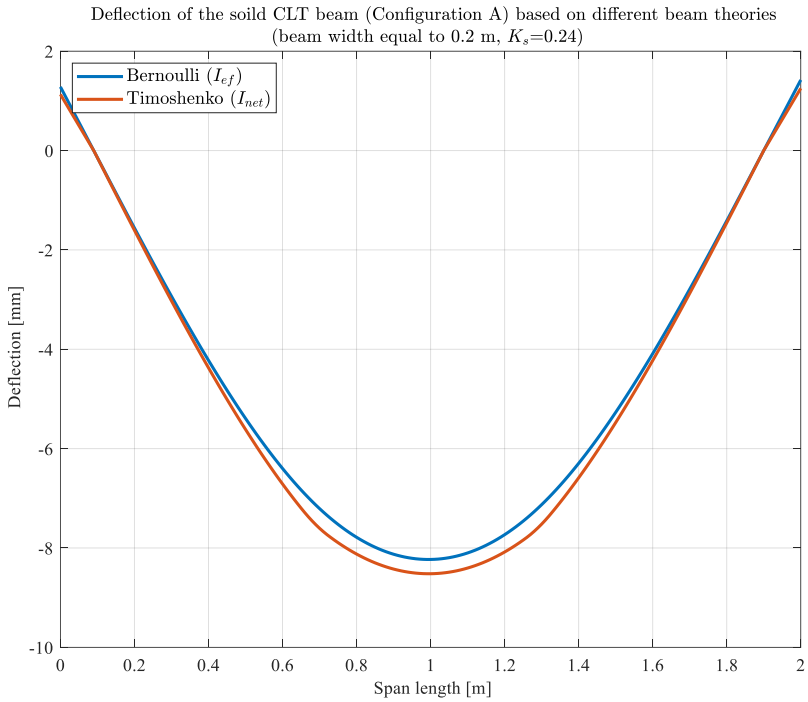

Figure 4-16 Deflection of a solid CLT panel (Configuration A) using different beam theories in a four points bending test for P=5 kN.

The same method applied for a CLT panel with centered airgaps is applied; for the second configuration, the airgaps dimensions are 12 cm, and for the third configuration, the airgaps dimensions are 6 cm. To consider the airgaps effect on the Bernoulli equations need to be modified. For calculations of the moment of inertia, the Gamma 1 factor is modified as below:

$$\gamma_{1,modified} = \frac{1}{1 + \frac{\pi^2 E_{x,1} t_1}{l_{ref}^2} \frac{t_2}{\lambda\, G_{9090,2}}} \tag{4-5}$$

For the Timoshenko method, the mean value of the cross-section can be modified by the equation below:

$$G_{mean} = \frac{G_{LT}(t_1 + t_2 + t_3) + \lambda\, G_{RT}(t_2 + t_4)}{h} \tag{4-6}$$

Where λ is the void ratio, see section 3.1.1.1

The results for each configuration are shown in Figure 4-17 and Figure 4-18, respectively.

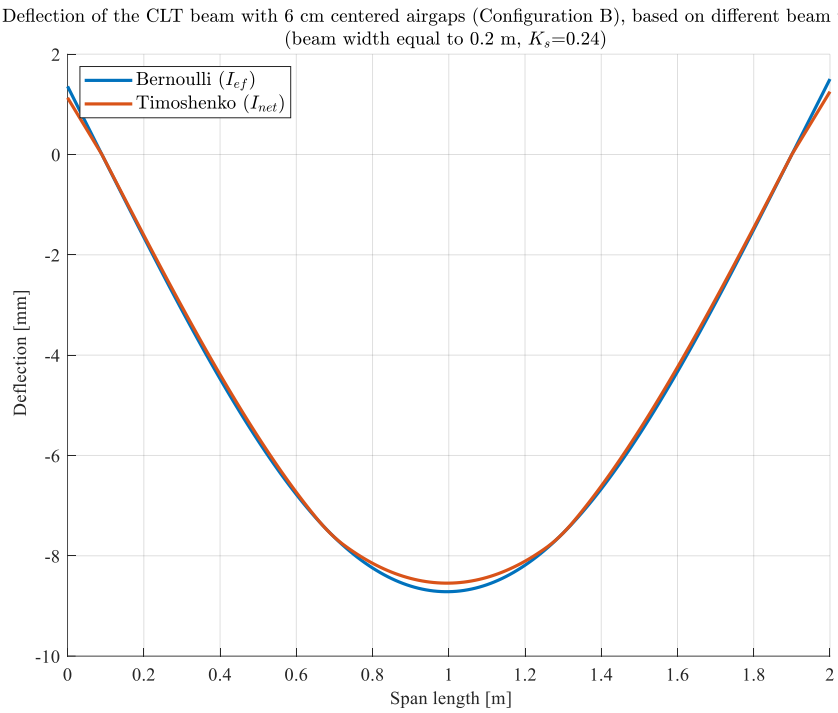

Figure 4-17 Deflection of a CLT panel with air gaps equal to 12 cm (Configuration B) using different beam theories and different methods of applying moment of inertia in a four points bending test for P=5 kN.

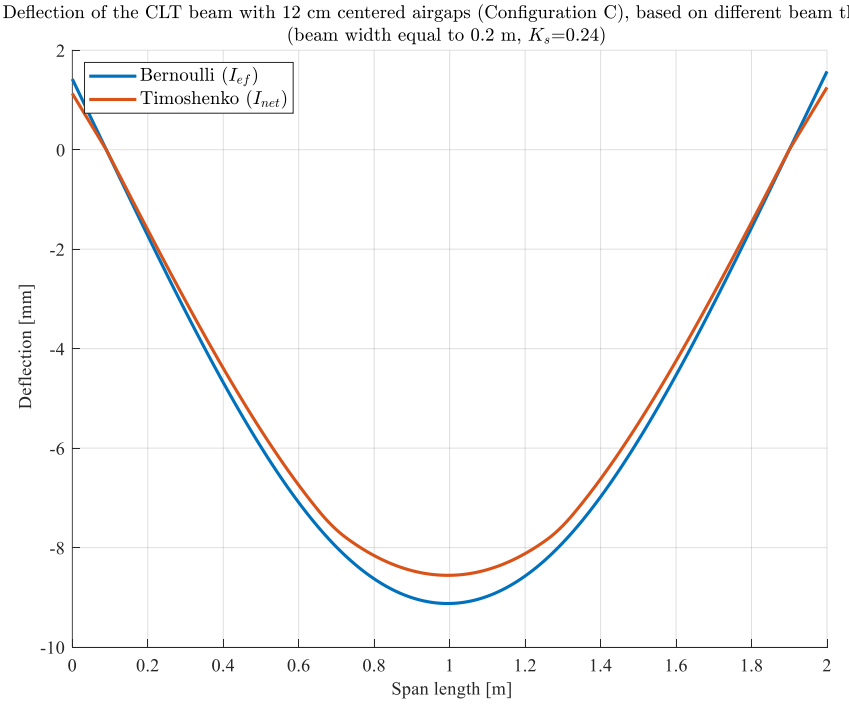

Figure 4-18 Deflection of a CLT panel with air gaps equal to 6 cm (Configuration C) using different beam theories and different methods of applying moment of inertia in four points bending test for P=5 kN.

A study of the effect of the width of CLT panels on beam deflection is also conducted. The figure below shows that the maximum beam deflection is the same for both the Timoshenko theory and the Bernoulli theory when the width of the CLT panel is increased, see Figure 4-19.

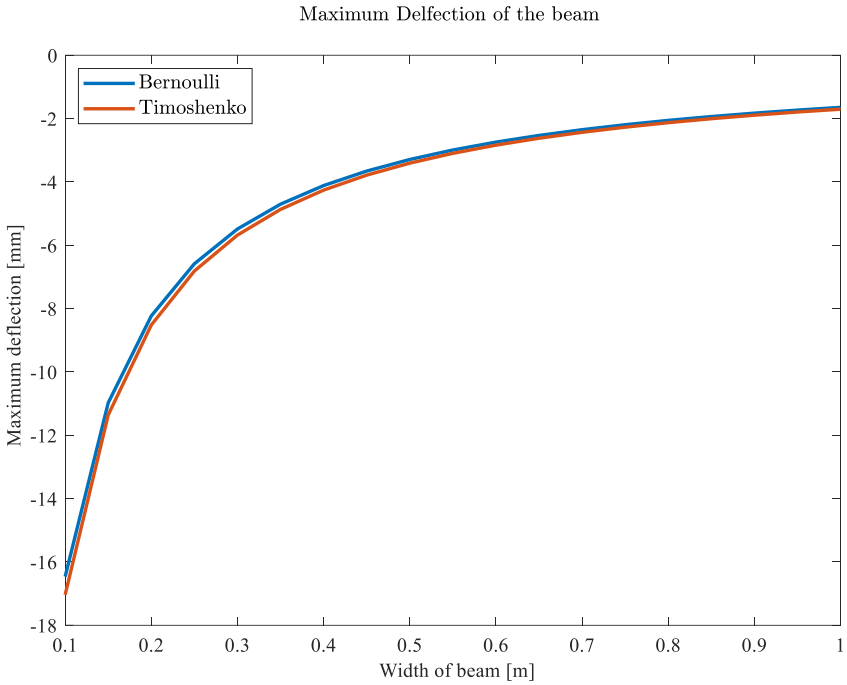

Figure 4-19 Maximum deflection of a beam for different widths, based on the Bernoulli and Timoshenko beam theories.

4.1.10 Deflection calculation by experimental test

Based on the test configuration shown in Figure 2-13, the local and global deflection can be measured by using the LVDT sensors installed in the positions indicated in the Figure Figure 4-20.

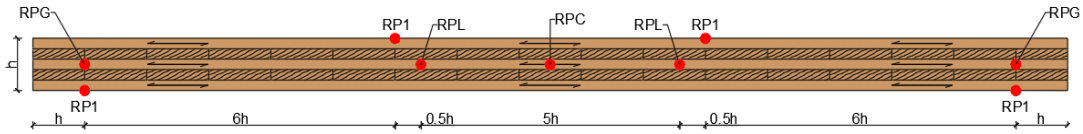

Figure 4-20 Configuration of the four-point bending test setup and the location of sensors for measurement deformation of the beam

The positioned sensors are installed on the beam as it is shown in Figure 4-20, the symbol RPL is for local reference points and RPG for global reference points, and RPC represents the deflection of the center line of the beam.
Based on the assumption of a linear relation between load and deflection between 10% and 40% of the maximum load, the below equations can calculate the global and local deflection:

$$w_{global}(F_{max}) = (w_{RPC}(0.4F_{max}) - w_{RPG}(0.4F_{max})) - (w_{RPC}(0.1F_{max}) - w_{RPG}(0.1F_{max})) \quad (4\text{-}7)$$

$$w_{local}(F_{max}) = (w_{RPC}(0.4F_{max}) - w_{RPL}(0.4F_{max})) - (w_{RPC}(0.1F_{max}) - w_{RPL}(0.1F_{max})) \quad (4\text{-}8)$$

Based on these equations, the local and global stiffness can be calculated based on the equations presented in section 2.4.2.

4.1.11 FEM modelling in ABAQUS

4.1.11.1 Modeling of the elements

A CLT panel's elements are constructed as 3D deformable elements, while the supports and the rollers for applying the load are modeled in 3D, with a solid shape and discrete rigid type. The width of the panel is equal to 200 mm, and the length is equal to 2000 mm. The width of the lamellas for cross-layers is set to 120 mm; to see the dimension of the panels for different configurations, see sections 4.1.3, 4.1.4, and 4.1.5. The supports are modeled as a rigid cylinder with diameters of 70 mm, and the roller for applying the load is modeled as a rigid cylinder with a diameter of 40 mm, see Figure 4-21.

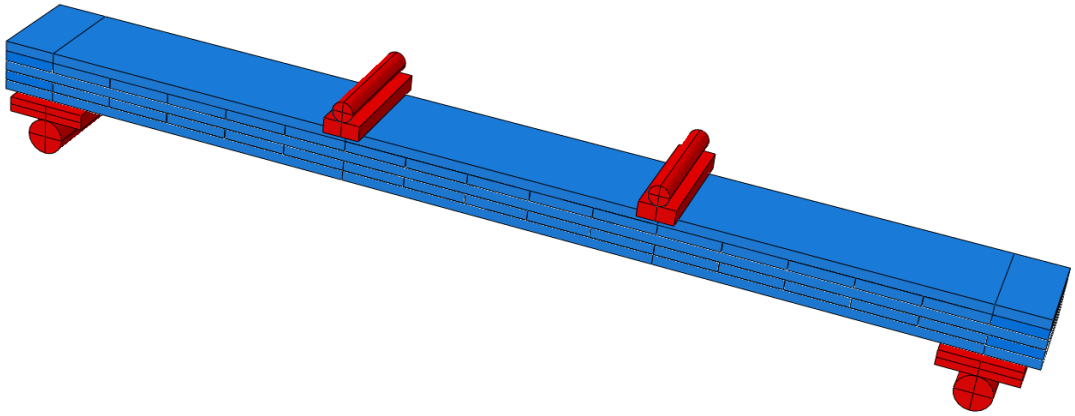

Figure 4-21 Geometry of the beam modeled in ABAQUS (Configuration A).

4.1.11.2 Material properties

C24 boards are used for the production of the CLT panels. The density of the wood is considered 490 kg/m^{3,} and the orthotropic elastic behavior is set for the mechanical properties of CLT panels. The properties of the materials are shown in the table below.

Table 4-5 Material properties of a wood lamellas.

E_1 (MPa)	E_2 (MPa)	E_3 (MPa)	G_{12} (MPa)	G_{13} (MPa)	G_{23} (MPa)	n_{12}	n_{13}	n_{23}
11000	400	400	780	780	78	0.4	0.50	0.51

The stiffness matrix elements are calculated using the equation in section 2.5; the results are presented in the table below.

Table 4-6 Stiffness matrix elements.

D_{1111}	D_{2222}	D_{3333}	D_{1122}	D_{1133}	D_{2233}	D_{1212}	D_{1313}	D_{2323}
11342	552	554	365	392	288	780	780	78

Also, as explained in section 2.1.4, the local coordinate system is used to distinguish the orientation of the cross-layers from longitudinal layers.

4.1.11.3 Interaction

The tie constraints are used for applying the interaction between the cross-layers and the longitudinal layers. For the connection between the rollers in supports

positioned and for applying a load, a type of surface-to-surface contact constraint is used by considering the normal and tangential behavior with a friction coefficient of 0.2, see Figure 4-22

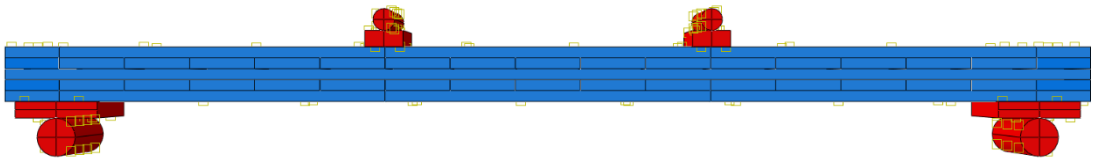

Figure 4-22 Interaction between the support roller and the beam (Configuration A).

4.1.11.4 Boundary conditions

The boundary conditions are applied to the model to represent the four-point testing in the numerical analysis. For supports, the displacements are restricted for the three main directions. At the same time, for the rollers in the positions of applying load, the displacements are limited in all directions except in the direction of the applied load (vertical), see Figure 4-23.

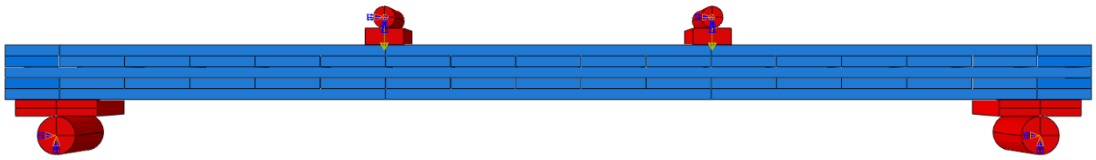

Figure 4-23 Boundary condition applied to the model in ABAQUS (Configuration A).

4.1.11.5 Mesh

The accuracy of the results obtained from an FEA simulation largely depends on the quality of the mesh. A mesh convergence study is important for validating FEA simulations and optimizing the mesh size for a given problem.

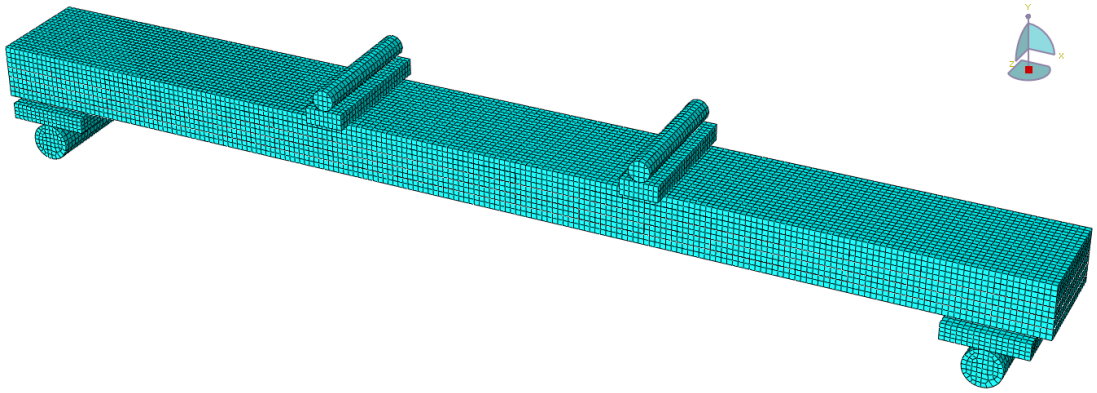

Figure 4-24 Sample of mesh applied to the model in ABAQUS, mesh size 10 mm (Configuration A).

Therefore, the convergence mesh study is done for the four-point bending test.The different mesh size with element type of C3D8R is used for a model, and the maximum deflection of a model is extracted and compared until the difference between results is not significant.

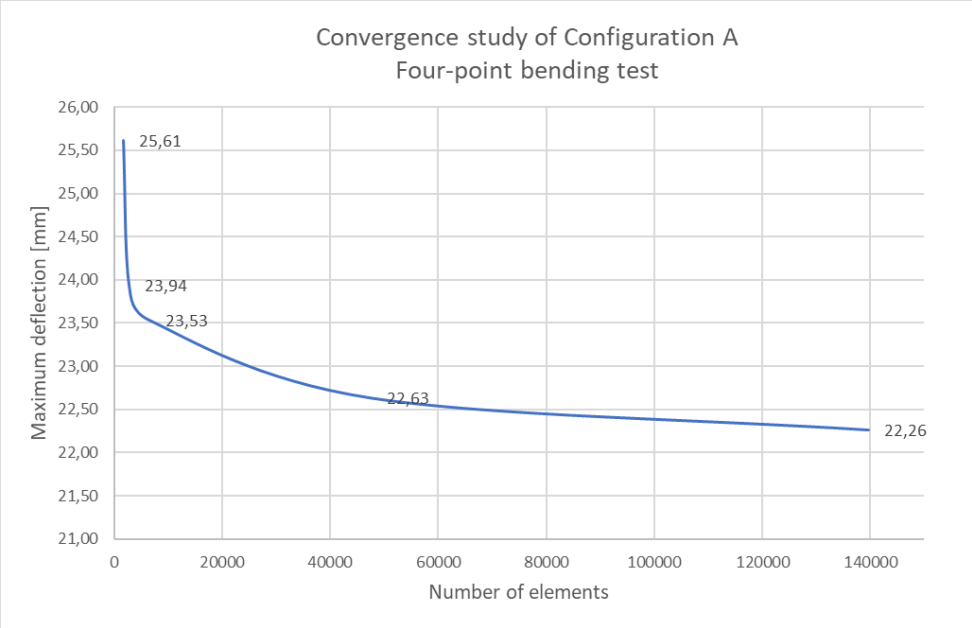

Figure 4-25 Convergence study of CLT panel (Configuration A) in four-point bending test.

As shown in Figure 4-25, the maximum deflection of a CLT beam for a mesh size below 10 mm becomes almost constant; therefore, the mesh size number 10 mm is selected for further analysis and for other configurations, see Figure 4-24. The maximum deflection for each mesh size is presented in Table 4-7.

Table 4-7 The deflection of a CLT beam in Configuration A for different mesh sizes and the number of elements for the load 14 kN.

Mesh size [mm]	Number of elements	Maximum deflection [mm]
40	1758	25.61
30	2794	23.94
20	6574	23.53
10	47636	22.63
7	139684	22.26

4.2 Results

4.2.1 Results from the experiment

4.2.1.1 Configuration A

4.2.1.1.1 Failure modes

The test results and parameters, including the maximum load and displacement, time of failure, and loading rate, are presented in Table 4-8. In addition, the maximum load for the first loading sequence, the minimum load of unloading, and the failure modes are indicated.

Table 4-8 Four-point bending test result's data and failure modes of samples of Configuration A.

No.	Max. failure load [kN]	Max. disp. at failure [mm]	Time of failure [s]	Loading rate [mm/ min]	Max. load at loading [kN]	Min. load at unloading [kN]	Failure mode
1	11.92	19.66	110.5	10	11	2	Finger joint failure
2	16.53	35.56	694	5	10	2.5	Tensile failure
3	16.48	26.9	573.8	5	10	2.5	Tensile failure

The figures below show the detailed test results and the failure modes for samples of Configuration A. A detailed explanation can be found in section 0 together with ARAMIS images.

4.2.1.1.1.1 Sample 1

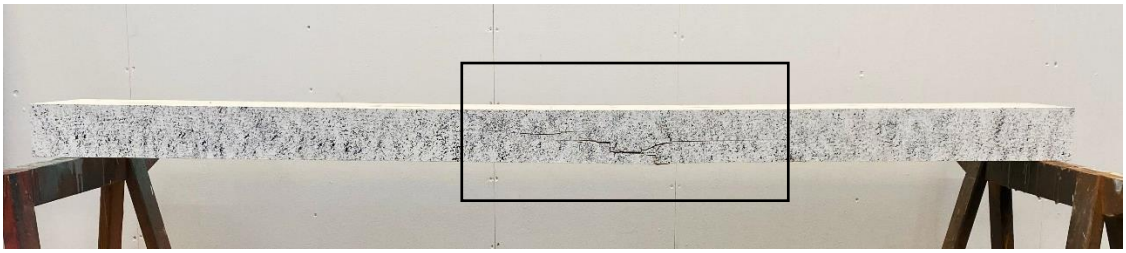

Figure 4-26 Test results and failure mode of Sample 1 of Configuration I. The black rectangle shows the location of the failure.

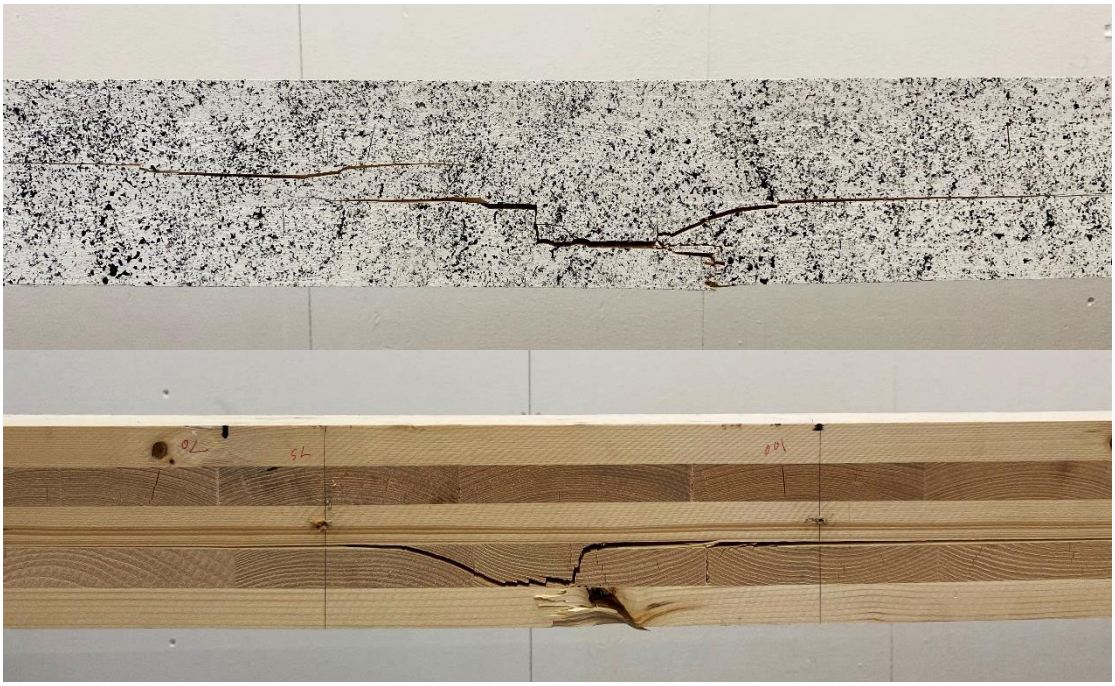

Figure 4-27 Detailed pictures of the failure for Sample 1 of Configuration A. The picture at the top depicts the front side, and the bottom one shows the unpainted backside of the beam.

4.2.1.1.1.2 Sample 2

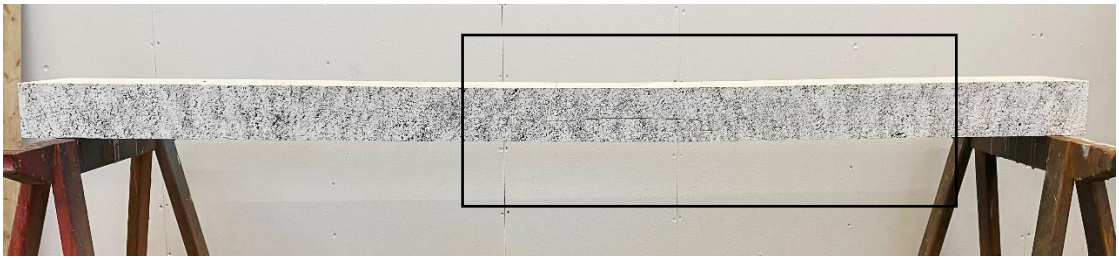

Figure 4-28 Test results and failure mode of Sample 2 of Configuration A. The black rectangle indicates the location of the failure.

Figure 4-29 Detailed pictures of the failure for Sample 2 of Configuration A. The picture at the top depicts the front side and the bottom one shows the unpainted backside of the beam.

4.2.1.1.1.3 Sample 3

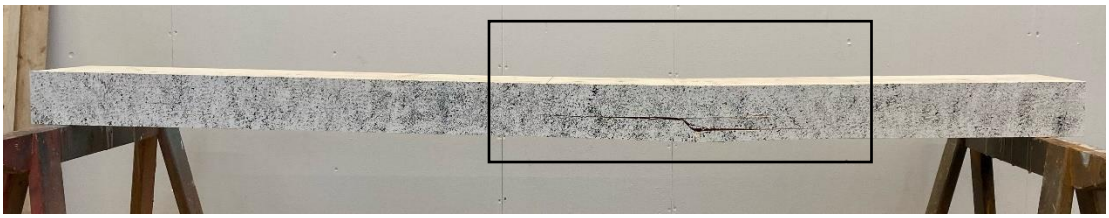

Figure 4-30 Test results and failure mode of Sample 3 of Configuration A. The black rectangle shows the location of the failure.

Figure 4-31 Detailed pictures of the failure for Sample 3 of Configuration A. The picture at the top depicts the front side, and the bottom one shows the unpainted backside of the beam.

4.2.1.1.2 Load deformation curves

Figure 4-32 presents the load-deformation curves for solid CLT panels of Configuration A. The peak load of Sample 1 was the lowest out of all samples and reached 11.92 kN. That probably happened because of the loading rate that was set to 10 mm/min, and it was decided that this value was too high so it was changed to 5 mm/min for the next samples. The maximum failure load of Sample 2 and Sample 3 was equal to 16.53 and 16.48, respectively. The curves of these two samples dramatically fall to about 50% of the maximum load after the peak is reached and slightly climb again. On the other hand, Sample 1 reached the maximum load already at the first stage of loading, and after unloading, it went back to a similar value when the failure occurred. Based on the curves, it can be seen that the failure of all three samples was ductile.

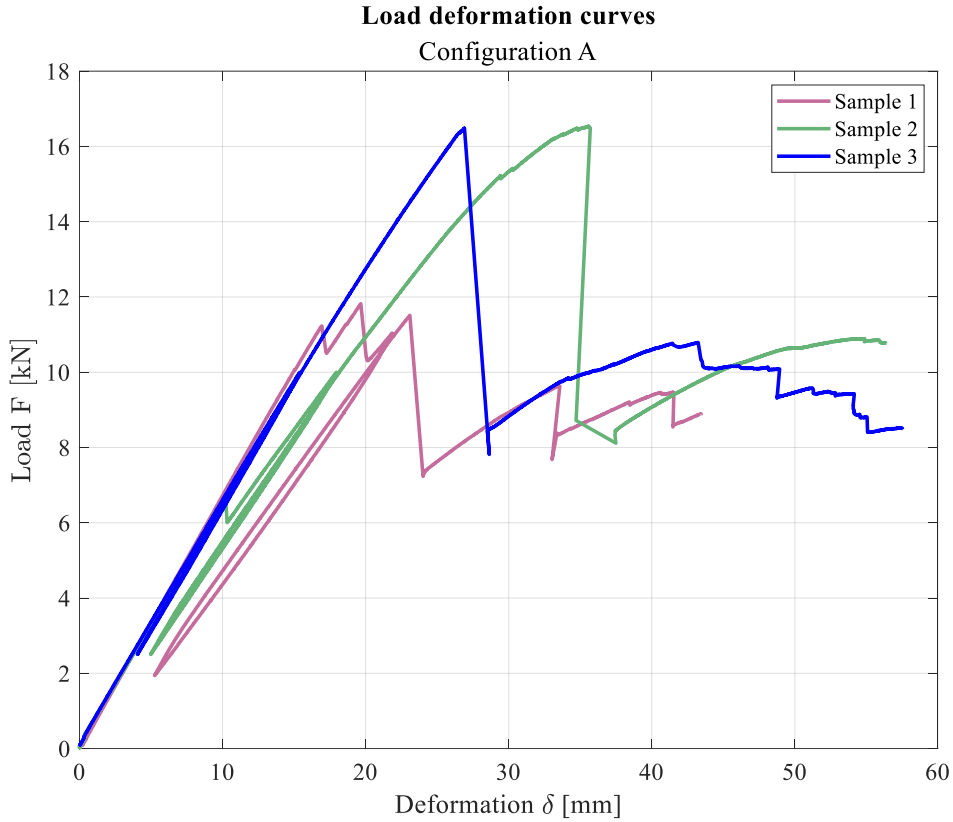

Figure 4-32 Load-deformation curves for the midpoint of the beam, Configuration A.

4.2.1.1.3 Shear strain from ARAMIS software

4.2.1.1.3.1 Sample 1

The strain distribution of Sample 1 of Configuration A is shown in the Figures below. Figure 4-33 shows the strain distribution at the load when the first crack happened in the outermost longitudinal layer at the position of a finger joint; by increasing the load, the crack propagated until the second crack occurred in the cross-layer at time 117 sec, Figure 4-34. Another interesting point is that it can be seen that in the area between the support and applied load position, due to shear force, the higher strain distribution is in the cross-layer in this area, while in the middle part, due to zero shear force, the strain is negligible.

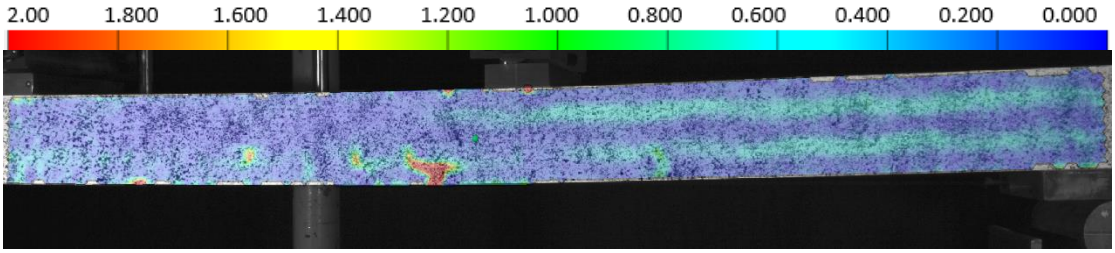

Figure 4-33 The strain distribution of Sample 1 at time 104 s and the load 10.98 kN [ARAMIS data, Configuration A].

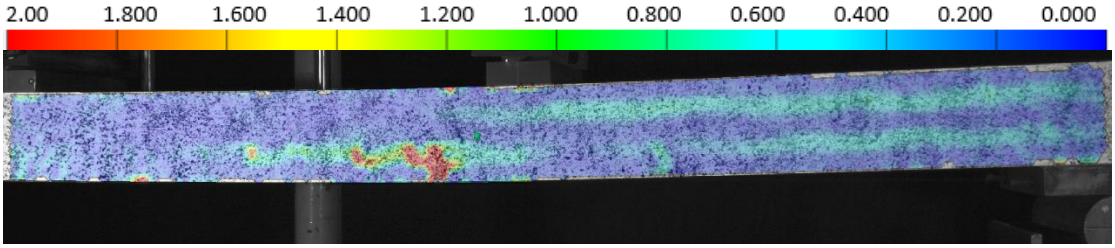

Figure 4-34 The strain distribution of Sample 1 at time 117 s and the load 11.73 kN [ARAMIS data, Configuration A].

Figure 4-35 shows the strain distribution of the beam before starting unloading; it can be seen that the more areas of wood around the main crack position had higher strain values.

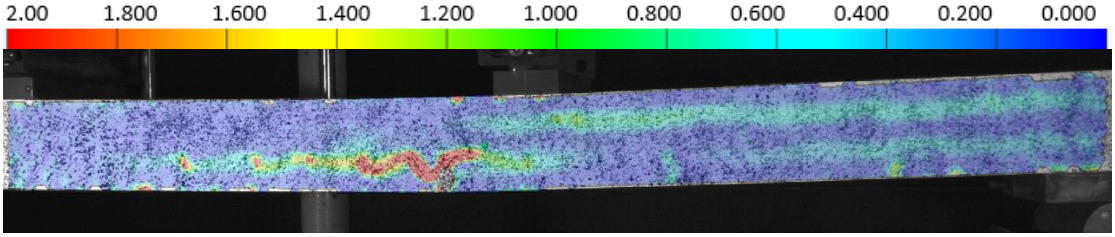

Figure 4-35 The strain distribution of Sample 1 at time 126 s and the load 10.95 kN [ARAMIS data, Configuration A].

After unloading and loading the beam, the cracks propagated in the cross layers with lower shear strength until the beam failed at a load of almost 22 kN. The failure mode was brittle at this moment, and the beam lost nearly half its strength.

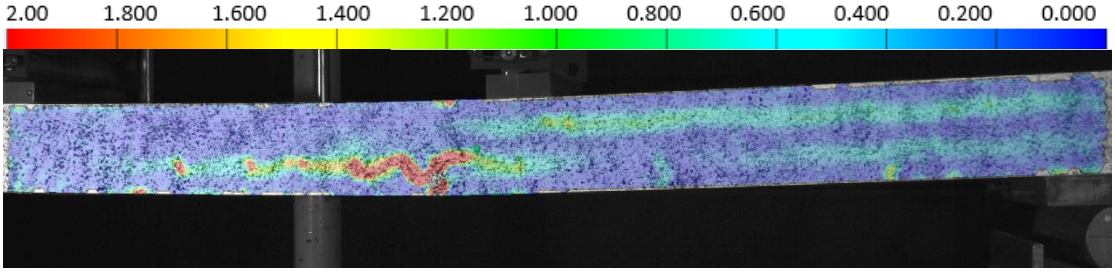

Figure 4-36 The strain distribution of Sample 1 at time 312 s and the load 11.39 kN [ARAMIS data, Configuration A].

Figure 4-37 is shown the shape of the beam before stopping the test. The failure of a finger joint in the outermost longitudinal layer is evident in this picture and after the failure of the cross-layer due to rolling shear stress.

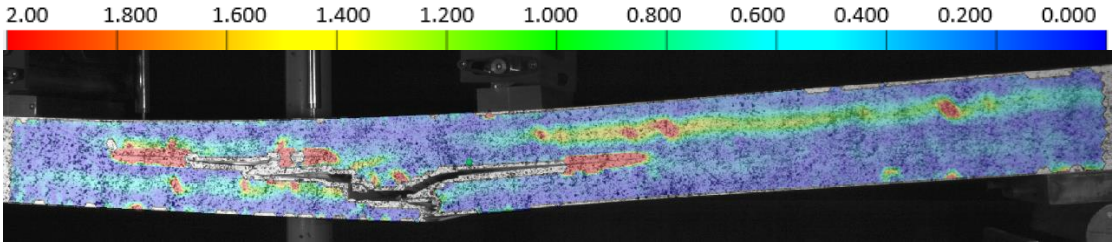

Figure 4-37 The strain distribution of Sample 1 at time 430 s and the load 8.72 kN [ARAMIS data, Configuration A].

4.2.1.1.3.2 Sample 2

For sample 2, the unloading and reloading cycle was controlled by force instead of displacement, and it was set to 10 kN for the unloading point and 2.5 kN for the reloading. Figure 4-38 is shown the strain distribution before the failure. It can be seen that the outermost longitudinal layer was supposed to have the higher strain, and it failed.

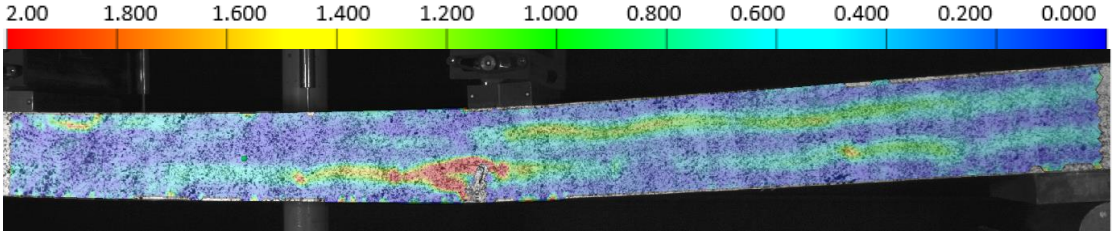

Figure 4-38 The strain distribution of Sample 2 at time 694 s and the load 16.5 kN [ARAMIS data, Configuration A].

Figure 4-39 is shown the beam after the failure; the failure mode was brittle in his case. By comparing Figure 4-38 and Figure 4-39, it can be seen that the crack started from the outermost layer and propagated through the bottom cross-layer due to rolling shear failure, and then the interface between the cross-layer and middle longitudinal layer failed.

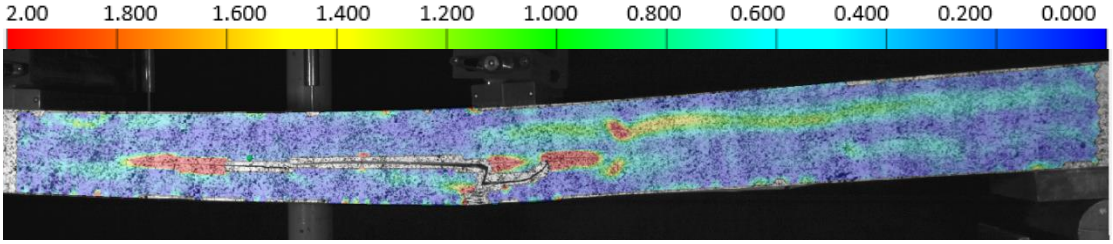

Figure 4-39 The strain distribution of Sample 2 at time 701 s and the load 8.45 kN [ARAMIS data, Configuration A].

4.2.1.1.3.3 Sample 3

The stain distribution for Sample 3 of Configuration A is shown in Figure 4-40. The area with high strains is marked with a red circle in the figure. By looking at Figure 4-31 from section0 4.2.1.3.3.3, there is a knot in the position of the right circle that leads to stress concentration at this point and, finally, failure of the beam at this point.

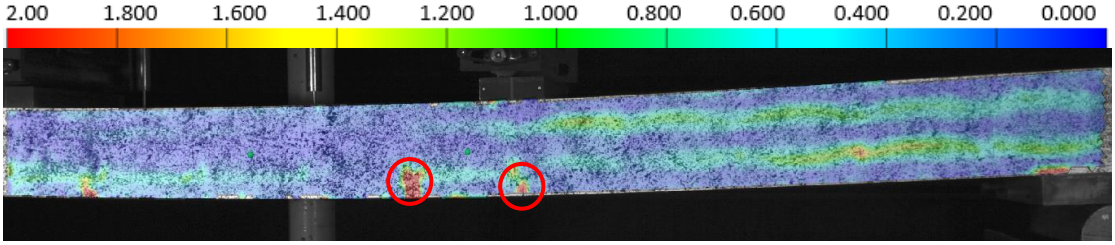

Figure 4-40 The strain distribution of Sample 3 at time 576 s and the load 16.4 kN [ARAMIS data, Configuration A].

Figure 4-41 shows the strain distribution after the crack and the crack pattern due to the failure of the beam. As a result of the crack propagating through the beam, the cross-layer failed due to rolling shear after the failure of the outermost longitudinal layer.

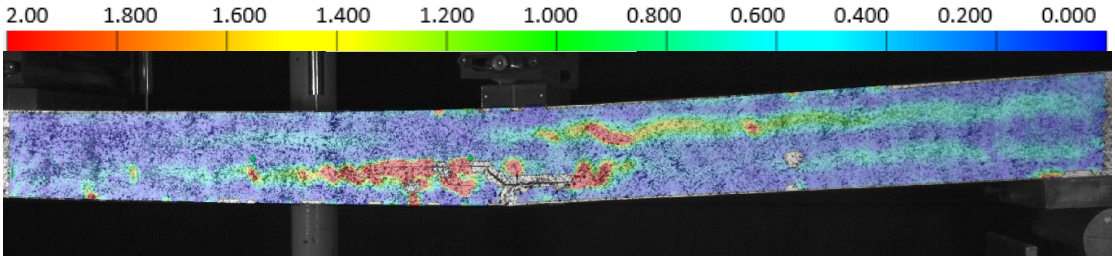

Figure 4-41 The strain distribution of Sample 3 at time 581 s and the load 8.92 kN [ARAMIS data, Configuration A].

4.2.1.1.4 Stiffness

Table 4-9 presents the calculated experimental end theoretical values of bending stiffness based on section 2.4.2.

Table 4-9 Summary of comparison of bending stiffness of Configuration A calculated based on different methods.

Specimen	Global stiffness [*10^10 Nmm2]			Local stiffness [*10^10 Nmm2]	Theory stiffness [*10^10 Nmm2]	
	$EI_{Bernoulli}$	$EI_{Timoshenko}$	EI_{EN408}	$EI_{local,EN789}$	EI_{eff}	EI_{net}
1	14.02	16.92	14.47	16.25	12.45	14.52
2	11.34	13.17	11.64	16.01		
3	13.38	16	13.8	19.6		

Figure 4-42 shows the graphic representation of the data. It can be seen that the local bending stiffness gives higher values than the ones calculated based on theoretical equations (marked as green and purple dash lines) for all three samples. The local bending stiffness might be higher because the formula is dependent only on bending and does not include the effect of shear. Furthermore, the local stiffness is calculated based on the local deflection, and the magnitude of it is not as high as the magnitude of the global deflection. Additionally, for all three samples, global bending stiffnesses calculated based on Bernoulli theory and EN408 standard give very similar values, and for Sample 1 they are closer to

theoretical net stiffness, but for Sample 2 they are closer to effective stiffness. For Sample 3 these stiffnesses are in the range between EI_{eff} and EI_{net}. For all three samples, the stiffness calculated based on the Timoshenko method gives the highest values from global bending stiffnesses.

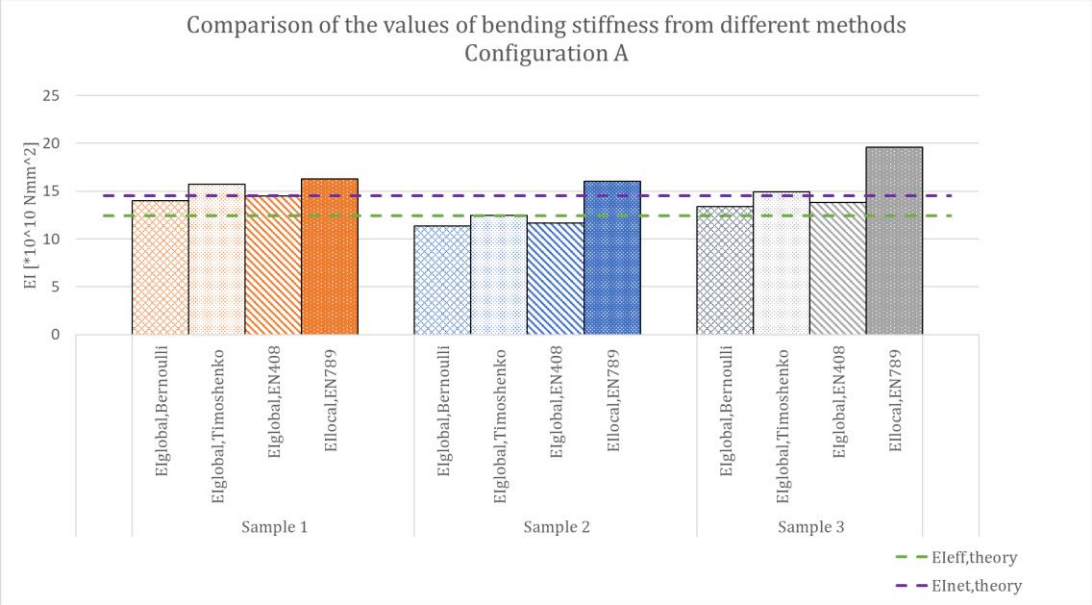

Figure 4-42 Comparison of the different bending stiffness values calculated based on different methods.

4.2.1.2 Configuration B

4.2.1.2.1 Failure modes

The test results and parameters, including the maximum load and displacement, time of the failure, and loading rate of the samples of Configuration B are presented in Table 4-10. In addition, the maximum load for the first loading sequence, the minimum load of unloading, and the failure modes are indicated.

Table 4-10 Four-point bending test results data and failure modes of samples of Configuration B.

No.	Max. failure load [kN]	Max. disp. at failure [mm]	Time of failure [s]	Loading rate [mm/min]	Max. load at loading [kN]	Min. load at unloading [kN]	Failure mode
1	16.76	30.19	532.6	5	8	2	Shear failure
2	17.16	30.73	549.8	5	8	2	Shear failure
3	14.9	37.11	668.6	5	8	2	Tensile failure

The figures below show the detailed test results and the failure modes for samples of Configuration B. A detailed explanation can be found in section 4.2.1.2.3, together with ARAMIS images.

4.2.1.2.1.1 Sample 1

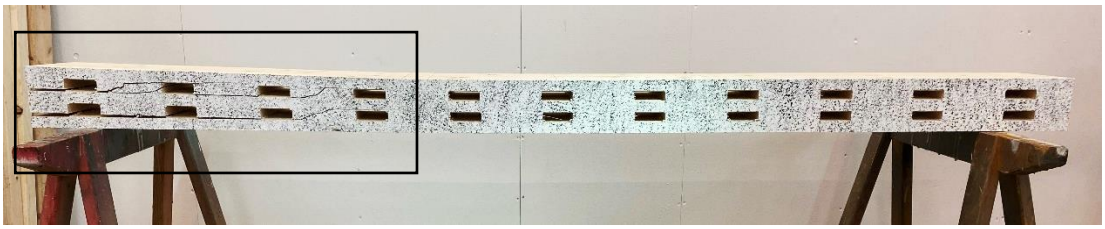

Figure 4-43 Test results and failure mode of Sample 1 of Configuration B. The black rectangle shows the location of the failure.

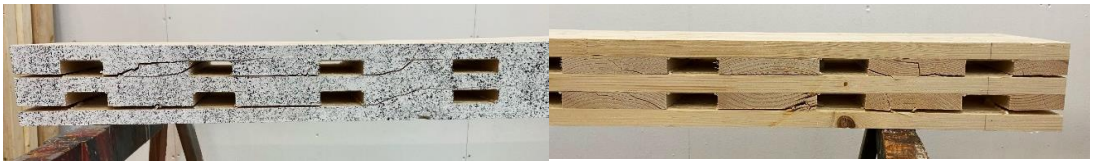

Figure 4-44 Detailed pictures of the failure for Sample 1 of Configuration B. The picture at the top depicts the front side and the bottom one shows the unpainted backside of the beam.

4.2.1.2.1.2 Sample 2

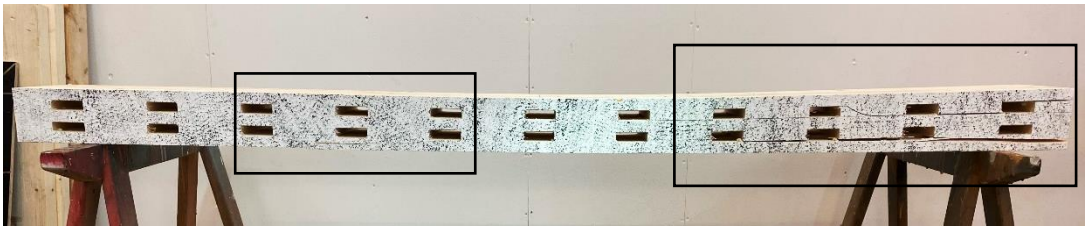

Figure 4-45 Test results and failure mode of Sample 2 of Configuration B. The black rectangles present the locations of the cracks and the failure.

Figure 4-46 Detailed pictures of the failure for Sample 2 of Configuration B. The picture at the left depicts the front side and the right one shows the unpainted backside of the beam.

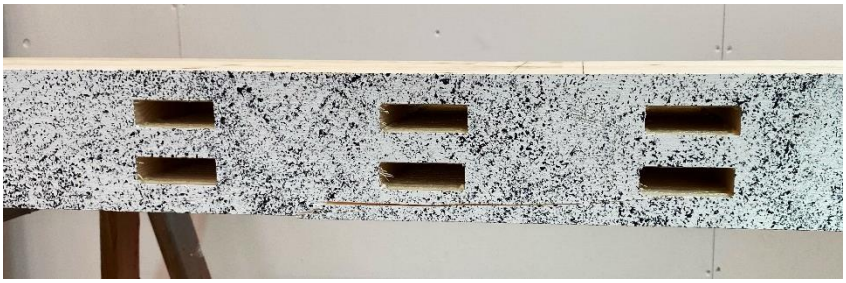

Figure 4-47 Detailed picture of the crack of Sample 2, Configuration B.

4.2.1.2.1.3 Sample 3

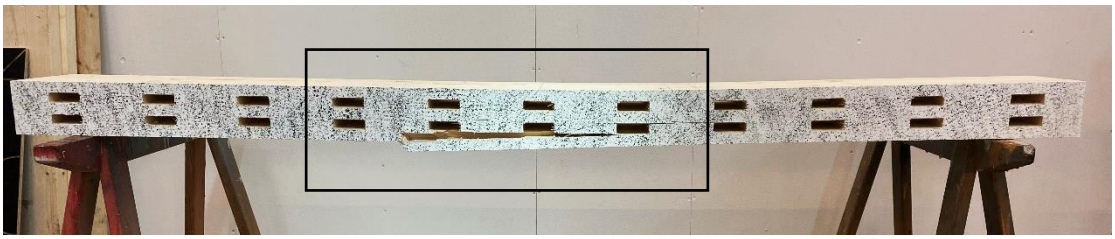

Figure 4-48 Test results and failure mode of Sample 3 of Configuration B. The black rectangle marks the location of the failure.

Figure 4-49 Detailed pictures of the failure for Sample 3 of Configuration B. The picture at the left depicts the front side and the right one shows the unpainted backside of the beam.

4.2.1.2.2 Load deformation curves

Figure 4-50 shows the load-deformation curves for samples of Configuration B for the four-point bending test. The highest value of the maximum failure load was reached by Sample 2, and it is equal to 17.16 kN. The failure load of Sample 1 was lower, and it was 16.76 kN. The curves fluctuated after reaching the failure load before a sharp decrease, so both failures were ductile. On the other hand, the failure of Sample 3 was brittle because the curve fell dramatically after reaching the maximum load of 14.9 kN.

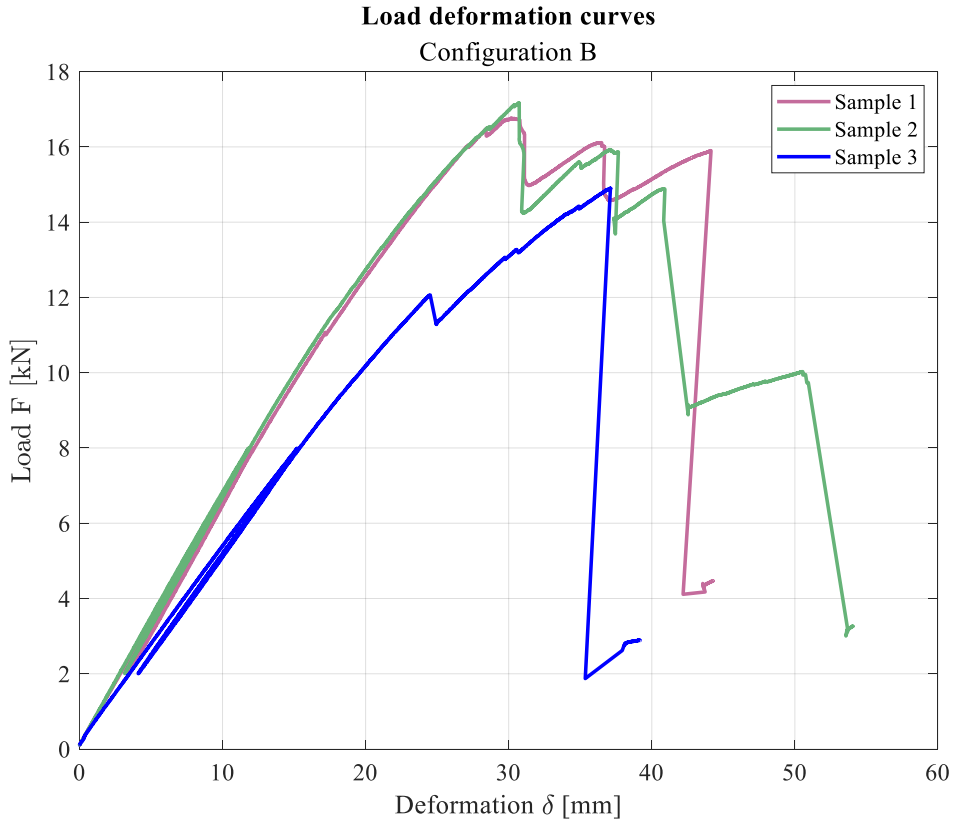

Figure 4-50 Load-deformation curves for the midpoint of the beam, Configuration B.

4.2.1.2.3 Shear strain from ARAMIS software

4.2.1.2.3.1 Sample 1

The strain distribution of Sample 1 of Configuration B for the failure is shown in Figure 4-51. As can be seen, the cross-layers were exposed to a higher strain compared to the longitudinal ones.

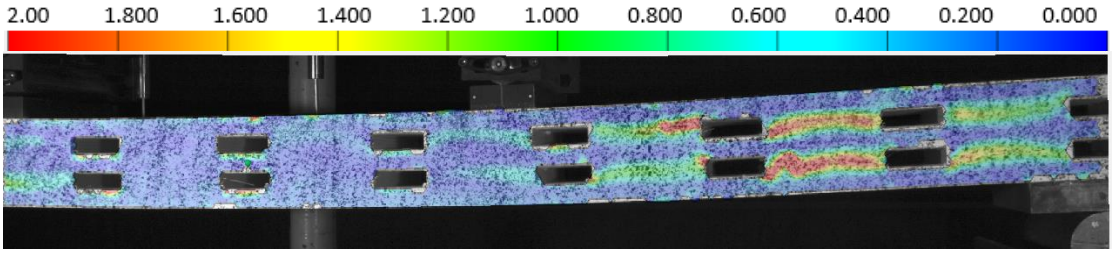

Figure 4-51 The strain distribution of Sample 1 at time 535 s and the load 16.65 kN [ARAMIS data, Configuration B].

For this sample, the failure happened on the left side, which was not covered by the DIC system. The area of the failure is marked by a circle in Figure 4-52. For more detail, see section 4.2.1.1.1.

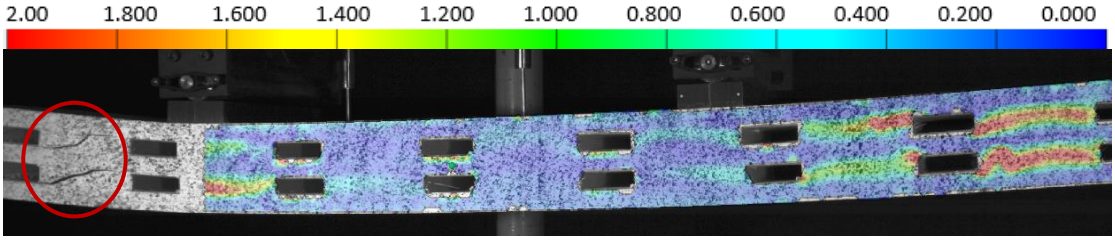

Figure 4-52 The strain distribution of Sample 1 at time 691 s and the load 15.73 kN [ARAMIS data, Configuration B].

4.2.1.2.3.2 Sample 2

The strain distribution of Sample 2 of Configuration B at failure load is shown in the figure below. As can be seen, the highest strain happened in the cross-layers due to the air gaps that let the cross-layer move between the longitudinal layers.

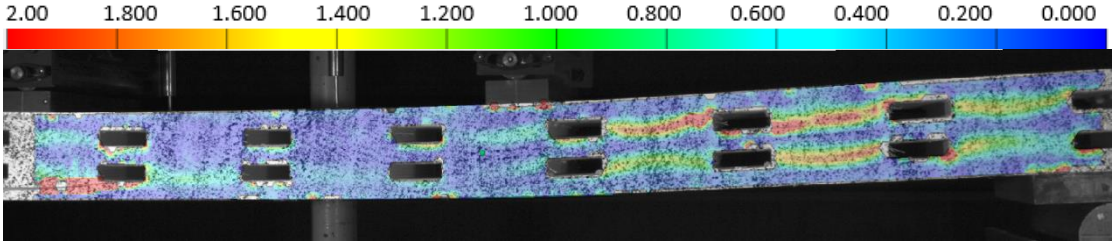

Figure 4-53 The strain distribution of Sample 2 at time 551 s and the load 17.08 kN [ARAMIS data, Configuration B].

The failure happened in the cross-layer due to rolling shear failure, and the failure mode was ductile. The location of the first crack is marked in Figure 4-54.

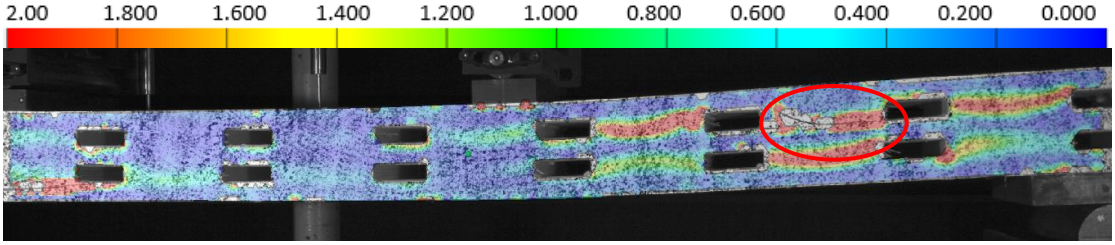

Figure 4-54 The strain distribution of Sample 2 at time 557 s and the load 15.82 kN [ARAMIS data, Configuration B].

Eventually, the cross layers collapsed due to increased load over time. Figure 4-55 shows how the crack propagated through the interface between the cross-layers and the middle longitudinal layer.

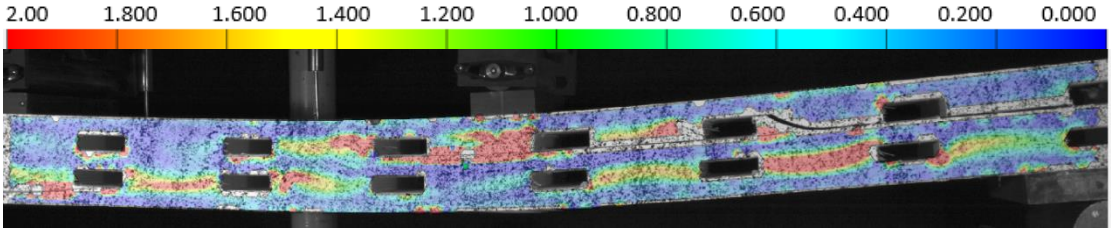

Figure 4-55 The strain distribution of Sample 2 at time 680 s and the load 9.10 kN [ARAMIS data, Configuration B].

4.2.1.2.3.3 Sample 3

The stain distribution of Sample 3 is presented in Figure 4-56. Before the failure, the highest train occurred in the cross-layers as a result of the air gaps between them.

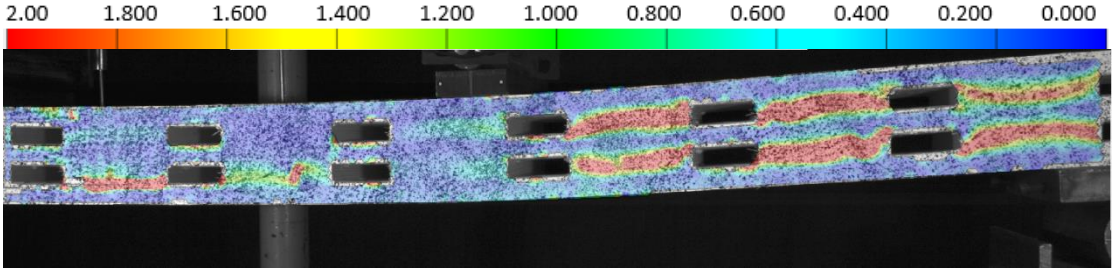

Figure 4-56 The strain distribution of Sample 2 at time 663 s and the load 14.79 kN [ARAMIS data, Configuration B].

Figure 4-57 illustrates the failure mode for this sample, which was brittle due to the failure of the outermost longitudinal layer in tension in the middle part of the beam.

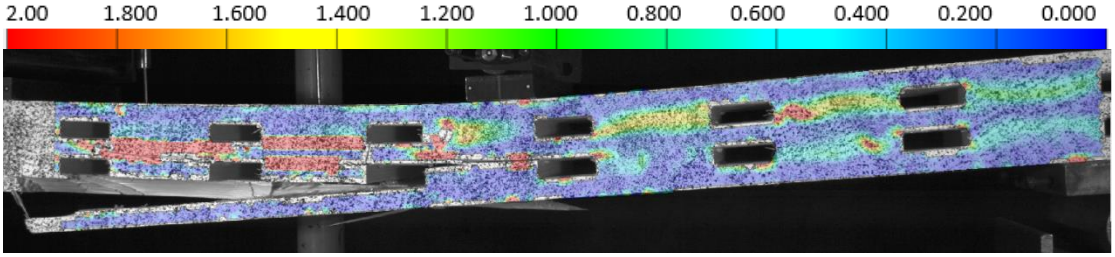

Figure 4-57 The strain distribution of Sample 2 at time 665 s and the load 2.67 kN [ARAMIS data, Configuration B].

4.2.1.2.4 Stiffness

Table 4-11 Summary of comparison of bending stiffness of Configuration B calculated based on different methods.

Specimen	Global stiffness [*10^10 Nmm2]			Local stiffness [*10^10 Nmm2]	Theory stiffness [*10^10 Nmm2]	
	$EI_{Bernoulli}$	$EI_{Timoshenko}$	EI_{EN408}	$EI_{local,EN789}$	EI_{eff}	EI_{net}
1	13.54	15.12	13.96	17.57	11.63	14.52
2	13.88	15.56	14.33	21.34		
3	10.76	11.73	11.02	14.35		

Table 4-11 shows the calculated values of bending stiffness based on experimental data and theoretical values - EI_{eff} and EI_{net}. The results are plotted in the graph below, Figure 4-58. The pattern is very similar to the one for Configuration A. The local bending stiffness is the highest for Samples 1 and 2 and it is higher than three other global stiffnesses for Sample 3. The bending stiffness calculated based on Bernoulli theory and EN408 standard give similar values, and they almost reach EI_{net}. Global bending stiffness based on the Timoshenko method is the highest of all global stiffnesses for all samples. For Sample 3 all global bending stiffnesses are closer to EI_{eff}.

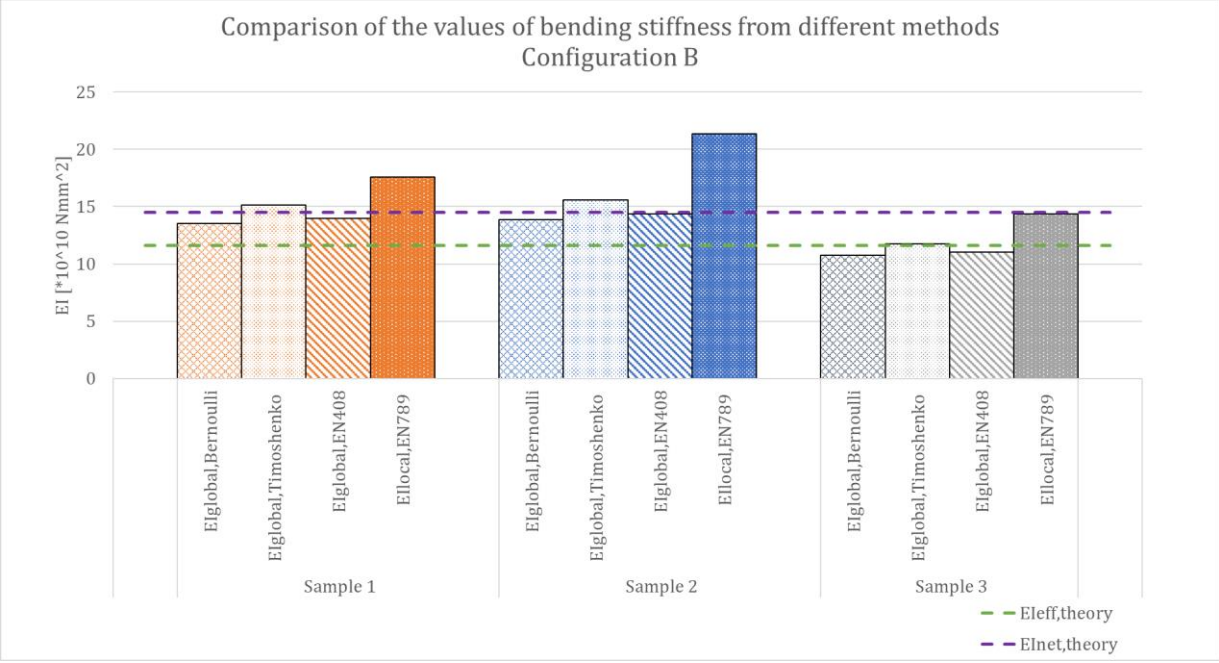

Figure 4-58 Comparison of the different bending stiffness values calculated based on different methods for Configuration B.

4.2.1.3 Configuration C

4.2.1.3.1 Failure modes

The test results and parameters, including the maximum load and displacement, time of the failure, and loading rate of the samples of Configuration C are presented in Table 4-12. In addition, the maximum load for the first loading sequence, the minimum load of unloading, and the failure modes are indicated.

Table 4-12 Four-point bending test results data and failure modes of samples of Configuration C.

No.	Max. failure load [kN]	Max. disp. at failure [mm]	Time of failure [s]	Loading rate [mm/min]	Max. load at loading [kN]	Min. load at unloading [kN]	Failure mode
1	11.57	29.58	606.01	5	7	1	Tensile failure
2	12.7	30.85	635.25	5	7	1	Tensile failure
3	11.87	33.04	664.26	5	7	1	Shear failure

The figures below show the detailed test results and the failure modes for samples of Configuration C. A detailed explanation can be found in section 4.2.1.3.3 together with ARAMIS images.

4.2.1.3.1.1 Sample 1

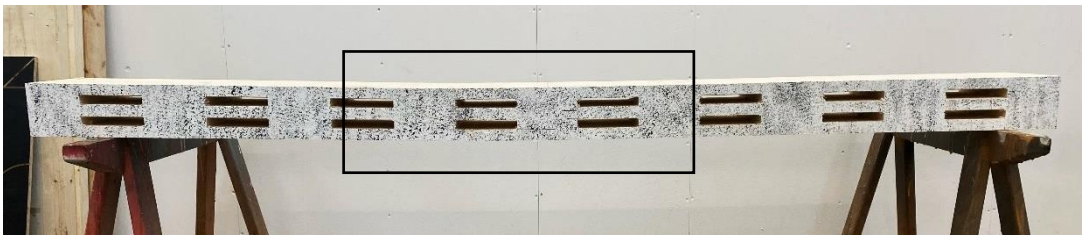

Figure 4-59 Test results and failure mode of Sample 1 of Configuration C. The black rectangle shows the location of the failure.

Figure 4-60 Detailed pictures of the failure for Sample 1 of Configuration C. The picture at the top depicts the front side and the bottom one shows the unpainted backside of the beam.

Figure 4-61 Tensile failure at the bottom of Sample 1.

4.2.1.3.1.2 Sample 2

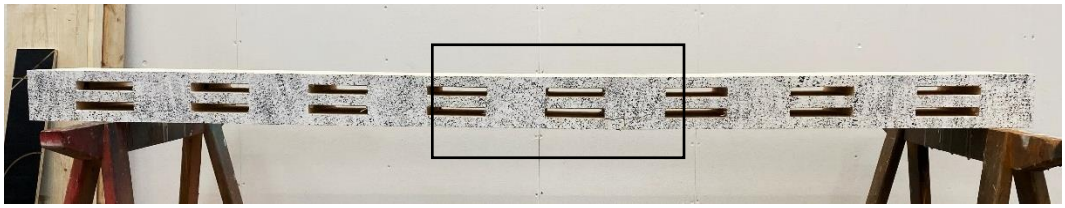

Figure 4-62 Test results and failure mode of Sample 2 of Configuration C. The black rectangle presents the location of the failure.

Figure 4-63 Detailed pictures of the failure for Sample 2 of Configuration C. The picture at the left depicts the front side and the right one shows the unpainted backside of the beam.

Figure 4-64 Tensile failure at the bottom of the Sample 2.

4.2.1.3.1.3 Sample 3

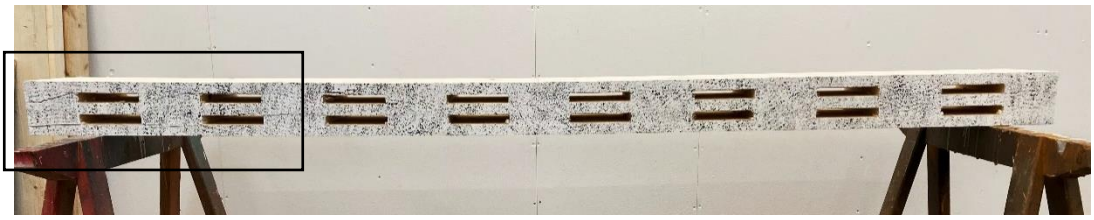

Figure 4-65 Test results and failure mode of Sample 3 of Configuration C. The black rectangle marks the location of the failure.

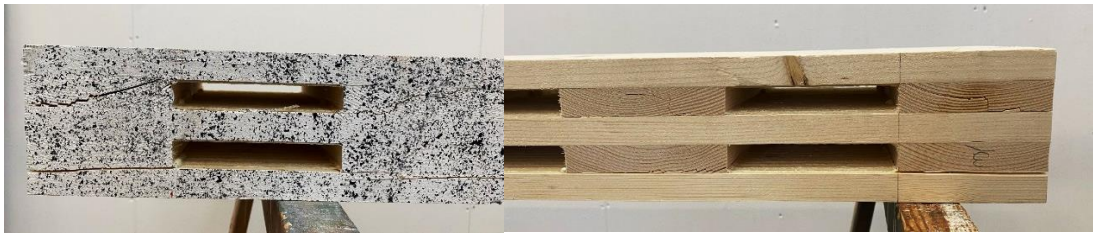

Figure 4-66 Detailed pictures of the failure for Sample 3 of Configuration C. The picture at the left depicts the front side and the right one shows the unpainted backside of the beam.

4.2.1.3.2 Load deformation curves

The load-deformation curves four-point bending test for Configuration C is presented in the graph below, Figure 4-67. The maximum failure load is reached by Sample 2, and it is 12.7 kN. The failure load of Sample 1 and Sample 3 is 11.57 kN and 11.87 kN, respectively. After reaching the failure load, the curves drop dramatically, but the failure of Sample 2 is more ductile.

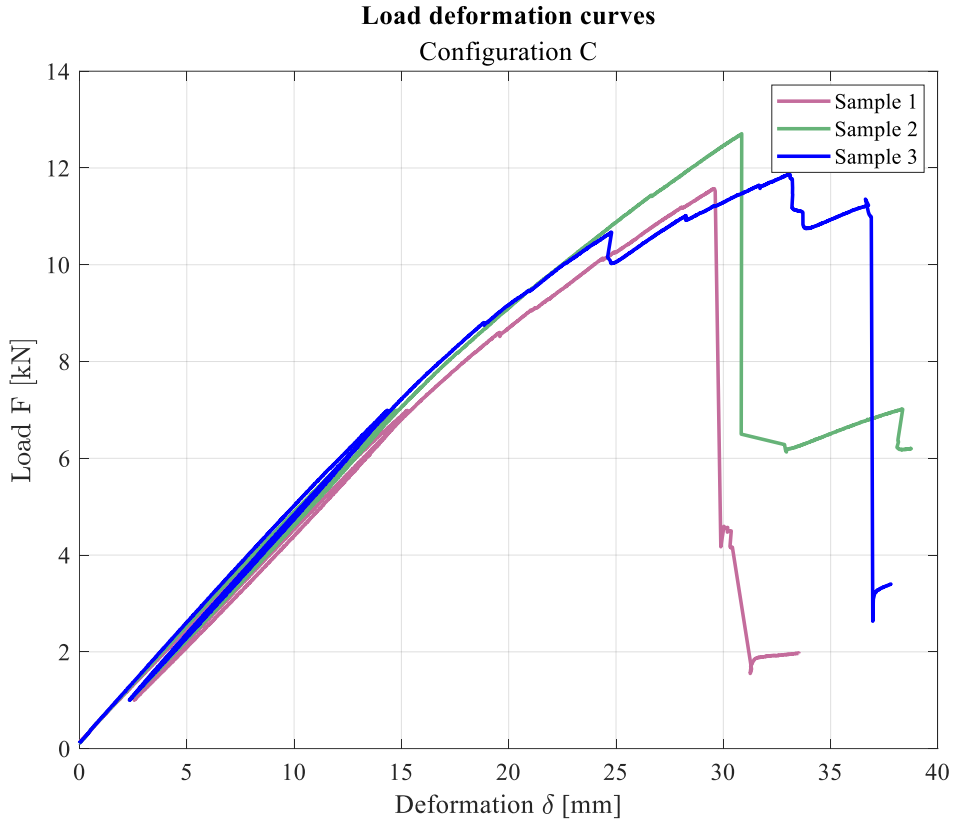

Figure 4-67 Load-deformation curves for the midpoint of the beam, Configuration C.

4.2.1.3.3 Shear strain from ARAMIS software

4.2.1.3.3.1 Sample 1

The strain distribution over the specimen for Sample 1 of Configuration C is shown in the below figure, Figure 4-68. In contrast to longitudinal layers, cross-layers are subjected to higher strain due to air gaps that provide less restriction for cross-layer movement.

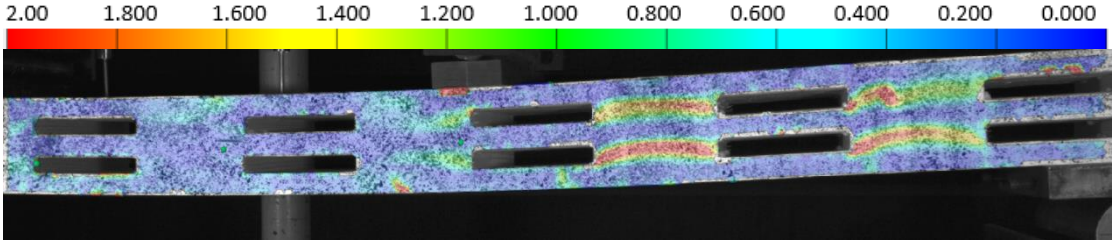

Figure 4-68 The strain distribution of Sample 1 at time 603 s and the load 11.33 kN [ARAMIS data, Configuration C].

Figure 4-61 of Sample 1 in section 4.2.1.3.1.1 shows three big knots at the bottom outermost layer, which cause stress concentrations in this area. At the middle of the beam, the outermost longitudinal layer failed, followed by the cross-layer.

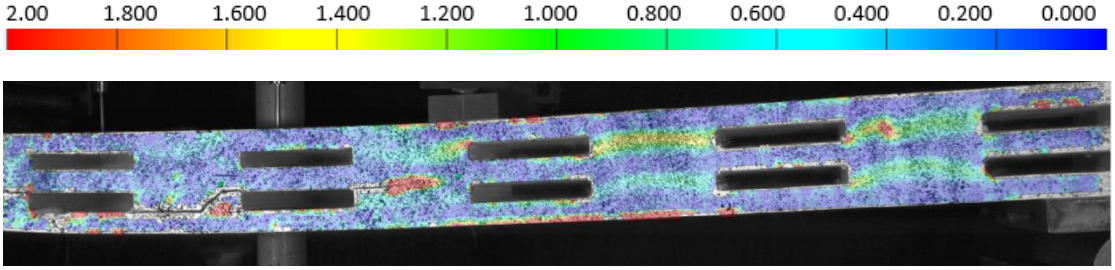

Figure 4-69 The strain distribution of Sample 1 at time 608 s and the load 7.13 kN [ARAMIS data, Configuration C].

4.2.1.3.3.2 Sample 2

Figure 4-70 presents the strain distribution of Sample 2 of Configuration C before the failure. It can be seen that the strain in the cross-layers is higher. Furthermore, there is a higher strain in the outermost longitudinal layer as well. A reason for this can be found in the Figures of Sample 2, see Figure 4-64, in section 4.2.1.3.1.2, which shows three knots in that region causing stress concentration.

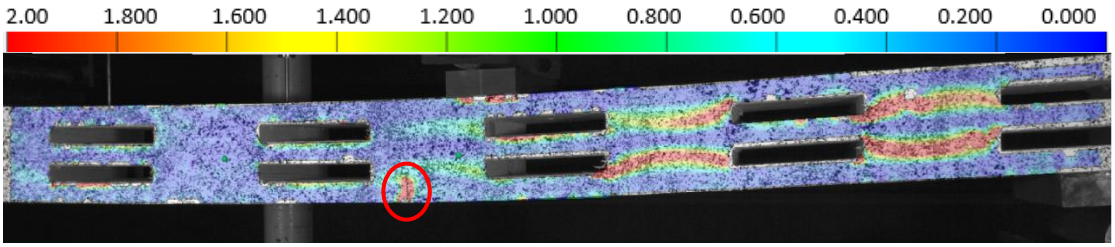

Figure 4-70 The strain distribution of Sample 2 at time 637 s and the load 12.65 kN [ARAMIS data, Configuration C].

Due to the reason mentioned above, the failure happened in the outermost longitudinal layer; see Figure 4-71.

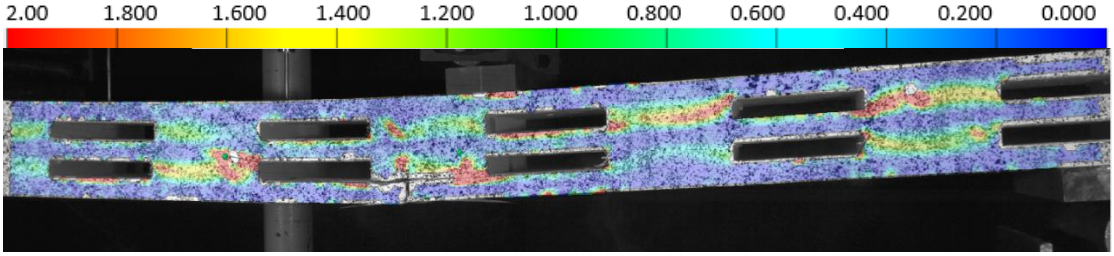

Figure 4-71 The strain distribution of Sample 2 at time 639 s and the load 6.12 kN [ARAMIS data, Configuration C].

Increasing the load propagated the crack to the cross-layer, increasing the beam strength to 12.77 kN, however, as the cross-layers have a lower strength, the cross-layer also failed at that area also in another region marked in Figure 4-72.

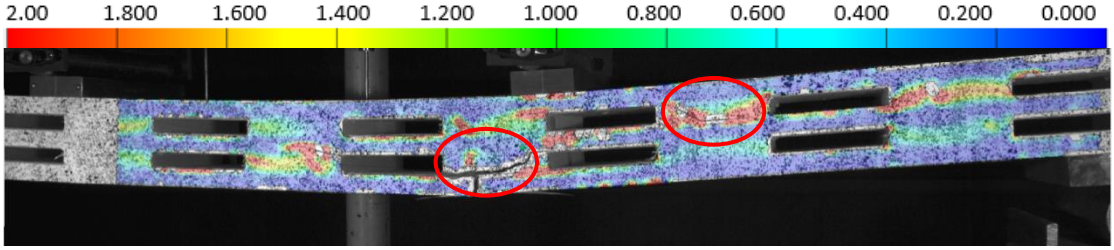

Figure 4-72 The strain distribution of Sample 2 at time 694 s and the load 6.39 kN [ARAMIS data, Configuration C].

4.2.1.3.3.3 Sample 3

Figure 4-73 shows the strain distribution of Sample 3 of Configuration C before the maximum failure load. As a result of air gaps between the cross layers, the stain in these layers is higher compared to the longitudinal ones.

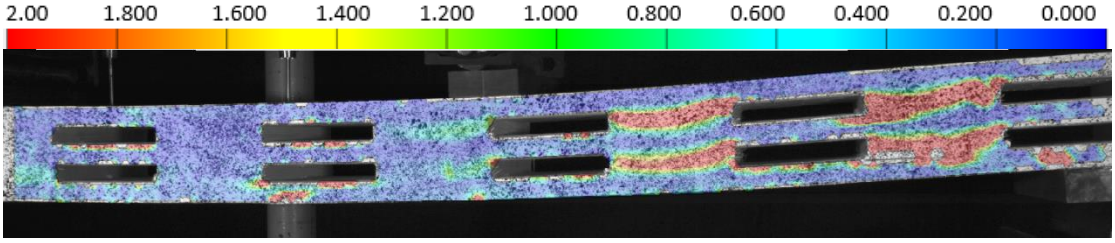

Figure 4-73 The strain distribution of Sample 3 at time 666 s and the load 6.39 kN [ARAMIS data, Configuration C].

This sample failed on the left side, which was not covered by the DIC system. The failure occurred in a cross-layer with ductile behavior, and it was caused by rolling shear failure.

4.2.1.3.4 Stiffness

Table 4-13 Summary of comparison of bending stiffness of Configuration C calculated based on different methods.

Specimen	Global stiffness [*10^10 Nmm2]			Local stiffness [*10^10 Nmm2]	Theory stiffness [*10^10 Nmm2]	
	$EI_{Bernoulli}$	$EI_{Timoshenko}$	EI_{EN408}	$EI_{local,EN789}$	EI_{eff}	EI_{net}
1	9.51	10.27	9.72	11.98	11.02	14.52
2	9.79	10.6	10.01	14.51		
3	10.11	10.97	10.34	15.42		

(2-27) shows the calculated experimental end theoretical values of bending stiffness based on section 2.4.2. Figure 4-74 shows the graphic representation of the data. It can be seen that the local bending stiffness gives the highest values of bending stiffness. However, the formula takes only local deflection, which is lower than the global, and the formula does not include the effect of shear. Additionally, for all three samples, global bending stiffnesses calculated based on other methods give very similar values, and they are a bit lower than theoretical effective bending stiffness.

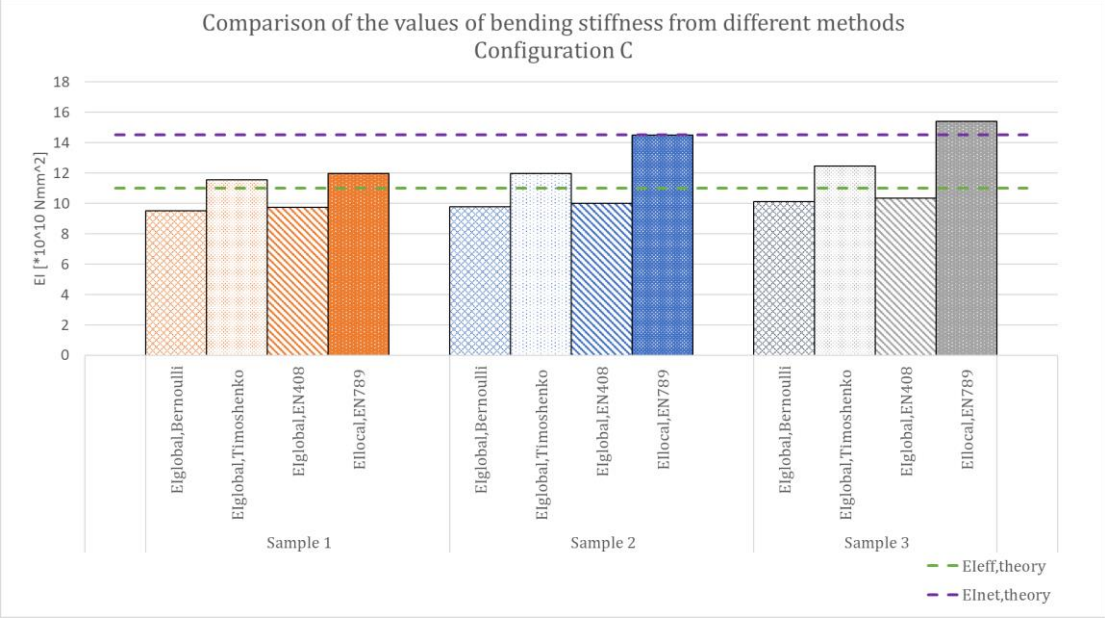

Figure 4-74 Comparison of the different bending stiffness values calculated based on different methods for Configuration C.

4.2.1.4 The summary of average bending stiffness of each configuration

The provided graph illustrates the average bending stiffness comparison among different methods for each configuration. It is evident that in Configuration B, where air gaps are introduced and the material reduction is 13%, the calculated bending stiffness values closely resemble those of solid specimens. Conversely, in Configuration C, with 12 cm air gaps and a material reduction of 19%, there is a

considerable decrease in bending stiffness. The disparity between solid specimens and Configuration C ranges from 19% to 26% depending on the method employed to calculate bending stiffness.

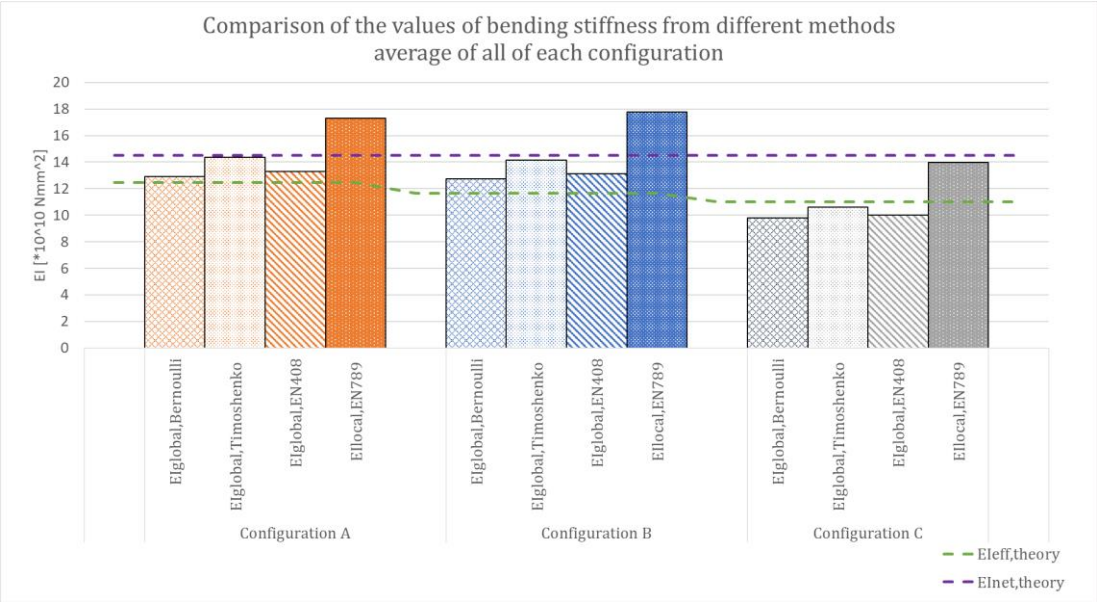

Figure 4-75 Average bending stiffness of each configuration of the specimen calculated based on different methods.

4.2.2 Results from ABAQUS

4.2.2.1 Deflection

The deflection of a beam for a path in the center of the beam, see Figure 4-76, is plotted for three different configurations.

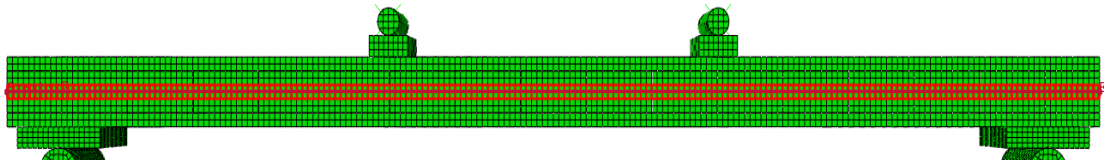

Figure 4-76 The path location for plotting the deflection of a CLT panel.

The comparison for the deflection of the three configurations is shown in below Figure; see Figure 4-77. As can be seen, the CLT panel with larger air gaps has a higher deflection. A load equal to 5 kN is chosen for comparison, which is in the elastic part.

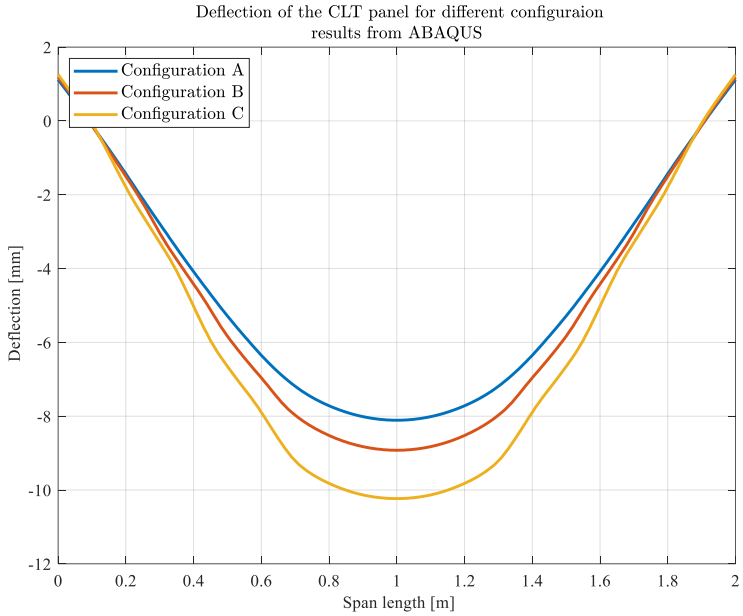

Figure 4-77 Deflection of the CLT panels for different configurations in the path located in the middle of the beam, ABAQUS results.

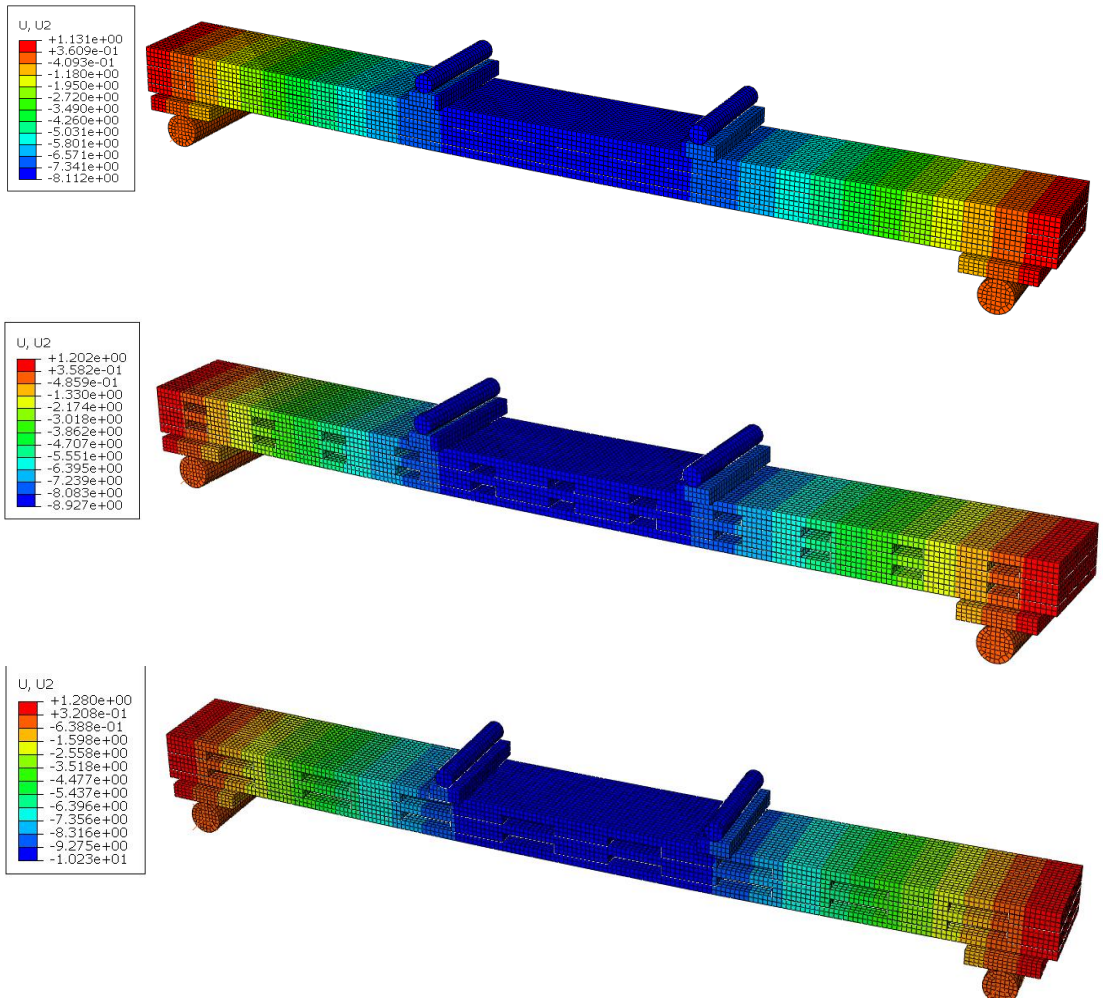

Figure 4-78 Deflection of a CLT panel for different configurations at a load equal to 5kN, ABAQUS [mm].

4.2.2.2 Normal Stress

ABAQUS provides the normal stress contours for each configuration; see Figure 4-79. The results indicate that by adding air gaps between the cross-layer and by increasing the size of the air gaps, the maximum normal stress increased due to the decrease in the stiffness of the section.

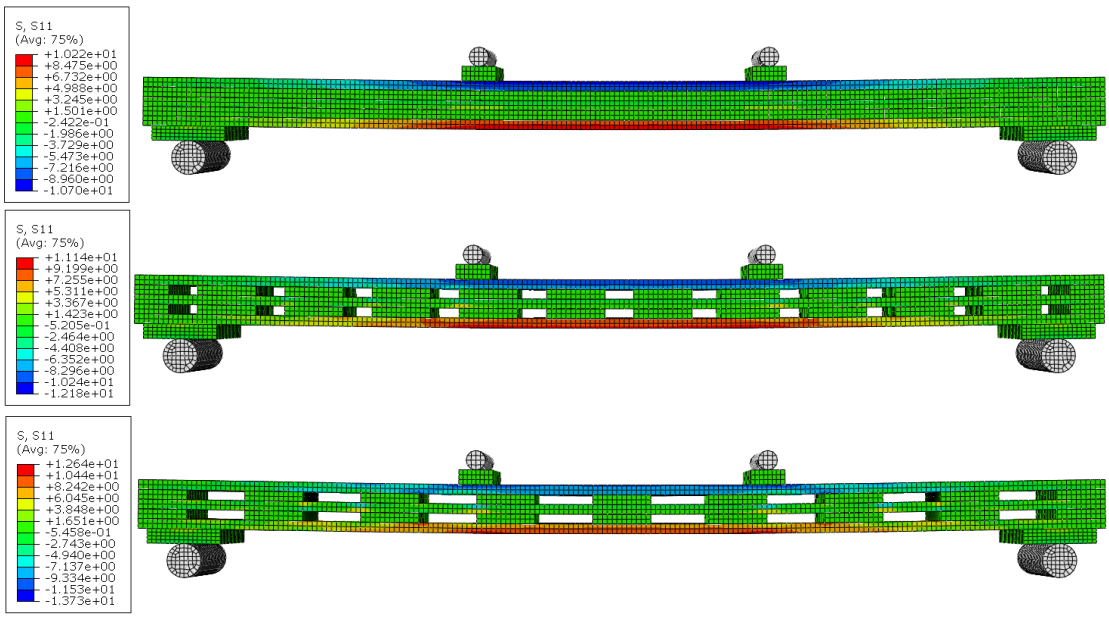

Figure 4-79 Normal stress S11 for Configurations A, B, and C, respectively, ABAQUS [MPa].

A comparison between the maximum normal stress of the three configurations is presented in Table 4-14 below:

Table 4-14 The comparison for maximum normal stress in different CLT panel configurations for a load equal to 5 kN, ABAQUS.

Configuration	Maximum normal stress (MPa)	Difference [%]
Configuration A	10.7	-
Configuration B	12.18	13.83%
Configuration C	13.73	28.32%

4.2.2.3 Shear stress

For different configurations, ABAQUS results for shear stress are presented in Figure 4-80, along with a comparison of maximum shear stresses in Table 4-15. The shear stress was significantly increased for Configuration C due to the increased air gaps in the cross layers, which were almost double higher than for Configuration A.

Table 4-15 The comparison for maximum shear stress in different CLT panel configurations for a load equal to 5 kN, ABAQUS.

Configuration	Maximum shear stress [MPa]	Difference [%]
Configuration A	4.02	-
Configuration B	6.03	40%
Configuration C	8.10	101.5%

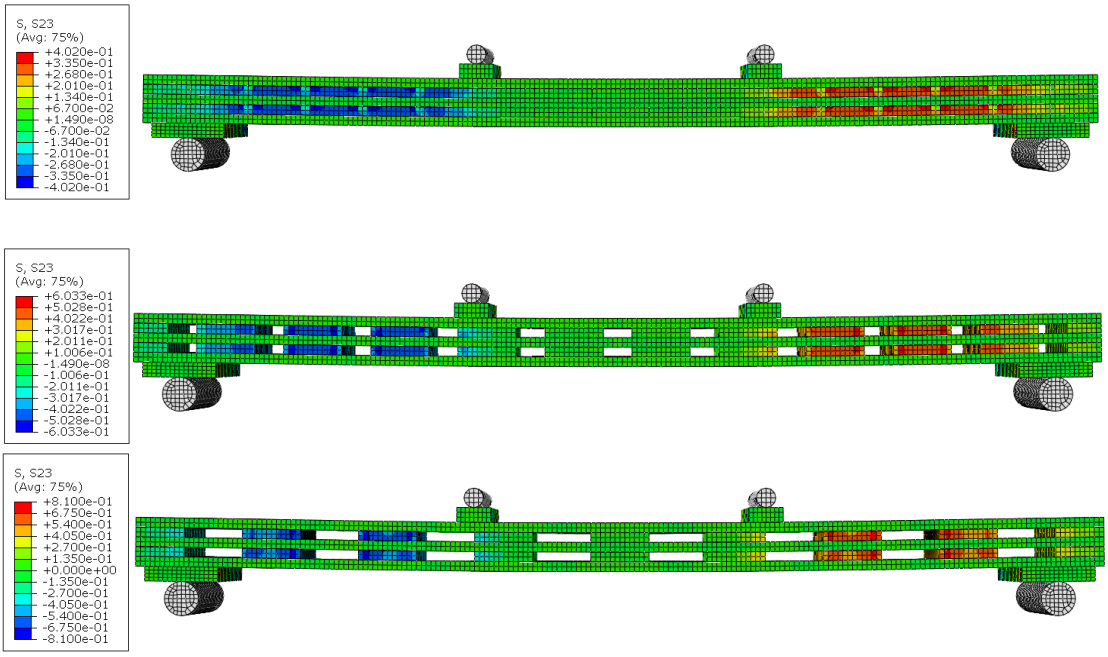

Figure 4-80 Shear stress S23 for Configurations A, B, and C respectively, ABAQUS [MPa].

4.2.3 Comparison between MATLAB and ABAQUS results and experimental data

Table 4-16 presents the maximum deflection that was obtained from the experiment and calculated based on different methods. The table also includes a difference in percentage between the experimental deflection and the calculated one. In each method, the introduction of air gaps (Configuration B) and the increase in their dimensions (Configuration C) lead to a higher maximum deflection. It can be seen that numerical analysis by ABAQUS predicts the maximum deflection quite well for Configuration A and C where the difference between values is 6.85 % and -0.10 %, respectively. The highest difference is for Configuration B where the difference is 12.33 %. Furthermore, Bernoulli's theory gives 8.23 % distinction from the experimental method for Configuration A, 9.56 % difference for Configuration B, and -10.94 % of Configuration C. In the end, it can be concluded that deflection calculated based on Timoshenko's method, when κ_s is equal to 0.24, gives the highest difference of values than the ones from the experiment, and there are 10.81 %, 7.42 %, and -16.50 % of the difference for each configuration, respectively. Additionally, all the methods overestimate the maximum deflection except for Configuration C, which is underestimated in FE calculation.

Table 4-16 A comparison of the maximum deflection obtained from the experiment and different methods of FE calculation: ABAQUS, based on Bernoulli theory, based on Timoshenko theory. Additionally, the difference in percentage is included between the value from the experiment and each calculation method.

Maximum deflection							
Conf.	**An average from the experiment [mm]**	**From ABAQUS [mm]**	**Difference [%]**	**Based on Bernoulli's theory [mm]**	**Difference [%]**	**Based on Timoshenko's theory [mm]**	**Difference [%]**
A	7.59	8.11	6.85	8.23	8.43	8.51	10.81
B	7.95	8.93	12.33	8.71	9.56	8.54	7.42
C	10.24	10.23	-0.10	9.12	-10.94	8.55	-16.50

Figure 4-81, Figure 4-82, and Figure 4-83 shows a graphical representation of the deflection of the beam in each configuration calculated based on different methods. The boxplot presents experimental data from the global sensor (in the middle) and two local ones. For Configuration A, the most similar result with the experimental value gives ABAQUS numerical analysis but Bernoulli and Timoshenko's method gives a difference of 8.43 % and 8.51 %, respectively. For Configuration B the calculated values from FEM analysis result in very similar values and the range of the difference fluctuates between 7.42 % and 12.33 %. The deflection based on Timoshenko's theory is the closest one to experimental deflection. The most significant differences between the experimental deflections and numerical ones were found for Configuration C for Bernoulli and Timoshenko theories and the methods underestimate the experimental results.

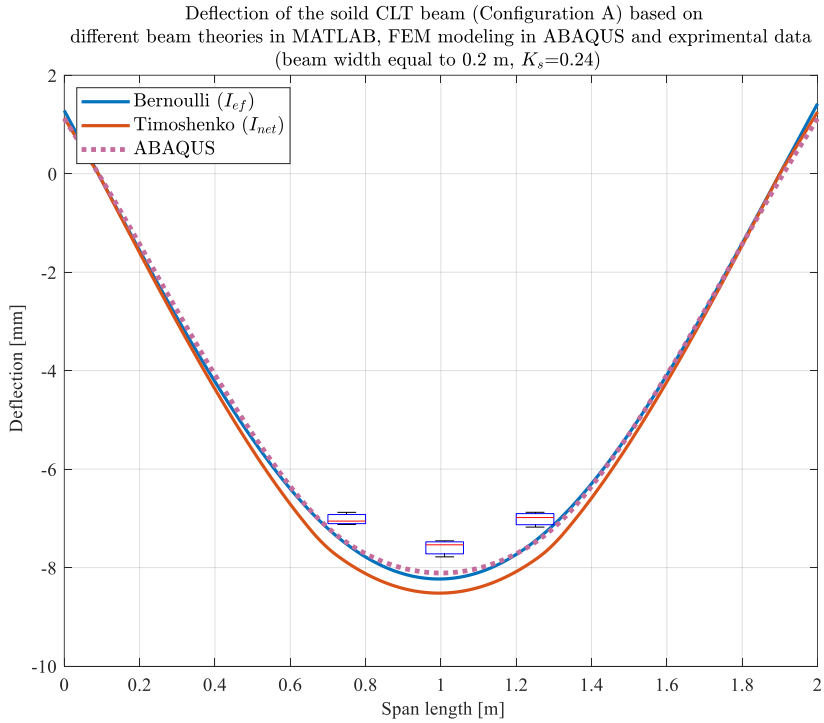

Figure 4-81 The deflection of the beam of Configuration A calculated based on different methods. Boxplots show the values of global and local deflections obtained in the experiment.

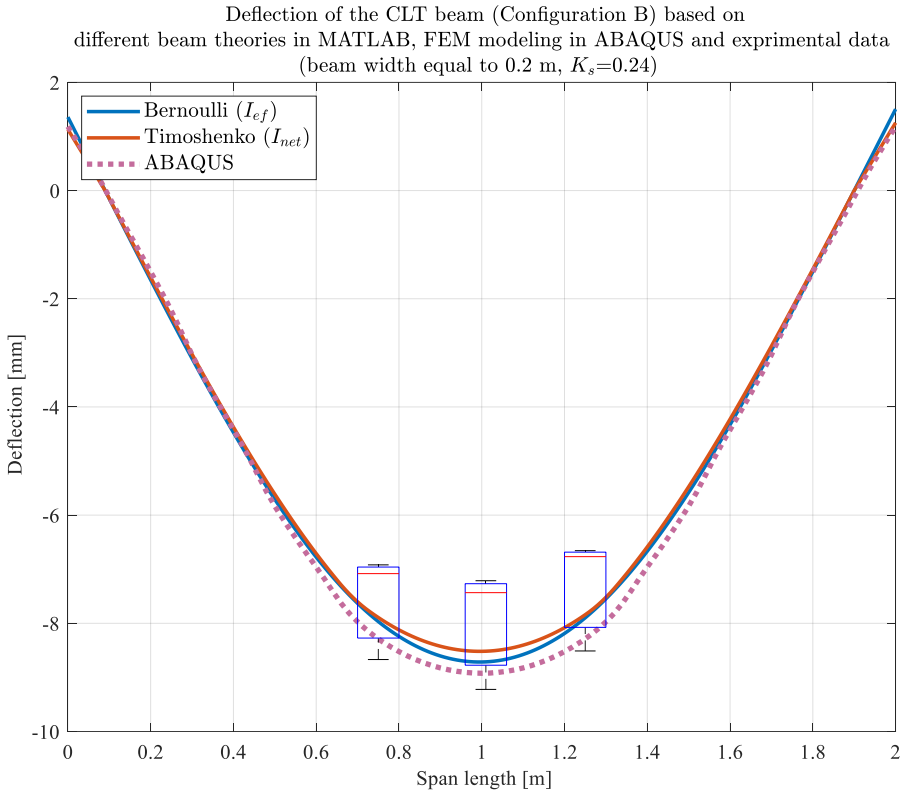

Figure 4-82 The deflection of the beam of Configuration B calculated based on different methods. Boxplots show the values of global and local deflections obtained from the experiment.

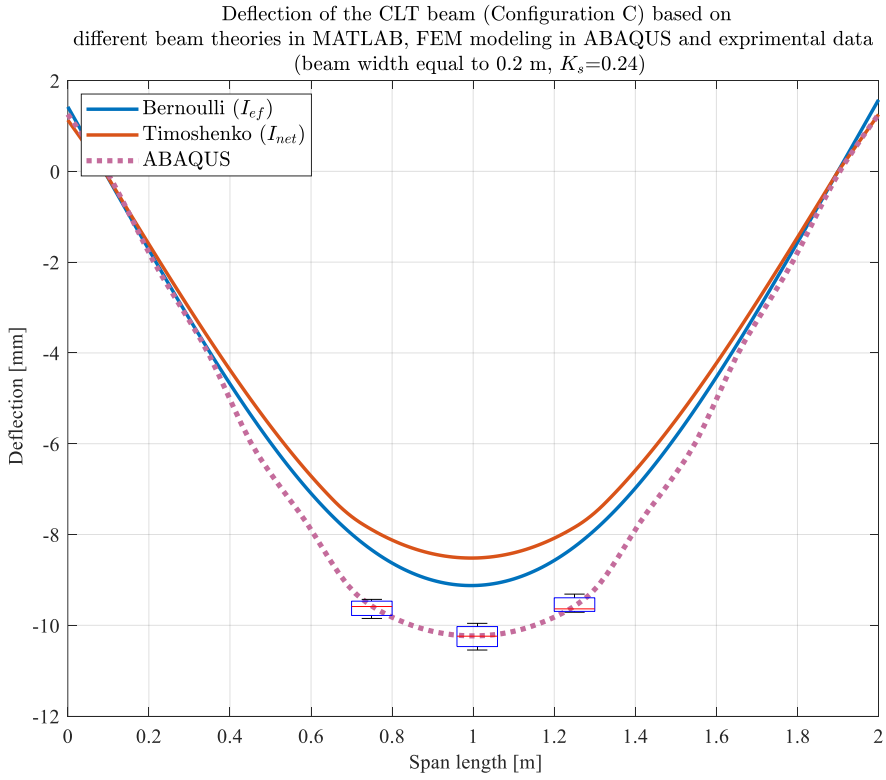

Figure 4-83 The deflection of the beam of Configuration C calculated based on different methods. Boxplots show the values of global and local deflections obtained from the experiment.

4.2.4 The effect of κ_s in the prediction of deflection in the Timoshenko method and comparison with ABAQUS and experimental results

In Configuration A, which involves a solid CLT panel, the variation in beam deflection predictions between different beam theories (Bernoulli and Timoshenko) and the ABAQUS result is not substantial. However, the experimental results indicate a slightly lower beam deflection value, approximately 7% smaller than the minimum value obtained from the three mentioned methods, as explained in the previous section. And, also as it is necessary to mention that in Timoshenko's method, the κ_s factor is set to 0.24 recommended by Jöbstl [19].

In Configuration B, characterized by a 6 cm air gap between cross-layers, the ABAQUS model yielded a higher beam deflection value. On the other hand, Timoshenko's method predicted a deflection approximately 5 % lower than the ABAQUS model. As previously mentioned, the κ_s factor was initially set to 0.24, but considering the reduced material usage in the panel, a lower value for the κ_s factor seems reasonable. By adjusting this value from 0.24 to 0.18, Timoshenko's method aligns with the ABAQUS model in terms of deflection prediction. Experimental test results indicate that the predicted deflections by the FEM models are higher than the mean value obtained from the three sample tests, which is approximately 17% lower than the ABAQUS and Timoshenko models with the new κ_s factor, see Figure 4-84.

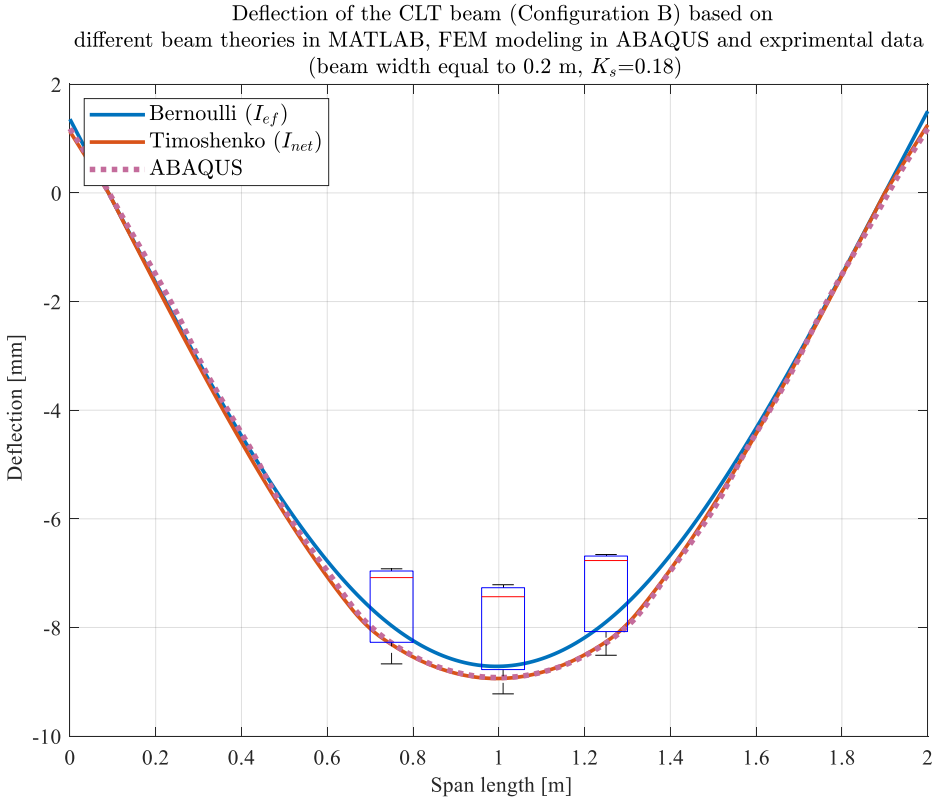

Figure 4-84 The deflection of the beam of Configuration B calculated based on different methods with modified deflection calculated based on Timoshenko theory by κ_s equal to 0.18.

In Configuration C, featuring 12 cm air gaps between cross-layers, Timoshenko's method with a κ_s factor of 0.24 predicted deflections lower than the ABAQUS model by approximately 11%. In contrast, the experimental test results closely matched the ABAQUS model with a mere 0.06% difference. Similar to Configuration B, adjusting the κ_s factor from 0.24 to 0.1 would bring the Timoshenko method's deflection predictions in line with both the ABAQUS model and the experimental test results, with a difference of only 0.4% compared to the experimental results, see Figure 4-85. It can be concluded that the deflection calculated based on Timoshenko's theory is very sensitive to κ_s that should be changed while calculating the deflection of the beams with air gaps.

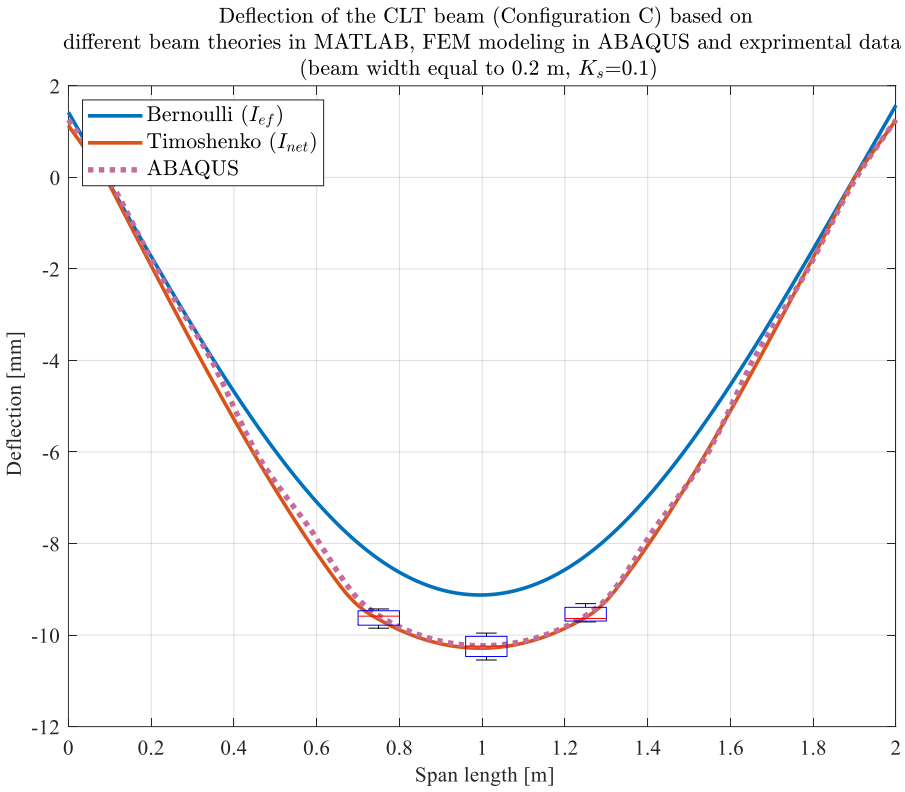

Figure 4-85 The deflection of the beam of Configuration C calculated based on different methods with modified deflection calculated based on Timoshenko theory by κ_s equal to 0.10.

4.2.5 Effect of κ_s on panel's bending stiffness

Additionally, an investigation was conducted to assess the impact of modifying the κ_s factor to 0.10, instead of the previously used value of 0.24, in Configuration C of Timoshenko's method on the bending stiffness. The figure presented below illustrates a comparison of different calculated bending stiffness values using various methods, including Timoshenko's theory with κ_s equal to 0.24 (as discussed in section 4.2.1.3.4), and with κ_s set to 0.10 (depicted by the yellow bar). The results indicate that reducing the kappa factor amplifies the influence of shear, which subtracts from the bending effect in formula (2-34), resulting in a higher final value of bending stiffness.

In the preceding section, it was mentioned that the deflection obtained using Timoshenko's method with κ_s equal to 0.10 exhibited a strong agreement with

experimental deflection. Therefore, it could be anticipated that utilizing the same factor value in Timoshenko's method for calculating bending stiffness would yield accurate predictions. However, to obtain more precise results and increase research samples, it is recommended to draw a strong conclusion based on a larger number of specimens.

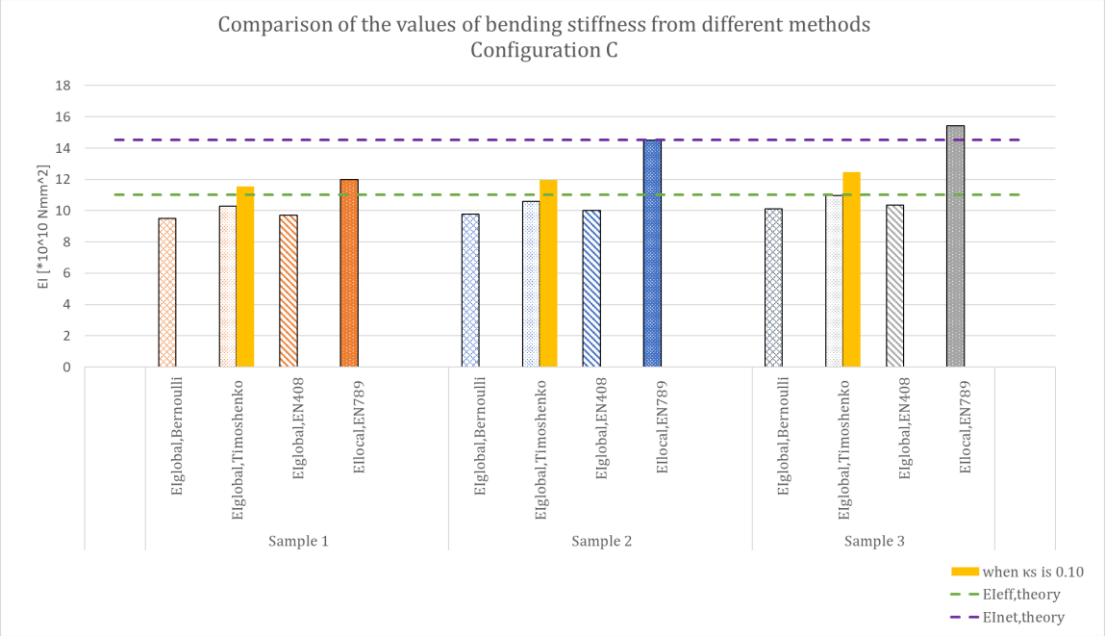

Figure 4-86 Comparison of the values of bending stiffness from different methods and Timoshenko's theory when κ_s is equal to 0.24 and κ_s is equal to 0.10 (yellow bar).

5 Conclusion

This master's thesis aimed to investigate the impact of incorporating air gaps between cross-layers within a Cross-Laminated Timber (CLT) panel. Following the guidelines of EN 16351, two distinct types of tests were conducted to examine the effects. The shear test was performed on small specimens of CLT panels produced in the workshop at Chalmers University of Technology. Additionally, a four-point bending test was carried out on large-scale samples manufactured by Stora Enso company. By studying the influence of introducing air gaps on both small and large specimens, this research seeks to enhance understanding of the structural behavior and performance of CLT panels, contributing valuable insights to optimize their design and construction practices.

5.1 Shear test

In conclusion, the shear testing of CLT panels with different configurations of air gaps has provided valuable insights into their structural behavior and performance. The results showed that the shear strength and rolling shear modulus varied among the different configurations with air gaps between cross-layers.

5.1.1 Effect of overlapping between cross-layers in different layers

According to the findings, Configuration III, characterized by shifted air gaps and overlapping cross-layers, exhibited the highest average rolling shear modulus and net shear strength among the configurations with air gaps. This specific configuration, with a 2 cm overlap, showed a 29% decrease in net shear strength compared to a solid panel while saving 13% of the material. If the overlap is reduced to 1 cm, the material saving increases to 16%, but the average net shear strength decreases by approximately 39% compared to the solid configuration.

Notably, when the overlap is eliminated entirely in Configuration V, resulting in a material saving of 20%, the net shear strength decreases significantly by about 56% compared to the solid configuration. To improve the net shear strength while still achieving a 20% material saving, Configuration IV with centrally arranged cross-layers can be utilized instead of Configuration V. By adopting this change, the net shear strength can increase by approximately 16% compared to Configuration V while remaining approximately 50% lower than the solid configuration.

5.1.2 Effect of the air gap size in a central arrangement of cross-layers

Based on the findings from the shear tests, enlarging the air gap between the cross-layers in centrally arranged configurations leads to a decrease in net shear strength. Specifically, when the air gap size is doubled, going from 6 cm in Configuration II to 12 cm in Configuration IV, the net shear strength experiences a reduction of approximately 16%.

5.1.3 Comparison between the FEM model and experimental

The experimental data generally aligned with the expected results from FEM modeling, indicating that configurations with higher stress concentrations resulted in lower average net shear strength.

5.2 Bending test

In this study, four-point bending tests were conducted on CLT panels with varying configurations and air gaps between cross layers. The objective was to investigate the structural behavior and stiffness characteristics of these panels. Additionally, stiffness results obtained from different methods and FEM modeling were analyzed. The findings from this research shed light on the performance of CLT panels, highlighting the influence of different configurations and air gaps on their bending behavior and stiffness properties.

5.2.1 Comparison of bending stiffness results between different configurations

The analysis of different configurations, namely Configuration A, Configuration B, and Configuration C, provides insight into the samples' bending stiffness characteristics. In Configuration A, the local bending stiffness results in higher values due to the absence of shear effects and reliance on bending alone. Local stiffness shows larger magnitudes than global deflection. Global bending stiffness calculated using Bernoulli theory and EN408 standard yields similar values across samples, with Sample 1 closer to net stiffness and Sample 2 closer to effective stiffness. Sample 3 falls between EI_{eff} and EI_{net}, while the Timoshenko method provides the highest global bending stiffness values for all samples.

In Configuration B, a similar trend is observed. The local bending stiffness gives higher values for Samples 1 and 2 and exceeds other global stiffness measures for Sample 3. The bending stiffness calculated using Bernoulli theory and EN408 standard yields comparable values, approaching EInet. The Timoshenko method produces the highest global bending stiffness values for all samples, with Sample 3 aligning closer to EI_{eff} compared to other global stiffness measures.

Lastly, in Configuration C, the local bending stiffness exhibits the highest bending stiffness values. However, this calculation solely considers local deflection, which is typically lower than global deflection, and does not account for shear effects. The global bending stiffness calculations using alternative methods yield similar values for all three samples, slightly lower than the theoretical effective bending stiffness.

5.2.2 The results of the deflection based on experimental and FE calculations

Experimental results indicate that beam deflection increases as air gaps between cross layers are increased. Similarly, the finite element model (FEM) also displays this behavior due to the reduction in stiffness in panels with air gaps between cross layers.

The results showed that when the dimension of the air gaps in CLT panels increases, the deflection that was experienced on tested specimens as well as the one calculated based on the FE method increase.

It was found that the deflection of Configuration I calculated by ABAQUS software matches the experimental value with the lowest difference of 6.62 %. For Configuration B with 6 cm air gaps, the lowest difference was found between the experimental value and the deflection calculated based on Timoshenko theory as 7.16 % while κ_s was equal to 0.24. Furthermore, for Configuration C it was only 0.10 % of the difference while the displacement was computed by ABAQUS. For the deflection calculated based on Timoshenko's theory κ_s factor was used as 0.24 which was recommended by Jöbstl [19], however, this value should be changed for the panels with introduced air gaps. For example, while κ_s was changed to 0.10 in the calculation of Configuration C based on Timoshenko's theory, the maximum deflection was changed to 10.28 mm and it was only 0.004% of the difference compared to the experimental value. It means that the deflection calculated based on Timoshenko's method can perfectly predict the reality if κ_s is correctly defined and takes into account the geometry of the panel.

5.2.3 Final remarks on comparison of the bending stiffness calculated based on different methods

The higher deflection in the panels with wider air gaps leads to a reduction of the bending stiffnesses of the CLT panels of Configuration B and C compared to the solid ones. The bending stiffnesses were calculated based on different methods and compared with theoretical values. The results show that the global stiffnesses give similar values to the analytical solutions, differently than local stiffness that reached usually a higher value. Timoshenko, Bernoulii, and the deflection calculated based on the EN408 standard gave the values in the range between EI_{net} and EI_{eff} that were calculated analytically for Configuration A and B however for Configuration C the methods gave the values lower than EI_{net} and EI_{eff}. The bending stiffness based on Timoshenko's theory was calculated when κ_s was equal to 0.24 and when κ_s was equal to 0.10. A significant influence of the factor was noticeable on the final value of bending stiffness so due to the sensitivity of the results, this factor should be modified based on the geometry and arrangement of the air gaps of particular configuration.

5.2.4 Further analysis

In summary, the inclusion of air gaps in CLT panels has demonstrated an influence on their shear characteristics and overall structural performance. Additional research and investigations are necessary to determine the optimum configuration for overlapping dimensions of cross-layers by introducing air gaps between them in CLT panels and to assess the potential material savings associated with these configurations. Moreover, an analysis of the behaviour of a CLT panel when it is subjected to in-plane load needs to be studied to calculate the shear stiffness. It would be also beneficial to analyze the structural behavior of the panels with air gaps and different amounts of layers. Also, further research is needed to explore additional configurations and assess long-term behavior and durability. In addition the other aspects like fire, and sound resistance, moisture safety of a CLT panel with air-gaps between the cross-layers should be analyzed.

5.2.5 Final remark on the optimization of the CLT panel by introducing air gaps between cross layers

After analyzing the results of shear strength, shear modulus, deflection, and bending stiffness of CLT panels with and without air gaps between cross-layers, it is difficult to determine a single configuration that outperforms the others in terms of overall performance. The concept of optimization varies depending on the specific application of a CLT panel. For instance, in certain applications, the design is governed by the serviceability limit state (SLS) behavior, making the maximum deflection limit a critical factor. In other cases, shear capacity may not be a significant concern in the design. Therefore, it can be concluded that the introduction of air gaps between cross layers in a CLT panel should be carefully considered, taking into account the various aspects already studied in this master thesis as well as other factors suggested for future investigation. After that, based on the specific application requirements, the most suitable configuration can be selected and implemented in the design.

6 References

[1] '2022 Global Status Report for Buildings and Construction', UN Environment Program, 2022. [Online]. Available: https://globalabc.org/our-work/tracking-progress-global-status-report

[2] A. Gustafsson, *The CLT Handbook*. Swedish Wood, 2019.

[3] P. Mayencourt, I. M. Rasid, and C. Mueller, 'Structural Optimization of Cross-Laminated Timber Panels', *Proceedings of IASS Annual Symposia*, vol. 2018, no. 20, pp. 1–8, Jul. 2018.

[4] Swedish Wood, *The CLT Handbook, CLT structures – facts and planning*, First. Svenskt Trä, 2019. [Online]. Available: www.svenskttra.se

[5] Guttmann, 'Guttmann: Brettsperrholz: Ein Produktporträt [Cross laminated timber: a product profile]', 2008.

[6] Moser, 'Moser K (1995) Dickholz durch Vakuum [Dickholz through vacuum]. Bauen mit Holz 11:941–947 (in German)'. 1995.

[7] A. Gülzow, 'Nondestructive evaluation of elastic material properties of cross laminated timber (CLT)', presented at the Conference COST E53, Delft, The Netherlands, 2008.

[8] R. Brandner, G. Flatscher, A. Ringhofer, G. Schickhofer, and A. Thiel, 'Cross laminated timber (CLT): overview and development', *Eur. J. Wood Prod.*, vol. 74, no. 3, pp. 331–351, May 2016, doi: 10.1007/s00107-015-0999-5.

[9] Francesca Pierobon, 'Environmental benefits of using hybrid CLT structure in midrise non-residential construction_ An LCA based comparative case study in the U.S. Pacific Northwest | Elsevier Enhanced Reader', *Journal of Building Engineering*, vol. 26, 2019, doi: https://doi.org/10.1016/j.jobe.2019.100862.

[10] P. Mayencourt, I. M. Rasid, and C. Mueller, 'Structural Optimization of Cross-Laminated Timber Panels', 2018.

[11] Toosi, 'Cross laminated timber: The market opportunities.', 2001.

[12] CAWBIOM, 'California Assessment of Wood Business Innovation Opportunities and Markets (CAWBIOM)'. 2015.

[13] A. T. Gregor Silly Manfred Augustin, *OPTIONS FOR THE RESOURCE OPTIMISED PRODUCTION OF LAMINAR LOAD CARRYING MEMBERS BASED ON WOOD PRODUCTS*. 2016.

[14] A. L. Lorenzo Franzoni Florent Lyon, Gilles Foret, *BENDING BEHAVIOR OF REGULARLY SPACED CLT PANELS*. 2016.

[15] Anna Moberg, Linda Xiao, 'New Genration CLT, Material optimisation of CLT with regard to structural performance by the introduction of an air gaps in the cross-layers', Chalmers university of technology, 2022.

[16] *Canadian CLT Handbook*, 2019th ed., vol. 1. [Online]. Available: fpinnovations.ca

[17] E. L. Sebastian Svensson Meulmann, 'Modelling and testing of CLT panels for evaluation of stiffness', Master Thesis, Linnaeus University, Sweden.

[18] Amar Khennane, *Introduction to Finite Element Analysis Using MATLAB and Abaqus*. Taylor & Francis Group, 2013. [Online]. Available: www.crcpress.com

[19] J. K. Markus Wallner-Novak Kurt Pock, *Cross-Laminated Timber Structural Design, Basic design and engineering principles according to Eurocode.*, 1st ed. proHolz Austria, 2014.

[20] C. S. Hans Joachim Blab, *Timber engineering principles for design*. Karlsurher Institut fur technologie, 2017. [Online]. Available: www.ksp.kit.edu

[21] Dassault Systèmes, 'Abaqus 6.11 Analysis User's Manual Volume III: Materials'. 2011.

[22] *CALFEM a Finite Element Toolbox, Version 3.4*. The Division of Structural Mechanics, Lund University. [Online]. Available: http://www.byggmek.lth.se/Calfem

7 Appendix

7.1 Stiffness matrix elements

$E_1 := 11000\ MPa$

$G_{12} := 780\ MPa$

$E_2 := 400\ MPa$

$G_{13} := 780\ MPa$

$E_3 := 400\ MPa$

$G_{23} := 78\ MPa$

$v_{12} := 0.40$

$v_{23} := 0.51$

$v_{13} := 0.50$

$$v_{21} := \frac{E_2}{E_1} \cdot v_{12} = 0.015$$

$$v_{31} := \frac{E_3}{E_1} \cdot v_{13} = 0.018$$

$$v_{32} := \frac{E_3}{E_2} \cdot v_{23} = 0.51$$

$$\Upsilon := \frac{1}{1 - v_{12} \cdot v_{21} - v_{23} \cdot v_{32} - v_{31} \cdot v_{13} - 2 \cdot v_{21} \cdot v_{32} \cdot v_{13}} = 1.394$$

$D_{1111} := E_1 \cdot (1 - v_{23} \cdot v_{32}) \cdot \Upsilon = 11342.265\ MPa$

$D_{2222} := E_2 \cdot (1 - v_{13} \cdot v_{31}) \cdot \Upsilon = 552.367\ MPa$

$D_{3333} := E_3 \cdot (1 - v_{12} \cdot v_{21}) \cdot \Upsilon = 554.192\ MPa$

$D_{1122} := E_1 \cdot (v_{21} + v_{31} \cdot v_{23}) \cdot \Upsilon = 365.12\ MPa$

$D_{1133} := E_1 \cdot (v_{31} + v_{21} \cdot v_{32}) \cdot \Upsilon = 392.434\ MPa$

$D_{2233} := E_2 \cdot (v_{32} + v_{12} \cdot v_{31}) \cdot \Upsilon = 288.346\ MPa$

$D_{1212} := G_{12} = 780\ MPa$

$D_{1313} := G_{13} = 780\ MPa$

$D_{2323} := G_{23} = 78\ MPa$

7.2 Estimated load capacity of a CLT panel in four-point bending test

$f_{m.k} := 24\ MPa$

$f_{t.0.k} := 14.5\ MPa$

$f_{t.90.k} := 0.4\ MPa$

$f_{c.90.k} := 2.5\ MPa$

$f_{v.k} := 4.0\ MPa$

$f_{c.0.k} := 21\ MPa$

$f_{v.9090.k} := 1.1\ MPa$

$E_{m.0.mean} := 11000\ MPa$

$E_{m.0.05} := 7400\ MPa$

$G_{mean} := 690\ MPa \qquad G_{9090} := 69\ MPa$

$\rho_k := 350\ \frac{kg}{m^3}$

$\rho_{mean} := 420\ \frac{kg}{m^3}$

$t := 20\ mm$

$b_x := 1000\ mm$

$b_y := 200\ mm$

$l_{ref} := 1800\ mm$

$a_1 := 40\ mm$

$a_2 := 20\ mm$

$h := 5 \cdot t = 100\ mm$

$z_x := \frac{h}{2} = 50\ mm \qquad z_y := 30\ mm$

$A_{x.net} := b_x \cdot (5 \cdot t) = (1 \cdot 10^5)\ mm^2$

$I_{x.net} := 3 \cdot \frac{1}{12}\ b_x \cdot t^3 + 2 \cdot \left(b_x \cdot t \cdot a_1^{\ 2}\right) = (6.6 \cdot 10^7)\ mm^4$

$$W_{x.net} := \frac{I_{x.net}}{z_x} = (1.32 \cdot 10^6)\ mm^3$$

$$S_{x.net} := b_x \cdot t \cdot a_1 = (8 \cdot 10^5)\ mm^3$$

$$\gamma_1 := \frac{1}{\left(1 + \frac{\pi^2 \cdot E_{m.0.mean} \cdot t}{l_{ref}^{\ 2}} \cdot \frac{t}{G_{9090}}\right)} = 0.837$$

$$\gamma_3 := 1$$

$$\gamma_5 := \gamma_1 = 0.837$$

$$I_{x.ef} := 3 \cdot \left(\frac{b_x \cdot t^3}{12}\right) + 2 \cdot \left(\gamma_1 \cdot b_x \cdot t \cdot a_1^{\ 2}\right) = (5.559 \cdot 10^7)\ mm^4$$

$$A_{y.net} := 2 \cdot b_y \cdot t = (8 \cdot 10^3)\ mm^2$$

$$I_{y.net} := 2 \cdot \frac{1}{12}\ b_y \cdot t^3 + 2 \cdot \left(b_y \cdot t \cdot a_2^{\ 2}\right) = (3.467 \cdot 10^6)\ mm^4$$

$$S_{y.net} := b_y \cdot t \cdot a_2 = (8 \cdot 10^4)\ mm^3$$

$$W_{y.net} := \frac{I_{y.net}}{z_y} = (1.156 \cdot 10^5)\ mm^3$$

$$\gamma_1 := \frac{1}{\left(1 + \frac{\pi^2 \cdot E_{m.0.mean} \cdot t}{l_{ref}^{\ 2}} \cdot \frac{t}{G_{9090}}\right)} = 0.837$$

$$\gamma_3 := 1$$

$$\gamma_5 := \gamma_1 = 0.837$$

$$I_{y.ef} := 2 \cdot \left(\frac{b_y \cdot t^3}{12}\right) + 2 \cdot \left(\gamma_1 \cdot b_y \cdot t \cdot a_2^{\ 2}\right) = (2.946 \cdot 10^6)\ mm^4$$

$$h = 100\ mm$$

$$c_1 := 6 \cdot h = 600\ mm$$

$$c_2 := c_1 + 6 \cdot h = (1.2 \cdot 10^3)\ mm$$

Load based on bending stress verification:

$$f_{m.xlay.mean} := f_{m.k} \cdot 1.4 = 33.6 \ \textbf{MPa}$$

$$\sigma_{m.y.d} := \frac{M_{max}}{W_{x.net}} \qquad \text{and} \qquad M_{max} := P_{max} \cdot c_1$$

$$P_{mean.m} := \frac{f_{m.xlay.mean} \cdot W_{x.net}}{c_1} = 73.92 \ \textbf{kN}$$

Load based on shear stress verification:

$$\tau_{v.xz.d} := \frac{S_{y.net} \cdot V_{max.x}}{I_{y.net} \cdot b_x} \qquad f_{v.9090.ylay.mean} := f_{v.k} \cdot 1.4 = 5.6 \ \textbf{MPa}$$

$$V_{max.x} := P_{mean.v}$$

$$P_{mean.v} := \frac{f_{v.9090.ylay.mean} \cdot I_{y.net} \cdot b_x}{S_{y.net}} = 242.667 \ \textbf{kN}$$

Load based on rolling shear stress verification:

$$\tau_{rv.yz.d} := \frac{S_{x.net} \cdot V_{max.y}}{I_{x.net} \cdot b_y} \qquad f_{v.9090.xlay.mean} := f_{v.9090.k} \cdot 1.4 = 1.54 \ \textbf{MPa}$$

$$V_{max.y} := P_{mean.r}$$

$$P_{mean.r} := \frac{f_{v.9090.xlay.mean} \cdot I_{x.net} \cdot b_y}{S_{x.net}} = 25.41 \ \textbf{kN}$$

7.4 Stiffness calculation for a CLT panel in four-point bending test

```
clear all, close all
% read data extracted from ABAQUS
filename = 'ABAQUS results';
sheet = 1;
subsetA = xlsread(filename,sheet);

% everything with %%% in front is from old 1D spring example

% Define input properties:
E_L=11000*10^6;    %(Pa) Longitudinal stiffness
G_RT=78*10^6;     %(Pa)
G_LT=780*10^6;     %(Pa)
% Define input geometry
h=0.1;      %(m) CLT thickness
a=6*h;
b1=6*h;
L=2;
L_ref=L;      %
b=0.2;   % Lamella width
t=0.02;  % Lamella thickness
P=5*10^3/7;    %KN
qx=0;
qy=0;
ne=200; % Number of element
% Claculate effective stiffness based on Gamma method
Ks=0.24;
% Nodal positions:
coord=zeros(ne+1,2);
for i=2:ne+1
   coord(i,1)=coord(i-1,1)+L_ref/ne;
end
% b=0.1:0.05:1; % A loop for calculation withe different width of the beam
b=0.2; % width of the beam
def_b=zeros(size(b,2),1);
def_t=zeros(size(b,2),1);

for j=1:size(b,2)
G_1=1/(1+(pi^2*E_L*t^2)/(L_ref^2*G_RT));
a_1=2*t;
I_ef=b(j)*(t^3/4+2*G_1*t*a_1^2);
%  w_max(i)=-P*a*(3*L^2-4*a^2)/(24*E_L*I_ef)
A=5*t*b(j);
I_net=b(j)*(t^3/4+2*t*a_1^2);
dof=zeros(ne+1,3);
for i=2:size(dof,1)
   dof(1,:)=[1 2 3];
```

```
   dof(i,:)=[dof(i-1,end)+1 dof(i-1,end)+2 dof(i-1,end)+3];
end
Edof=zeros(ne,7);
for i=1:size(Edof,1)
  Edof(i,:)=[i dof(i,:) dof(i+1,:)];
end
[Ex,Ey] = coordxtr(Edof,coord,dof,2);

%% Bernoulli with Ief Config A
K=zeros(size(dof,1)*size(dof,2));     % initialise stiffness matrix
f=zeros(size(dof,1)*size(dof,2),1);   % initialise load vector
ep = [E_L A I_ef];
eq = [qx qy];
% Assemble stiffness
for i=1:size(Edof,1)    % number of elements is equal to number of rows
   [Ke,fe]=beam2e(Ex,Ey,ep,eq) ;              % in Edof
   K(Edof(i,2:end),Edof(i,2:end)) = K(Edof(i,2:end),Edof(i,2:end)) + Ke;
   f(Edof(i,2:end),1)=f(Edof(i,2:end),1)+fe;
end

%% Bernoulli with Inet  Config A
K_n=zeros(size(dof,1)*size(dof,2));     % initialize stiffness matrix
f_n=zeros(size(dof,1)*size(dof,2),1);   % initialize load vector
ep_n = [E_L A I_net];
eq = [qx qy];
% Assemble stiffness
for i=1:size(Edof,1)    % number of elements is equal to number of rows
   [Ke,fe]=beam2e(Ex,Ey,ep_n,eq) ;              % in Edof
   K_n(Edof(i,2:end),Edof(i,2:end)) = K_n(Edof(i,2:end),Edof(i,2:end)) + Ke;
   f_n(Edof(i,2:end),1)=f_n(Edof(i,2:end),1)+fe;
end

%% Bernoulli with Ief 1/3 air gap Config B
K_2=zeros(size(dof,1)*size(dof,2));     % initialize stiffness matrix
f=zeros(size(dof,1)*size(dof,2),1); % initialize load vector
G_2=1/(1+(pi^2*E_L*t^2)/(L_ref^2*2/3*G_RT));
I_ef2=b(j)*(t^3/4+2*G_2*t*a_1^2);
ep_2 = [E_L A I_ef2];
eq = [qx qy];
% Assemble stiffness
for i=1:size(Edof,1)    % number of elements is equal to number of rows
   [Ke,fe]=beam2e(Ex,Ey,ep_2,eq) ;              % in Edof
   K_2(Edof(i,2:end),Edof(i,2:end)) = K_2(Edof(i,2:end),Edof(i,2:end)) + Ke;
   f(Edof(i,2:end),1)=f(Edof(i,2:end),1)+fe;
end

%% Bernoulli with Ief 0.48 air gap Config C

K_3=zeros(size(dof,1)*size(dof,2));     % initialize stiffness matrix
```

```
f=zeros(size(dof,1)*size(dof,2),1); % initialize load vector
G_3=1/(1+(pi^2*E_L*t^2)/(L_ref^2*0.52*G_RT));
I_ef3=b(j)*(t^3/4+2*G_3*t*a_1^2);
ep_3 = [E_L A I_ef3];
eq = [qx qy];
% Assemble stiffness
for i=1:size(Edof,1)    % number of elements is equal to number of rows
   [Ke,fe]=beam2e(Ex,Ey,ep_3,eq) ;                % in Edof
   K_3(Edof(i,2:end),Edof(i,2:end)) = K_3(Edof(i,2:end),Edof(i,2:end)) + Ke;
   f(Edof(i,2:end),1)=f(Edof(i,2:end),1)+fe;
end

%% Timoshenko I_net Config A
G_mean=(G_LT*3*t+G_RT*2*t)/h;
K_t=zeros(size(dof,1)*size(dof,2));     % initialize stiffness matrix
f=zeros(size(dof,1)*size(dof,2),1);    % initialize load vector
ep_t = [E_L G_mean A I_net Ks ];
eq = [qx qy];
% Assemble stiffness
for i=1:size(Edof,1)    % number of elements is equal to number of rows
   [Ke,fe]=beam2t(Ex,Ey,ep_t,eq) ;                % in Edof
   K_t(Edof(i,2:end),Edof(i,2:end)) = K_t(Edof(i,2:end),Edof(i,2:end)) + Ke;
   f(Edof(i,2:end),1)=f(Edof(i,2:end),1)+fe;
end

%% Timoshenko with I_ef  Config A
G_mean=(G_LT*3*t+G_RT*2*t)/h;
K_tef=zeros(size(dof,1)*size(dof,2));     % initialize stiffness matrix
f=zeros(size(dof,1)*size(dof,2),1);    % initialize load vector
ep_tef = [E_L G_mean A I_ef Ks ];
eq = [qx qy];
% Assemble stiffness
for i=1:size(Edof,1)    % number of elements is equal to number of rows
   [Ke,fe]=beam2t(Ex,Ey,ep_tef,eq) ;                % in Edof
   K_tef(Edof(i,2:end),Edof(i,2:end)) = K_tef(Edof(i,2:end),Edof(i,2:end)) + Ke;
   f(Edof(i,2:end),1)=f(Edof(i,2:end),1)+fe;
end

%% Timoshenko with I_ef 1/3 airgap Config B
G_2T=1/(1+(pi^2*E_L*t^2)/(L_ref^2*2/3*G_RT));
I_ef2T=b(j)*(t^3/4+2*G_2T*t*a_1^2);
G_mean1=2/3*(G_LT*3*t+G_RT*2*t)/h;
K_tef2T=zeros(size(dof,1)*size(dof,2));     % initialize stiffness matrix
f=zeros(size(dof,1)*size(dof,2),1);    % initialize load vector
ep_tef2T = [E_L G_mean1 A I_ef2T Ks ];
eq = [qx qy];
% Assemble stiffness
for i=1:size(Edof,1)    % number of elements is equal to number of rows
   [Ke,fe]=beam2t(Ex,Ey,ep_tef2T,eq) ;                % in Edof
```

```
   K_tef2T(Edof(i,2:end),Edof(i,2:end)) = K_tef2T(Edof(i,2:end),Edof(i,2:end)) +
Ke;
   f(Edof(i,2:end),1)=f(Edof(i,2:end),1)+fe;
end

%% Timoshenko with I_ef 0.48 airgap Config C
G_3T=1/(1+(pi^2*E_L*t^2)/(L_ref^2*0.52*G_RT));
I_ef2T=b(j)*(t^3/4+2*G_3T*t*a_1^2);
G_mean2=0.6*(G_LT*3*t+G_RT*2*t)/h;
K_tef3T=zeros(size(dof,1)*size(dof,2));      % initialize stiffness matrix
f=zeros(size(dof,1)*size(dof,2),1);    % initialize load vector
ep_tef3T = [E_L G_mean2 A I_ef2T Ks ];
eq = [qx qy];
% Assemble stiffness
for i=1:size(Edof,1)    % number of elements is equal to number of rows
   [Ke,fe]=beam2t(Ex,Ey,ep_tef3T,eq) ;                % in Edof
   K_tef3T(Edof(i,2:end),Edof(i,2:end)) = K_tef3T(Edof(i,2:end),Edof(i,2:end)) +
Ke;
   f(Edof(i,2:end),1)=f(Edof(i,2:end),1)+fe;
end
%% Add any external forces
%  f(5) =-P;
%  f(11)=-P;
% element_l=L_ref/ne;
% neup_1=(L_ref/4)/element_l;
% neup_2=ne-neup_1;
%  position_1=dof(neup_1+1,2);
%  position_2=dof(neup_2+1,2);

% Based on convergence study for number of element equal to 200
f(200) =-P;f(203) =-P;f(206) =-P;f(209) =-P;f(212) =-P;f(215) =-P;
f(218) =-P;f(380) =-P;f(383) =-P;f(386) =-P;f(389) =-P;f(392) =-P;
f(395) =-P;f(398) =-P;f_n(200) =-P;f_n(203) =-P;f_n(206) =-P;
f_n(209) =-P;f_n(212) =-P;f_n(215) =-P;f_n(218) =-P;f_n(380) =-P;
f_n(383) =-P;f_n(386) =-P;f_n(389) =-P;f_n(392) =-P;f_n(395) =-P;
f_n(398) =-P;
% Add boundary condition
%%% bc = [3 0];          % dof 1 is prescribved to zero
% bc = [1 0;
%     2 0;
%      ne*3+2 0    ];
bc = [10 0;13 0;16 0;19 0;22 0;25 0;28 0;29 0;31 0;34 0;37 0;40 0;43 0;46 0;49
0;550 0;553 0;
     556 0;559 0;562 0;565 0;568 0;571 0;572 0;574 0;577 0;580 0;583 0;586
0;589 0];
%% Solve
[a,r] = solveq(K,f,bc); % Bernoulli with Ief Config A
[a_n,r_n] = solveq(K_n,f_n,bc); % Bernoulli with Inet  Config A
[a_2,r_2] = solveq(K_2,f,bc); % Bernoulli with Ief 1/3 air gap Config B
```

```
[a_3,r_3] = solveq(K_3,f,bc); % Bernoulli with Ief 0.48 air gap Config C
[a_t,r_t] = solveq(K_t,f,bc); % Timoshenko I_net Config A
[a_tef,r_tef] = solveq(K_tef,f,bc); % Timoshenko with I_ef  Config A
[a_tef2,r_tef2] = solveq(K_tef2T,f,bc); % Timoshenko with I_ef 1/3 airgap Config
B
[a_tef3,r_tef3] = solveq(K_tef3T,f,bc); % Timoshenko with I_ef 0.48 airgap Config
C
%% Find maximum deflection
def_b(j,1)=min(a(2:3:end,1)');
def_n(j,1)=min(a_n(2:3:end,1)');
def_2(j,1)=min(a_2(2:3:end,1)');
def_3(j,1)=min(a_3(2:3:end,1)');
def_t(j,1)=min(a_t(2:3:end,1)');
def_tef(j,1)=min(a_tef(2:3:end,1)');
def_tef2(j,1)=min(a_tef2(2:3:end,1)');
def_tef3(j,1)=min(a_tef3(2:3:end,1)');
end

%% results from the expriments
U_RPC=[7.4567 7.7817 7.5372];
U_RPLL=[6.8776 7.0557 7.1242];
U_RPLR=[6.8768 7.1775 6.9837];
U=[-1*U_RPLL',-1*U_RPC',-1*U_RPLR'];
U_RPC_II=[7.4337 7.2131 9.2222];
U_RPLL_II=[7.0817 6.920 8.6701];
U_RPLR_II=[6.7677 6.6573 8.5114];
UII=[-1*U_RPLL_II',-1*U_RPC_II',-1*U_RPLR_II'];
U_RPC_III=[10.5444 10.2396 9.9567];
U_RPLL_III=[9.8492 9.5861 9.4289];
U_RPLR_III=[9.7120 9.6379 9.3127];
UIII=[-1*U_RPLL_III',-1*U_RPC_III',-1*U_RPLR_III'];

%% (Configuration A)
figure (1)
grid on
x=(coord(:,1)');  % x=(coord(:,1)'/L_ref);
position=[x(76) x(102) x(126)];
hold on
ha= plot(x,1000*a(2:3:end,1)','linewidth',2);
hold on
hc=   plot(x,1000*a_t(2:3:end,1)','linewidth',2);
hold on
plot(subsetA(:,2),subsetA(:,3),':','color','#C46C9C','linewidth',3);
hold on
he=boxplot(U,'Positions',position,'Widths',0.1);
ylim([-10 2]);
xlim([0 2])
xticks(0:0.2:2);
xticklabels('auto')
```

```
legend('Bernoulli ($I_{ef}$)', 'Timoshenko
($I_{net}$)','ABAQUS','Location','northwest','FontSize',12,'interpreter','latex')
xlim([0 2]);
grid on
set(gca,'FontSize',12,'fontname','Times New Roman')
xlabel(' Span length [m]','FontSize',12)
ylabel('  Deflection [mm] ','FontSize',12)
title({' Deflection of the soild CLT beam (Configuration A) based on' ,'different
beam theories in MATLAB, FEM modeling in ABAQUS and experimental data',
'(beam width equal to 0.2 m, $K_s$=0.24) '},'FontSize',12,'fontname','Times New
Roman','fontweight','bold','interpreter','latex')
%% (Configuration B)
figure (2)
grid on
x=(coord(:,1)');  % x=(coord(:,1)'/L_ref);
hold on
plot(x,1000*a_2(2:3:end,1)','linewidth',2);
hold on
plot(x,1000*a_t(2:3:end,1)','linewidth',2);
hold on
plot(subsetA(:,5),subsetA(:,6),':','color','#C46C9C','linewidth',3);
hold on
heII=boxplot(UII,'Positions',position,'Widths',0.1);
ylim([-10 2])
hold on
xlim([0 2])
xticks(0:0.2:2);
xticklabels('auto')
legend('Bernoulli ($I_{ef}$)', 'Timoshenko
($I_{net}$)','ABAQUS','Location','northwest','FontSize',12,'interpreter','latex')
xlim([0 2])
grid on
set(gca,'FontSize',12,'fontname','Times New Roman')
xlabel(' Span length [m]','FontSize',12)
ylabel('  Deflection [mm] ','FontSize',12)
title({' Deflection of the CLT beam (Configuration B) based on' ,'different beam
theories in MATLAB, FEM modeling in ABAQUS and experimental data', '(beam
width equal to 0.2 m, $K_s$=0.24) '},'FontSize',12,'fontname','Times New
Roman','fontweight','bold','interpreter','latex')
%%  (Configuration C)
figure (3)
grid on
x=(coord(:,1)');  % x=(coord(:,1)'/L_ref);
hold on
plot(x,1000*a_3(2:3:end,1)','linewidth',2)
hold on
plot(x,1000*a_t(2:3:end,1)','linewidth',2)
hold on
plot(subsetA(:,8),subsetA(:,9),':','color','#C46C9C','linewidth',3)
```

```
hold on
heIII=boxplot(UIII,'Positions',position,'Widths',0.1);
ylim([-12 2])
hold on
xlim([0 2])
xticks(0:0.2:2)
xticklabels('auto')
legend('Bernoulli ($I_{ef}$)', 'Timoshenko
($I_{net}$)','ABAQUS','Location','northwest','FontSize',12,'interpreter','latex')
xlim([0 2])
grid on
set(gca,'FontSize',12,'fontname','Times New Roman')
xlabel(' Span length [m]','FontSize',12)
ylabel('  Deflection [mm] ','FontSize',12)
title({' Deflection of the CLT beam (Configuration C) based on' ,'different beam
theories in MATLAB, FEM modeling in ABAQUS and experimental data', '(beam
width equal to 0.2 m, $K_s$=0.24) '},'FontSize',12,'fontname','Times New
Roman','fontweight','bold','interpreter','latex')
```